



The University of
Nottingham

Unsteady Wind Effects on Natural Ventilation

Bo Wang, Bsc.

Department of Architecture and Built Environment

Thesis submitted to the University of Nottingham

For the degree of Doctor of Philosophy

June 2010

Abstract

Ventilation stacks are becoming increasingly common in the design of naturally ventilated buildings. The overall aim of the work described is ultimately to improve design procedures for such buildings.

This thesis presents the experimental and theoretical investigation of unsteady wind effects on natural ventilation of a single envelope with multiple openings for both wind alone, and wind and buoyancy combined cases. There are two types of openings: namely the sharp-edged orifice and the long opening (stacks being treated as long openings). Two methods are adopted: 1) direct wind tunnel measurements using the hot-wire technique; 2) theoretical analysis using steady and unsteady envelope flow models. For the wind alone experiments, the influences of wind speed, wind direction and opening configuration on flow patterns are studied. For the wind and buoyancy combined tests, the transitional process between wind dominated and buoyancy dominated states are investigated. The direct velocity measurements provide the criteria for testing the validity of the theoretical models, and ways to improve them. Additionally, improvements are made to the experimental techniques: e.g. a precise unsteady calibration method of the hot-wire is developed; improvements of pressure measurements are also investigated.

The experimental technique works well with multiple stacks. Even though small openings are used, some dependence of the mean pressure coefficient on opening configuration is observed. The theoretical models also work reasonably well with multiple stacks, yet it is observed that the accuracy of the theoretical models decrease with the increasing number of openings, and is sensitive to the chosen discharge coefficient which defines the characteristics of ventilation openings.

Acknowledgement

I would like to thank my parents and family for their patience, faith and support throughout my PhD as well as all my friends.

I would also like to thank the technicians at the School of the Built Environment for their assistance, especially Mr. David Oliver, Mr. David Taylor, and Mr. Robert Clarke, without their hard work, it is impossible to carry out the experiments. And I also appreciate the support of Prof. Masaaki Ohba from Tokyo Polytechnique University for providing the wind-tunnel instrument.

Funded by the EPSRC, their support is greatly acknowledged.

Most importantly, my special gratitude goes to my supervisor Dr. David Etheridge for his guidance and excellent supervision all through my research.

Contents

Abstract	i
Acknowledgement	ii
Contents	iii
List of Figures	vii
List of Tables	xiii
Glossary of Notation	xiv
1 Introduction.....	1
1.1 Background to research.....	2
1.1.1 Original project proposal	2
1.1.2 Objective and scope	3
1.1.3 Summary of previous research.....	4
1.2 Outline of the thesis.....	5
2 Theoretical models of envelope flow.....	7
2.1 Introduction.....	7
2.2 Steady model.....	9
2.2.1 Flow rate determination	9
2.2.2 Pressure difference.....	10
2.2.3 Mass conservation of an enclosed envelope	13
2.2.4 Solution of set of equations.....	14
2.2.5 Uncertainties about C_z and C_p	14
2.3 QT model	15
2.3.1 Envelope flow equation	15
2.3.2 Pressure difference.....	17
2.3.3 Mass conservation.....	17
2.3.4 Solutions of set of equations of QT model	18
2.4 Nondimensional QT model.....	19

2.5 Summary	20
3 Experiments – wind alone tests.....	21
3.1 Introduction.....	21
3.2 Experimental techniques	22
3.2.1 Model description	22
3.2.2 Calibration of instruments.....	28
3.2.3 Stack flow & pressure measurements and data acquisition	34
3.2.3 Similarity analysis.....	36
3.3 Experiment scope.....	38
3.4 Experiment results and analysis.....	40
3.4.1 Mean flow balance	40
3.4.2 Instantaneous flow balance	45
3.4.3 Investigation of flow reversal	47
3.5 Summary and conclusions	56
4 Important parameters – C_z and C_p	57
4.1 Introduction.....	57
4.2 C_p - literature review	58
4.3 C_p – results and analysis	60
4.3.1 Effect of building Reynolds number.....	60
4.3.2 Effect of wind direction	60
4.3.3 Effect of stack geometry	61
4.3.4 Effect of opening configuration	62
4.3.5 C_p correlations between openings.....	66
4.3.6 C_p correlations between opening pressure and internal pressure.....	69
4.4 C_z - literature review	71
4.4.1 Sharp-edged openings.....	71
4.4.2 Long openings.....	74
4.4.3 Special openings	74
4.5 C_z – results and analysis.....	75
4.5.1 Observed effect of wind speed on dimensionless flow rate.....	75
4.5.2 Still-air C_z values	77
4.5.3 Unsteady C_z values - external flow effects	78

4.6	Summary and conclusions	82
4.6.1	C_p – conclusions.....	83
4.6.2	C_z – conclusions	83
5	Experiments – wind and buoyancy combined	84
5.1	Literature review	84
5.1.1	Buoyancy and wind opposing ventilation modes	85
5.1.2	Multiple solutions of steady ventilation modes	86
5.1.3	Transitions between multiple steady states.....	88
5.2	Experiment descriptions.....	90
5.2.1	Temperature measurements	90
5.2.2	Similarity analysis.....	91
5.2.3	Experiment scope and procedure	93
5.3	Results and analysis	96
5.3.1	Transitions between displacement ventilation and mixing ventilation.....	96
5.3.2	Initial condition effects	106
5.4	Summary and conclusions	113
6	Theoretical calculations and comparisons with measurements	115
6.1	Introduction.....	115
6.1.1	Structure of chapter.....	115
6.1.2	Range of calculations.....	116
6.2	Determination of flow direction from pressures.....	117
6.3	Envelope flow model comparisons - wind alone tests.....	122
6.3.1	Variation of nondimensional flow rate with wind direction.....	122
6.3.2	Variation of nondimensional flow rate with building Reynolds number (wind speed).....	127
6.4	Reversal flow prediction using QT model for wind alone ventilation.....	131
6.4.1	Comparisons for instantaneous flow rate and internal pressure	131
6.4.2	Flow reversal and wind direction.....	133
6.4.3	Flow reversal and Reynolds number.....	134
6.4.4	Reversal and $\Delta C_p / \sigma_{\Delta C_p}$	136
6.5	Wind and Buoyancy combined.....	136
6.5.1	Steady model calculations.....	136

6.5.2	QT model calculations	138
6.6	Summary and conclusions	144
7	Improvements in experimental techniques	146
7.1	Introduction.....	146
7.2	Comparison of instantaneous pressure and hot-wire measurements	146
7.2.1	Effect of fixing the rod.....	148
7.3	Precise unsteady calibration of hot-wire.....	151
7.4	Tests of split film probe	158
7.5	Improvements of pressure measurements.....	166
7.5.1	Introduction.....	166
7.5.2	Inaccuracy in pressure parameter and possible reasons.....	166
7.5.3	Investigation of the possible reasons	168
7.5.4	Improvements made by covering P_{in} and taking the average pressure of P_{st}	176
7.6	Summary and conclusions	178
8	Conclusions, discussion, and suggestions for future work	180
8.1	Overview of chapter.....	180
8.2	Summary of the thesis.....	180
8.2.1	Improvements of experimental techniques	180
8.2.2	Widening the scope of the technique to multiple stacks, and buoyancy and wind combined tests.....	181
8.2.3	The effects of opening configuration on pressure coefficient and the effects of external flow on discharge coefficient.....	182
8.2.4	Assessment of theoretical models.....	182
8.3	Originality and contribution to knowledge.....	182
8.4	Discussion about possibilities of integrating the findings of this thesis into design guides/tools.	183
8.5	Suggestions for future work.....	185
Appendix I	Matlab programme.....	186
Appendix II	Deduction of nondimensional equations of QT model.....	198
Appendix III	Three-dimensional CFD simulation.....	204

List of Figures

Figure 1.1 Thesis structure.....	6
Figure 2.1 The envelope with an opening separating two spaces.....	9
Figure 2.2 Pressure measurement	12
Figure 3.1 Two-stack model and wind direction ϕ	22
Figure 3.2 Plan view of IBT wind tunnel (source: (Chiu, 2004)).....	23
Figure 3.3 Four stack model shown with and without stack boxes	24
Figure 3.4 Stack geometry and hot-wire probe.....	25
Figure 3.5 Plan view of stack and orifice positions, with wind direction.....	26
Figure 3.6 Section of the environmental boundary layer wind tunnel.....	27
Figure 3.7 Photos of the TPU wind tunnel working section and the four stack model	27
Figure 3.8 Wind profile at working section.....	27
Figure 3.9 Arrangement for steady calibration and C_z measurement	29
Figure 3.10 Arrangement of unsteady calibration	30
Figure 3.11 Photo of the piston.....	30
Figure 3.12 Combined steady and unsteady calibration	31
Figure 3.13 Final curve fitting	31
Figure 3.14 Calibration of pressure transducers and digital anemometer	32
Figure 3.15 Linear fitting of PT1 (pressure against voltage output).....	33
Figure 3.16 Linear fitting of digital anemometer using reference PT6	33
Figure 3.17 Stack flow and pressure measurement; data acquisition	34
Figure 3.18 Dependence of C_z and C_p on Re	37
Figure 3.19 Wooden box between two stacks and the separation distance	41
Figure 3.20 Variation of r and r_v with the separation distance	42
Figure 3.21 Rod fixed inside the model.....	43
Figure 3.22 Mean flow rate balance of (S1234).....	44
Figure 3.23 Instantaneous velocity of (S1234).....	45
Figure 3.24 Spectral analysis of velocity sum of (S1234); with wind speed of 5 m/s and 2 m/s	46
Figure 3.25 Spectral analysis of velocities of stack 1 and 2 for (S1234), with a wind speed of 5 m/s.....	46

Figure 3.26 Spectral analysis of pressure of Orifice 1 for (S1234), with a wind speed of 5 m/s	47
Figure 3.27 Variation of r with Re_b (S34 O12 S3 denotes stack 3 for the case of S34_O12 ..	49
Figure 3.28 Variation of r with wind direction – two stacks, four orifices (S13_O1234).....	49
Figure 3.29 C_p variation with wind direction – two stacks, four orifices (S13_O1234)	50
Figure 3.30 Flow reversal variation with wind direction for Stack 3 (S34_O12)	51
Figure 3.31 Stack C_p variation with wind direction and stack geometry.....	52
Figure 3.32 Flow reversal variation with wind direction for stack 1,2,3 and 4 (S1234_O12) 53	
Figure 3.33 Flow reversal variation with wind direction of stacks 1,2,3 and 4 (S1234_O1234)	54
Figure 3.34 Flow reversal of Stack 3 for different wind directions and opening configurations	55
Figure 3.35 Variation of r with $\Delta C_p/\sigma_{\Delta C_p}$ (“Ref” is (Cooper and Etheridge, 2007)).....	55
Figure 4.1 Variation of C_p with U_{ref} (S1234_O12).....	60
Figure 4.2 C_p variation with wind direction (S1234).....	61
Figure 4.3 C_p variation with wind direction (S13_O1234).....	61
Figure 4.4 Stack C_p variation with wind direction and stack geometry.....	62
Figure 4.5 Stack C_p variation with increasing number of orifices, $\phi = 0$	63
Figure 4.6 Stack and orifice C_p with increasing number of orifices, $\phi = 90$	64
Figure 4.7 Stack and orifice C_p with increasing number of orifices, $\phi = 0$	64
Figure 4.8 Orifice C_p with increasing number of orifices in the cases of different wind directions.....	65
Figure 4.9 Stack C_p with increasing number of orifices in the cases of different wind directions.....	65
Figure 4.10 Variation of stack pressure correlations with Re_b for $\phi = 0$ (S1234).....	67
Figure 4.11 Variation of stack pressure correlations with wind directions (S1234)	67
Figure 4.12 Variation of stack pressure correlations with the increasing number of orifices for $\phi = 90$	68
Figure 4.13 Variation of stack pressure correlations with the increasing number of orifices for $\phi = 0$	69
Figure 4.14 Stack pressure correlation with internal pressure with increasing number of orifices, $\phi = 0$	70

Figure 4.15 Stack pressure correlation with internal pressure with increasing number of orifices, $\phi=90$	70
Figure 4.16 Variation of u_{st}/U_{ref} with U_{ref} (S1234)	76
Figure 4.17 Variation of u_{st}/U_{ref} with U_{ref} (S1234_O12)	77
Figure 4.18 Still-air C_z against Re_{st} for inward and outward flow	78
Figure 4.19 Variation of C_z with Re_{st} wind on case obtained from (S1234)	79
Figure 4.20 Variation of C_z with Re_{st} wind on case obtained from (S1234_O12)	80
Figure 4.21 Variation of C_z with Re_{st} compared with still-air results	81
Figure 4.22 Variation of C_z with Re_{st} compared with still-air results of inward flow; Ref 1 (Costola and Etheridge, 2007), Ref 2 (Cooper and Etheridge, 2007)	81
Figure 4.23 Variation of C_z with Re_{st} compared with still-air results of outward flow	82
Figure 5.1 Localised heat source ventilation: (1) displacement ventilation driven by a localised heat source alone; (2) displacement ventilation driven by buoyancy and opposing wind; (3) mixed ventilation driven by buoyancy and strong opposing wind	85
Figure 5.2 Multiple solutions of steady states when buoyancy opposes wind (solid line: wind dominated ventilation; dashed line: buoyancy dominated ventilation)	87
Figure 5.3 Model with heater and temperature measurements	91
Figure 5.4 Transition from wind dominated to buoyancy dominated, and then back to wind dominated ventilation for two-stack case (stacks 1 and 3)	96
Figure 5.5 Variation of temperature and reversal percentage of stack 3 for $U_{ref}=1.2$ m/s (S13_O1234_U1.2)	97
Figure 5.6 Variation of temperature and reversal percentage of stack 3 for $U_{ref}=1.4$ m/s (S13_O1234_U1.4)	97
Figure 5.7 Reversal percentage against difference between the averaged box temperature and T_{room}	98
Figure 5.8 Transitions from displacement ventilation to mixing ventilation, and then back to displacement ventilation	99
Figure 5.9 Variation of temperature and reversal percentage of stack 3 for $T_l=57$ °C (S13_O1234_T57)	99
Figure 5.10 Variation of temperature and reversal percentage of stack 3 for $T_l=60$ °C (S13_O1234_T60)	100
Figure 5.11 Reversal percentage against wind speed	101

Figure 5.12 Transition from wind dominated ventilation to buoyancy dominated ventilation	102
Figure 5.13 Temperatures and flow direction change with time	102
Figure 5.14 Reversal percentage, flow rate of stack 3 (q) and ventilation flow rate (fresh air) of the box (q_f) against temperature difference	103
Figure 5.15 Dimensionless flow rate against relative wind force and buoyancy force	104
Figure 5.16 Dimensionless ventilation rate against $1/Ar$	105
Figure 5.17 Reversal percentage against relative wind force and buoyancy force for all cases	106
Figure 5.18 Initial condition effects of two-stack (stack 1 and stack 3) case	107
Figure 5.19 Initial condition effects of four-stack case	107
Figure 5.20 Initial condition effects of four stack and one orifice (Orifice 1).....	108
Figure 5.21 Velocities of initial condition effects for the case of two stacks (stacks 1 and 3)	109
Figure 5.22 Effect of heat source fluctuation.....	111
Figure 5.23 Temperature and velocity fluctuations of buoyancy alone two-stack case (stacks 1 and 3)	112
Figure 6.1 Calculated $\overline{\Delta C_{pi}}$ and measured u_i/U_{ref} of stack 1 (S1234)	119
Figure 6.2 Calculated $\overline{\Delta C_{pi}}$ and measured u_i/U_{ref} of stack 3 (S1234)	119
Figure 6.3 Calculated $\overline{\Delta C_{pi}}$ and measured u_i/U_{ref} of stack 1 (S1234_O12)	120
Figure 6.4 Calculated $\overline{\Delta C_{pi}}$ and measured u_i/U_{ref} of stack 3 (S1234_O12).....	120
Figure 6.5 Calculated $\overline{\Delta C_{pi}}$ and measured u_i/U_{ref} of stack 1 (S1234_O1234).....	121
Figure 6.6 Calculated $\overline{\Delta C_{pi}}$ and measured u_i/U_{ref} of stack 3 (S1234_O1234).....	121
Figure 6.7 Variation of q/AU_{ref} (S1234) – steady model	123
Figure 6.8 Variation of q/AU_{ref} (S1234_O12) – steady model and QT model	124
Figure 6.9 Variation of q/AU_{ref} (S13_O1234) – steady model	124
Figure 6.10 C_z of sharp-edged orifice for steady (still-air) and unsteady (wind) conditions.	125
Figure 6.11 Variation of q/AU_{ref} (S13_O1234); changed C_z – steady model and QT model	126
Figure 6.12 Effect of Reynolds number (S1234) – steady model.....	127
Figure 6.13 Effect of Reynolds number (S1234_O12) – steady model.....	128
Figure 6.14 Flow directions for two cases (S1234) and (S1234_O12).....	128

Figure 6.15 Calculated effect of Reynolds number (S1234_O12) with changed C_z – steady model.....	129
Figure 6.16 Calculated and measured effect of Reynolds number (S1234_O12) with changed C_z - QT model	130
Figure 6.17 Comparison for stack flow rate; stack 1 (S1234_O12)	131
Figure 6.18 Comparison for stack flow rate; stack 2 (S1234_O12)	132
Figure 6.19 Comparison for internal pressure (S1234_O12).....	132
Figure 6.20 Reversal percentage from measurements (S1234_O12)	133
Figure 6.21 Reversal percentage from QT model (S1234_O12).....	133
Figure 6.22 Comparison of reversal percentage of scale model (S1234_O12)	134
Figure 6.23 Predictions of reversal percentage for full scale cases (1:100)	135
Figure 6.24 Variation of r with $\log(Re_b)$ for model scale and full scale.....	135
Figure 6.25 Variation of r with $\Delta C_p / \sigma_{\Delta C_p}$ – measurement and QT model	136
Figure 6.26 Comparison of flow rate between steady envelope model and measurements for two opening configurations (S3_O1), (S13_O1234).....	137
Figure 6.27 Assumptions about buoyancy term	138
Figure 6.28 Comparison of instantaneous flow rate of wind alone case (S3_O1)	140
Figure 6.29 Comparison of instantaneous flow rate of wind and buoyancy combined case (S3_O1).....	140
Figure 6.30 Comparison of instantaneous internal pressure (S3_O1); Second graph x axis expanded	141
Figure 6.31 Comparison of instantaneous flow rates (Stack 1,3; Orifice 1,2,3,4).....	142
Figure 6.32 Comparison of instantaneous internal pressure (S13_O1234), measurements of P_1 and P_3 are presented as reference.....	143
Figure 6.33 Comparison of reversal percentage of stack 3 as a function of dT (S3_O1).....	144
Figure 6.34 Comparison of reversal percentage of stack 3 (Stack 1,3; Orifice 1,2,3,4).....	144
Figure 7.1 Comparison of pressure and velocity measurement.....	147
Figure 7.2 Velocity and pressure signals from tapping different parts of the model.....	148
Figure 7.3 Comparison of pressure measurement and velocity measurements (graphs in the right column are with the rod fixed)	150
Figure 7.4 New sensor for unsteady calibration	152
Figure 7.5 Photo of the piston with the new sensor	152

Figure 7.6 Signal from the sensor over a period of 0.02 s	153
Figure 7.7 Curve fittings of four different oscillating frequencies of the piston	155
Figure 7.8 Velocity profile of accelerating and decelerating period within a half oscillating circle (accelerating: solid line; decelerating: dashed line)	156
Figure 7.9 velocity signal of (S14_O34_90).....	157
Figure 7.10 Final curve fitting	157
Figure 7.11 Split-film probe	159
Figure 7.12 Hot-wire and split-film probe fitted in the stack box	159
Figure 7.13 Results for 0.76 Hz.....	160
Figure 7.14 Results for 1.56 Hz.....	162
Figure 7.15 time lag of the probes	164
Figure 7.16 Variation of r with $\Delta C_p / \sigma_{\Delta C_p}$ for two –stack and four-stack cases compared with Ref (Cooper and Etheridge, 2007)	166
Figure 7.17 Pressure measurement	167
Figure 7.18 Pressure measurements and wind direction.....	168
Figure 7.19 Model with the cup with no top above the internal pressure tapping.....	172
Figure 7.20 Meshing of model section	174
Figure 7.21 Velocity vectors of the flow field with no cover above internal pressure tapping	174
Figure 7.22 Velocity vectors of the flow field with a cover above internal pressure tapping	175
Figure 7.23 r against $\Delta C_p / \sigma_{\Delta C_p}$ with P_{in} covered and the average pressure of P_{st} was taken, compared with results from TPU	176
Figure 7.24 C_z variation with Re_{st} compared with steady state (still-air) result of inward flow; Ref 1 (Costola and Etheridge, 2007), Ref 2 (Cooper and Etheridge, 2007)	177
Figure 7.25 C_z variation with Re_{st} compared with steady state (still-air) result of outward flow; Ref 1 (Costola and Etheridge, 2007)	178

List of Tables

Table 3.1 Experiment scope of four-stack model	39
Table 3.2 Reversal percentages of two-stack model.....	41
Table 3.3 Reversal percentage with and without the rod.....	43
Table 4.1 Pressures of stack outlets with different orifices	63
Table 5.1 Experimental scope of wind and buoyancy combined tests	94
Table 6.1 Determination of flow direction from pressures.....	116
Table 6.2 Steady model calculations of wind alone cases (high-lighted cases are also calculated with QT model).....	117
Table 6.3 QT model calculations of wind and buoyancy combined cases	117
Table 6.4 C_z values of orifices.....	126
Table 7.1 Oscillation frequency and maximum velocity of unsteady calibration	153
Table 7.2 Time lag to detect flow reversal for the two probes	165
Table 7.3 Comparison of average pressure measurements with the one fixed position measurements.....	169
Table 7.4 Pressure difference between P_{in} and P_{wall}	170
Table 7.5 Comparisons between two TPU tests (S14*_O12_90) and (S14*_O1234_90)....	171
Table 7.6 Comparisons of P_o - P_{in} between P_{in} covered and P_{in} exposed.....	172

Glossary of Notation

Symbol	Meaning	Unit
A	Area of opening	$[\text{m}^2]$
a	Coefficient in quadratic equation, eq. (2.26)	$[\text{Pa s}^2/\text{m}^6]$
Ar	Archimedes number, eq. (5.3)	
B	Specific buoyancy flux, eq. (2.51)	
b	Coefficient in quadratic equation, eq. (2.26)	$[\text{Pa s}^2/\text{m}^3]$
C, D	Coefficients in equation (2.24)	
c	Speed of sound	$[\text{m/s}]$
C_p	Pressure coefficient, eq. (2.10)	
ΔC_p	Difference of pressure coefficient	
C_z	Discharge coefficient, eq. (2.4)	
$C_{z\infty}$	Discharge coefficient at high Reynolds number	
d	Diameter of opening	$[\text{m}]$
D	Compressibility parameter, eq. (2.53)	
E	Voltage output of hot-wire	$[\text{V}]$
F	Inertia parameter, eq. (2.52)	
g	Gravitational force per unit mass	$[\text{m/s}^2]$
H	Reference building dimension	$[\text{m}]$
l_e	Effective inertial length of opening, eq. (2.21)	$[\text{m}]$
L	Length of opening	$[\text{m}]$
N	Number of openings	
P	Pressure	$[\text{Pa}]$
ΔP	Pressure difference	$[\text{Pa}]$
P_{ref}	Reference pressure	$[\text{Pa}]$

P_w	Surface (static) pressure of the wind	[Pa]
p_w	Dynamic wind pressure	[Pa]
q	Volume flow rate through opening	[m ³ /s]
q'	Nondimensional flow rate defined by (Eq. 3.15) [-].	
Re_o	Opening Reynolds number. eq. (4.2)	
Re_{st}	Stack Reynolds number	
Re_b	building Reynolds number, eq. (3.6)	
r	Time reversal percentage	[%]
r_v	Volume reversal percentage	[%]
S_i	Flow sign	
S	Distance between stack and obstruction	[mm]
t	time	[s]
t'	tU/H	
T	temperature	[°C]
u	Mean velocity through the opening	[m/s]
$U (U_{ref})$	Reference velocity	[m/s]
V	volume of space	[m ³]
	Cross flow velocity parallel to the wall	[m/s]
z	Height of opening	[m]
γ	Ratio of specific heats	
ρ	Density	[kg/m ³]
$\Delta\rho$	Density difference	[kg/m ³]
ΔT	Temperature difference	[K]
ϕ	Wind direction	[°]
μ	Viscosity	
ν	Kinematic viscosity ($\nu = \mu/\rho$)	
$\sigma_{\Delta C_p}$	Standard deviation of ΔC_p [-].	
U_b	Buoyancy velocity. Eq. (5.6)	

Subscripts

1,2,3,4	Opening number.
f	Fresh air
I, in	Internal.
room	External space outside the model box
S, st	Stack
o	Orifice

1 Introduction

Natural ventilation for buildings is widely acknowledged to be an energy efficient ventilation strategy with several advantages such as popularity, lower cost than other ventilation systems, and minimum maintenance (Liddament, 1996). In a mild climate, such as the UK, mechanical systems are difficult to justify, especially in housing. For this reason, reliable and well-controlled natural ventilation systems have important commercial benefits. The advantages as well as associated problems were summarised by Chiu (2004). Natural ventilation aims at best utilising natural wind energy and stack effect generated by the building occupants, heating system, office equipments, and incident gains. The aim of ventilation is to provide sufficient fresh air and thermal comfort for the occupants, meanwhile avoiding possible failures during operation like cold draught caused by reversing flow of a chimney. To achieve these however, there are difficulties in the design stage due to uncertainties. The uncertainties associated with the unsteadiness of the natural wind are what this thesis is concerned with.

Starting from a simple case, to design a natural ventilation strategy for a single cell envelope to meet required ventilation rate, the following questions arise. Where to locate the openings; what are the sizes of the openings; are the pressure coefficient data source on a building envelope e.g. CIBSE AM10 (2005) applicable universally in practice? Having determined the locations and sizes of the openings, in reality will they behave as expected for the hypothetical condition of steady wind force? Taking into account the unsteadiness of the wind, the resultant airflows are influenced by the following factors (Haghighat et al., 1991): the resistance of the openings; the inertia of the air mass in the openings; and the compressibility of the room air. In terms of the wind force, the uncertainties are the wind direction, wind speed, the frequency characteristics of the wind pressures, their power spectra and the correlation between them.

1 Introduction

Ventilation stacks are becoming increasingly common in the design of naturally ventilated buildings. They offer a method for achieving a fixed flow pattern irrespective of internal and external conditions e.g. upward stack flow should be maintained under all wind conditions and opening configurations, at least with positive buoyancy, by positioning the stack outlet at high level in a region of relatively low wind pressure. However, undesirable flow reversal may still occur due to the fluctuating wind force which yields a high pressure in the stack outlet region. How to characterise the resistance of a stack in the theoretical envelop model? What are the criteria for the occurrence of flow reversal? How do stacks interact in a multiple stack ventilation system? In a wind and buoyancy combined situation, how does the stack/stacks behave? All these questions above will be studied in this thesis.

In this chapter, the background to research in this thesis is presented. Then the objectives are listed, followed by the methodologies. Finally, the structure of this thesis is outlined.

1.1 Background to research

1.1.1 Original project proposal

The research described is a continuation of work previously carried out at Nottingham on unsteady flow in natural ventilation stacks (e.g. (Chiu, 2004)). The work was funded as an EPSRC project (responsive mode) and the project proposal formed the framework. In that proposal the following technical objectives were listed

- 1) To improve the basic hot-wire technique – calibration, characterisation
- 2) To widen the range of use of the technique – multiple stacks, buoyancy
- 3) To generate data under a wider range of conditions relevant to design procedures
- 4) To assess theoretical models (QT and CFD)
- 5) To formulate and disseminate the results for design purposes (and PhD write-up).

Tasks 3 and 4 will be carried out in collaboration with TPU.

1 Introduction

As the project proceeded some changes were made to these objectives and the actual work carried out is described in Section 1.1.2 below:

1.1.2 Objective and scope

The research in this thesis is an EPSRC (Engineering and Physical Science Research Council) project. The overall objectives of this project are to investigate the unsteady wind effects on natural ventilation by experiments (hot-wire technique), to assess theoretical models and to formulate the results so as to improve design procedures for naturally ventilated buildings. In addition, it was proposed as a collaborative project with TPU (Tokyo Polytechnique University), therefore the author carried out part of the tests using a TPU wind tunnel.

The scope of the thesis is listed as the four tasks below:

Task 1. Improvement of hot-wire technique – calibration and configuration

To optimize the hot-wire technique we need to know more about the characteristics of the technique under a wider range of operating conditions. The intention is to carry out unsteady calibration using a precise piston (see Chapter 8) that generates a known fluctuation of volume flow rate against time, as well as steady calibration using a fan across a wide range of resistance. A completely different type of probe configuration (e.g. split-fibre film) will also be tested to see if it is better than the dual hot-wire (Chapter 7).

Task 2. Widening the scope of the technique – multiple stacks, wind and buoyancy combined.

This is the first time that simultaneous instantaneous measurements have been made in multiple stacks. Firstly, undesirable interaction among multiple stacks will be detected by varying the geometry of the building and the stacks (Chapter 3). Secondly, the effects of buoyancy on stack flow will be investigated. The status of flow through multiple stacks could depend on the initial conditions. Reproduction of this initial condition effects are to be carried out using the hot-wire technique (Chapter 5).

Task 3. Studying the external flow effects on discharge coefficient and the effects of building configuration on pressure coefficient.

1 Introduction

Previous research has shown that the discharge coefficient can be significantly reduced by the presence of cross-flow (flow component parallel to the envelope). The new tests will concentrate on the external flow effects on long openings (stacks) (Chapter 4). Additionally, the effects of opening configuration on pressure coefficient and the correlation between pressure coefficients are discussed (Chapter 4).

Task 4. Assessment of theoretical models and design suggestions

A number of test configurations (model, openings, wind, and buoyancy) will be chosen for assessment of steady and unsteady envelope flow models (Chapter 6). How to transfer research outcomes of this thesis into design guides/tools will be discussed (Chapter 8).

1.1.3 Summary of previous research

To appreciate the above objectives it is helpful to summarise the previous research at Nottingham.

Firstly, a novel hot-wire technique had been developed to measure the instantaneous magnitude and direction of the flow rate in a stack at model scale in a wind tunnel. The technique was then used for the case of an envelope with a single stack and a single orifice opening. Most tests were done with wind alone, with some preliminary tests with buoyancy. A key objective was to extend the investigations to an envelope with multiple stacks and multiple orifices, firstly for the wind alone case and then with buoyancy. Much of the originality of the thesis lies in this objective. As far as is known no such work has been done before.

Secondly, in the previous work an unsteady envelope model (QT model) had been developed. This was compared with the wind tunnel measurements and encouraging agreement had been found, thus indicating that the model could be used for full-scale design. Another important objective therefore was to extend the QT model to multiple openings and to validate it with the experimental measurements.

1 Introduction

A third important area in the previous research was the effect of external flow on the discharge coefficients of openings. Significant effects were found under certain conditions and these are important to design. It was therefore necessary to investigate these effects further. The dependency of pressure coefficient on wind speed were studied, further studies of the effects of opening configurations on the pressure coefficients will be carried out.

Another important area was to investigate the possibility of improving the hot-wire technique. The technique had been shown to be very repeatable, but there seemed to be some scope for improving accuracy e.g. by improving the calibration or by using a different type of sensor.

The underlying reason for all the above work is to improve design procedures for ventilation stacks. This work has been extended not only by looking at the performance of the QT model but also at conventional steady models.

1.2 Outline of the thesis

Chapter 1 gives a background of unsteady natural ventilation; and a brief introduction of this thesis. Chapter 2 introduces the theoretical envelope flow models, including the steady model and unsteady model (QT). Chapter 3 describes the experimental technology and the analysis of the results of wind alone tests, with a focus on flow reversal through stacks. Chapter 4 discusses two important parameters in the envelope flow model: the wind pressure coefficient and discharge coefficient. It also presents some results of these two parameters from wind alone tests. Chapter 5 presents the wind and buoyancy combined tests and focuses on transitions between different ventilation modes and the effects of initial conditions. Chapter 6 contains the calculations of both steady and unsteady models using data input from Chapter 3 and 5, with comparisons between the calculations and measurements. Chapter 7 describes some explorations during the experiments and some improvements in experimental techniques. Chapter 8 gives some design suggestions based on the research carried out in this

1 Introduction

thesis, summarises originality and contribution to knowledge, and provides some suggestions for future research. Figure 1.1 shows the structure of the thesis.

There has been relatively little work done on wind-induced unsteady natural ventilation and much of this has been done at Nottingham. In view of this, the review of previous work is covered in individual Chapters as appropriate.

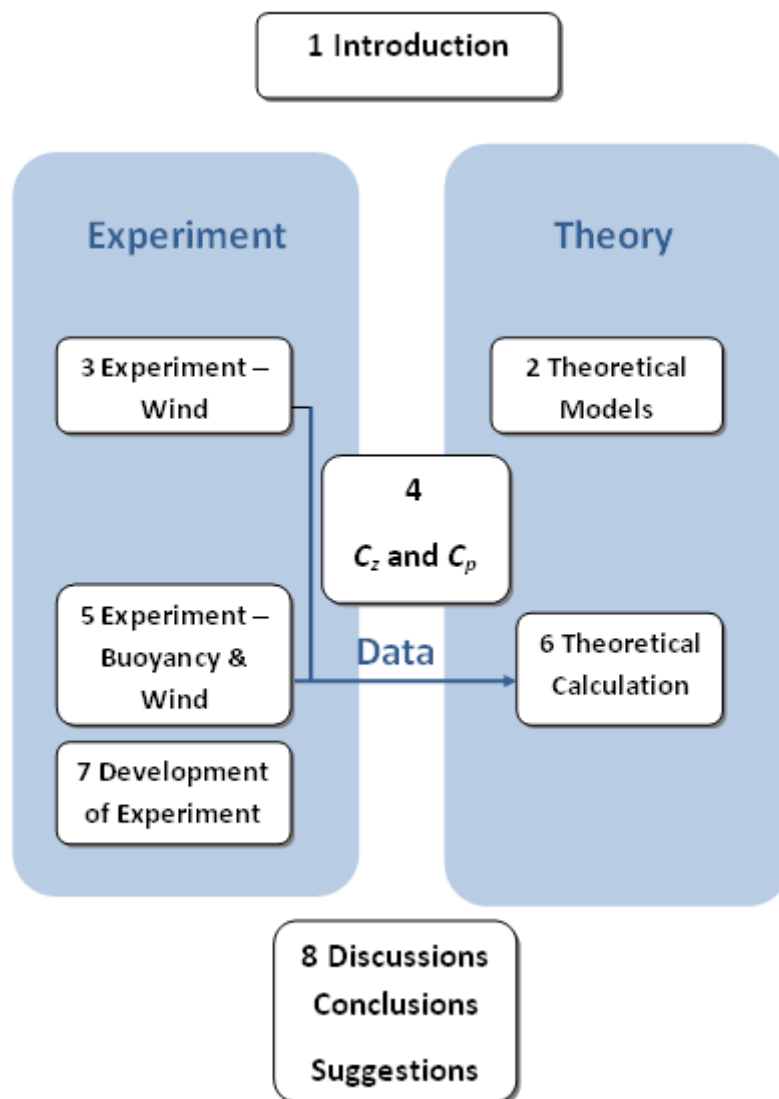


Figure 1.1 Thesis structure

2 Theoretical models of envelope flow

2.1 Introduction

‘Envelope flow models solve the equations that govern the flow of air through openings in the envelope of a building’ (CIBSE AM10, 2005, pp. 39-41). Physical details of flow through envelope openings can be found in Etheridge and Sandberg (1996, pp. 42-48). Provided a pressure difference acts across the opening as a driving force, the air will be forced to pass through the opening. Equation (2.1) applies

$$|u| = C_z \sqrt{\frac{2|\Delta P|}{\rho}} \quad (2.1)$$

where u is the mean velocity through the opening. C_z is the discharge coefficient of the opening, which can be measured in laboratory tests, once it is known, to calculate the flow rate, the left unknown term is the pressure difference. $|\Delta P|$ includes two parts: one is contributed by the density difference between the air separated by the envelope (if the temperatures are different from inside and outside the envelope); the other is contributed by the wind approaching the envelope. At the stagnation point of the envelope, all the kinetic energy of the wind should turn into the static pressure, which then contributes to the overall pressure difference. But apart from the stagnation point, at other areas of the envelope, the kinetic energy of the wind will partly turn into the static pressure. Here another coefficient is defined, namely the pressure coefficient, which can be obtained through wind-tunnel tests. Mass flow rate of all the openings in an envelope should sum up to zero based on mass conservation.

The above paragraph is a simple explanation of envelope flow model. The actual situation is much more complicated. It can be treated with several assumptions about the uncertain

2 Theoretical models of envelope flow

factors like the unsteadiness of the wind, the applicability of the coefficients obtained from steady states, internal temperature distribution. The steady envelope model does not take account of the unsteadiness of the wind. It can be relatively easily adopted in design process, calculation examples can be found in CIBSE AM10 (2005); but it can only give mean values of flow rates, it is also not applicable when flow reversal occurs through the opening simply because the calculated mean ventilation rate may be zero whereas it is not in practice when air fluctuates through openings. Taken into account the unsteady wind effects, the unsteady model is more accurate, and applicable for reversing flows. It can be used to calculate both mean and instantaneous flow rates. However, it requires instantaneous and simultaneous input of pressures, which can only be obtained from wind tunnel or field tests; which gives difficulty in design process.

Taking into account both the unsteadiness of the wind and the inertia and compressibility of the air, the QT (*quasi-steady temporal inertia*) model was developed by Etheridge (2000a; 2000b). The set of equations of QT model were converted to nondimensional form and solved in that form. Nondimensional graphs are used in natural ventilation design in Etheridge (2002). Based on the steady model, parametric studies were carried out. Etheridge and Sandberg (1984) dealt with buoyancy and wind combined ventilation on a building with openings on two side walls. The same parametric method was used by Etheridge and Stanway (1988) studying the influence of the layout of the openings on a single cell envelope with a changing driving force (wind and buoyancy). Details of the parametric study methods are provided in Etheridge and Sandberg (1996, pp. 159-172).

In this chapter, the steady model and QT model will be introduced respectively in Section 2.2 and 2.3. The nondimensional unsteady model is provided in Section 2.4.

2 Theoretical models of envelope flow

2.2 Steady model

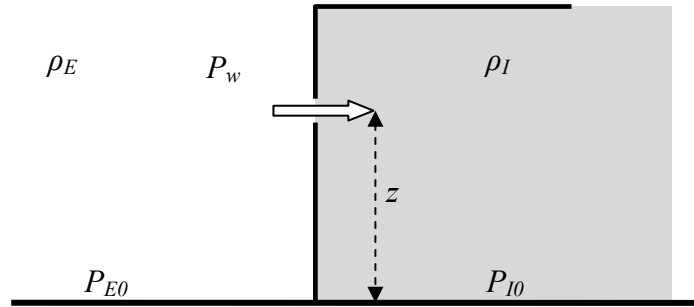


Figure 2.1 The envelope with an opening separating two spaces

Figure 2.1 shows the terms related to an envelope flow. ρ_E is the external air density, ρ_I is the internal density, z is the height of the opening, P_{I0} and P_{E0} are the internal and external absolute hydrostatic pressures at zero height level, P_w is the surface (static) pressure of the wind.

2.2.1 Flow rate determination

The air flow rate through an opening q is determined by the total driving force, which is the pressure difference across the opening, ΔP , and a nondimensional coefficient representing the characteristic of the opening (geometry), namely the discharge coefficient C_z (equation (2.2)). A is the specified geometric area of the opening.

$$|q| = C_z A \sqrt{\frac{2|\Delta P|}{\rho_E}} \quad (2.2)$$

The discharge coefficient is obtained from laboratory tests, by measuring the pressure difference across the opening and the flow rate through the opening, under a still air condition with no temperature difference between the two spaces, when $\rho_E = \rho_I$ in Figure 2.1. C_z is defined by rearranging equation (2.2)

$$C_z \equiv \frac{|q|}{A} \sqrt{\frac{\rho}{2|\Delta P|}} \quad (2.3)$$

2 Theoretical models of envelope flow

2.2.2 Pressure difference

The pressure difference across the opening ΔP is induced by temperature (density) difference between the two spaces and the surface (static) pressure generated by the wind.

In the absence of wind, the outside pressure at the opening height (z) is given by the hydrostatic equation (2.4). The same equation applied to the internal air, gives the internal pressure at the opening level as equation (2.5). The pressure difference induced by density difference is equation (2.6).

$$P_E = P_{E0} - \rho_E g z \quad (2.4)$$

$$P_I = P_{I0} - \rho_I g z \quad (2.5)$$

$$\Delta P = P_{E0} - P_{I0} - \Delta \rho g z \quad (2.6)$$

where $\Delta \rho = \rho_E - \rho_I$

If the internal temperature is not uniform (e.g. stratified), the internal density will vary with the height z , then equation (2.6) becomes

$$\Delta P = P_{E0} - P_{I0} - \rho_E g z + g \int_0^z \rho_I dz \quad (2.7)$$

The pressure difference induced by the wind p_w is calculated using equation (2.8), given the approaching wind velocity U

$$p_w = 0.5 \rho U^2 C_p \quad (2.8)$$

The pressure coefficient C_p is an important term obtained from wind tunnel tests. It varies across the outer surface of the envelope, and is defined by equation (2.9)

$$C_p = \frac{p_{wm}}{0.5 \rho U^2} \quad (2.9)$$

where p_{wm} is the measured pressure at which pressure coefficient is being evaluated. In wind tunnel tests, it is measured by the pressure transducer against a reference pressure P_{ref} in the freestream (i.e. remote from any disturbance). U is the freestream velocity of the fluid. The

2 Theoretical models of envelope flow

reference pressure P_{ref} measuring point can be set at a space outside the wind tunnel without any disturbance (e.g. put the pressure tap in an empty box). Figure 2.2 illustrates how is p_m actually being measured.

1) For the measured wind pressure:

$$p_{wm} = P_2 - P_1 \quad (2.10)$$

$$P_2 = P_w + \rho_E g(z - z_m) \quad (2.11)$$

$$P_1 = P_{ref} + \rho_E g(z_{ref} - z_m) \quad (2.12)$$

$$\text{therefore } p_{wm} = P_w - P_{ref} + \rho_E g(z - z_{ref}) \quad (2.13)$$

In the external flow, the density is uniform and the absolute pressure is the sum of the hydrostatic pressure (due to gravity alone) and the pressure due to motion

$$P_w = P_{E0} - \rho_E g(z - z_0) + p_w \quad (2.14)$$

$$P_{ref} = P_{E0} - \rho_E g(z_{ref} - z_0) + p_{ref} \quad (2.15)$$

where p_w and p_{ref} are the pressures due to motion. As stated above, in the wind tunnel tests, P_{ref} is measured without any disturbance, thus the pressure due to motion is 0, i.e. $p_{ref} = 0$

Substituting equation (2.14) and (2.15) into equation (2.13) gives

$$p_{wm} = p_w \quad (2.16)$$

2 Theoretical models of envelope flow

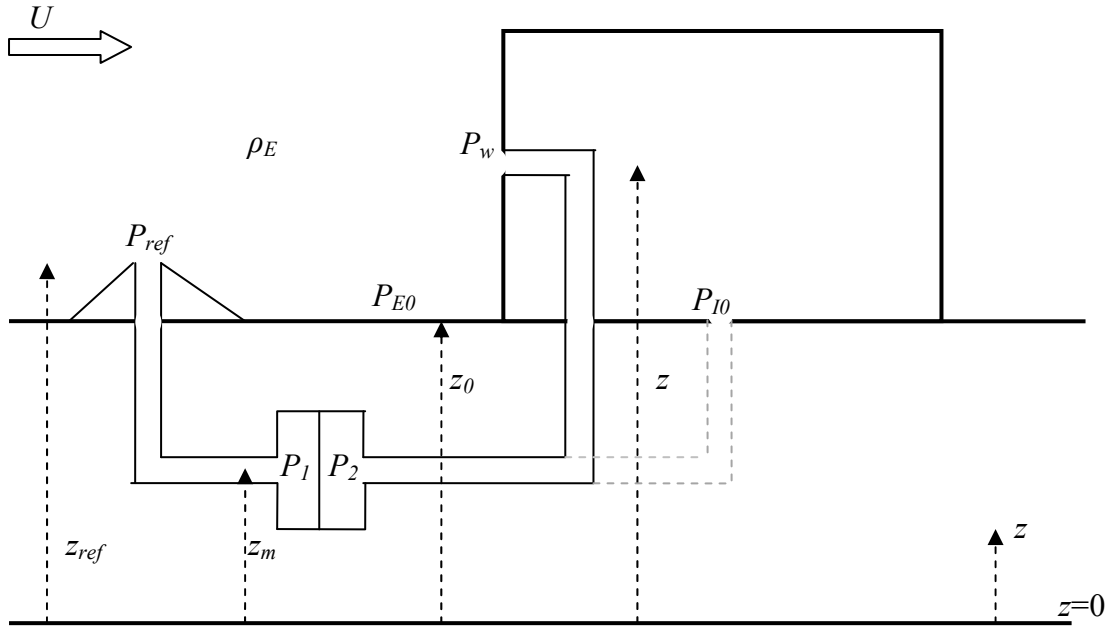


Figure 2.2 Pressure measurement

2) For the measured internal pressure:

$$p_{I0m} = P_2 - P_1 \quad (2.17)$$

$$P_2 = P_{I0} + \rho_E g(z_0 - z_m) \quad (2.18)$$

$$P_1 = P_{ref} + \rho_E g(z_{ref} - z_m) \quad (2.19)$$

$$\text{therefore } p_{I0m} = P_{I0} - P_{ref} + \rho_E g(z_0 - z_{ref}) \quad (2.20)$$

$$P_{I0} = P_{E0} + p_{I0} \quad (2.21)$$

$$P_{ref} = P_{E0} - \rho_E g(z_{ref} - z_0) + p_{ref} \quad (2.22)$$

where p_{I0} is the internal pressure due to motion, p_{ref} the reference pressure due to motion, which can be ignored ($p_{ref} = 0$).

Substituting equation (2.21) and (2.22) into equation (2.20) gives

$$p_{I0m} = p_{I0} = P_{I0} - P_{E0} \quad (2.23)$$

2 Theoretical models of envelope flow

To sum up, the pressure difference induced by both density difference and wind force, the resultant pressure difference across the opening is given by equation (2.24), where $P_{E0} - P_{I0}$ is the hydrostatic pressure difference at zero height level, which is the measured internal pressure.

$$\Delta P = P_{E0} - P_{I0} - \Delta\rho gz + p_w \quad (2.24)$$

$$\Delta P = -p_{I0m} - \Delta\rho gz + p_{mw} \quad (2.25)$$

It should be noted that equation (2.24) is based on two assumptions:

- 1) Density is uniform in the exterior space so that wind pressure adds to hydrostatic pressure.
- 2) Ignore the effect of internal air motion. However there are exceptions, when the overall pressure difference ΔP is very small, the effect of internal air motion is not negligible (see Chapter 7, Section 7.4)

2.2.3 Mass conservation of an enclosed envelope

Assume that there are N openings on the envelope, the total mass flow rate of all the openings should sum up to zero, which gives:

$$\sum_{i=0}^n \rho_i q_i = 0 \quad (2.26)$$

The term q_i includes the flow directions. The flow entering the envelope is defined as positive, the flow sign $S_i = 1$; and the flow exiting the envelope is defined as negative, the flow sign $S_i = -1$.

In the context of ventilation design, the variation of densities can usually be ignored, so equation (2.26) can be simplified to

$$\sum_{i=0}^n q_i = 0 \quad (2.27)$$

2 Theoretical models of envelope flow

2.2.4 Solution of set of equations

The set of equations for an enclosed envelope with N openings are:

$$q_i = C_z A_i S_i \sqrt{\frac{2|\Delta P_i|}{\rho_E}} \quad (2.28)$$

$$\Delta P_i = -p_{I0m} - \Delta \rho g z_i + 0.5 \rho U^2 C_{pi} \quad (2.29)$$

$$\sum_{i=0}^n q_i = 0 \quad (2.30)$$

The equations can be solved by two methods.

1) Implicit method

C_z and C_{pi} are obtained from laboratory tests. For steady model, in the design process, if the height and area of the openings are known, given the wind speed, there are $N+1$ unknowns, which are q_i and ΔP_0 . Substituting equation (2.29) into (2.28) for each opening, there will be $N+1$ equations. The final solutions are obtained by iterations, adjusting p_{I0m} by steps till the mass conservation equation is satisfied.

2) Explicit methods

This method is only applicable for a single cell envelope. If q_i are known (e.g. based on ventilation requirements), and p_{I0m} is specified corresponding to a given flow pattern, the purpose is to determine the area of each opening (A_i are the unknowns). Given the wind speed and the heights of each opening, the set of the equations can be solved directly without iterations.

2.2.5 Uncertainties about C_z and C_p

There are two important parameters in the envelope flow model which associate some uncertainties. For example

- 1) C_z is determined in still air cases; could it be affected by the wind?
- 2) C_p provided in design books are measured in the absence of openings; will they be affected by the presence of the openings?

These issues are investigated in more detail in Chapter 5.

2.3 QT model

In the steady model, it is assumed that the approaching wind is steady, thus the external surface pressure and the internal pressure do not fluctuate. In the unsteady model, the unsteadiness of the air through the opening and the compressibility of the internal air are taken into account. QT model is short for ‘quasi-steady temporal inertia’ model.

2.3.1 Envelope flow equation

‘The quasi-steady assumption is that at each instant of time the flow behaves as if it were truly steady’ (Etheridge, 2000a) apart from the inertia term. Thereby the momentum equation will include two terms: the steady term and the acceleration term

$$\Delta P(t) = f_s(q) + \rho \alpha l_e \quad (2.31)$$

where $\Delta P(t)$ is the pressure difference across the opening at time t

$f_s(q)$ is from the steady flow equation (2.2), expressed by equation (2.31)

$$f_s(q) = \frac{\rho q^2}{2c_z^2 A^2} \quad (2.32)$$

α is the acceleration of the air through the opening

l_e is the effective inertia length

Since $\rho \alpha l_e = \rho \frac{du}{dt} l_e = \rho \frac{dq}{dt} \frac{l_e}{A}$, equation (2.31) becomes

$$\Delta P(t) = f_s(q) + \rho \frac{dq}{dt} \frac{l_e}{A} \quad (2.33)$$

The distance over which the inertia is significant should include the ‘distance’ at the inlet and outlet of the opening, and the distance along the opening L . The former is empirical, and it is expressed by the diameter d of the opening times a constant factor obtained from experiments, which is $1.67d$ (Etheridge, 2000a). So the expression of the effective length of the acceleration distance is

$$l_e = L + 1.67d \quad (2.34)$$

2 Theoretical models of envelope flow

For a sharp-edged orifice, the length along the opening is zero, so the effective length will be $l_e = 1.67d$.

As stated in Section 2.2.1, the discharge coefficient is obtained from laboratory tests. For a sharp-edged orifice, it is a constant, so equation (2.32) can be expressed as

$$f_s(q) = aq^2 \quad (2.35)$$

$$a = \frac{\rho}{2c_z^2 A^2} \quad (2.36)$$

For a long opening, C_z has dependency on the flow through the opening, which is expressed by equation (2.37), where C and D are constant factors obtained from laboratory tests

$$\frac{1}{C_z^2} = C \frac{L}{Re_{st}d} + D \quad (2.37)$$

Re_{eo} is the opening Reynolds number

$$Re_{st} = \frac{ud}{\nu} \quad (2.38)$$

where u is the average velocity through the opening, ν (m^2/s) is the kinematic viscosity of the air. Equation (2.37) can be equally expressed by equation (2.39).

$$f_s(q) = aq^2 + bq \quad (2.39)$$

$$a = \frac{\rho D}{2A^2} \quad (2.40)$$

$$b = \frac{CL\rho v\pi}{8A^2} \quad (2.41)$$

The steady slow equation of $f_s(q)$ can also be expressed in a power law form. But it was found that the quadratic equation performs better than the power law (Chiu and Etheridge, 2002). The quadratic equation is used in this thesis.

Equation (2.39) applies when the flow is laminar over the length of the long opening. Transition from laminar to turbulent flow occurs when $2000 < Re_{eo} < 4000$. The model scale tests in this thesis are laminar flows. For the cases with completely turbulent flow in the opening which may occur at full scale, equations (2.42) and (2.43) (Etheridge and Sandberg, 1996, pp. PP.86-87) apply.

2 Theoretical models of envelope flow

$$\frac{1}{C_z^2} = C \frac{L}{Re_{st}^{0.25} d} + D \quad (2.42)$$

$$f_s(q) = aq^2 + bq^{1.75} \quad (2.43)$$

$$a = \frac{\rho D}{2A^2} \quad (2.44)$$

$$b = \frac{CL\rho v^{0.25} \pi^{0.625}}{2 \times 4^{0.625} A^{2.375}} \quad (2.45)$$

To sum up, for laminar flow, the flow equations are:

$$\text{Long opening} \quad \Delta P(t) = aq^2 + bq + \rho \frac{dq l_e}{dt A} \quad (2.46)$$

$$\text{Sharp edged opening} \quad \Delta P(t) = aq^2 + \rho \frac{dq l_e}{dt A} \quad (2.47)$$

N.B. long opening and sharp-edged opening have different a values.

2.3.2 Pressure difference

The pressure difference across an opening is the same as that in the steady model (equation (2.25)), but in an instantaneous form

$$\Delta P(t) = -p_{I0m}(t) - \Delta\rho gz + p_{wm}(t) \quad (2.48)$$

2.3.3 Mass conservation

For the air contained within an envelope with N openings, the mass conservation equation is

$$V \frac{d\rho_I}{dt} = \sum_{i=0}^n \rho_i(t) q_i(t) \quad (2.49)$$

The individual density depends on the flow directions.

For the air within the envelope (Etheridge, 2000a),

$$\frac{P_{I0}(t)}{\rho_I(t)^n} = K \quad (2.50)$$

K is a constant, $P_{I0}(t)$ is the absolute pressure of the internal air, whose differential is the same as the differential of the measured internal pressure $p_{I0m}(t) = P_{I0}(t) - P_{E0}$, i.e.

2 Theoretical models of envelope flow

$\frac{dP_{I0}(t)}{dt} = \frac{dp_{I0m}(t)}{dt}$. n equals to 1 for a constant temperature process and equals to γ for an isentropic process, where γ is the ratio of the specific heat of the air.

$$\frac{1}{\rho_I} V \frac{d\rho_I(t)}{dt} = \frac{V}{np_{I0}(t)} \frac{dp_{I0m}(t)}{dt} \quad (2.51)$$

$$\frac{V}{n} \frac{1}{\bar{p}_{I0}} \frac{dp_{I0m}(t)}{dt} = \sum_{i=0}^n q_i(t) \quad (2.52)$$

2.3.4 Solutions of set of equations of QT model

Substituting equation (2.51) into equations (2.46) and equation (2.47), the set of equations of the QT model for an enclosed envelope with N openings are

$$\frac{V}{n} \frac{1}{\bar{p}_{I0}} \frac{dp_{I0m}(t)}{dt} = \sum_{i=0}^n q_i(t) \quad (2.53)$$

$$\text{Long opening} \quad \rho \frac{dq_i(t)}{dt} \frac{l_{ei}}{A_i} = -p_{I0m}(t) - \Delta\rho g z_i + p_{wm}(t) - a q_i(t)^2 - b q_i(t) \quad (2.54)$$

$$\text{Sharp-edged opening} \quad \rho \frac{dq_i(t)}{dt} \frac{l_{ei}}{A_i} = -p_{I0m}(t) - \Delta\rho g z_i + p_{wm}(t) - a q_i(t)^2 \quad (2.55)$$

At each instant of time, there are $N+1$ unknowns are q_i and p_{I0m} , and $N+1$ differential equations, which are solved numerically in their non-dimensional forms. One needs to give the initial values of $q_i(0)$ and $p_{I0m}(0)$, which are the values of the first time step; the initial values of the next time step are the solutions from the previous step. Matlab is employed (Matlab programme attached in Appendix I).

Here raises questions again, the factors a and b are obtained from steady states tests when there are no unsteady wind effects. It comes from the 'quasi-steady' assumptions. In other words, the time-averaged discharge coefficients obtained in steady states for both types of openings are used in QT model regardless of the external flow effects on the discharge coefficients. The wind effect on discharge coefficient will be discussed in Chapter 5. Tests

2 Theoretical models of envelope flow

carried out in still-air cases for hot wire calibration, and the obtained factors a and b are used for both opening types in the theoretical calculations. Details will be provided in Chapter 6.

2.4 Nondimensional QT model

The nondimensional equations are (for the dimensionless process, see Appendix II)

$$\text{Long opening} \quad \frac{dq'_i}{dt'} = \frac{F_i}{2C_{zi\infty}} (-C_{pI} - 2B_i + C_{Pi} - S_i q_i'^2 - \frac{b}{U} \sqrt{\frac{2}{\rho a}} q_i') \quad (2.56)$$

$$\text{Sharp-edged opening} \quad \frac{dq'_i}{dt'} = \frac{F_i}{2C_{zi\infty}} (-C_{pI} - 2B_i + C_{Pi} - S_i q_i'^2) \quad (2.57)$$

$$\frac{dC_{pI}}{dt'} = \sum_{i=0}^n D_i q_i' \quad (2.58)$$

where C_{pI} is the internal pressure coefficient $C_{pI} = \frac{p_{I0m}}{0.5\rho U^2}$

S_i is the flow sign, $S_i = 1$ for inward flow, $S_i = -1$ for upward flow

The nondimensional terms are:

$$\text{Nondimensional flow rate} \quad q'_i(t) \equiv \frac{q_i(t)}{C_{zi\infty} A_i U} \quad (2.59)$$

$$\text{Nondimensional time} \quad t' \equiv t \frac{U}{H} \quad (2.60)$$

$$\text{Buoyancy} \quad B_i \equiv Ar \frac{z_i}{H} \quad (2.61)$$

$$\text{Inertia} \quad F_i \equiv \frac{H}{l_{ei}} \quad (2.62)$$

$$\text{Compressibility} \quad D_i \equiv \frac{2C_{i\infty} A_i H c^2}{V U^2} \quad (2.63)$$

where $C_{zi\infty}$ is the discharge coefficient at high Reynolds number

H is the reference height which is chosen arbitrarily, e.g. the height of the model/building

V is the volume enclosed by the envelope

c is the speed of sound

2 Theoretical models of envelope flow

Ar is the Archimedes number, which will be discussed in more detail in Chapter 4.

N.B. for long openings, the discharge coefficient against opening Reynolds number curve fittings are different for different directions, i.e. C and D in equation (2.42) have different values for inward and upward flow. Thereby one should use individual C_z values for different flow directions through the stack in theoretical calculations. In Appendix II, the equations are provided.

2.5 Summary

The envelope flow model was explained in this chapter. Both the steady model and QT model were introduced specifically, and their solution methods. The equations were provided for a single-cell multi-opening envelope; for multi-cell buildings, the same theory applies yet with a group of equations for each cell. There are two important coefficients introduced in the envelope flow model, which are the discharge coefficient and the pressure coefficient. They are investigated in more detail in Chapter 5.

Examples of solutions for both steady and unsteady models will be provided in Chapter 6, with comparisons to the wind-tunnel measurements.

3 Experiments – wind alone tests

3.1 Introduction

For the purpose of natural ventilation design, the wind tunnel tests usually include three techniques. The tracer gas technique, pressure transducers for pressure measurement, and the hot-wire technique for air velocity measurement. The tracer gas technique (Etheridge and Sandberg, 1996, pp. 591-626) can be used on its own to measure the ventilation rate (Kato et al., 2006). The pressure measurements can also work on its own to obtain the pressure distribution on the model surfaces, obtaining pressure coefficients which can be used as inputs for envelope flow model calculations. Coupling tracer gas or hot-wire technique with pressure measurements, one can obtain the opening characteristics, i.e. the discharge coefficient. Using visible tracer gas can visualise flow patterns. There are examples of using three techniques together to study cross ventilation (Sawachi et al., 2004; Kobayashi et al., 2006). The hot-wire technique is commonly used for single-sided or cross ventilation with large openings (Nishizawa et al., 2004; Eftekhari et al., 2003). The direct measurement of the flow fluctuation through long openings (stacks) was first developed by Chiu and Etheridge (2004). The investigation in this thesis is a continuation of the work reported in (Chiu and Etheridge, 2007; Cooper and Etheridge, 2007; Costola and Etheridge, 2007). In those investigations a single stack and orifice were tested.

In this chapter, the experimental details are introduced in Section 3.2, including model description, calibration of instruments, measurement description, data acquisition and similarity analysis. There are two models used in this thesis, a two-stack model and a four-stack one. The former was only used for preliminary tests to check the flow balance and consistency of velocity and pressure measurements. Two wind tunnels are used, one is the IBT (Institute of Building Technology, the University of Nottingham) wind tunnel, the other is the TPU wind tunnel. All the wind alone tests are carried out in the TPU wind tunnel with

3 Experiments – wind alone tests

the four-stack model. The preliminary tests using the two-stack model and the wind and buoyancy combined tests using the four stack model were carried out in the IBT wind tunnel.

In Section 3.3 of this chapter, the testing scope of wind alone case is introduced. The testing results of flow balance, and flow reversal are presented in Section 3.4. Results of C_z and C_p are investigated separately in Chapter 4. Conclusions of this chapter are in Section 3.5.

3.2 Experimental techniques

3.2.1 Model description

3.2.1.1 Two-stack model and IBT wind tunnel

As shown in Figure 3.1, the dimension of the rectangular model is 500 mm×250 mm×200 mm. There are two stacks fixed on the roof of the box: stack 1 is a circular one whose length is 188 mm and internal diameter is 16.8 mm; stack 2 is a rectangular one whose length is 80 mm and internal dimension is 9.5 mm×30 mm. The direction of the incoming wind is varied by rotating the turntable of the wind tunnel. The wind direction is defined as the angle ϕ which can be seen in Figure 3.1.

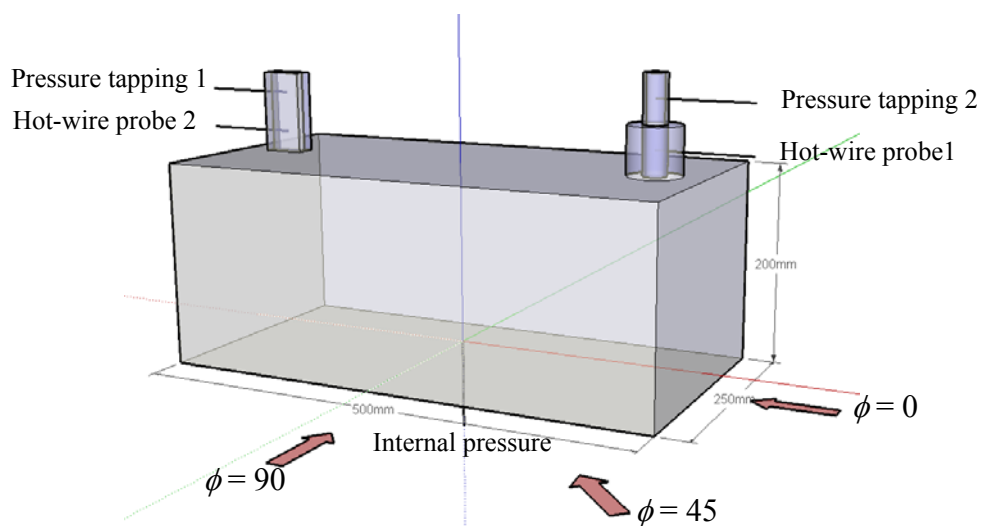


Figure 3.1 Two-stack model and wind direction ϕ

3 Experiments – wind alone tests

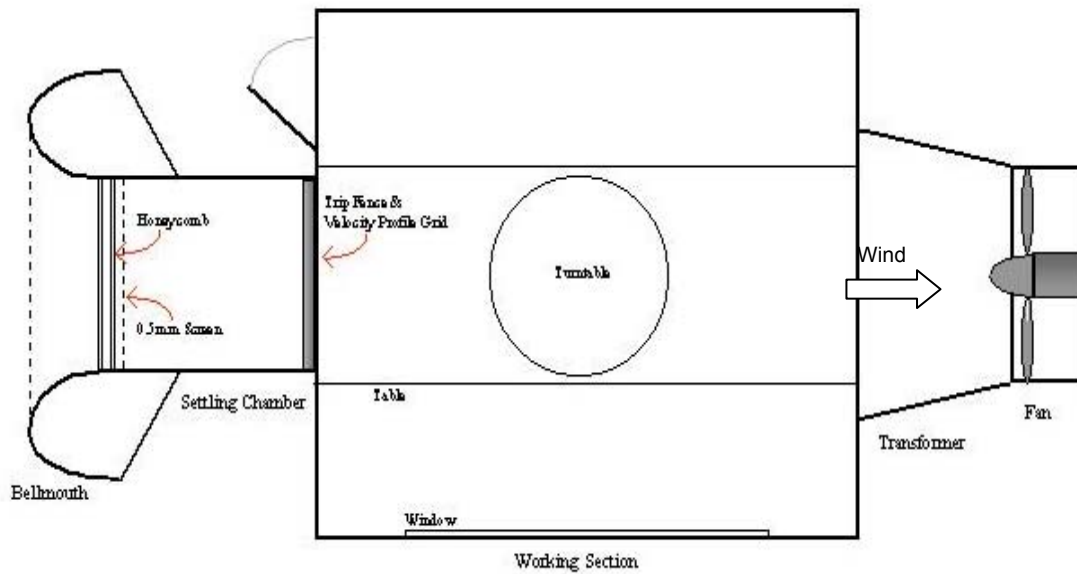


Figure 3.2 Plan view of IBT wind tunnel (source: (Chiu, 2004))

The IBT wind tunnel (Figure 3.2) is of the open-circuit type and the working section is 1 m wide, 0.75 m high and 2.25 m long. A turntable is in the centre of the working section and allows wind direction to be adjusted. The suction mode wind tunnel has a maximum wind velocity of approximately 6 m/s generated by a fan. The air enters the wind tunnel through a bellmouth, shaped so as to minimise uncontrolled turbulence in the inlet section. It immediately passes through two layers of honeycomb for straightening the flow and a 0.5 mm mesh to further reduce turbulence. The upstream velocity profile is generated by a 50 mm fence and horizontal slats placed at the entrance to the working section. The entrance dimensions are height, 0.78 m, width, 1.07 m, and the dimensions of the room containing the working section are height, 2.14 m, width, 3.21 m and length, 2.25 m.

3 Experiments – wind alone tests

3.2.1.2 Four stack and four orifice model and TPU wind tunnel

As shown in Figure 3.3, the dimension of the rectangular model is the same as the two-stack one, which is 500 mm*250 mm*200 mm. There are four identical circular stacks fixed on each corner of the roof. The total length of the stack is 188 mm, the diameter of the stack is 16.8 mm and the venturi diameter is 10 mm. The diameter of the sharp-edged orifice is the same as the stack. Most tests were done with the stack boxes; otherwise it is stated without the stack boxes.

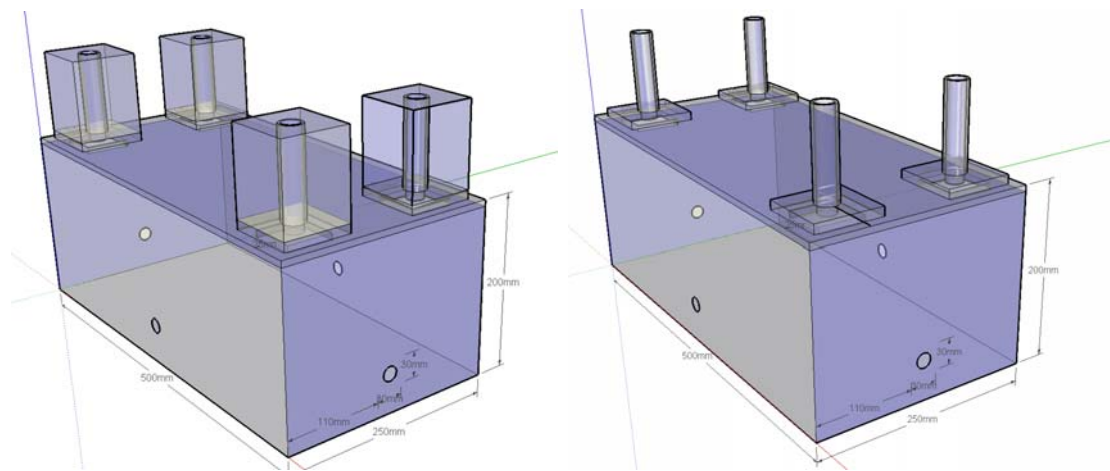


Figure 3.3 Four stack model shown with and without stack boxes

3 Experiments – wind alone tests

instant the upstream wire can be identified and hence the direction and magnitude of the velocity can be obtained. The direction of the stack flow is determined by comparing the voltage outputs of the two parallel hot-wires within each one of the stacks. The upstream wire should give higher voltage output. The magnitude of the stack flow is calculated using the higher voltage given by the upstream wire.

A plan view of stack and orifice positions relative to the wind direction, ϕ , is shown in Figure 3.5.

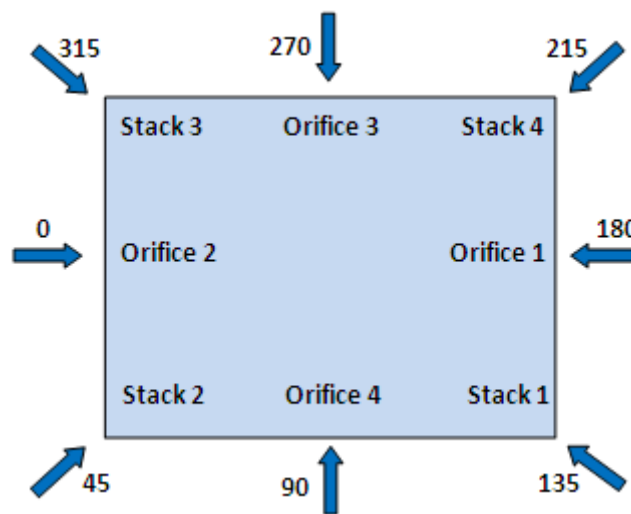


Figure 3.5 Plan view of stack and orifice positions, with wind direction

The TPU environmental boundary layer wind tunnel (Figure 3.6) is an open-circuit low-speed wind tunnel designed for wind environmental assessment and ventilation studies. It has a test section of 1.2 m wide, 1.0 m high and 14m long (Figure 3.7). This low speed wind tunnel is capable of investigating a wide range of different flow fields with wind speeds from 0.2 to 15 m/s. The blower is on the left hand side and the wind is moving from left to right. The test section on the right hand side is equipped with the turntable (marked with dashed line).

3 Experiments – wind alone tests

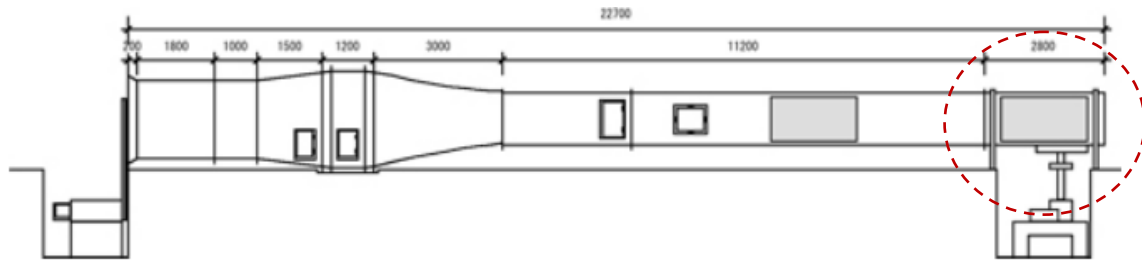


Figure 3.6 Section of the environmental boundary layer wind tunnel.



Figure 3.7 Photos of the TPU wind tunnel working section and the four stack model

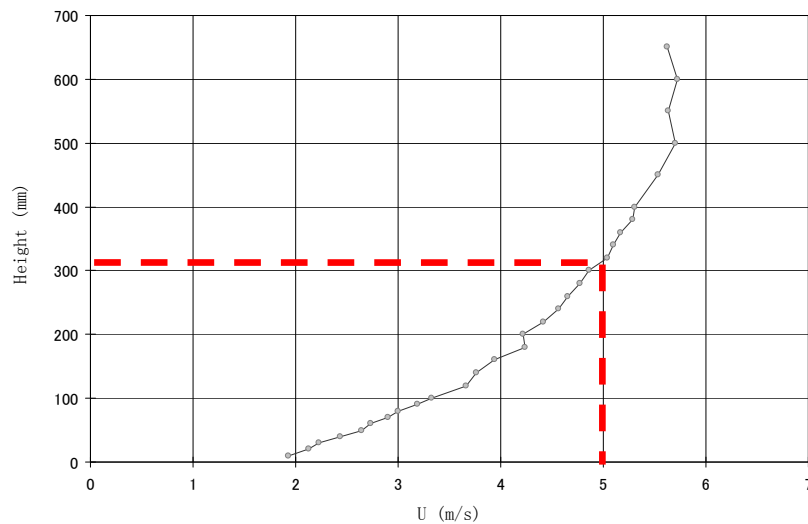


Figure 3.8 Wind profile at working section

The wind profile was calibrated against a reference point, which is the highest edge (facing the approaching wind) of the model placed in centre of the turntable. Figure 3.8 shows the wind profile of 5 m/s at the reference point (height 300 mm). The velocity profile equation is:

3 Experiments – wind alone tests

$$U = U_{ref} \left(\frac{h}{h_{ref}} \right)^{0.33} \quad (3.1)$$

where U_{ref} is the setting velocity (m/s) (marked with dashed lines in Figure 3.8)

h_{ref} is the height of the setting velocity (mm)

3.2.2 Calibration of instruments

3.2.2.1 Calibration of hot-wire

The methodology of hot-wire calibration is given in Chiu and Etheridge (2004). It is adopted in this thesis and is described as follows. The calibration of the hot-wire is comprised of two parts, steady calibration and unsteady calibration. The reason for doing unsteady calibration is that the shape of velocity profile in the stack will change unpredictably while fluctuation (e.g. flow reversal) occurs, causing uncertainty in measuring the instantaneous flow rate. Therefore, by using an oscillating piston which can generate known (nominally sinusoidal) fluctuation of volume flow rate against time to get unsteady calibration factors, the uncertainty in measurement could possibly be minimized. The steady calibration, which is a traditional method, is carried out as a complement of the unsteady calibration (higher velocity). Additionally, the steady calibration also gives accurate measure of the still air discharge coefficient C_z of a stack. One can also measure the C_z for the sharp-edged orifice in this way (seal all the openings apart from the sharp-edged orifice being measured).

For both of the unsteady and steady calibration, the driving force of the air movement (piston or fan) is connected to one of the sharp-edged orifices. While one of the hot-wire probe is being tested, the outlet of the other stacks and sharp-edged orifices are covered to stop the air flow.

1) Steady calibration of hot-wire

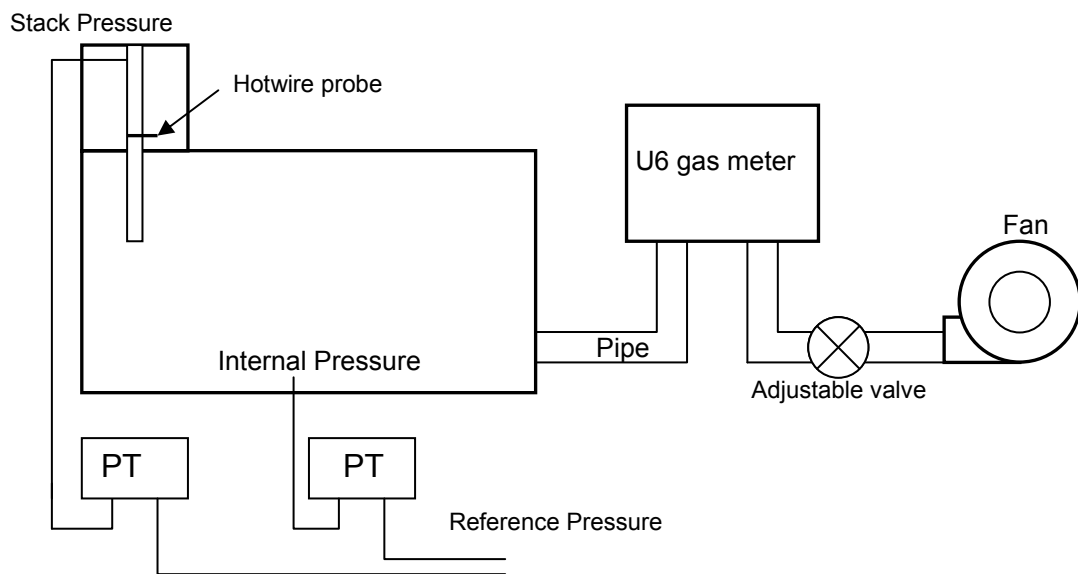


Figure 3.9 Arrangement for steady calibration and C_z measurement

As shown in Figure 3.9, the steady calibration was carried out using a gas meter (U6 type) and a fan. The gas meter was used to measure the time averaged volume flow rate, and the fan was used to provide constant inward or upward flow (sucking or blowing) in the stack. The data points used for curve fitting was time-averaged values of velocities (calculated from gas meter) and voltage outputs of the hot-wire. The two parallel hot-wires of one probe were calibrated separately. A fan was used to suck air into the stack to calibrate the upper wire, and to blow air out of the stack to calibrate the lower wire.

2) Unsteady calibration of hot-wire

For unsteady calibration, the two parallel hot-wires of one stack are calibrated at the same time. The instantaneous flow direction in the stack is detected by comparing the instantaneous voltage outputs of the two hot-wires. Each of the hot-wires was calibrated using the instantaneous higher voltage output, which means this hot-wire is the upstream one. Quartic curve fitting was done to each of the hot-wires using instantaneous data points: velocities (the volume flow rate is calculated from the frequency and stroke) against voltage outputs of the hot-wire. Ideally, the oscillating piston would be able to generate a range of volume flow rates which could mostly cover the range of air flow rate over which flow

3 Experiments – wind alone tests

reversal occurs. To achieve this, two frequencies were used (0.716 Hz and 1.546 Hz). Yet a more precise piston which can provide higher frequencies might be desirable (for reasons of this and descriptions of the unsteady calibration using a precise piston, see Chapter 7).

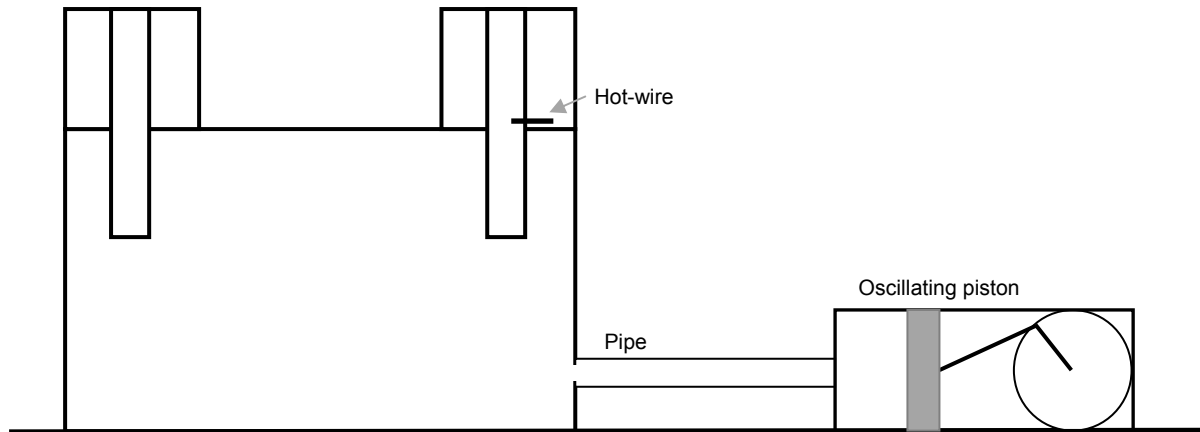


Figure 3.10 Arrangement of unsteady calibration

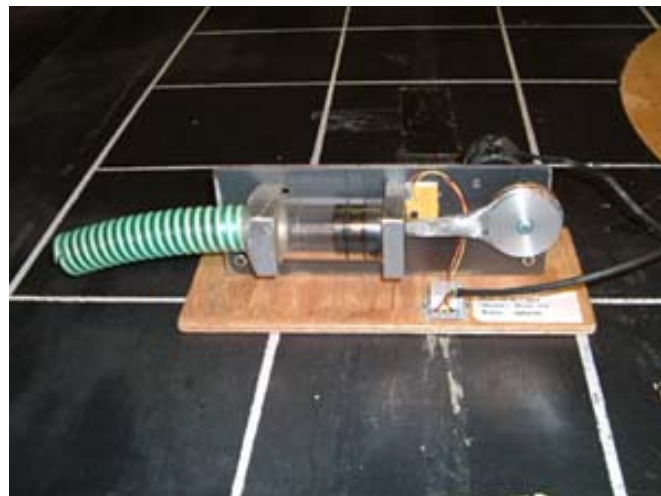


Figure 3.11 Photo of the piston

3) Final curve fit of hot-wire calibration

The final curve fitting was carried out using a combination of the unsteady curve and the steady data points. Example of calibration results (upper wire of one probe) are shown

3 Experiments – wind alone tests

in Figure 3.12 and Figure 3.13 in terms of velocity $\frac{q}{A}$ against voltage. N.B. the term A is the area of the stack, not the venturi area.

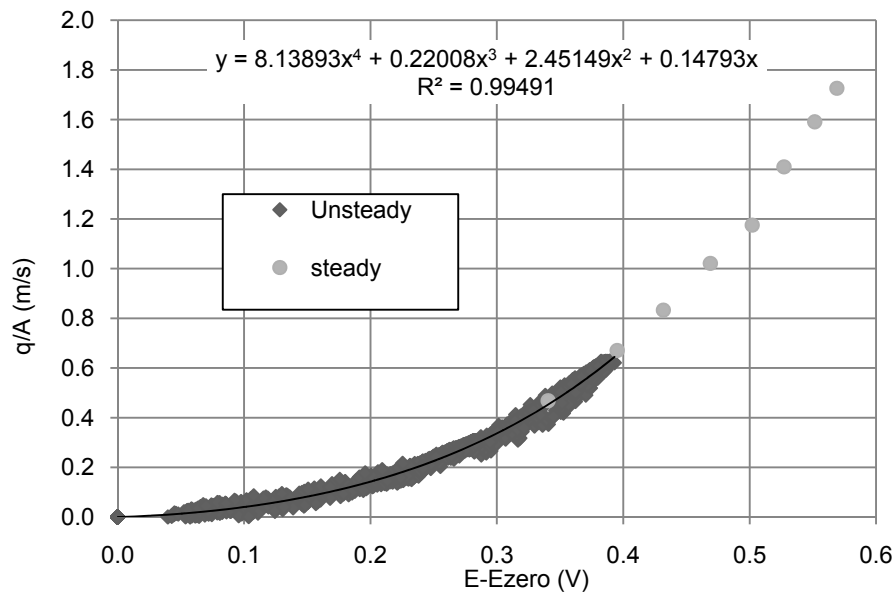


Figure 3.12 Combined steady and unsteady calibration

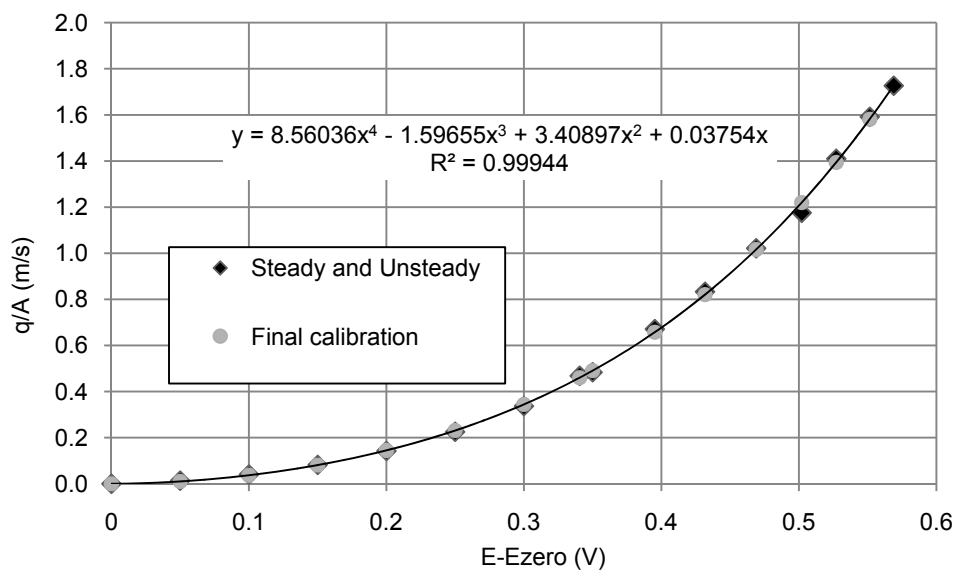


Figure 3.13 Final curve fitting

3.2.2.2 Calibration of pressure transducer

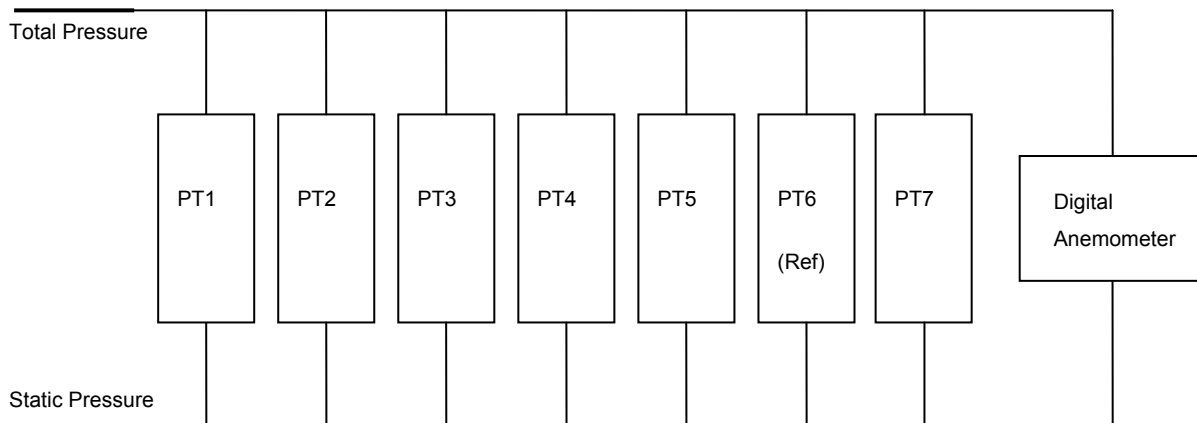


Figure 3.14 Calibration of pressure transducers and digital anemometer

Connections of the pressure transducers and the digital anemometer for calibration are shown in Figure 3.14. One of the pressure transducer (PT6) was used as the reference. Using the calibration results of PT6 provided by ‘Furness Controls Ltd’, the other pressure transducers and the digital anemometer were calibrated against PT6 so that they give consistent results during tests. The transducers were connected in parallel to a pitot-static tube in the wind tunnel. The procedure was to do a zero run before switching on the tunnel to eliminate the zero shift when the measured pressure is zero Pa, then gradually vary wind speeds from low to high to control the dynamic pressure. A linear curve fit was obtained for each transducer and the digital anemometer. Figure 3.15 shows the linear curve fit of PT1 as an example. The digital anemometer displays the dynamic pressure (Pa), it was also calibrated against PT6 (Figure 3.16).

3 Experiments – wind alone tests

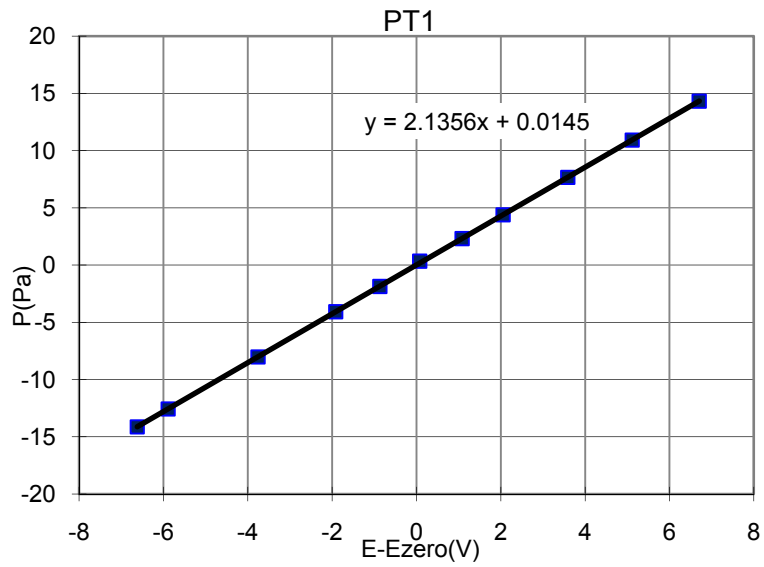


Figure 3.15 Linear fitting of PT1 (pressure against voltage output)

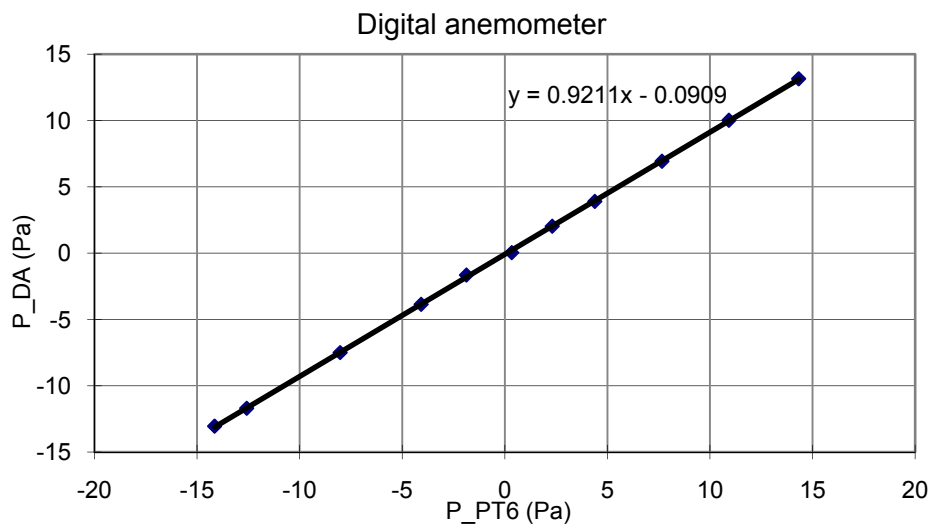


Figure 3.16 Linear fitting of digital anemometer using reference PT6

3.2.3 Stack flow & pressure measurements and data acquisition

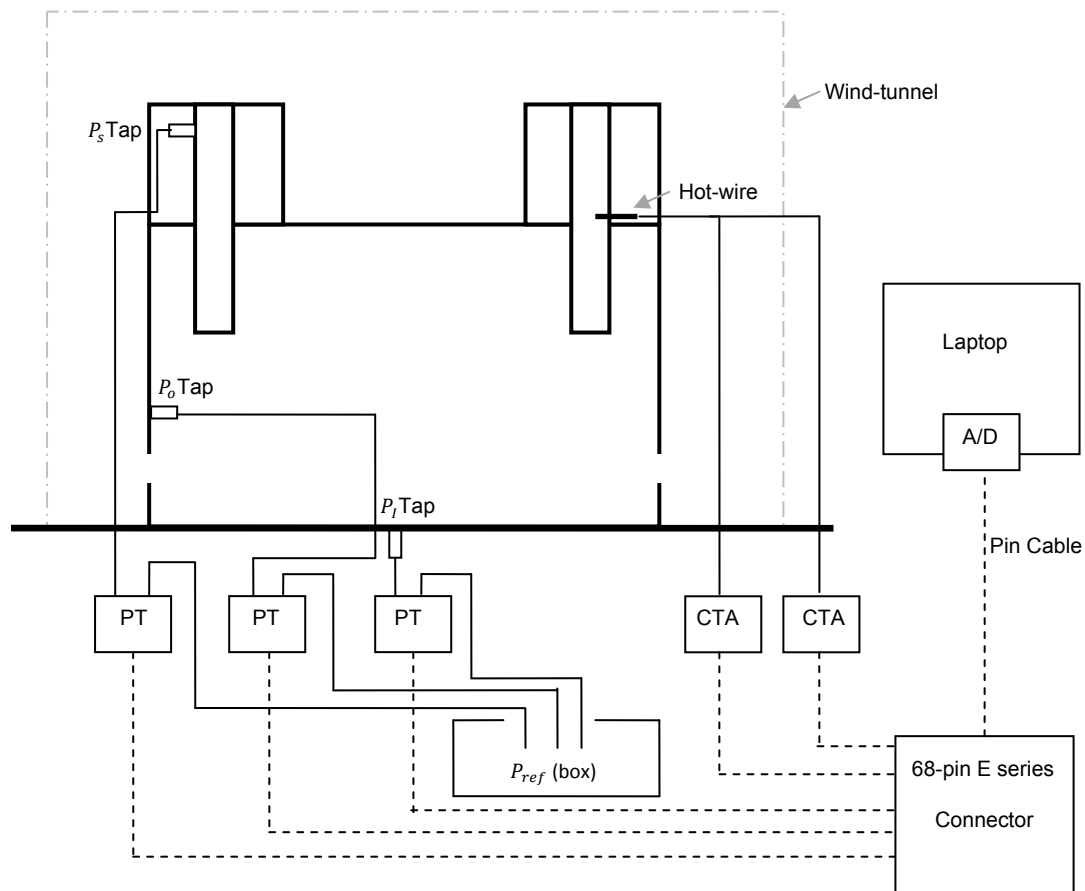


Figure 3.17 Stack flow and pressure measurement; data acquisition

1) Stack flow measurement

Since the interest here is with stacks, it is necessary to determine the direction as well as the magnitude of the flow through each stack. The concept of a time-averaged flow direction is valid, e.g. it is defined as upward flow when this occurs for more than 50% of the time and vice versa. But it is not very meaningful in the sense that a so-called upward flow stack that has reversed flow for 49 % of the time clearly is not performing satisfactorily. It is therefore necessary to consider the reversal percentage, r %. To determine r it is necessary to record instantaneous flow rates.

3 Experiments – wind alone tests

As shown in Figure 3.17, a hot-wire probe (Dantec 55P71s) was mounted in the middle of each stack. The standard 55P71 probe consists of two parallel hot-wires. Each hot-wire was connected to a Dantec MiniCTA anemometer. The direction of the stack flow is determined by comparing the voltage outputs of the two parallel hot-wires within each of the stacks. The upstream wire should give a higher voltage output due to the downstream wire receiving heat from the upstream wire. The magnitude of the stack flow is calculated using the higher voltage given by the upstream wire. Prior to each measurement, the zero flow voltage is measured and this is used to account for any changes in tunnel air temperature. i.e. the calibration is in the form of $E - E_o \sim q$, where E_o is the voltage for $q = 0$.

2) Pressure measurement

Three pressure tappings were used on the two-stack model, one for each stack and one for the internal pressure (Figure 3.1). Nine pressure tappings were used on the four-stack model (Figure 3.17): one for each of the stacks and the orifices and one internal tapping. Each tapping was connected to its own pressure transducer (Furness FC044), with the other side of the transducer connected to a reference pressure. The reference pressure was taken within an empty box in the still air of the wind-tunnel laboratory. Due to the limited number of pressure transducers, a maximum of seven pressure tappings could be used simultaneously. A pitot-static tube was mounted in the upstream of the wind tunnel to measure the dynamic pressure, displaying on the digital anemometer, from which the reference wind speed U_{ref} was obtained.

3) Data acquisition

The measured physical quantities (velocity and pressure) are transferred into analogue signals (voltage) in the Mini CTA and the pressure transducer. The analogue signals are transferred into the 68-pin E series connector, then through the pin cable, they are transferred to the PCMCIA A/D converter. The converted digital signals are placed into the cells of an Excel worksheet by a data acquisition software DAS-Wizard (Figure 3.17). Readings are taken at a sampling frequency of 120 Hz for periods of 34 s.

3.2.3 Similarity analysis

In terms of wind alone ventilation, the basic similarity requirement is that the model and prototype flows should be dynamically similar, which means that fluid elements which are initially at corresponding points in the two systems will follow corresponding paths, i.e. the mean streamlines are geometrically similar (Etheridge and Sandberg, 1996, p. 649).

The prerequisites are satisfaction of geometrical similarity and boundary condition similarity.

- 1) Geometrical similarity: the prototype building is accurately reproduced at model scale, the length scale is

$$\lambda_l = \frac{l_p}{l_m} \quad (3.2)$$

where l_p is the length of prototype building, l_m is the corresponding model length

- 2) Boundary similarity: the boundary layer of the prototype building is reproduced in the wind tunnel.

In terms of dynamic similarity, it means that at the corresponding points of the two systems, every force component acting upon the corresponding particles of the two systems should maintain the same scale factors. For wind alone cases, the two relevant forces are inertial force and shear force. The ratio of inertial force and shear force is defined as Reynolds number. To meet dynamic similarity, the ratio of the two forces at all corresponding points of the two systems should be the same, i.e. their Reynolds number should be the same

$$Re_p = Re_m \quad (3.3)$$

$$\frac{u_p l_p}{\nu} = \frac{u_m l_m}{\nu} \quad (3.4)$$

Where u is the wind speed, ν is the viscosity of air

However it is almost impossible for the model tests to achieve the prototype Reynolds number. For example, if the length scale $\lambda_l = 100$, the velocity in the wind tunnel should be 100 times of the prototype to meet the prototype Re . Due to the limit of the speed range in the wind tunnel, Re_m is usually much smaller than Re_p . Then is wind tunnel test still useful? The

3 Experiments – wind alone tests

answer is yes. First let us talk about what parameters are dependent on Reynolds number. Referring to the envelope flow equation (equation (2.3))

$$|q| = C_z A \sqrt{\frac{2|\Delta P|}{\rho}} = C_z A U_{ref} \sqrt{|\Delta C_p|} \quad (3.5)$$

The flow through openings are related to ΔC_p and C_z . If they are independent of Re , then there is no need to achieve the prototype Reynolds number at model scale. For sharp-edged structures (sharp-edged orifices, rectangular buildings, etc.), the flow pattern is primarily determined by flow separation, thus sharp-edged structures are insensitive to Reynolds number except at very low wind speed when separation is hard to occur. In that sense, ΔC_p and C_z of sharp-edged orifices are independent of Re above a critical Reynolds number. For example, if $\lambda_l = 12$, to achieve the critical $Re = 2000$, the required wind speed is about 0.5 m/s (Etheridge and Sandberg, 1996, pp. 674-676). The required minimum speed varies with the length scale λ_l .

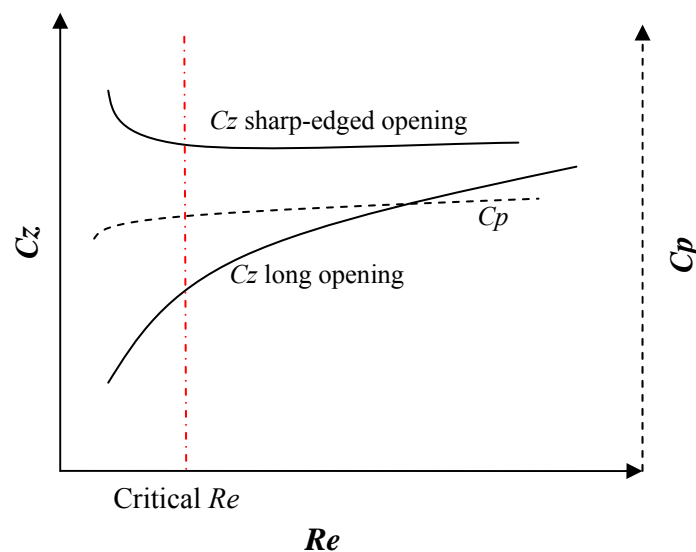


Figure 3.18 Dependence of C_z and C_p on Re

Nevertheless, for long openings, because their geometry (length) makes the viscous shear force more important, the C_z of long openings has a dependency on Re over the whole

3 Experiments – wind alone tests

velocity range. Therefore, there is no critical Re for long openings, neither could the wind tunnel generate a wind speed high enough to meet the prototype Reynolds number. However there is an approximate solution, to compensate for the C_z error of long openings at model scale by modifying the opening area. For example, if value of C_z at full prototype Re is 10 % greater than that of model scale, we can enlarge the opening area by 10 % as a solution. This is not an accurate compensation; it depends on the slope of the C_z curve (Figure 3.18) (Chiu and Etheridge, 2007). But due to other uncertain factors like wind direction and fluctuation, the solution may be good enough, thus the nondimensional graphs plotted using model scale data can be used at full scale.

To sum up, the requirement is to meet the critical Reynolds number at model scale, i.e. using a wind speed greater than a certain value of course within the wind tunnel speed range. One may also wish to modify the long opening area to compensate for the C_z error. Since the models used in this thesis are not representing a particular building, there is no such issue of changing the opening area of long openings. However Re effects are important for design and need to be considered. For the purpose of validating the QT model with measurements, Re effects are not important.

3.3 Experiment scope

For the two-stack tests, a wooden box was placed on top of the model between the two stacks to generate flow reversal (see Figure 3.19); reversal percentage varies with the changing separation distance of the wooden box. Two reference wind speeds were used: $U_{ref} = 1.35 \text{ m/s}$ ($P_d = 1.1 \text{ Pa}$); $U_{ref} = 2.74 \text{ m/s}$ ($P_d = 4.5 \text{ Pa}$). At each wind speed, three wind directions were tested: $\phi = 0$, $\phi = 45$, and $\phi = 90$.

3 Experiments – wind alone tests

The scope of the four-stack model tests are shown in Table 3.1

Table 3.1 Experiment scope of four-stack model

No.	Stacks	Orifices	Wind speed (U)	Wind direction (\emptyset)	Stack boxes	Identifier
1	1 2 3 4	0	range	0	Yes	S1234_ \emptyset _U
2	1 2 3 4	0	max	0, 45, 90	Yes	S1234_ \emptyset
3	1 2 3 4	1 2	range	0	Yes	S1234_O12_ \emptyset _U
4	1 2 3 4	1 2	max	0, 45, 90	Yes	S1234_O12_ \emptyset
5	1 3	0	max	0, 90, 180	Yes	S13_ \emptyset
6	1	2	range	67.5	Yes	S1_O2_ \emptyset _U
	1	2	max	0, 22.5, 45, 67.5, 90	Yes/No	S1_O2_ \emptyset
7	1 3	1 2 3 4	max	0, 45, 90, 135	Yes	S13_O1234_ \emptyset
8	3 4	1 2	range	67.5	yes	S34_O12_ \emptyset _U
9	3 4	1 2	max	0, 45, 90, 270, 315	Yes/No	S34_O12_ \emptyset
10	3 4	3 4	max	0, 45, 90, 270, 315	Yes	S34_O34_ \emptyset
11	3 4	1 2 3 4	max	0, 45, 90, 270, 315	Yes	S34_O1234_ \emptyset
12	1 4	1 2	max	0, 45, 90, 135, 180	Yes/No	S14_O12_ \emptyset
13	1 4	3 4	max	0, 45, 90, 135, 180	Yes	S14_O34_ \emptyset
14	1 4	1 2 3 4	max	0, 45, 90, 135, 180	Yes	S14_O1234_ \emptyset
15	1 2 3 4	1 2	max	0, 90, 180, 270	Yes/No	S1234_O12_ \emptyset
16	1 2 3 4	1 2 3*4 *	max	0, 90, 180, 270	Yes/No	S1234_O123*4*_ \emptyset
17	1 2 3 4	1*2*3 4	max	0, 90, 180, 270	Yes/No	S1234_O1*2*34_ \emptyset

Notes for the table:

- 1) “max” means 5 m/s at model height above turn table, the corresponding U_{ref} of the upstream wind is about 6.5 m/s; “range” means speed at model height varied from 1 m/s to 5 m/s by a step of 1 m/s.
- 2) Stacks and openings are sealed when not listed in Table.
- 3) When a stack is used always use a pressure transducer.

3 Experiments – wind alone tests

- 4) When four openings and four stacks are used, use pressure transducers for two openings, marked by * in the identifier.
- 5) If wind direction \emptyset is not specified in the identifier, the default value is 0 degree.
- 6) Identifiers are used in this thesis for simplicity.
e.g. S1234_O12_45_2 means an opening configuration of stacks 1,2,3,4 and orifices 1,2. The wind direction is 45 degree, and the wind speed $U_{ref} = 2m/s$.
S13_O12 means an opening configuration of stacks 1 and 3, orifices 1 and 2, the wind direction is 0 degree, and the wind speed $U_{ref} = 6.5m/s$.

3.4 Experiment results and analysis

3.4.1 Mean flow balance

Simultaneous hot-wire measurements on multiple stacks with no other openings, provides a stringent and unique check on the overall accuracy of the technique, in the sense that the measured volume flow rates should satisfy the continuity equation (conservation of mass). Preliminary tests were carried out on an earlier model under flow reversal conditions. They were prompted by a concern that the model was not sufficiently rigid, leading to the possibility of volume changes.

1) Two-stack model

The preliminary tests were carried out at the IBT wind tunnel on a relatively simple two-stack model which has the same external dimensions as the four-stack model (Figure 3.19). A wooden block (370 x 126 x 200 mm) was used to generate different reversal percentages of the two stacks by changing the separation distance S between the block and the circular stack. To check the accuracy of the technique, the sum of the volume reversal percentages of the two stacks should be 100%. The flow reversal percentage was calculated in two ways, one was based on flow direction, calculating the percentage of time that flow reversal occurs, r %; the other was based on flow volume rate, calculating the percentage of volume that reversed, r_v %. (N.B. r % needs not necessarily sum to 100 %)

3 Experiments – wind alone tests

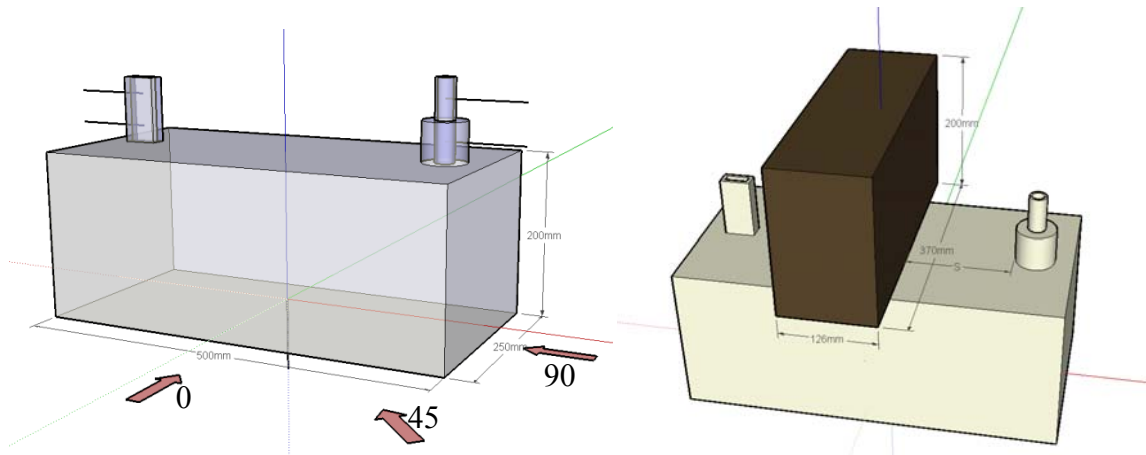


Figure 3.19 Wooden box between two stacks and the separation distance

Table 3.2 Reversal percentages of two-stack model

$\phi=45, U_{ref} = 2.74 \text{ m/s}$							
Time reversal percentage (r %)				Volume reversal percentage (r_v %)			
S (mm)	Stack1	Stack2	Sum	S (mm)	Stack1	Stack2	Sum
No Block	0.12	94.04	94.17	No Block	0.01	97.49	97.50
110	99.73	0.10	99.83	110	99.94	0.01	99.95
140	62.70	33.59	96.29	140	64.87	17.68	82.55
145	58.54	36.94	95.48	145	59.54	20.58	80.12
150	13.62	76.76	90.38	150	5.15	79.89	85.03
180	99.73	0.10	99.83	180	99.94	0.01	99.95

3 Experiments – wind alone tests

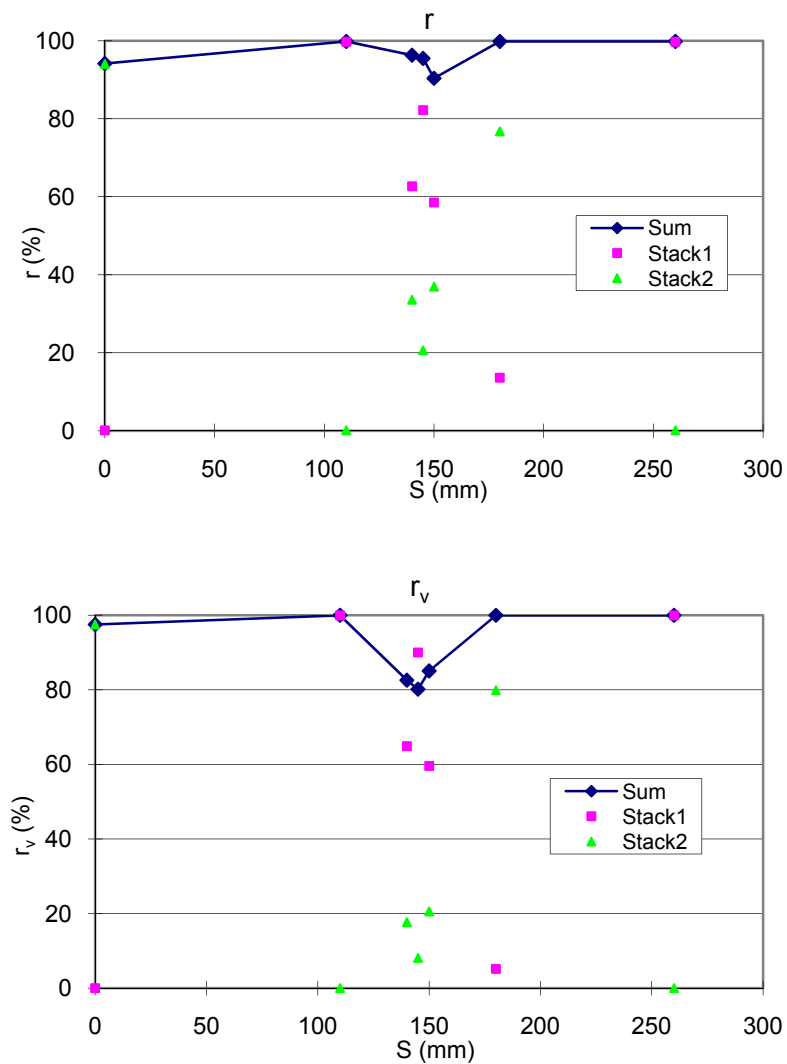


Figure 3.20 Variation of r and r_v with the separation distance

As shown in Table 3.2 and Figure 3.20, when flow reversal (fluctuating flow) occurs, for most of the cases, the sum of the reversal percentage (both of the time reversal percentage and the volume reversal percentage) of the two stacks is less than 100 %. The nearer the reversal percentage is close to 50 %, the lesser is the sum of the two stacks.

3 Experiments – wind alone tests

Since the velocities of the stacks are very low, and hence sensitive to the vibration of the model, especially for cases of reversal percentages around 50%, a rod was fixed into the model between the two parallel walls to make the box more rigid (Figure 3.21).

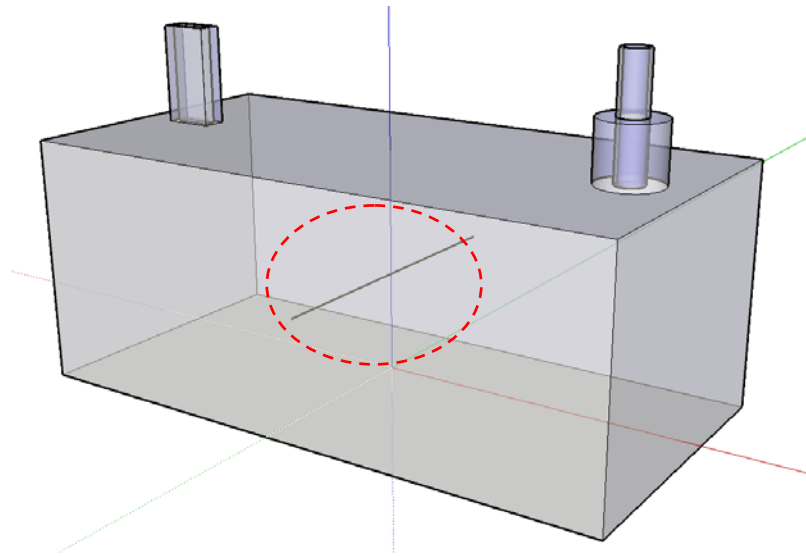


Figure 3.21 Rod fixed inside the model

Table 3.3 Reversal percentage with and without the rod

Time reversal percentage ($r^0\%$)				Volume reversal percentage ($rv^0\%$)			
S (mm)	Stack1	Stack2	Sum	S (mm)	Stack1	Stack2	Sum
$45^\circ, U_{ref} = 2.74 \text{ m/s}$							
140	62.70	33.59	96.29	140	64.87	17.68	82.55
Rod 140	82.20	20.60	102.80	Rod 140	89.99	8.11	98.10
$45^\circ, U_{ref} = 1.35 \text{ m/s}$							
140	75.98	22.34	98.32	140	72.15	9.88	82.03
Rod 140	94.40	5.80	100.20	Rod 140	96.79	1.36	98.15
$90^\circ, U_{ref} = 2.74 \text{ m/s}$							
230	22.71	70.02	92.73	230	8.85	77.91	86.76
Rod 230	14.20	85.20	99.40	Rod 230	8.95	93.00	101.95
$90^\circ, U_{ref} = 1.35 \text{ m/s}$							
210	44.02	49.32	93.34	210	31.84	39.71	71.55
Rod 210	19.00	80.70	99.70	Rod 210	3.60	88.32	91.92

3 Experiments – wind alone tests

Table 3.3 shows the comparisons of reversal percentages before and after the rod was fixed inside the model. One can see obvious improvements in the sum of reversal percentages of the two stacks; the errors are less than 3% for r and less than 9% for r_v . In view of this the model used for the TPU tests was made more rigid, by using thicker material and by fixing the side walls to a base plate.

2) Four-stack model

Figure 3.22 shows results for a symmetrical configuration, where the flows through stacks 1 and 4 were inward at all times (and virtually equal in magnitude). Similarly for stacks 2 and 3, except the flows were outward. The sum of the flow rates is also shown. Relative to the total outflow, the sum ranges from 5 % to 8 % of the total ventilation rate. In a truly steady flow the sum should be equal to zero and this is clearly not so. However, an error less than 10 % in the measurement of ventilation rate is not bad. It compares favourably with other techniques, such as tracer gas techniques. The most likely cause of the error lies in the calibration of the hot-wires. The systematic nature of the error (increasing with U_{ref}) is consistent with this. On this basis, an uncertainty of +/- 10 % in the mean flow rates is probably a reasonable estimate of the accuracy of the technique.

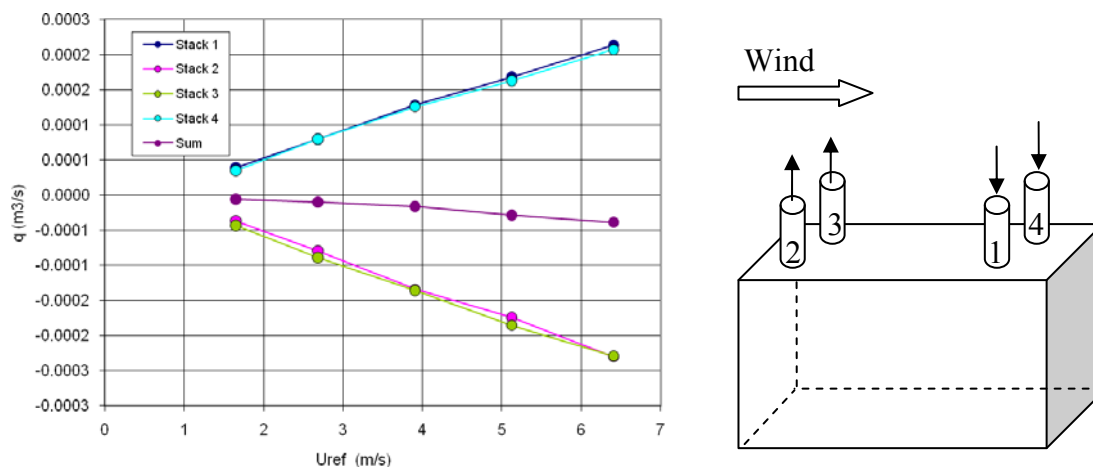


Figure 3.22 Mean flow rate balance of (S1234)

3.4.2 Instantaneous flow balance

In Section 3.4.1, the mean flow balances were examined for two-stack and four-stack cases (with no orifices). As a result of the two-stack tests, the structure of the four-stack model was strengthened. In the following the instantaneous flow balance for the four-stack case is considered. It is the same case as that shown in Figure 3.22, for the highest U_{ref} . It is of course to be expected that that the instantaneous imbalance will at times be greater than the mean imbalance.

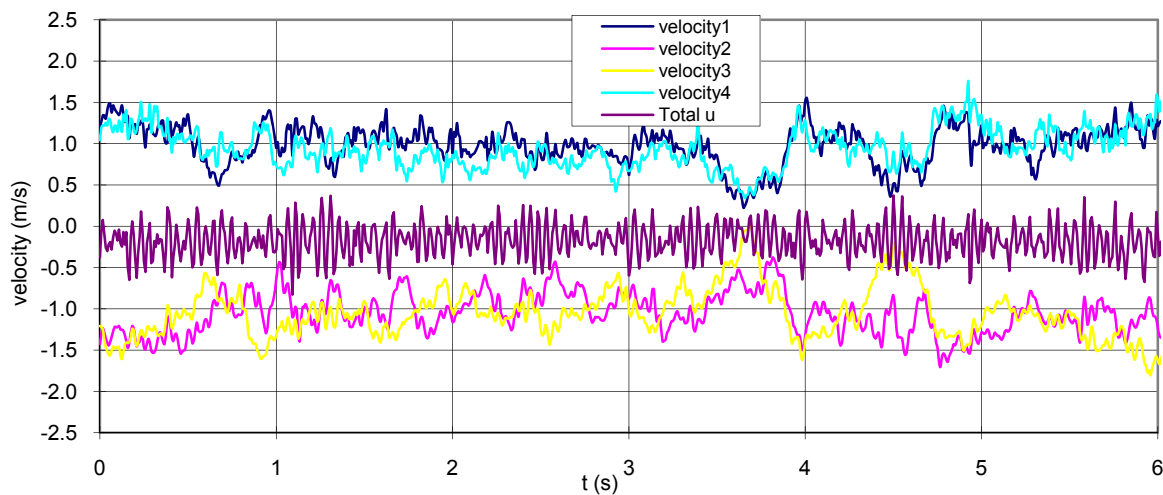


Figure 3.23 Instantaneous velocity of (S1234)

Figure 3.23 displays instantaneous velocities of the four stacks over a period of six seconds, for the case of 0 degree, $U_{ref} = 5$ m/s. The flows through stacks 1 and 4 were inward at all times and outward for stacks 2 and 3. The important point to note is that the instantaneous sum of the velocities has a discrete frequency component. This can be clearly seen in the power spectrum of the velocity sum, as shown in Figure 3.24, the spectra of the stack velocities (Figure 3.25), and the spectra of pressure measurement (Figure 3.26). All figures show results for a wind speed $U_{ref} = 5$ m/s, but Figure 3.24 also shows results for $U_{ref} = 2$ m/s.

3 Experiments – wind alone tests

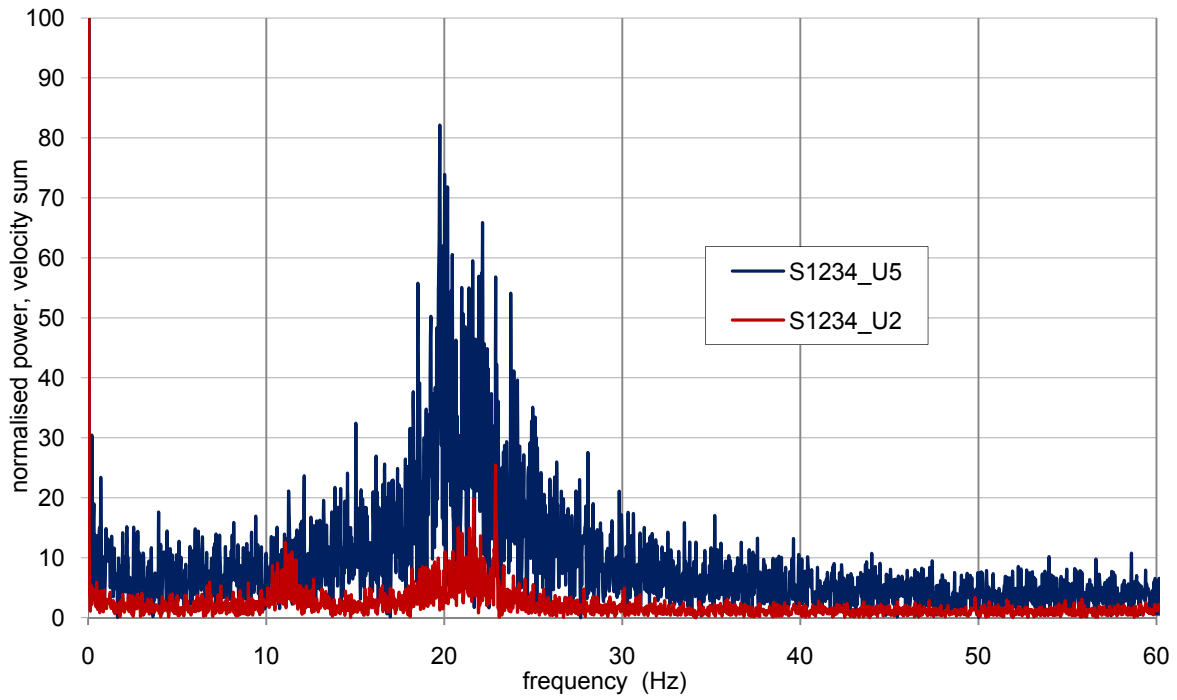


Figure 3.24 Spectral analysis of velocity sum of (S1234); with wind speed of 5 m/s and 2 m/s

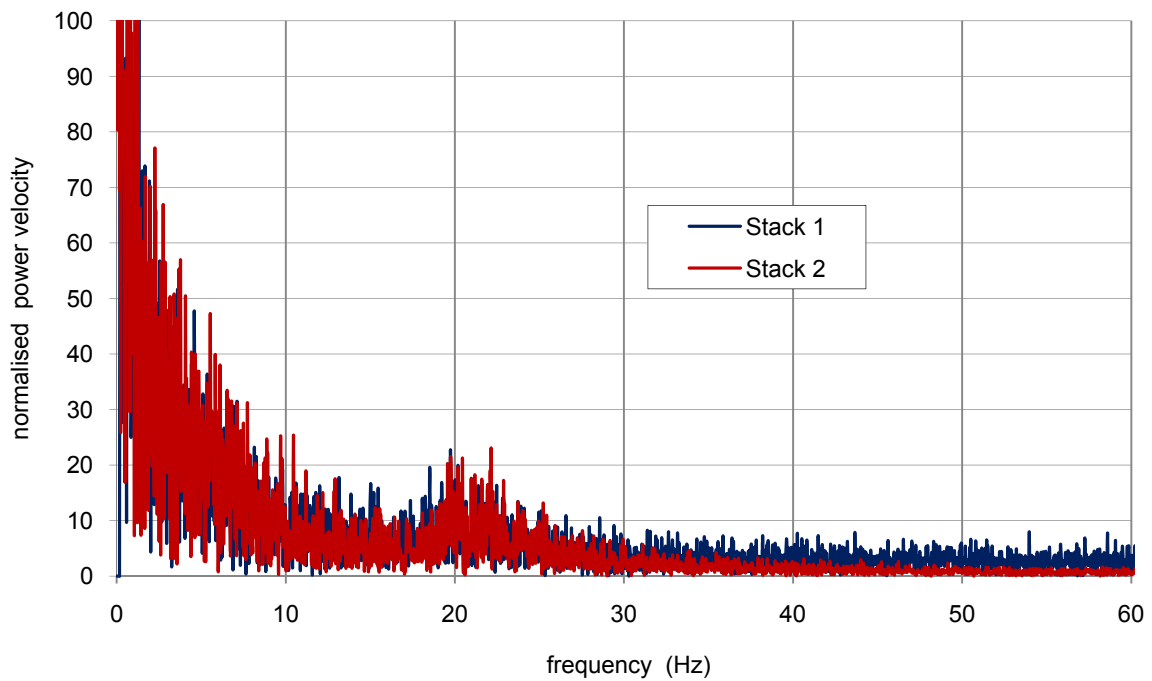


Figure 3.25 Spectral analysis of velocities of stack 1 and 2 for (S1234), with a wind speed of 5 m/s

3 Experiments – wind alone tests

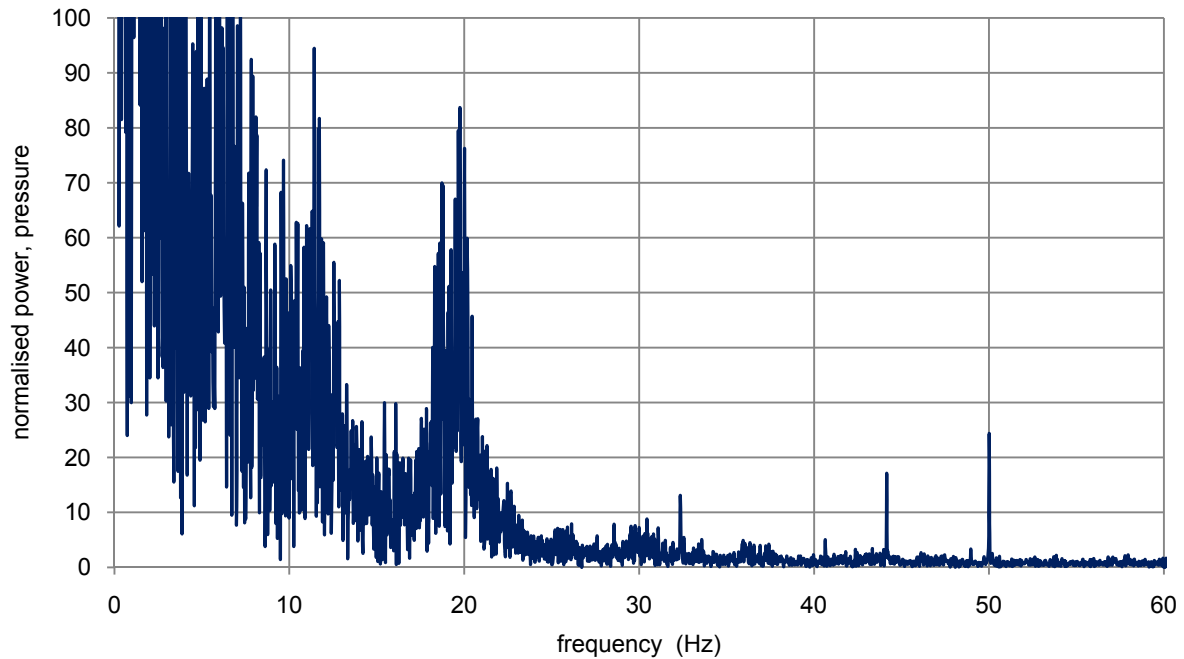


Figure 3.26 Spectral analysis of pressure of Orifice 1 for (S1234), with a wind speed of 5 m/s

The fact that a frequency of around 22 Hz is clearly apparent in all results of velocity and pressure measurements shown in Figure 3.24, Figure 3.25 and Figure 3.26, implies that the phenomenon is independent of wind speeds. In which case, a likely explanation is that a resonant frequency of the box structure is excited. However, at the low wind speed, there is also evidence of resonance around 11 Hz. The resonance can be eliminated by software signal filtering. The results imply that the stiffening of the box was not entirely successful. However, there are limits as to what can be achieved, because only an extremely small change in volume is required to generate the observed changes in pressure.

3.4.3 Investigation of flow reversal

A simple parameter is used to characterize flow reversal of the stacks. i.e. the percentage of time that the flow is reversed, r . The results are presented below in the form that might be appropriate when the technique is used as part of a building design exercise i.e. as plots of r against wind direction ϕ . The comments are based on the assumption that, when orifices are present, upward flow is to be maintained in the stacks. Results for several different stack and

3 Experiments – wind alone tests

orifice configurations are presented. Where the opening configuration has symmetry, it has been assumed that symmetry with wind direction applies, so some results are repeated.

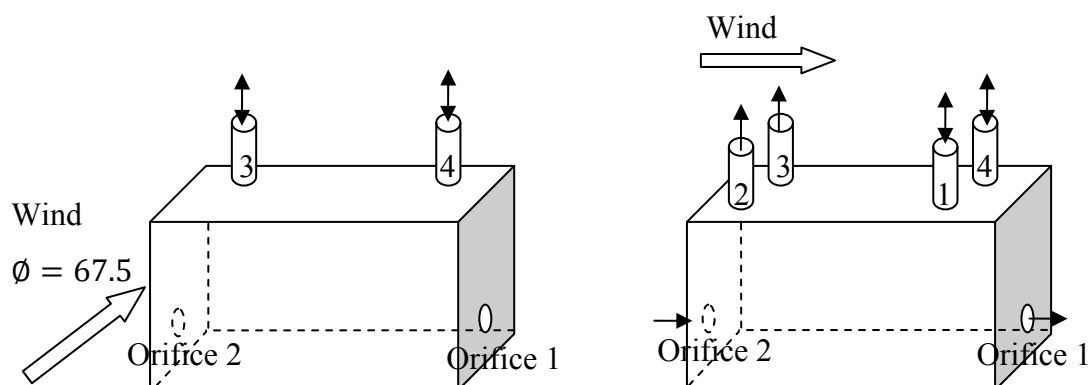
3.4.3.1 Effect of Building Reynolds number on r

The building Reynolds number is defined as

$$Re_b = \frac{\rho U_{ref} H}{\mu} \quad (3.6)$$

where ρ denotes the density of air (kg/m^3), H the height of the building (m), and μ the viscosity (Ns/m^2).

Previous investigations (Cooper and Etheridge, 2007) with a single stack and orifice have shown that the degree of flow reversal r is closely related to the properties (mean and standard deviation) of the instantaneous pressure difference across the two openings. The fact that there were only two openings for those investigations makes interpretation and analysis of results easier. The present investigation is concerned with flow reversal with multiple stacks. Figure 3.27 shows the dependence of r on Re_b of two opening configurations, e.g. two stacks, two orifices (S34_O12_67.5) and four stacks, two orifices (S1234_O12_0). One can see a dependence of r on Re_b , which indicates that higher r is expected at full scale. Calculations of this effect using the unsteady QT model are given in Chapter 6.



3 Experiments – wind alone tests

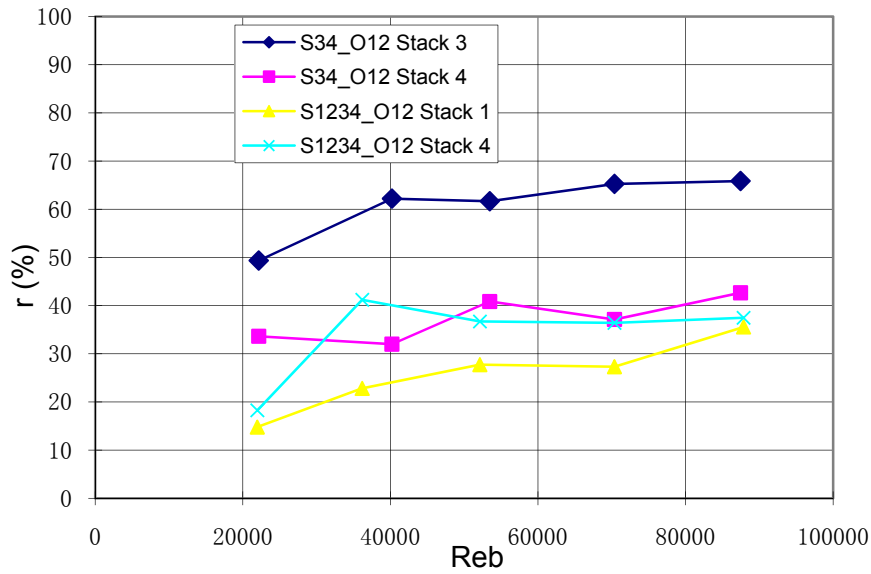


Figure 3.27 Variation of r with Re_b (S34 O12 S3 denotes stack 3 for the case of S34_O12)

3.4.3.2 Effect of wind direction and opening configuration on r

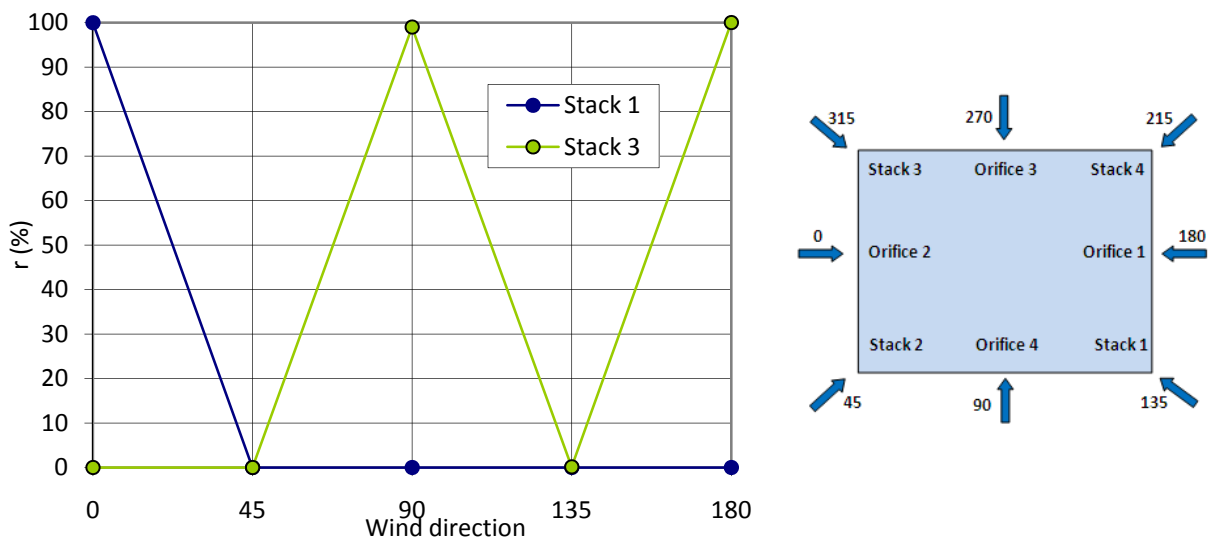


Figure 3.28 Variation of r with wind direction – two stacks, four orifices (S13_O1234)

3 Experiments – wind alone tests

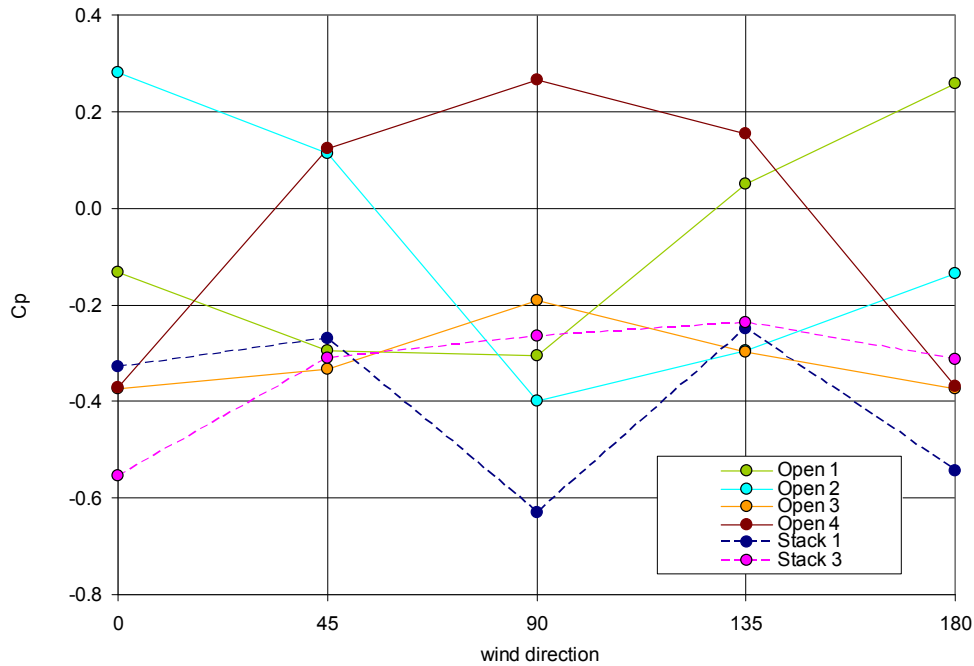


Figure 3.29 C_p variation with wind direction – two stacks, four orifices (S13_O1234)

Figure 3.28 shows the variation of r with wind direction for the two stacks and four orifices case, Figure 3.29 shows the corresponding C_p variation. Whether or not flow reversal occurs depends primarily on the relative values of C_p at the openings and on the relative sizes of the openings. For the wind-alone case, it is a relatively simple matter to calculate the flows with an envelope flow model. When buoyancy is involved, the problem is more difficult, since account needs to be taken of the dependence of stack temperature on flow direction (wind and buoyancy combined cases are in Chapter 5).

Simply using the values of C_p can be misleading, as shown by the fact that flow reversal was observed in Stack 3 for $\phi = 0, 90$ and 180 , but no flow reversal was observed for $\phi = 45$ and 135 . The stack C_p values are close to the orifice values for the first three wind directions of Stack 3, whereas the most negative stack C_p values were observed for the second two directions.

3 Experiments – wind alone tests

To maintain upward flow within the stacks, the pressures at the stack outlets are supposed to be lower than those at the orifices. Yet for all the wind directions above, there are certain orifice pressures lower than the stack outlet pressures by a small value, and the orifices which have lower pressures are mounted on the leeward wall, e.g. for the case of $\phi = 135$, pressures of orifice 2 and 3 are lower than the stacks. However, neither stack 1 nor stack 3 have reversal at $\phi = 135$. There were three cases when flow reversal occurred in one of the stacks:

- i) $\phi = 0$, $r = 100\%$ for stack 1
- ii) $\phi = 90$, $r = 100\%$ for stack 3
- iii) $\phi = 180$, $r = 100\%$ for stack 3

For all the cases above, the pressures of the stack outlet which maintained upward flow were more than twice as negative as those of the other stack which had reversed flow. From Figure 3.28 and Figure 3.29, one can see that the pressure differences between the stack outlets and orifices are the most important determinants of flow reversal, however pressure difference between stack outlets also play a role. A question arises: is it possible to predict flow directions using opening pressures? This is answered in Chapter 6, Section 6.2.

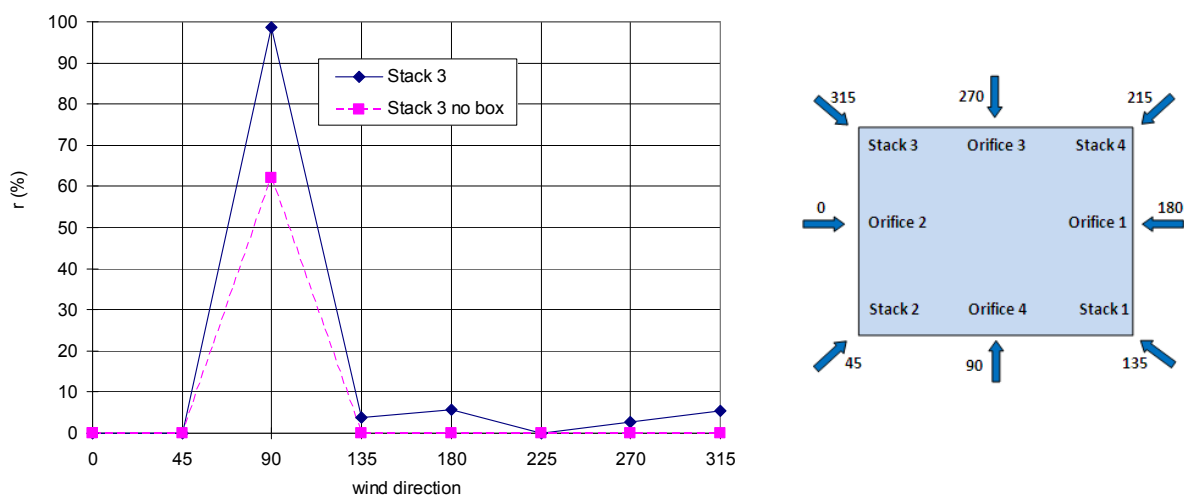


Figure 3.30 Flow reversal variation with wind direction for Stack 3 (S34_O12)

3 Experiments – wind alone tests

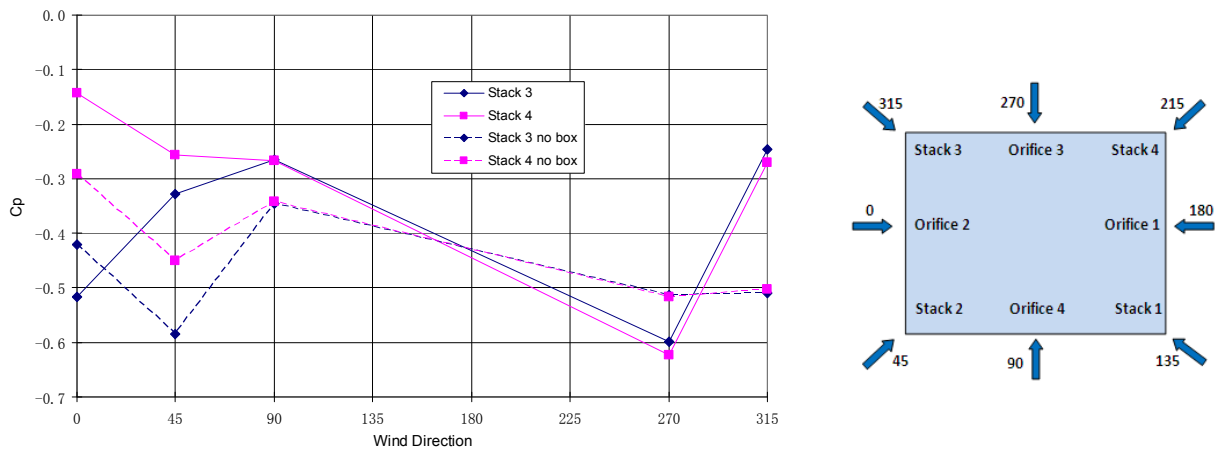


Figure 3.31 Stack C_p variation with wind direction and stack geometry

Figure 3.30 gives the reversal percentage of stack 3 for the case of (S34_O12). The figure also shows the effect of removing the stack boxes. It can be seen that, with the boxes, significant flow reversal occurs around $\phi = 90$, with some reversal at other wind directions. Removing the stack boxes improves the situation overall, but reversal ($r = 60\%$) is still significant around $\phi = 90$. The reduction of r at this wind direction is consistent with the more negative C_p values (Figure 3.31). The velocity fields at the top of the stacks will be affected by the removal of the boxes, and this could affect the pressure fields around the stack outlets.

It is discovered from Figure 3.28 and Figure 3.30 that all the stacks in which flow reversal occurs are the downstream ones. We should explain why the pressures around downstream stacks are higher than those around the upstream ones. The indication is that the velocity fields around the downstream stack outlets are influenced by the upstream stacks which act as shelters of the downstream ones. The downstream stacks are in the wakes of the shelters, the mean wind speeds in the wakes are less than the approaching wind speed. This situation generally affords the shelters (upstream stacks) in terms of lower mean pressures (Cook, 1985, pp. 184-185). However without the stack boxes, the thinner body of the upstream stacks have less effect on the mean wind speed in the wakes, thus less influence on the downstream.

3 Experiments – wind alone tests

Another possible reason is that the upstream stacks may cause flow separation and the downstream stack outlets are located in the flow reattaching zones (downward flow component).

Figure 3.32 shows the results of (S1234_O12). These results can be compared with Figure 3.33 which is for (S1234_O1234). Increasing the number of orifices has some effect (r reduces from 40 % to about 30 % at wind directions of 0 and 180), but it is not large. However there is not a particularly large increase in the effective area due to the small areas of the orifices.

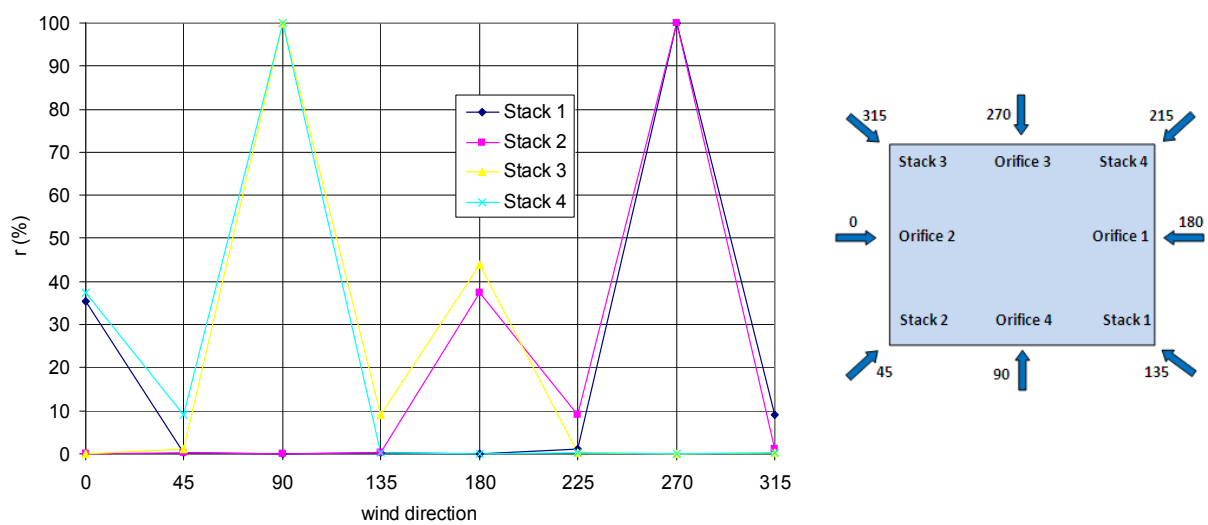


Figure 3.32 Flow reversal variation with wind direction for stack 1,2,3 and 4 (S1234_O12)

3 Experiments – wind alone tests

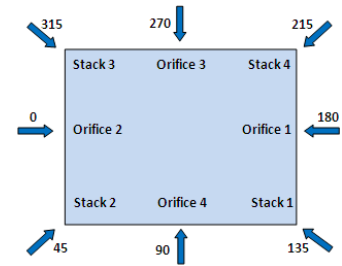
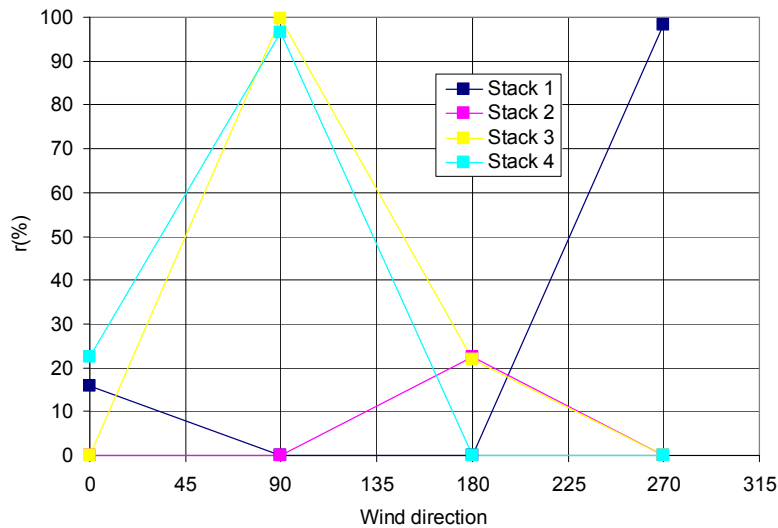


Figure 3.33 Flow reversal variation with wind direction of stacks 1,2,3 and 4 (S1234_O1234)

Figure 3.34 shows the reversal percentage of Stack 3 for different wind directions and opening configurations. Moving away the stack boxes reduces the reversal percentage, e.g. for the wind direction of 90 degree, comparing cases of (S34_O12) and (S34_O12 no box), r reduces from 100 % to 62 %. Increasing the orifice number also reduces the reversal percentage, e.g. for the wind direction of 180 degree, when the number of orifices increases from two to four (S1234_12) and (S1234_O1234), r decreases from 36 % to 22 %. However, the orifice area used in this research is very small, one should expect a higher decrease of r with a larger orifice area.

3 Experiments – wind alone tests

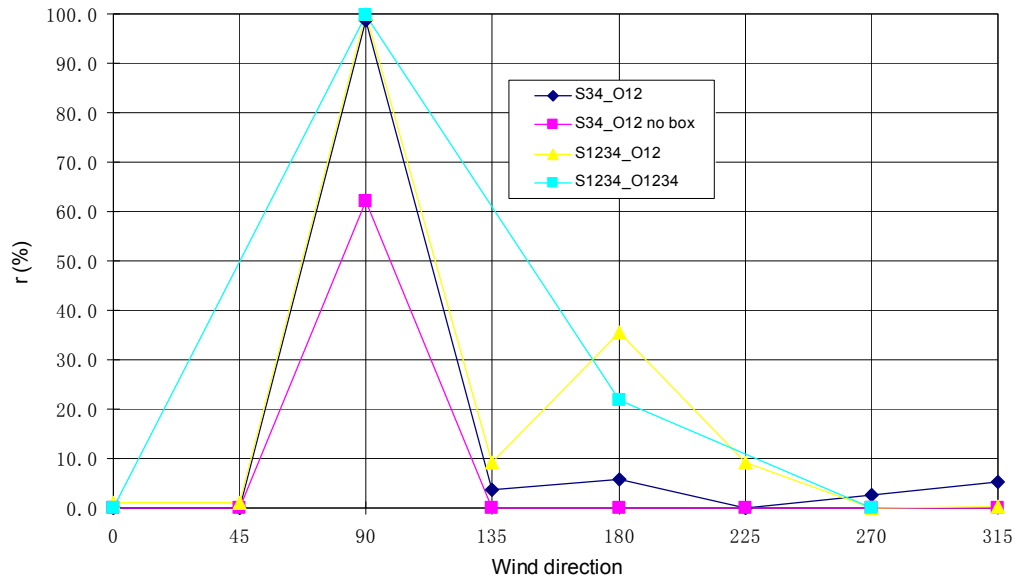


Figure 3.34 Flow reversal of Stack 3 for different wind directions and opening configurations

3.4.3.3 Reversal and $\Delta C_p / \sigma_{\Delta C_p}$

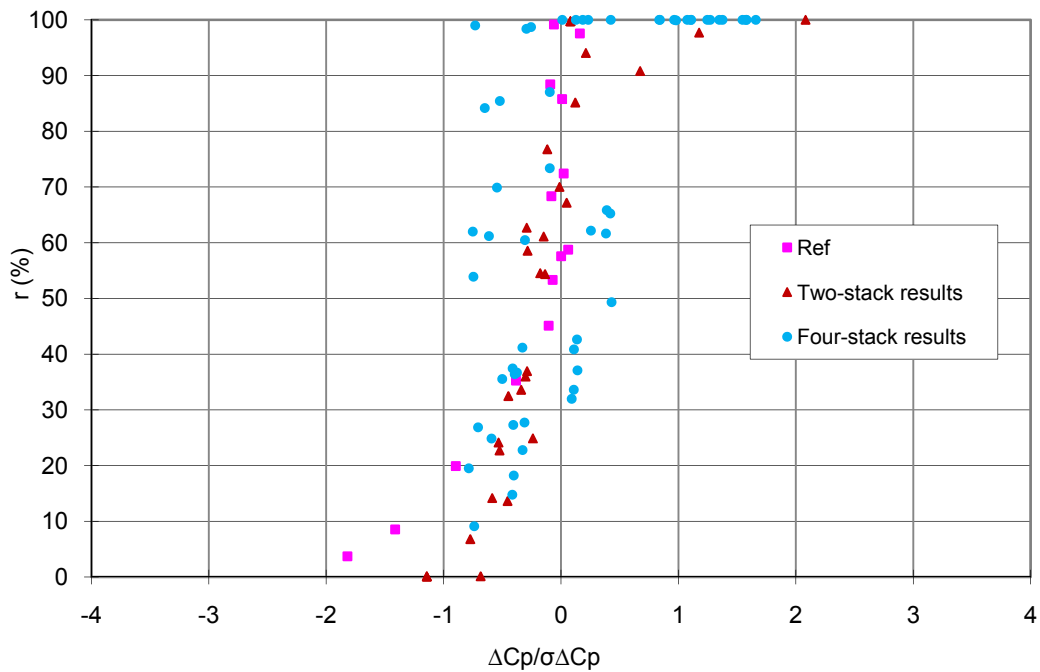


Figure 3.35 Variation of r with $\Delta C_p / \sigma_{\Delta C_p}$ ("Ref" is (Cooper and Etheridge, 2007))

3 Experiments – wind alone tests

Figure 3.35 shows r against pressure parameter across the stacks. $\Delta C_p/\sigma_{\Delta C_p}$ is an important pressure parameter which should describe whether or not reversal occurs, e.g. for $\Delta C_p/\sigma_{\Delta C_p} < -2$, no reversal occurs. The upward flow results ($r < 30\%$) of four-stack cases show agreement with the results of two-stack cases. Yet for r above approximately 30%, there are some disagreements. For a certain number of downward flow results, the value of $\Delta C_p/\sigma_{\Delta C_p}$ distribute between -1 and -0.5, which in theory should be positive. ΔC_p is defined by

$$\Delta C_p = \frac{P_{st} - P_{in}}{0.5\rho U_{ref}^2}, \text{ where } P_{st} \text{ is the measured stack pressure and } P_{in} \text{ is the internal pressure.}$$

The investigation of this phenomenon is discussed in Chapter 7.

3.5 Summary and conclusions

In this chapter the experimental techniques have been described and results for the wind alone case are presented. The main conclusions are as follows:

- 1) An uncertainty of less than 10 % in the measurement of ventilation rate is probably a reasonable estimate of the accuracy of the hot-wire technique. The most likely caused of the error lies in the calibration of the hot-wire.
- 2) The observations of the resonant frequency in the velocity and pressure for the four-stack model imply that the stiffening of the box was not entirely successful. The resonance can be eliminated by software signal filtering.
- 3) A dependence of r on Re_b was observed, which indicates that higher r is expected at full scale.
- 4) The most important determinants of flow reversal is the pressure differences between the stack outlets and the orifices, but the pressure difference between stack outlets also play a role. One can not totally rely on wind pressures to predict flow directions. Theoretical calculations are needed (see Chapter 6, Section 6.2 and Section 6.3).
- 5) All the stack reversals happen in the downstream stacks, indicating an influence of the stack geometry in the upstream.
- 6) Increasing the number of orifices has some effect in reducing the reversal percentage, yet it depends on the size the orifices relative to the façade area (porosity).

4 Important parameters – C_z and C_p

4.1 Introduction

The applicability of the equation (2.3) to envelope flow models is based on certain assumptions: 1) The pressure distribution on the building envelope is not affected by the presence of the openings; 2) The discharge coefficient obtained from still-air tests (no wind present) can be adopted for unsteady cases; 3) The dynamic pressure in the room can be neglected, which means the kinetic energy induced by the approaching wind passing through the opening is dissipated downstream of the opening (Heiselberg and Sandberg, 2005; Sandberg, 2004). These assumptions have an indication that the envelope flow model is meant to be used for small openings, when there is no stream tube within the envelope (e.g. cross ventilation). Therefore about the two parameters C_z and C_p of the envelope equation, these assumptions should be treated differently for small openings and large openings. N.B. only small openings are investigated in this thesis, discussions about large openings is presented in literature review (Section 4.4).

Assumption 1): It is generally accepted that the influence of the presence of small openings on the pressure distribution can be neglected (Karava et al., 2006). Yet, is the pressure distribution affected by small openings distributions? There will be some insights into this question based on wind tunnel testing results. If the answer were yes, then the ventilation flow pattern will be affected, although this is not an issue related to the validity of equation (2.3).

Assumption 2): The method used in Chapter 3 Section 3.3.2.1 is to measure C_z of small openings and long openings during the process of steady calibration i.e. the still-air case. But

4 Important parameters – C_z and C_p

in reality, the wind fluctuates and changes directions. Will the wind fluctuation and direction affect the C_z of small/long openings?

Assumption 3): Heiselberg and Sandberg (2005) suggested that the assumption regarding dissipation of kinetic energy is fulfilled for opening ratio of less than 1 %. The test models used in this thesis are equipped with small openings with porosities (ratio of opening area and façade area) less than 1% and long openings, thus assumption 3) is valid. For large opening cross ventilation, there is a stream tube within the envelope, thus the flow is not only driven by static pressure difference (the term $|\Delta P|$ in the envelope equation), the dynamic pressure should also be taken into account. The contribution of the dynamic pressure of the stream tube could be considered in the definition of C_z for large openings.

In this chapter, investigations of C_p and C_z will be presented separately. For each parameter, the discussions about the assumptions will be presented in the literature review, including both small/long openings and large openings. Then the testing results for C_p and C_z for small/long openings will be presented. Particular attention is paid to the questions in assumption 1) and assumption 2).

4.2 C_p - literature review

Wind pressure coefficients are influenced by a wide range of parameters, including building geometry, position on the façade, the degree of exposure, and wind direction and possibly opening configurations. Costola et al. (2009) stated that the results from wind tunnel tests or CFD (Moeske et al., 2005; Yuan, 2007; Costola and Alucci, 2007) could show large variations with databases in software even for simple building shapes. This is the first stage of uncertainty. Given the correct C_p database from wind-tunnel tests, there are still other uncertainties coming from the presence of the openings (since data was obtained from solid model without openings), and the location of the openings. Costola et al. (2010) provides information about the uncertainty in the calculated air flow rate due to the use of surface-averaged pressure coefficient data. The pressure coefficient database they used was from

4 Important parameters – C_z and C_p

wind tunnel tests. They calculated the error between using the localised and surface-averaged pressure coefficient for 15 different building shapes and a large number of opening configurations (locations on the envelope) and different wind directions. Apart from the opening locations associated with the highest error (i.e. openings located in the corners of the envelope are not considered), the error come from the majority of opening locations is still about 50%. Therefore one should use local values rather than the average values. One should expect a higher error when using secondary databases source such as design guide or database in software.

In addition to the mean pressure distribution, correlations between the unsteady wind pressure coefficients can also be important, because they can lead to errors in unsteady envelope flow models, particularly when mean pressure differences are small (Etheridge, 2000). If two surface pressures tend to increase and decrease at the same time (positively correlated), this will reduce the influence of fluctuation on flow rates. There are researches about pressure correlations on buildings but more to do with the approaching wind rather than the influence of the building configuration which is important in terms of natural ventilation. For example, Tieleman et al. (1998; 2003) talked about influence of surface roughness and velocity vibration on surface pressure correlations, which decrease with the increasing influencing factors. Another literature (Beste and Cermak, 2007) studies the pressure correlation between building surface pressures and internal pressure of a fixed building configuration.

What is more, pressure coefficients on building surfaces could also be affected by ground surface roughness and surrounding buildings (Tieleman et al., 2001; Chang and Meroney, 2003), which should be taken into account for design purposes. This is an additional source of uncertainty.

4.3 C_p – results and analysis

In the following, the effects of building Reynolds number, wind direction, stack geometry and opening configuration on mean pressure coefficients will be presented.

4.3.1 Effect of building Reynolds number

Ideally the nondimensional pressure results should be independent of building Reynolds number for buildings with small openings. Building Reynolds number is based on building height and wind speed, and is defined by equation (3.6). Figure 10 illustrates the dependence of C_p on reference wind speed for the case of (S1234_O12). Independence of both opening and internal C_p on Re_b can be seen for U_{ref} higher than about 4 m/s.

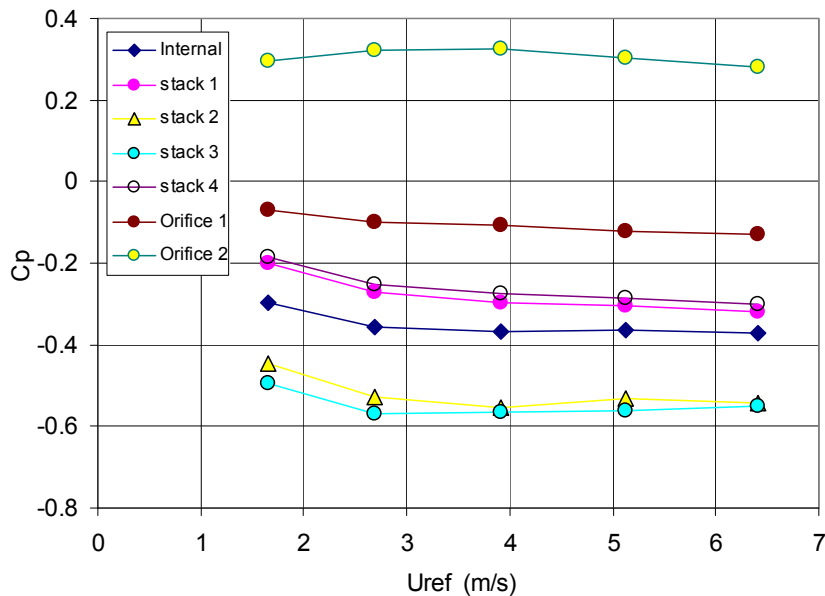


Figure 4.1 Variation of C_p with U_{ref} (S1234_O12)

4.3.2 Effect of wind direction

Wind direction and the shape of the building and stacks are the main determinants of C_p . Figure 4.2 and Figure 4.3 show respectively the variation of the pressure coefficients with wind direction for the (S1234) and (S13_O1234) cases at $U_{ref} = 5.3$ m/s. One would expect the C_p values for the stacks to be equal at certain wind directions by virtue of symmetry. For

4 Important parameters – C_z and C_p

example, at 0 degree wind direction in Figure 4.2, $C_{ps1} = C_{ps4}$ and $C_{ps2} = C_{ps3}$. Figure 4.3 also displays reasonable symmetry. One would also expect the C_p values for orifices on windward faces to be more positive than others, and this is evident in Figure 4.3.

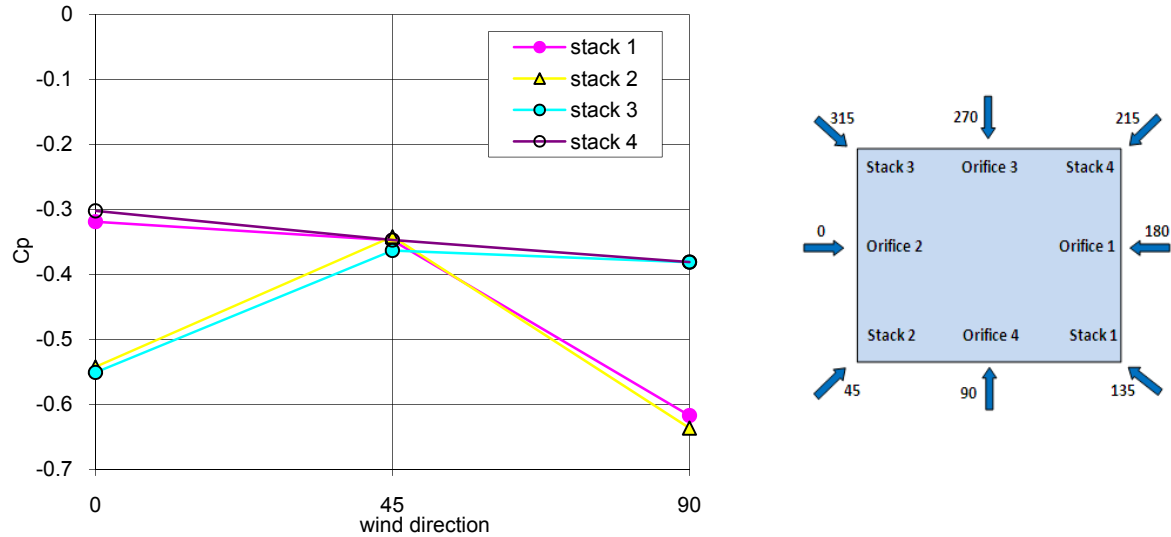


Figure 4.2 C_p variation with wind direction (S1234)

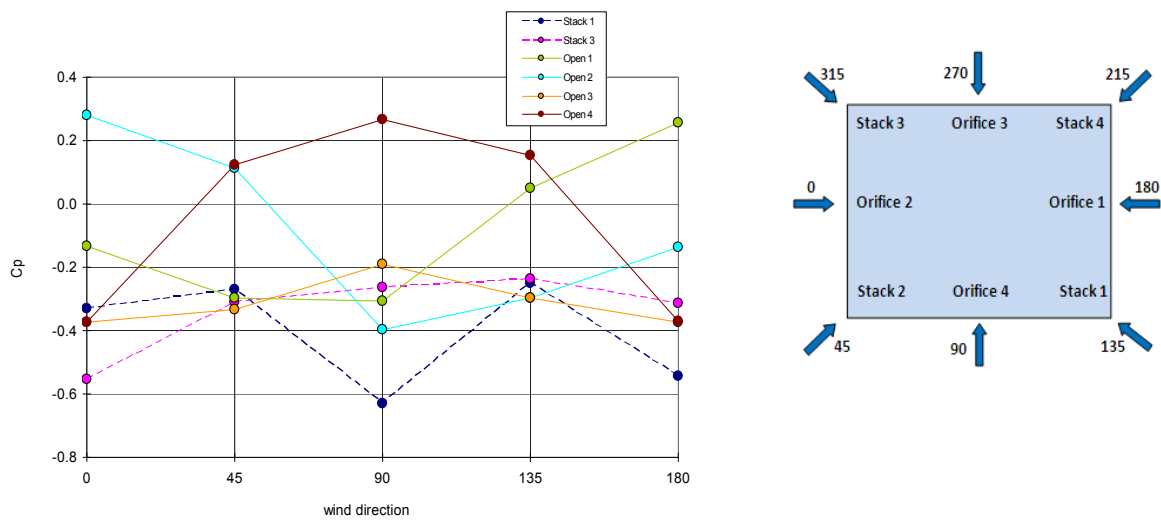


Figure 4.3 C_p variation with wind direction (S13_O1234)

4.3.3 Effect of stack geometry

Values for two stacks (stacks 3 and 4) at a fixed wind speed ($U_{ref} = 5.3$ m/s) are shown in Figure 4.4. It can be seen that the values with and without the stack boxes differ quite

4 Important parameters – C_z and C_p

considerably for all wind directions. The stack boxes decrease C_p for windward stacks, whereas they increase C_p for leeward stacks (for explanations of this phenomena, see Chapter 3, Section 3.4.3.2).

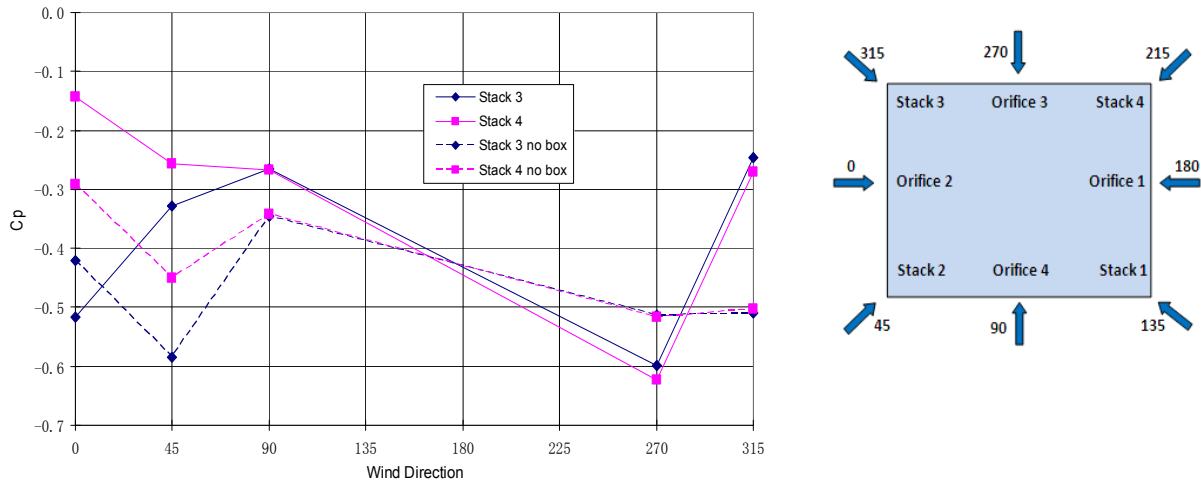


Figure 4.4 Stack C_p variation with wind direction and stack geometry

4.3.4 Effect of opening configuration

In principle one would expect the opening configuration to have little effect on the mean wind pressures, because the openings are flush and their areas are small in relation to the areas of the surfaces in which they lie (porosity less than 1 %). Now answering the question in assumption 1), most of the results satisfy this expectation, but not all, with exceptions of some stack C_p (e.g. some cases in Figure 4.5 presented as follows).

Table 4.1 shows values of stack C_p obtained with different opening configurations at two wind directions. Figure 4.5 shows the results for $\phi = 0$ in graphical form. For $\phi = 180$, when the orifice number increases from 2 to 4, no obvious changes in stack C_p are observed. For $\phi = 0$, it can be seen that C_{p1} and C_{p4} change considerably when two orifices are added, but not when a further two orifices are added. At this wind direction, stacks 1 and 4 are located at the leeward side.

4 Important parameters – C_z and C_p

Table 4.1 Pressures of stack outlets with different orifices

Wind direction	0	0	0	180	180
Opening	4S	4S 2O	4S 4O	4S 2O	4S 4O
C_{p1}	-0.32	-0.17	-0.16	-0.55	-0.52
C_{p2}	-0.54	-0.53	-0.54	-0.18	-0.16
C_{p3}	-0.55	-0.55	-0.56	-0.18	-0.15
C_{p4}	-0.30	-0.17	-0.16	-0.52	-0.50

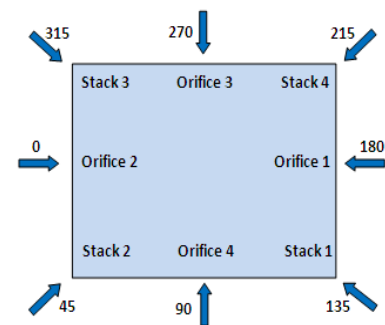
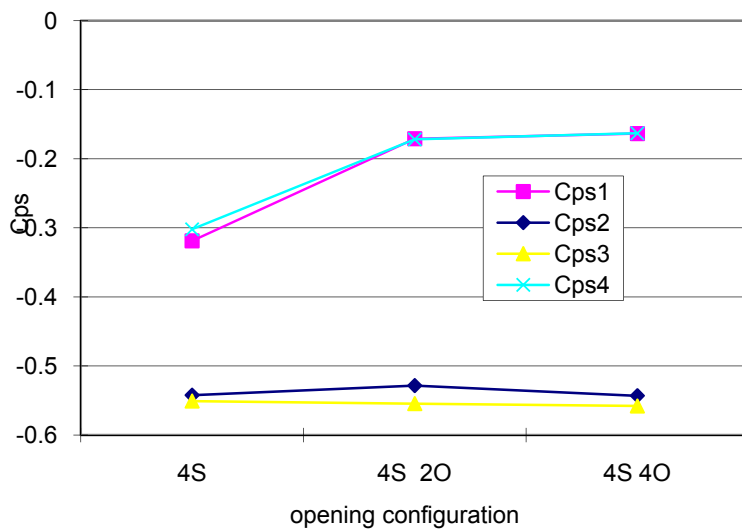


Figure 4.5 Stack C_p variation with increasing number of orifices, $\phi = 0$

Results for $\phi = 90$ are given in Figure 4.6 for stacks and orifices. It can be seen that none of the orifice C_p are affected, but only one of the two stacks (Stack 3).

4 Important parameters – C_z and C_p

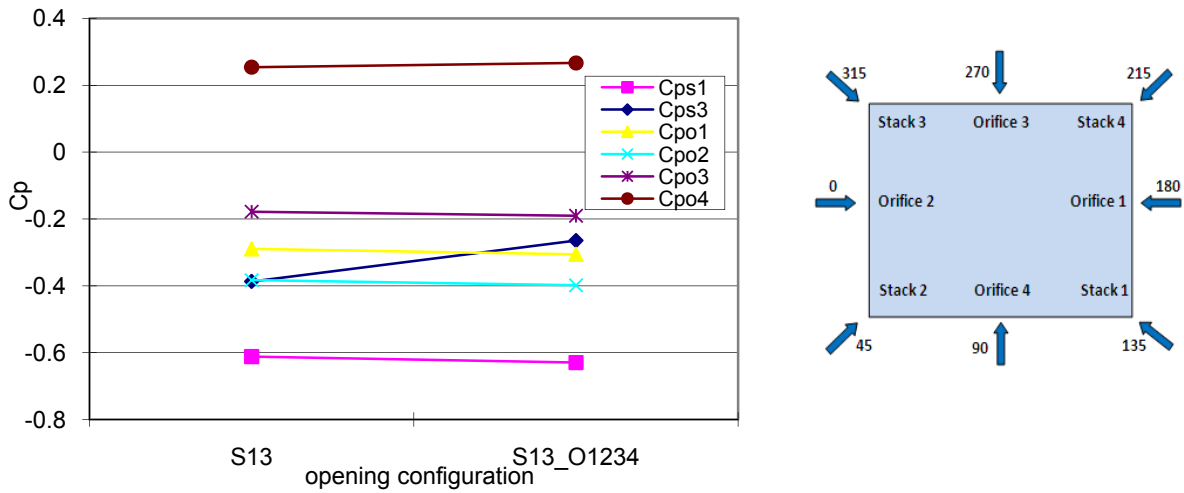


Figure 4.6 Stack and orifice C_p with increasing number of orifices, $\phi = 90$

Results for $\phi = 0$ are given in Figure 4.7 for stacks and orifices. It can be seen that none of the C_p are affected.

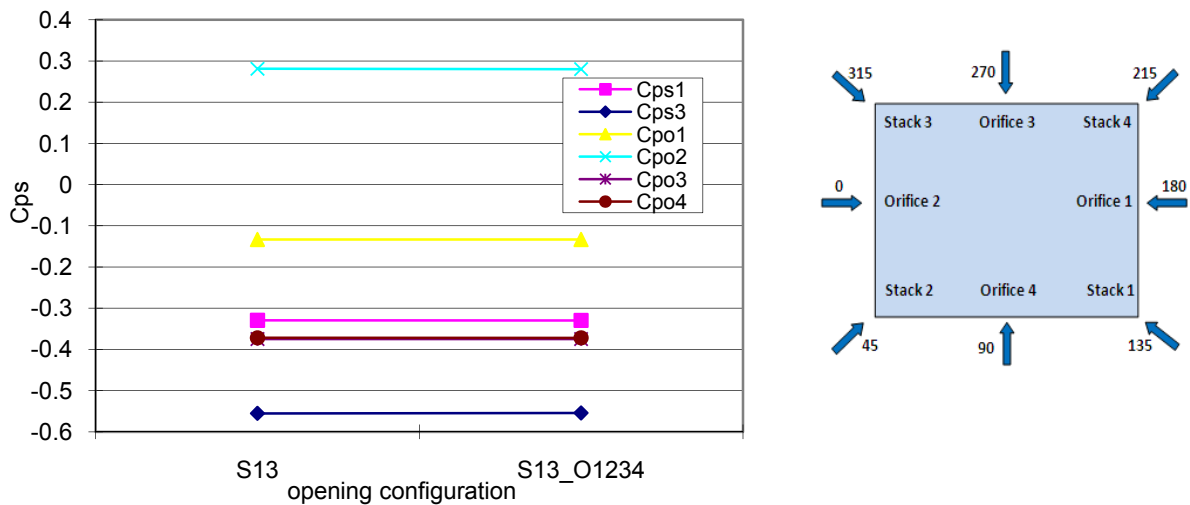


Figure 4.7 Stack and orifice C_p with increasing number of orifices, $\phi = 0$

Figure 4.8 and Figure 4.9 show for orifices and stacks respectively, the effect of opening configuration over the range of wind directions.

4 Important parameters – C_z and C_p

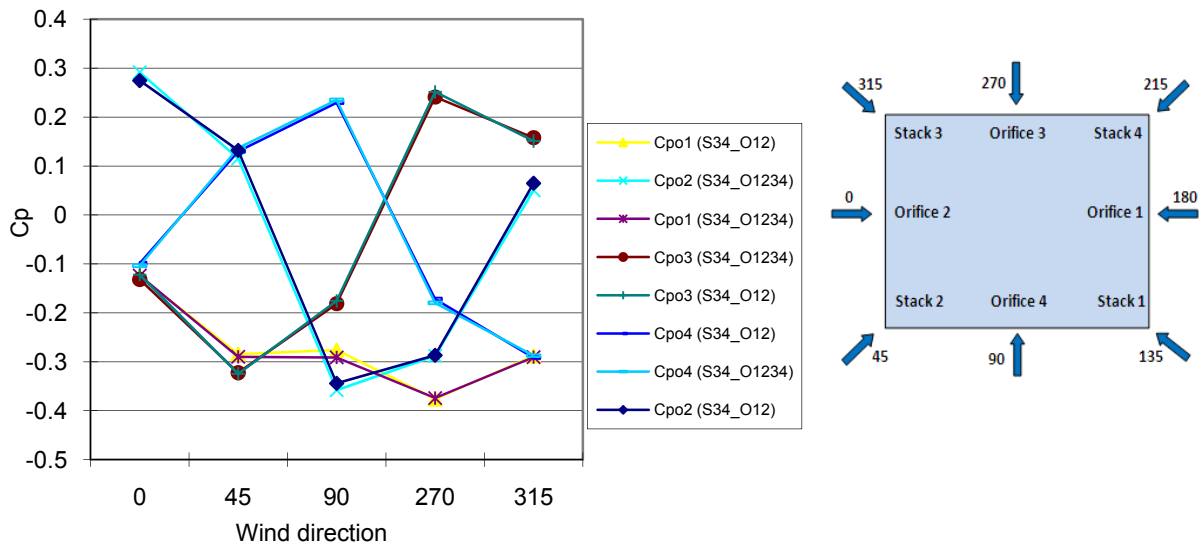


Figure 4.8 Orifice C_p with increasing number of orifices in the cases of different wind directions

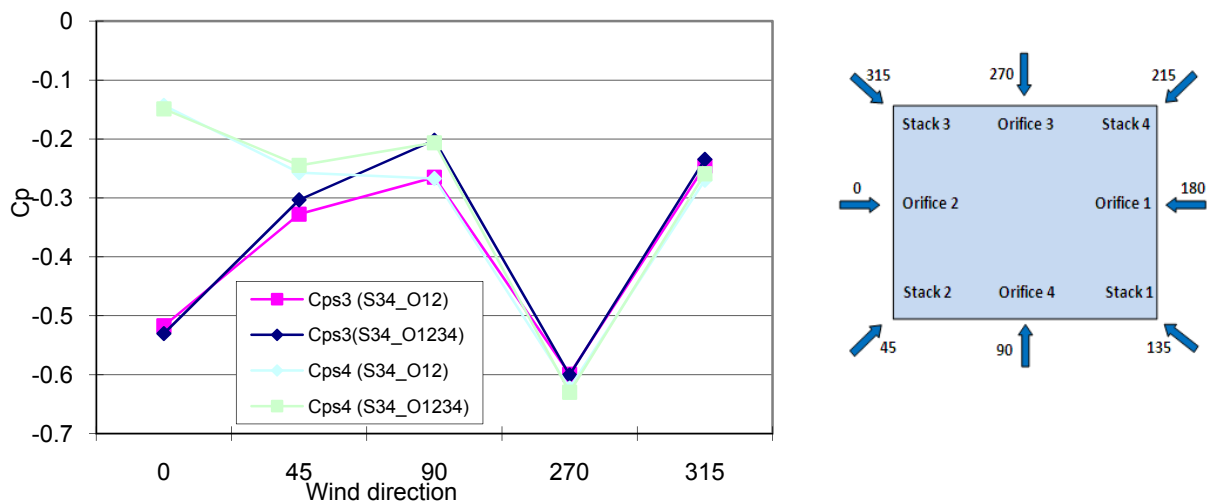


Figure 4.9 Stack C_p with increasing number of orifices in the cases of different wind directions

There is a clear indication in the above results that orifice C_p are not affected by the opening configuration, but the stack C_p can be affected (C_{ps3} and C_{ps4} for $\phi = 45$ and $\phi = 90$). The results for the orifices display very good repeatability, and any changes that occur are so small that they can be ignored in the design process.

4 Important parameters – C_z and C_p

The changes that have been observed for the stacks are significant, in the sense that they are not due to poor repeatability. Two possible explanations are as follows.

In terms of the flow around the exterior of the model, the presence of an opening corresponds to a source (outward flow) or a sink (inward flow). If the opening lies in an attached boundary layer, the flow through the opening will lead to a change in the local displacement thickness of the layer. The disturbance to the pressure distribution will be localized. However, if the opening lies in a separated flow region, with reattachment, the presence of the opening flow could change the shape of the separated region (and the nature of reattachment). A change in shape of a separation region is effectively a change in shape of the model, so the effects could be more far-reaching. Another possibility lies in the position of the tapping used for the stack C_p (for studies about this possibility, see Chapter 7, Section 7.4).

4.3.5 C_p correlations between openings

The correlation between two pressures (time serial values) is calculated by

$$\text{Correl}(P_1, P_2) = \frac{\sum_{i=0}^n (P_{1i} - \bar{P}_1)(P_{2i} - \bar{P}_2)}{\sqrt{\sum_{i=0}^n (P_{1i} - \bar{P}_1)^2 \sum_{i=0}^n (P_{2i} - \bar{P}_2)^2}} \quad (4.1)$$

As stated in the literature review, correlations between the unsteady wind pressure coefficients can be important, because they can lead to errors in unsteady envelope flow models, particularly when mean pressure differences are small. The observed influence of wind speed (building Reynolds number), wind direction and especially the opening configurations on the correlation between selected stack pressures are described in the following for selected stack outlet pressures.

1) Influence of wind speed

Figure 4.10 shows the pressure correlations for the case of (S1234), 0 degree wind direction, with increasing wind speed from 1 m/s to 5 m/s by a step of 1 m/s. (e.g. P1 & P4 means

4 Important parameters – C_z and C_p

correlation between P1 and P4). There is no clear trend with Re_b , but the influence is relatively small compared to the following.

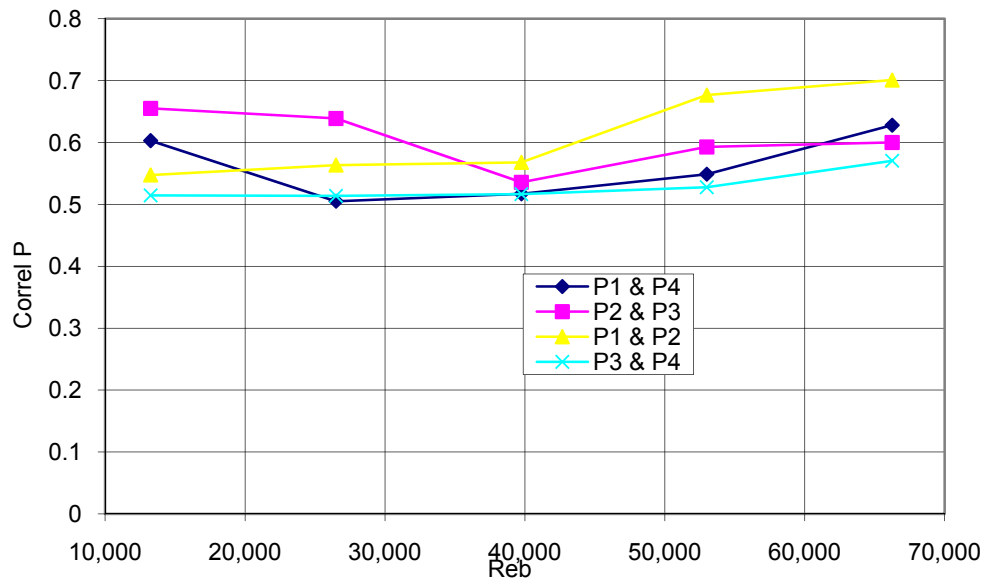


Figure 4.10 Variation of stack pressure correlations with Re_b , for $\phi=0$ (S1234)

2) Influence of wind direction

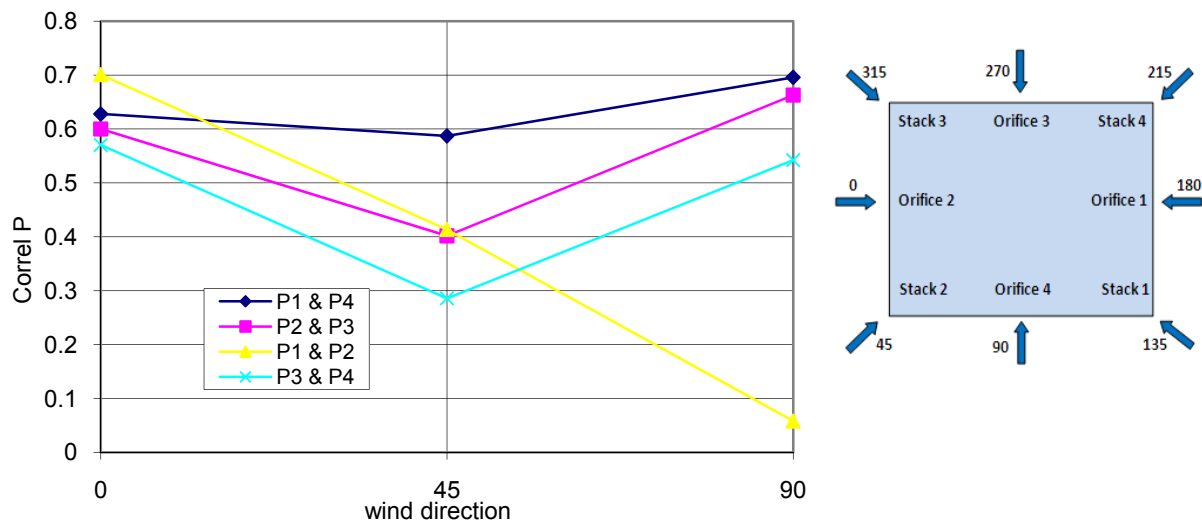


Figure 4.11 Variation of stack pressure correlations with wind directions (S1234)

4 Important parameters – C_z and C_p

Figure 4.11 shows the effect of wind direction. When the wind direction changes, the separation distance of the stack also changes. For wind direction of 0, stacks 2 and 3 are in the windward side of the roof, the correlation of P2 and P3 is 0.6; for wind direction of 90, stacks 1 and 2 are in the windward side, but the correlation of P1 and P2 decreases to less than 0.1. In other words, with a longer separation distance between stacks 1 and 2 than that between stacks 2 and 3 (while they are the ones facing the wind), the correlation of P1 and P2 decreases. Qualitatively, this is not unexpected.

3) Influence of opening configuration

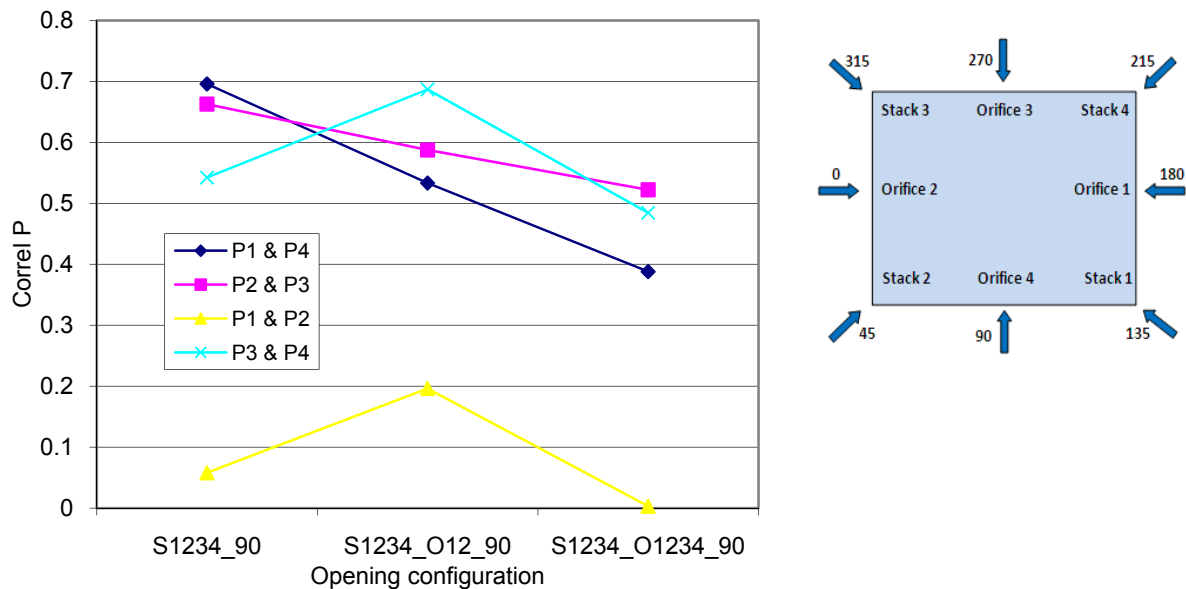


Figure 4.12 Variation of stack pressure correlations with the increasing number of orifices for $\phi=90$

Figure 4.12 shows that increasing the number of orifices has some effects on pressure correlations, but not large. There is an obvious difference between correlation of P1 and p2 and the others. When the wind direction is 90, stacks 1 and 2 are in the windward side of the roof. The results are consistent with Figure 4.11, which shows the effect of separation distance between stacks.

4 Important parameters – C_z and C_p

As stated in Section 4.3.4, orifice C_p are not affected by the opening configuration, but the stack C_p can be affected. For example, in Figure 4.5, C_{p1} and C_{p4} change considerably when two orifices are added. The corresponding changes of C_p correlations for the case in Figure 4.5 are shown in Figure 4.13. Apart from the pressure correlation between C_{p2} and C_{p3} , all the others are affected by the increasing number of orifices, which is consistent with Figure 4.5.

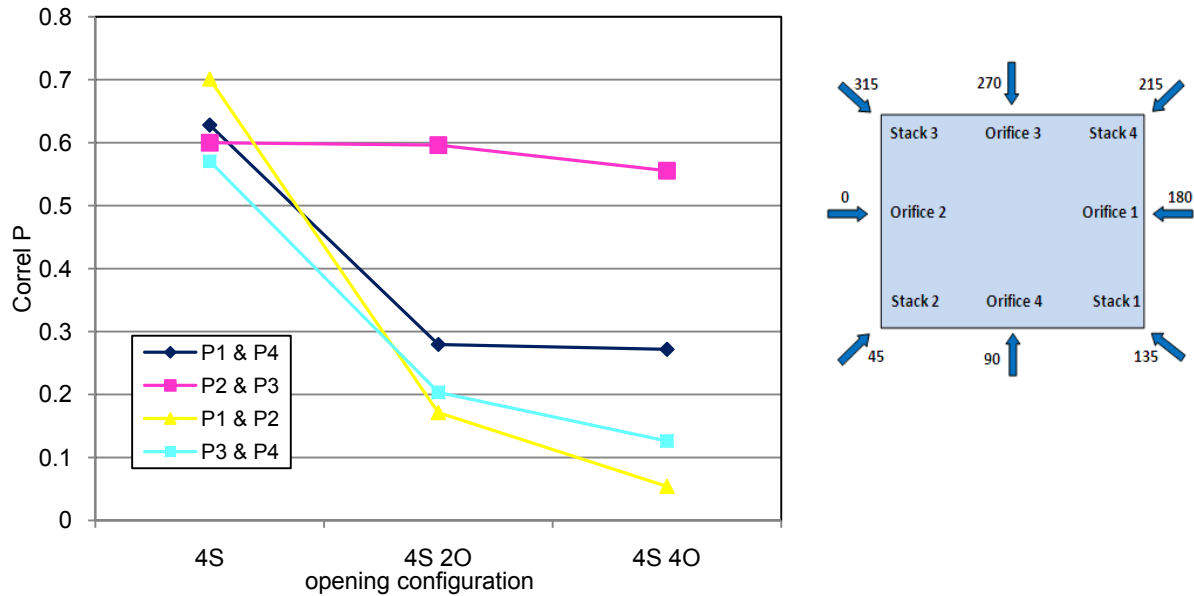


Figure 4.13 Variation of stack pressure correlations with the increasing number of orifices for $\phi=0$

4.3.6 C_p correlations between opening pressure and internal pressure

When there are multiple openings, the flow rate through openings are calculated using the differences between the outlet pressures and the internal pressure. If the opening outlet pressure and internal pressure tend to increase and decrease at the same time (positively correlated), this will reduce the influence of external fluctuations on flow rates. The observed influences of opening configurations are described in the following for selected stack outlet pressures. It is difficult to explain these observations because the instantaneous flow rates through the openings have a significant influence on P_{in} (see equation (2.49)). The QT model is intended as to model these effects. Thus this section is presented as a record of preliminary studies.

4 Important parameters – C_z and C_p

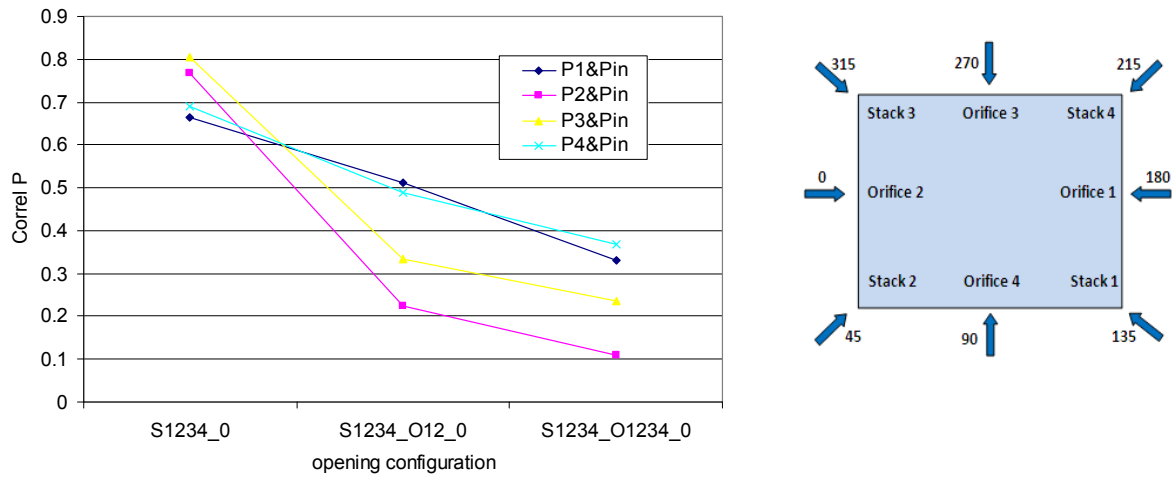


Figure 4.14 Stack pressure correlation with internal pressure with increasing number of orifices, $\phi=0$

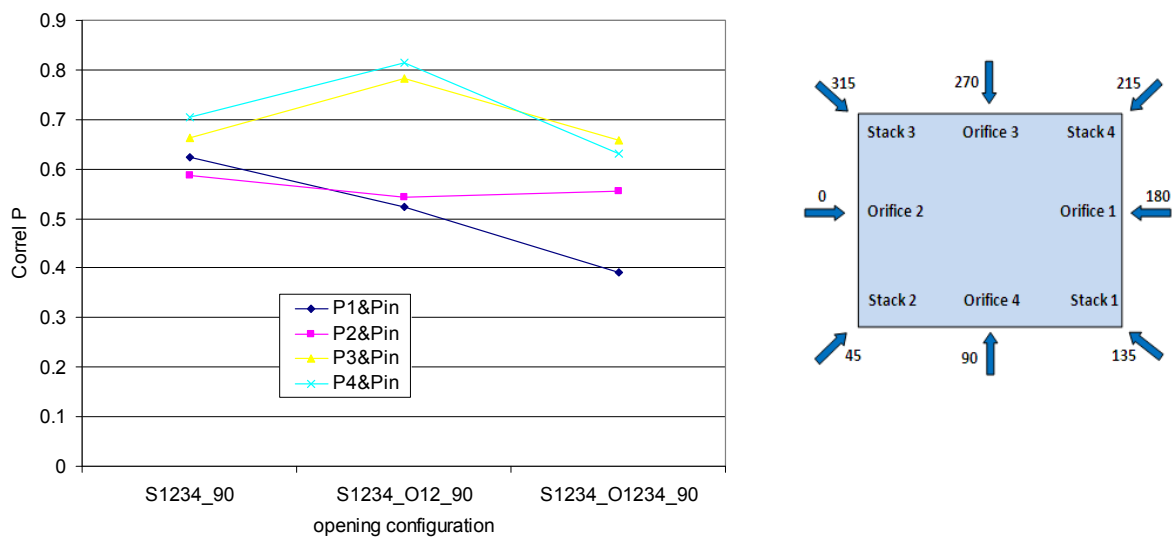


Figure 4.15 Stack pressure correlation with internal pressure with increasing number of orifices, $\phi=90$

Figure 4.14 and Figure 4.15 show the influence of increasing number of orifices for wind direction of 0 and 90 degree. Increasing the number of orifices perpendicular to the approaching wind (adding windward and leeward wall orifices 1 and 2 in Figure 4.14) has a significant effect on stack pressure correlation with internal pressure; whereas, openings on the side walls have less effect (adding side wall orifices 1 and 2 in Figure 4.15). Except for

4 Important parameters – C_z and C_p

the case of (S1234_0), when all the orifices were sealed, both graphs show that, the leeward stack pressures (stacks 1 and 4 in Figure 4.14, and stacks 3 and 4 in Figure 4.15) are more correlated to internal pressures. This phenomena is not consistent with that stated in Beste and Cermak (2007): pressures located at windward wall corner on the roof, above the dominant opening, which are in the high-suction zones are more correlated to internal pressure. Corresponding case is S1234_O12_0, in which P_2 and P_3 are less correlated to P_I . The possible reasons are: in Beste et al. (2007), there is a flat roof, thus one would expect the windward wall corner (in separation zone) to be more correlated with internal pressure. For the case in our research, there are four individual roofs of the stack boxes. The leeward stacks are located in the wake of the upward ones, which may be the reason why they are more related to the internal pressure.

4.4 C_z - literature review

The still-air discharge coefficient is the ‘characteristic’ of an opening: given a still-air pressure difference across an opening, C_z should only be determined by its geometry (and flow through the opening for long openings). In presence of the wind, the discharge coefficient is a result of the interaction between the approaching wind and the flow through the opening. Thereby C_z is also related to the building, e.g. porosity, and inlet area to outlet area ratio. In terms of the effects of the wind, three parts should be taken into account: 1) the presence of cross flow (flow component parallel to the wall); 2) unsteadiness of the external flow; 3) non-uniformity of the external surface pressure field around the opening (Chiu and Etheridge, 2007). It should be noted that it is the small sharp-edged orifice and the long opening that are studied in this thesis. Review of other type of openings (e.g. large opening) are presented for interests.

4.4.1 Sharp-edged openings

There is a review about C_z (Karava et al., 2004), summarising the up to date literature on discharge coefficients of orifices. They compared different studies considering different influencing factors on C_z , such as opening porosity, configuration, wind direction. Since then, there have been some new developments.

4 Important parameters – C_z and C_p

- 1) About opening porosity, Chu et al. (2009) studied the effects on small sharp-edged orifices. It was found that the C_z is a function of Reynolds number, and wind direction, but independent of external turbulence intensity and wall porosity (porosity less than 7%). Larger range of porosity was tested (Kurabuchi et al., 2006) in the wind tunnel, when the porosity is greater than 46%.
- 2) Inlet to outlet ratio (the ratio of inward flow opening area and outward flow opening area). Karava et al. (2005; 2007) studied the influence of inlet to outlet ratio on C_z and the internal pressure coefficient. It was observed that C_z increases with the increasing inlet to outlet ratio. Similar phenomena were discussed by Sandberg (2004).
- 3) About wind direction, there have been many studies, as summarised in Karava et al. (2004). With the increasing wind angle, typically there was a slightly increase in C_z , then a decrease to a much lower value till the minimum value when the wind is parallel to the wall. Among those studies, Kurabuchi et al. (2004) quantified the influencing factor of wind direction into a ‘local dynamic similarity model’, and put it into experimental investigations (Ohba et al., 2004). The dynamic pressure of the wind is decomposed into two parts: one parallel to the wall, one perpendicular to the wall. The discharge coefficient is defined as the square root of the ratio of dynamic pressure component perpendicularly entered the opening and the total pressure difference across the opening. Since the two components of the dynamic energy of the wind is a function of the wind direction, C_z can also be defined using the ratio of dynamic pressure parallel to the wall and the total pressure difference.

Chiu and Etheridge (2007) defined the C_z of a sharp-edged opening in terms of $C_z = f\left(\frac{V}{u}\right)$, where V is the wind velocity component parallel to the wall. This is of the same physical principle as that stated above but in a different form. CFD simulation

4 Important parameters – C_z and C_p

and wind tunnel tests were used to obtain the C_z value. When $\frac{V}{u}$ ranges from 0 to 9, C_z varies between 0.68 and 0.3. A lower C_z is expected with a greater $\frac{V}{u}$. It was noted that $\frac{V}{u}$ is a function of wind direction ϕ , independent of wind speed. Thereby, one can also use $C_z = f(\phi)$, which is more convenient for design process.

- 4) Unsteadiness of wind. With sharp-edged orifices, the flow pattern is primarily determined by the flow separation; thus the fluctuation of the wind has less effect on C_z than wind direction, and it can be neglected. There are CFD predictions to support this (Chiu and Etheridge, 2007).
- 5) C_z of outward orifice in the leeward wall. Most studies have treated the opening facing the wind. For cross-ventilation with two orifices, it is reasonable to consider C_z of the windward orifice, and take into account the leeward orifice in terms of inlet to outlet ratio. The exception is C_z of small openings, which should not be affected by other openings. However, if there are more than two openings, the orifices need to be treated individually. What C_z should be used for the leeward wall (outflow) orifice? Only a few results were obtained in Chiu and Etheridge (2007), finding that the outflow orifice exhibit lower C_z than the inward flow cases. During the theoretical process carried out in this thesis (Chapter 6), the author found that one should use a lower C_z for the outflow orifice in the leeward wall to obtain the flow pattern matching the measurements. Further studies are desirable.
- 6) Applicability of the envelope flow model. When there is a stream tube connecting the inward and outward orifices (this could only happen for very large openings located within limited distance), the driving force is no longer the static pressure difference, but also including the dynamic pressure. Therefore large opening cross-ventilation can not be treated with the conventional envelope flow model (Etheridge, 2004). However Sandberg (2004) stated an alternative view of using a ‘contraction

4 Important parameters – C_z and C_p

coefficient' in place of C_z , to make the static pressure difference as the driving force still applicable. This is based on shaping the stream tube within the envelope. Nevertheless, in practice cross-flow tube connecting the inward and outward orifice is not easy to occur, since there are obstacles in the building like partitions. Additionally, if the outward orifice locates at the side wall, the dynamic pressure may dissipate at the internal surface of the leeward wall, which may also increase the applicability of the conventional model.

4.4.2 Long openings

- 1) Chiu and Etheridge (2007) stated that C_z of long openings should be less affected by external flow conditions. Because for inflow C_z of long opening depends on the flow inside the opening; for outflow when the outlet lies in the external flow, the boundary condition of importance is the pressure around the outlet, rather than the velocity field. C_z was found to be dependent on the opening Reynolds number.

$$Re_o = \frac{\rho u d}{\mu} \quad (4.2)$$

where ρ denotes the density of air (kg/m^3), d the diameter of the opening (m), u the mean velocity in the opening ($u \equiv \frac{\bar{q}}{A}$) and μ the viscosity (Ns/m^2). If the opening is not symmetrical, C_z also depends on stack flow direction. The reversed inward flow has a larger C_z by about 10% than the outward flow. By putting a cover over the stack outlet, this 10% was eliminated for the wind on inward cases. In another study (Cooper and Etheridge, 2007), a peak of C_z value up to 2 was observed for the inward flow stack in a low Reynolds number range (500-1000). Similar phenomena are observed in this thesis, they will be compared with each other in Section 4.5.

4.4.3 Special openings

- 1) C_z of special openings were also studied. For example, Heiselberg et al. (2001) tested the discharge coefficient of hung windows. The external flow and installation effects on C_z of sharp-edged orifice and long openings were also tested (Etheridge et al.,

4 Important parameters – C_z and C_p

2004). It may be reasonable to put the factors like opening shape and attachment (e.g. a cowl) into an empirical term to modify C_z definition for design purpose. What is more, full scale C_z were also studied, Nishizawa et al. (2004) tested a full scale building model with large openings, and focused on the discharge coefficient changes with the wind directions. However wind direction is not the underlying cause of changes to C_z .

To sum up, the unsteady wind effects can be ignored for C_z of sharp-edged orifice. When there is no stream tube connecting inward and outflow orifices, C_z is only a function of wind velocity component parallel to the wall. For long openings, C_z is a function of opening Reynolds number; external flow affects C_z of inward flow stacks but not outward flow. By putting a cover over the stack outlet could reduce this effect. Additionally, definition of C_z is difficult with fluctuating flow of a long opening.

4.5 C_z – results and analysis

C_z of a sharp-edged orifice was generally investigated in Chiu and Etheridge (2007). Similar investigations are carried out here, in order to provide further information for the multiple stack case. For long openings, still-air C_z values of different flow directions were also investigated in Chiu and Etheridge (2007). It was found that C_z of inward flow show greater values than outward flow by about 10%. Therefore in this section, it is focusing on the repeatability of long opening C_z , and study the phenomena of the peak values occurring with downward flow. The only left remaining concern is about outflow orifice at leeward wall. Unfortunately it is not measured in this thesis, only indication is from theoretical calculation, a lower estimated C_z value of outflow orifice could make the flow rate results matching the measurements (see Chapter 6, Section 6.3.1).

4.5.1 Observed effect of wind speed on dimensionless flow rate

Figure 4.16 and Figure 4.17 illustrate the observed dependence of dimensionless flow rate u/U_{ref} on wind speed for two cases i.e. (S1234) and (S1234_O12). Flow into the box

4 Important parameters – C_z and C_p

(downward stack flow) is defined as positive. When the C_p are independent of wind speed, one would still expect to see a dependence of u/U_{ref} , due the dependence of C_z on Re_o . Rather surprisingly this is more evident in Figure 4.17 than in Figure 4.16. Figure 4.16 corresponds to the case where there are no sharp-edged orifices, so one would expect Re_o effects to be greater. However there is another factor at work, namely that the orifice C_z is also a function of V/u , so the windward orifice may have an unknown dependence on U_{ref} . This can lead to spurious indications of the effect of Re_b . The quantity V is the crossflow velocity in the external flow (parallel to the wall) close to the opening. These results were obtained with a fixed wind direction, so V/U_{ref} should be nominally constant.

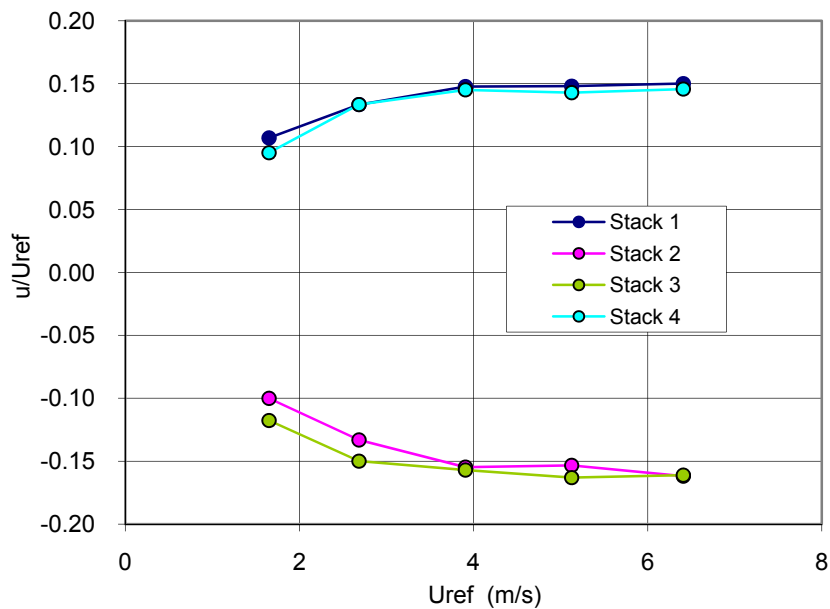


Figure 4.16 Variation of u_{st}/U_{ref} with U_{ref} (S1234)

4 Important parameters – C_z and C_p

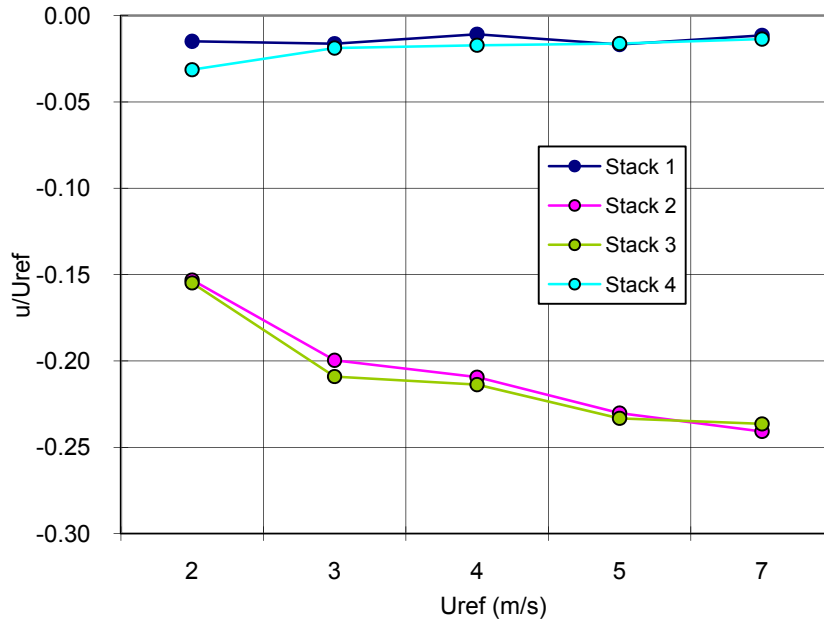


Figure 4.17 Variation of u_{st}/U_{ref} with U_{ref} (S1234_O12)

4.5.2 Still-air C_z values

As stated in the literature review, for a stack it has been found that the external flow has little effect on stack C_z for upward flow, and a significant effect for reversed flow. The basic reason for this is that with upward flow, the external flow only affects the outlet boundary condition. The present results for multiple stacks are examined in the light of the earlier findings and it will be seen that they are in agreement.

The still-air discharge coefficient C_z of an opening is defined in terms of the time-averaged values of the volume flow rate and the pressure difference across the opening.

$$C_z \equiv \frac{\bar{q}}{A} \sqrt{\frac{\rho}{2|\overline{\Delta P}|}} \quad (4.3)$$

where \bar{q} is the time-averaged value of flow rate

$\overline{\Delta P}$ is the time-averaged pressure difference across the opening. The pressure difference between stack outlet and internal pressure is

4 Important parameters – C_z and C_p

$$\overline{\Delta P} = \overline{P}_{st} - \overline{P}_I \quad (4.4)$$

Figure 4.18 shows results obtained from steady still-air calibration in the form of C_z against Re_{st} . The results are very similar to the earlier results, namely C_z is a function of Re_{st} and C_z with inward flow is greater than that with outward flow, due to the fact that C_p is obtained with one pressure tapping inside the stack (Chiu and Etheridge, 2007).

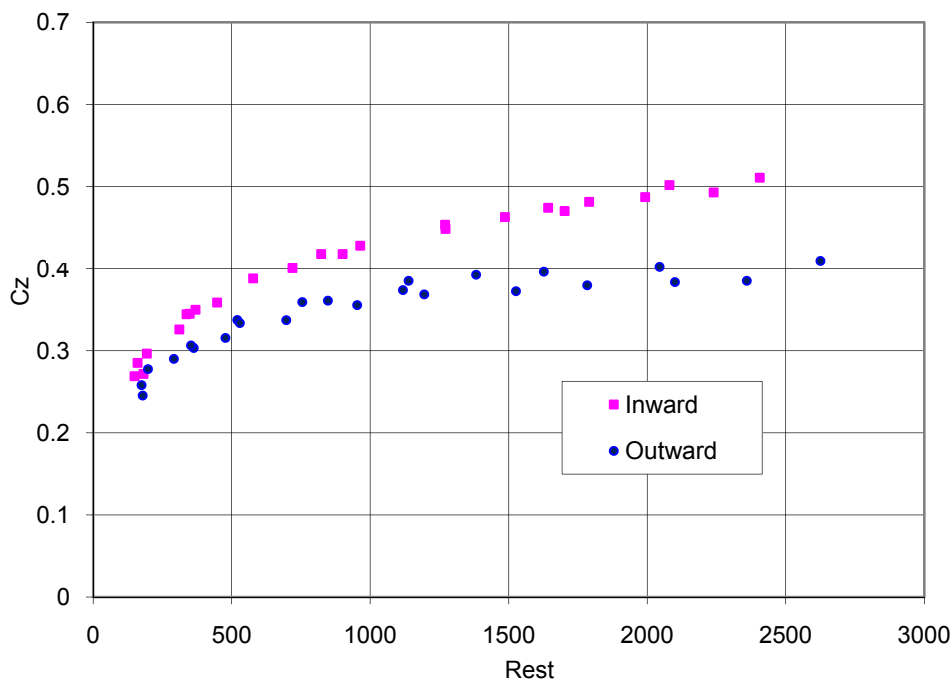


Figure 4.18 Still-air C_z against Re_{st} for inward and outward flow

4.5.3 Unsteady C_z values - external flow effects

Figure 4.19 and Figure 4.20 show the observed variation of stack C_z with Re_{st} for two opening configurations: (S1234) and (S1234_O12). In Figure 4.19 stacks 2 and 3 have outward flow and there is close agreement between them and with the still-air case (Figure 4.21). This reflects the fact that the outlet conditions have little effect on C_z of the upstream stacks. Stacks 1 and 4 have inward flow and their curves lie above the corresponding still-air curve. The high C_z values suggest that there is a downward momentum component in the external flow that contributes to the total driving force of the flow in the stacks. For these two cases a different definition of C_z would probably be appropriate i.e. one based on a total

4 Important parameters – C_z and C_p

pressure containing $0.5\rho V^2$ i.e. replace equation (4.4) by (4.5). In practice, this is not possible, because V is not known.

$$\overline{\Delta P} = \overline{P}_{st} + 0.5\rho V^2 - \overline{P}_I \quad (4.5)$$

The results for stacks 1 and 3 are not identical. This can probably be explained by differences between the external flow conditions at the stacks, although calibration errors may play a role.

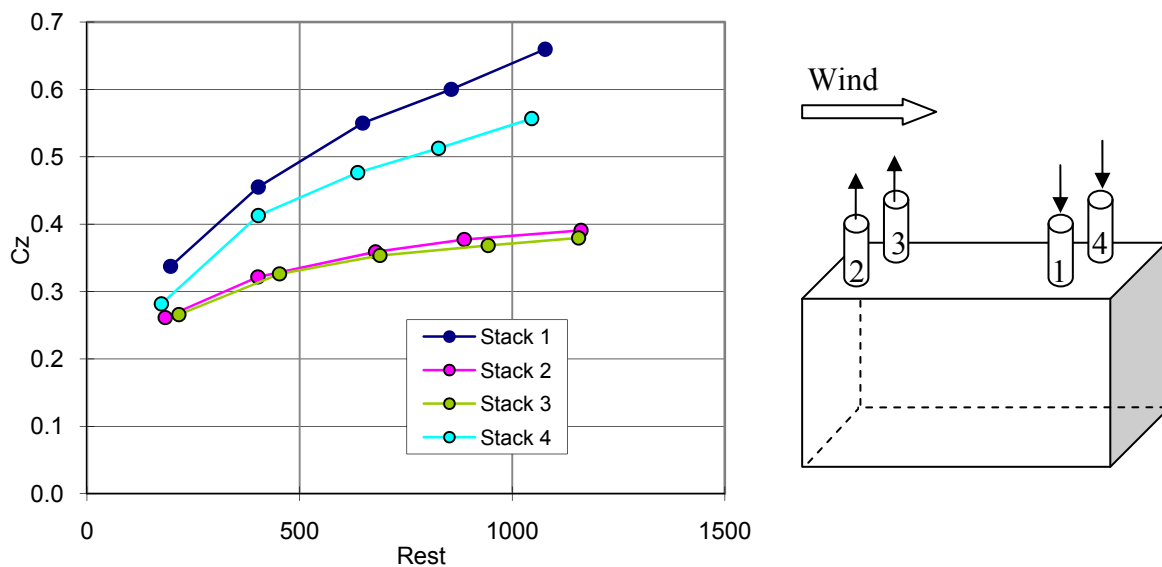


Figure 4.19 Variation of C_z with Re_{st} wind on case obtained from (S1234)

In Figure 4.20, all the stacks have outward flow, with reversal percentages less than 50%. There is some scatter, probably reflecting the fact that r is not zero in some cases (e.g. less than 10%).

4 Important parameters – C_z and C_p

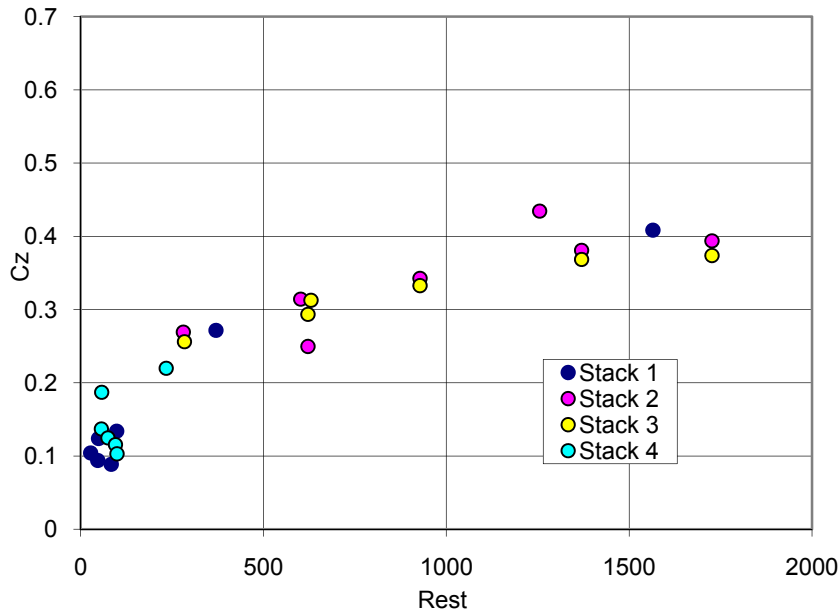


Figure 4.20 Variation of C_z with Re_{st} wind on case obtained from (S1234_O12)

Figure 4.21 compares the results in Figure 4.19 with still-air results (Figure 4.18). The underlying reasons for the behaviour in Figure 4.19 can be seen i.e. the good agreement between the unsteady and steady results for outward flow, and the differences that occur when the flow is inward. The significant differences between the C_z values of stacks 1 and 4 are not due to differences in the stack Reynolds numbers. They are probably caused by asymmetry of the external flow field, but slight differences in the stack box shapes and in the positions of pressure tappings may be contributory factors.

4 Important parameters – C_z and C_p

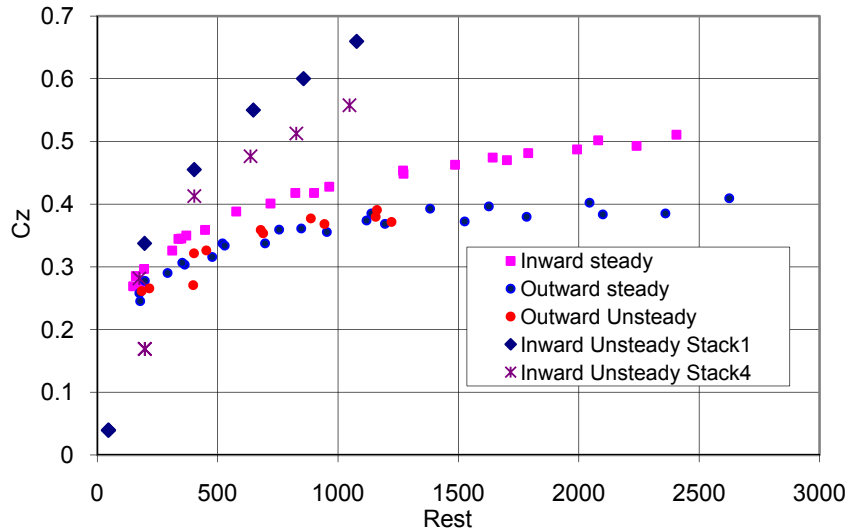


Figure 4.21 Variation of C_z with Re_{st} compared with still-air results

Figure 4.22 and Figure 4.23 show C_z against Re_{st} compared with steady data and some unsteady data from other references. One can see that for outward flow, C_z values are always consistent with steady cases; however, for inward flow, C_z values can go as high as 2.5, which makes it difficult to provide a fixed value for designing purposes.

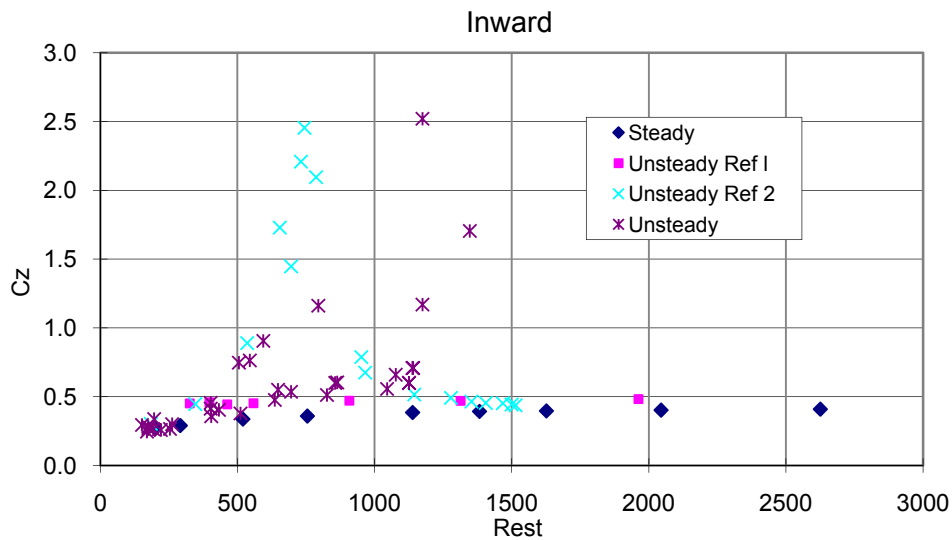


Figure 4.22 Variation of C_z with Re_{st} compared with still-air results of inward flow; Ref 1 (Costola and Etheridge, 2007), Ref 2 (Cooper and Etheridge, 2007)

4 Important parameters – C_z and C_p

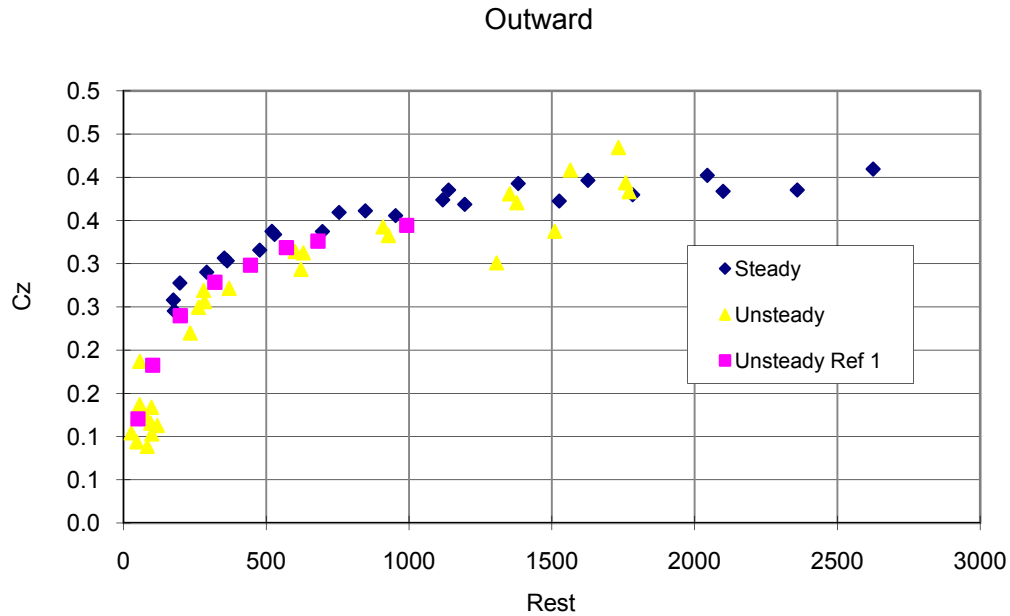


Figure 4.23 Variation of C_z with Re_{st} compared with still-air results of outward flow

There are two possible reasons for the occurrence of the C_z peak values. One is due to the reattaching of the separation flow, i.e. the reattaching distance from the upper edge of the stack box increases with the wind speed. The peak values occur when the reattaching distance is just about at the stack outlet. The other reason could be due to the position of the stack pressure tapping, and this is investigated in Chapter 7, Section 7.4.3.

4.6 Summary and conclusions

In this chapter, the up to date literature about pressure coefficient and discharge coefficient is reviewed and discussed. Testing results are presented respectively. The former focuses on the influence of opening configuration on C_p and the correlations among them. The latter focuses on C_z of long openings, especially the effects of external flow. Main conclusions are as follows.

4.6.1 C_p – conclusions

The main result relates to the effect of opening configuration on the external wind pressure coefficients. Some of the mean stack pressures showed a dependence on opening configuration, even though orifice pressures showed no dependence. Similar results were found for the correlations between stack pressures. This is important for envelope flow models. It implies that wind pressures should be measured with opening present to reduce errors.

4.6.2 C_z – conclusions

The present results for the C_z of stacks confirm the observations of Chiu and Etheridge (2007). C_z of stacks is a function of opening Reynolds number (C_z depends on flow through the openings). The external flow affects the C_z value with inward flow, but not with outward flow: with inward flow the C_z values increase by 10% compared to the still air values, except at a lower Reynolds number range where much higher peak values occur. This is probably not a Re effect, but an external flow effect associated with downward momentum.

5 Experiments – wind and buoyancy combined

In Chapter 3, the experiments of wind alone cases were described. Yet in reality, there are usually wind and buoyancy driving forces working together in buildings (Awbi, 1991, pp. p.87-89), providing a pressure difference across the openings of a building, especially for ventilation stacks, which are usually designed to utilise buoyancy forces, such as chimneys of dwelling houses and atriums of non-domestic buildings (Liddament, 1996, pp. 77-80). It is important to study the buoyancy effects with the model, especially focusing on when and how flow reversal occurs.

There are several works described in the literature, both theoretical and experimental as discussed in Section 5.1. To get some insights of buoyancy effects on stack ventilation, a heater was fixed onto the bottom of the model used in Chapter 3; specific descriptions of the experimental methodologies will be provided in Section 5.2. Since air was used as the testing medium, similarity analysis will be provided in Section 5.3. Section 5.4 and 5.5 present the testing results and conclusions.

5.1 Literature review

When buoyancy exists, in theory the flow condition within a single zone space can be classified into two categories, which are 1) buoyancy alone; 2) buoyancy and wind combined. When buoyancy is acting alone, or wind is assisting buoyancy source; it is relatively simple. This thesis will focus on wind opposing buoyancy cases. When wind is opposing buoyancy, different ventilation modes could occur; transitions between different ventilation modes could exhibit hysteresis; multiple solutions of three steady-state buoyancy opposing wind conditions exist theoretically, but only two of them can occur practically.

5.1.1 Buoyancy and wind opposing ventilation modes

There are two types of buoyancy source: localised heat source and area heat source (e.g. a heated floor). Linden et al (Hunt and Linden, 1999; Hunt and Linden, 2001; Hunt and Linden, 2004) studied the localised heat source buoyancy ventilation. A Series of buoyancy ventilation cases were studied by Woods et al (Gladstone and Woods, 2001; Lishman and Woods, 2006); but their laboratory work was using a heated floor which was an area heat source. Multiple local heat sources and different heights of heat source were also studied (Chenvidyakarn and Woods, 2010; Fitzgerald and Woods, 2004; Livermore and Woods, 2007).

For cases of area heat source, the room temperature will achieve uniformity as a steady state. Thermal stratification occurs with localised heat source when air enters in a lower opening and exits from an upper opening. This is defined as displacement ventilation or buoyancy domain ventilation. When the opposing wind is strong enough that pressure difference due to wind across openings are greater than that due to buoyancy, mixing ventilation will occur, which is also called wind domain ventilation (Hunt and Linden, 2004) (see Figure 5.1).

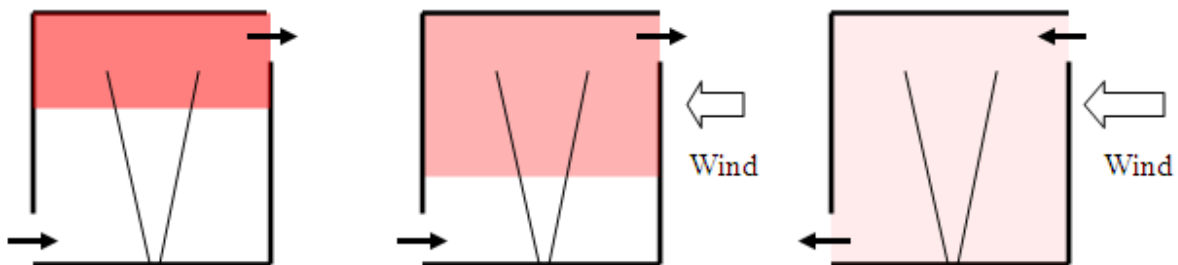


Figure 5.1 Localised heat source ventilation: (1) displacement ventilation driven by a localised heat source alone; (2) displacement ventilation driven by buoyancy and opposing wind; (3) mixed ventilation driven by buoyancy and strong opposing wind.

A theoretical model was developed to estimate the steady-state interface heights, stratification profiles and ventilation flow rates for this kind of heat source. It was found that the interface height is independent of the strength of the buoyancy flux from the source, but decided by the effective opening area. An increase in the heat flux will increase the upper layer temperature

5 Experiments – wind and buoyancy combined

but not change the height of the layer. With a fixed heat flux, the weak opposing wind will increase the thickness of the upper layer, yet decrease its temperature. Information of details of heat and mass transfer between stratification layers can be found in the literature (Turner, 1973). CFD modelling was studied by Ji et al. (2007), in which a localised heat source was used; thermal stratifications were predicted. The effects of size and location of ventilation openings, distribution of heating sources and wind strength on flow rates and temperature distribution were studied.

5.1.2 Multiple solutions of steady ventilation modes

5.1.2.1 Explanations of multiple solutions

Multiple solutions of steady states when buoyancy opposes wind were studied by several researchers (Lishman and Woods, 2006; Li and Delsante, 2010; Li et al., 2001; Hunt and Linden, 2004; Yuan and Glicksman, 2008). It should be noted that, multiple solution occur for both localised heat source and heated floor. The multiple solution of the nonlinear curve can be drawn in two forms (see Figure 5.2): (1) is in terms of dimensionless heat input against dimensionless temperature, (2) is in terms of gradient of dimensionless temperature with time against dimensionless temperature. The difference is the zero point of y axis. The solid line represents wind domain (mixing ventilation) state, the dashed line represents buoyancy domain (displacement ventilation) state. In theory, there are three steady state multiple solutions, which are corresponding to points a, b, and c in graphs (1) and (2), however, point b which is located on solid the line between point A and B is impossible to exist in practice. The explanation is: if there is a small perturbation of room temperature at b, the gradient of temperature will have the same sign as the perturbation, that is to say, if there is a small temperature increase, simultaneously a small decrease in flow rate (wind domain) will occur, resulting in a decrease in heat loss, which in return will enhance the temperature increase, and finally shift to steady state c. It is the same theory, but the opposite way, when there is a small temperature decrease, which will make it shift to steady state a. Therefore, there are only two steady states existing in practice, which are a and c. It should be noted that, the theoretical analysis for multiple solutions was based on the assumption that the room temperature is uniform, which will occur with a heated floor. However, laboratory work shows that multiple solutions also exist for localised heat source when stratifications happen.

5 Experiments – wind and buoyancy combined

Nevertheless, Etheridge (2009) claimed that the behaviour described is not of practical relevance, because steady states do not occur in practice due to continuously varying temperatures. Furthermore the above analysis ignores ventilation heat loss arising from wind turbulence.

5.1.2.2 Conditions for the existence of multiple solutions

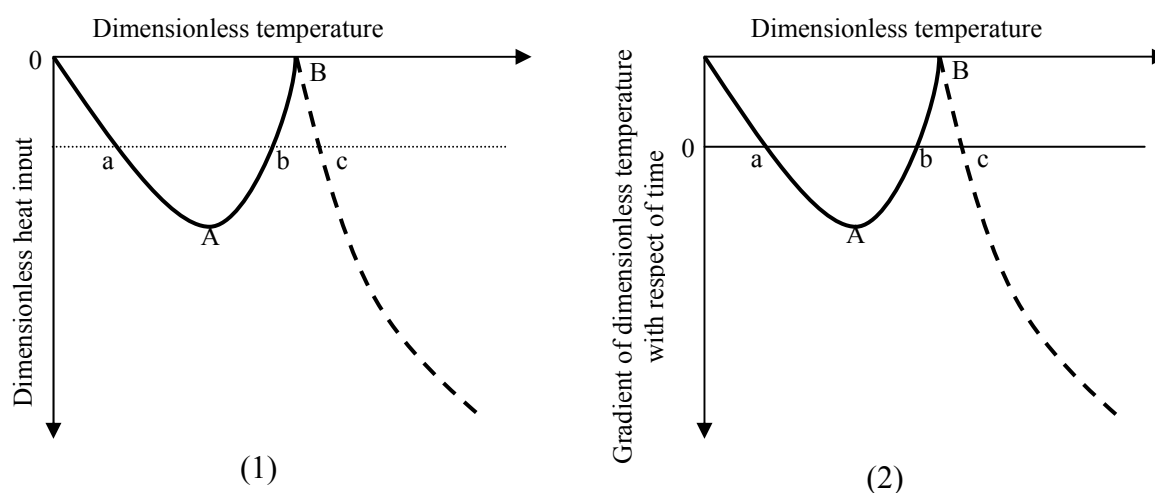


Figure 5.2 Multiple solutions of steady states when buoyancy opposes wind (solid line: wind dominated ventilation; dashed line: buoyancy dominated ventilation)

The curves shown in Figure 5.2 represent ideal cases, e.g. the building envelope is adiabatic (Yuan and Glicksman, 2008); there is no fluctuation of the wind (Etheridge, 2009); and the opening sizes are small enough not to be affected by the mean wind speed changes (Hunt and Linden, 2001). If the building envelope is not adiabatic, the curves in (2) Figure 5.2 will shift in the y axis direction, multiple solutions exist when $y(A) > 0$ and $y(B) < 0$. In terms of mean wind speed changes, Lishman & Woods (2006) stated that if there is a second downwind opening and it exceeds a critical area, then the multiple steady states are eliminated. This is simply because when the window is sufficiently large, the change of wind speed will cause a smooth shift from wind dominated to buoyancy dominated flow state, sizes of opening for this phenomena were quantitatively studied. The strength of turbulent wind fluctuations required to eliminate multiple solutions was quantitatively studied by Etheridge (2009). It

5 Experiments – wind and buoyancy combined

was stated that the coefficient of the difference between the time-mean external pressures at the openings, divided by its standard deviation, should not exceed a certain value. That is to say, the fluctuation factor of the wind should be great enough so that it could eliminate the multiple solutions.

Assume that all the conditions are satisfied the multiple solutions, how realistic is it in practice? Yuan and Glicksman (2008) provided an example of a hypothetical full scale single zone building. It was given that with a typical wind speed of 3 m/s, a typical environment temperature of 280-300 K, and a typical room height of 3 m, the inside air temperature must exceed the outside temperature by at least 30 degree. Otherwise, if the room height is increased to 10 m to enhance the buoyancy effect, the room temperature should be at least 9 K above the ambient. That is to say, for a typical building, buoyancy domain solution is hard to occur unless the wind speed is very low, or the room height is intentionally increased to enhance buoyancy effect, like an atrium. In other words, for a typical building, only one solution in Figure 5.2 (point a) exists in practice. That is why ventilation stacks are used in natural ventilation design to better utilise the buoyancy force to enhance the ventilation rates. Stack involved buoyancy ventilation was studied by Woods et al (Chenvidyakarn and Woods, 2005; Livermore and Woods, 2006); multiple steady states were discovered for a model with two stacks of different height and a low level opening; when there is buoyancy alone, flow direction through the stacks are different between those steady states. When there are multiple stacks, similar phenomena (different flow directions through stacks occur when there is buoyancy alone) was found in the experiments carried out in this thesis, which will be described in Section 5.4.

5.1.3 Transitions between multiple steady states

Hunt and Linden (2004) also investigated in the transitions between two ventilation flow patterns: buoyancy domain/displacement ventilation and wind domain /mixing ventilation. A localised heat source was used in this study theoretically and experimentally. Both buoyancy and wind forces were adjusted to generate different steady states. A dimensionless parameter F was defined, which is the relative magnitudes of the wind-driven velocity component and

5 Experiments – wind and buoyancy combined

the buoyancy-driven velocity component within the enclosure. It was found that transitions between the two flow patterns exhibit hysteresis. The tests carried out in this thesis also exhibit hysteresis, which will be discussed in Section 5.4. In terms of transition requirement, it was discovered that mixing to displacement ventilation occurs at a fixed value of F , whereas the opposite transition from displacement to mixing ventilation is not solely depend on the value of F but also on some other details such as time history of the flow and the geometry of the openings.

Similar results were discovered by Lishman and Woods (2009). The differences are: area heat source was used; only wind driving force was changed to generate different steady states. Again, it was stated that the transition from the wind dominated to buoyancy dominated mode occurs as the wind force decreases below a critical value, which is corresponding the fixed value of F in Linden's study. Similarly the opposite transition from buoyancy dominated to wind dominated mode occurs if there is a sufficiently large and rapid increase in the wind force.

Yuan and Glicksman (2007) theoretically investigated the transition between the two steady modes, in terms of perturbation of both heat source and wind source. It was found that a minimum perturbation magnitude and minimum perturbation time should be satisfied to make the transition happen. It was also suggested that special attention should be paid to wind perturbation which is more likely to occur in practice.

The transition studies in literature were all based on a typical building with two sharp openings. In this thesis, transition on a model with long opening will be studied, in which the process of transition can be 'slowed down'. This will be discussed in Section 5.4.

5.2 Experiment descriptions

5.2.1 Temperature measurements

The same model used in Chapter 3 was used for buoyancy and wind combined tests. A heater was fixed in the centre of the bottom (see Figure 5.3), the dimension of the heater is 12 cm wide, 12 cm long and 2.5 cm high. With a manually controlled power supply of 110~250 V, the heater generates a heating range of 60~200 W. There is a temperature probe (Dantec 55P33) fitted below the hot-wire in one of the four stacks (stack 3), to measure the ambient temperature of the hot-wire for instantaneous temperature corrections. To measure the box temperature, there are two thermocouples fixed within the space. One is 0.8 of the box height, the other is 0.25 of the box height, and both of them are half way distance to the centre in opposite corners. There is third thermocouple located under the turntable of the wind tunnel to measure the ambient environment temperature. The data acquisition of the temperature probe in the stack is the same system with the hot-wires, thereby the velocity and correction temperature measurements are synchronized. The data acquisitions of the three thermocouples are using a data logging system. The temperature measurements of the thermocouples were recorded simultaneously with the hot-wires, the error of the synchronization is up to one second. The temperatures measured by the three thermocouples and temperature probe are called T_1 , T_2 , T_{room} and T_{wire} . It should be noted that no correction is required for detecting flow reversal, correction is only required for calculating the magnitude of the flow rate. Temperature correction methods are given in Section 5.3.1.3.

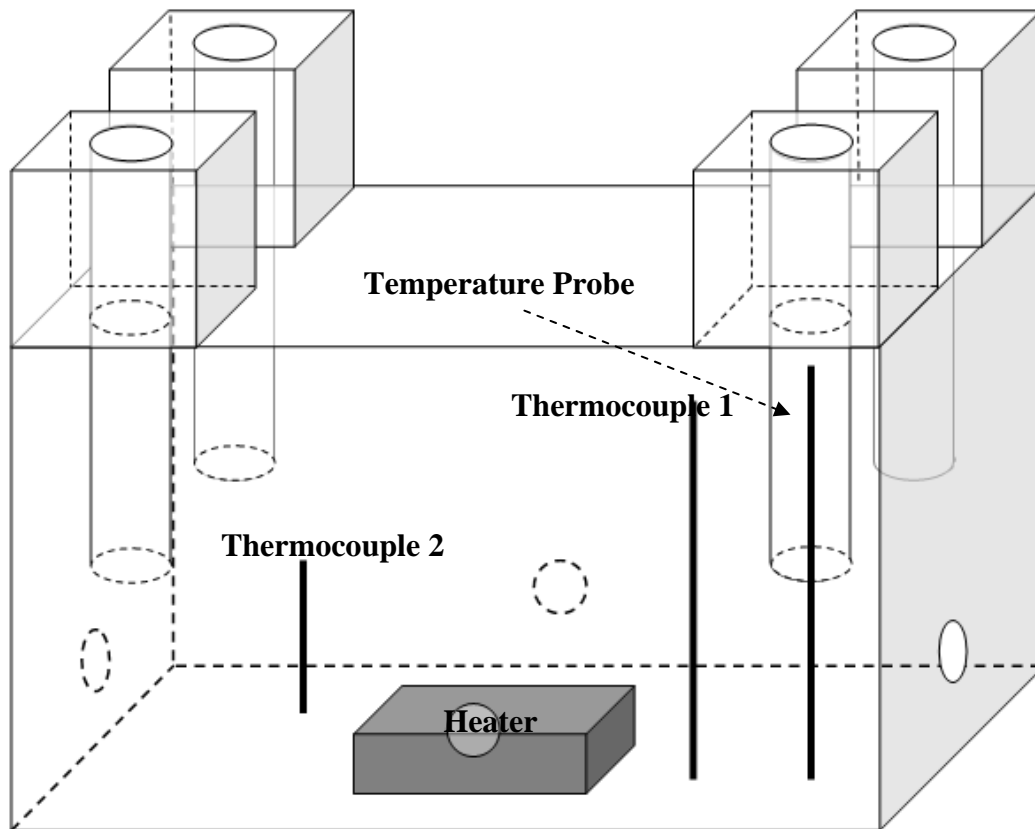


Figure 5.3 Model with heater and temperature measurements

5.2.2 Similarity analysis

There are certain dimensionless parameters regarding similarity requirements, namely Reynolds number and Archimedes number (Carey and Etheridge, 1999). The two relevant Reynolds numbers, namely building Reynolds number and opening Reynolds number, are defined by equation (3.6) and equation (4.2)

$$Re_b = \frac{\rho_{E0} U_{ref} H}{\mu} \quad (5.1)$$

$$Re_o = \frac{\rho_{E0} u d}{\mu} \quad (5.2)$$

The Archimedes number is defined by

5 Experiments – wind and buoyancy combined

$$Ar = \frac{\Delta\rho gh}{\rho_{E0} U_{ref}^2} = \frac{\Delta T gh}{T_{E0} U_{ref}^2} \quad (5.3)$$

where ρ_{E0} is the external air density at 0 height. $\Delta\rho$ is the density difference at a specified opening height, and ΔT is the temperature difference at the specified opening height.

A dependence of envelope flows on Re_b can be considered in two parts i.e. dependence of external pressure coefficient, C_p on wind tunnel speed (Re_b) and dependence of the discharge coefficient on flow rate (Re_o). For a long opening, C_z is dependent on Re_o especially at low flow rate. From the results in Chapter 3, we know that C_p is independent of the wind speed when U_{ref} is greater than 3 m/s at model scale. Assume that one knows the dependency equation for C_z and Re_o for full scale. Also, C_p values at low wind speed for full scale buildings could be provided, or the dependency on wind speed is small enough to be ignored. There left only one important requirement for buoyancy and wind combined ventilation especially during the transition processes. To give the required ratio between buoyancy and wind forces, a prototype Archimedes number has to be achieved. In other words, to apply model scale results to full-scale, it is necessary to achieve full-scale values of Ar .

The advantage of using the salt-bath technique is that there is no problem achieving high Reynolds numbers and also satisfying the prototype Archimedes number. But the problem is with boundary conditions. The main advantage of the direct wind tunnel technique is that the atmospheric boundary layer can be more accurately modelled in an environmental wind tunnel than in a water channel (Carey and Etheridge, 1999). By using air, one has to use a high temperature difference and/or a low wind speed to achieve full-scale Ar . An example of applying model scale results to full-scale is given as follows. Assume there is a geometric scaled building 50 times of the height of the box; the temperature difference between the inside and outside of the building is 5 °C; full scale wind speed is 3m/s. At model scale with a temperature of 30 °C, $\frac{5K \times g \times 50}{300K \times (3m/s)^2} = \frac{30K \times g \times 1}{300K \times U^2}$, the wind speed U_{ref} has to be as low as about 1 m/s to satisfy the prototype Archimedes number.

5.2.3 Experiment scope and procedure

The aims of the experiments are: 1) to investigate the transitional processes between wind dominated and buoyancy dominated states, and to study the hysteresis effects; 2) to investigate the effects of turbulent wind pressure fluctuations on stack flow rates; 3) to investigate the initial condition effects on the final flow pattern through multiple stacks.

5.2.3.1 Experiment scope

As stated in Section 5.2.2 for similarity, the temperature difference between the box and ambient room temperature should be as large as possible. Although the working environment of the hot-wire can be as high as 150 °C, the precise range of the temperature probe is below 60 °C, and temperature is also limited by the power of the heater. The tests carried out in this chapter are all below 65 °C. There are four sets of tests of multiple stacks, and one set of tests with one stack and one sharp edged orifice. In the first two tests, the wind speed was set constant, and the heater was adjusted up and down to produce the transitions from wind dominated ventilation to buoyancy dominated ventilation, and then back to wind dominated ventilation again. In the third and fourth tests, the two measured temperatures from the thermocouples (the temperature within the model was stratified) were set constant, and the wind speed was adjusted to produce the transitions the other way round. Similar tests of transitions from wind dominated ventilation to buoyancy dominated ventilation were done on the opening configuration of one stack and one orifice. What is more, stacks alone tests were carried out to investigate the initial condition effects. Details of experimental scope are shown in Table 5.1.

5 Experiments – wind and buoyancy combined

Table 5.1 Experimental scope of wind and buoyancy combined tests

1. Fixed Wind Speed			
U_{ref} (m/s)	T_2 range (°C)	Openings	Identifier
1.2	15 ~ 57	Stack 1 and 3, Orifice 1 2 3 4	S13_O1234_U1.2
1.4	16 ~ 60	Stack 1 and 3, Orifice 1 2 3 4	S13_O1234_U1.4
2. Fixed temperature in the box			
T_1, T_2 (°C)	U_{ref} range (m/s)	Openings	Identifier
60, 40	1.2 ~ 1.7	Stack 1 and 3, Orifice 1 2 3 4	S13_O1234_T57
57, 42	1.2 ~ 2.1	Stack 1 and 3, Orifice 1 2 3 4	S13_O1234_T60
3. One stack and one orifice, fixed wind speed			
U_{ref} (m/s)	T_2 range (°C)	Openings	Identifier
0.6	16 ~ 60	Stack 3, Orifice 1	S3_O1_U0.6
4. Initial condition effect tests			
T_2 (°C)	U_{ref} (m/s)	Openings	Identifier
60	1.7	Stack 1 and 3	S13_T60
60	4	Stack 1 2 3 4	S1234_T60
60	4	Stack 1 2 3 4, Orifice 1	S1234_T60

5.2.3.2 Experiment procedures

For the first two sets of tests, procedures are:

- 1) Set up the model with the required opening configurations.
- 2) Start the data logger recording for three thermocouples, synchronize the time record with the laptop.
- 3) Do a zero run for the hot-wires and the temperature probe.
- 4) Turn on the fan of the wind tunnel; adjust the wind speed to the required value referring to a digital pressure meter measuring the dynamic pressure of the wind.
- 5) Turn the heater on, with a power supply of 250 V.
- 6) Do a run with each increase of about 5 °C of T_1, T_2 , till the transition of the flow mode (flow directions in certain stacks totally changed)
- 7) Switch off the heater, do a run in a step of a corresponding temperature decrease, till the flow directions changed back to their original ones. It should be noted that the

5 Experiments – wind and buoyancy combined

heater is still heating up the air after being switched off, in other words buoyancy force still exists.

For the next two sets of tests, steps 1) 2) 3) are the same.

- 1) Turn on the heater to the maximum power (250 V), when T_2 is about 5 °C lower than the targeted value shown in Figure 5.3, slowly adjust it to a lower power supply (110 V ~ 150 V) to obtain a relatively steady buoyancy driven state of the box.
- 2) Turn on the fan of the wind tunnel, slowly increase the wind speed to 1.2 m/s, adjust the heater to make T_1 and T_2 stay at the targeted values, do a run.
- 3) Increase the fan speed by a step of 0.5 ~ 1 m/s, repeat adjusting the heater in each run; the maximum was decided when the transition of flow mode (flow directions in certain stacks totally changed) was finished.
- 4) Decrease the fan speed by similar steps, and repeat the runs till the flow directions turn back to their original ones.

For the initial condition effect tests, repeat steps 1) 2) and 3)

- 4) Turn on the heater to the maximum power, slowly adjust the power supply when T_2 comes near to the targeted value, to produce a steady buoyancy dominated ventilation state.
- 5) Turn on the fan, increase the wind speed to the targeted value (this value was decided when flow direction totally changed in certain stacks), wait 5 minutes till the system reaches another steady state, do a run.
- 6) Turn off the fan, wait about 10 minutes, do another run.

5.3 Results and analysis

5.3.1 Transitions between displacement ventilation and mixing ventilation

5.3.1.1 Fixed temperature, changing wind speed

The first two set of tests were the transition processes from mixing ventilation (wind dominated) to displacement ventilation (buoyancy dominated). Two stacks (1 and 3) and four orifices were used. The changing of flow directions are shown in Figure 5.4. Starting with only a fixed wind force, the flow direction in stack 3 is downward, i.e. the reversal percentage r of stack 3 is 100%. By gradually heating up the air within the box, the flow through stack 3 starts to fluctuate; r starts to decrease from 100% till 0% (flow direction sign from + to -), when the buoyancy force is great enough to make the flow direction of stack 3 totally change to upward. After the heater was turned off, the flow direction of stack 3 gradually turned back to downward again to its original status (flow direction sign changes from - to +).

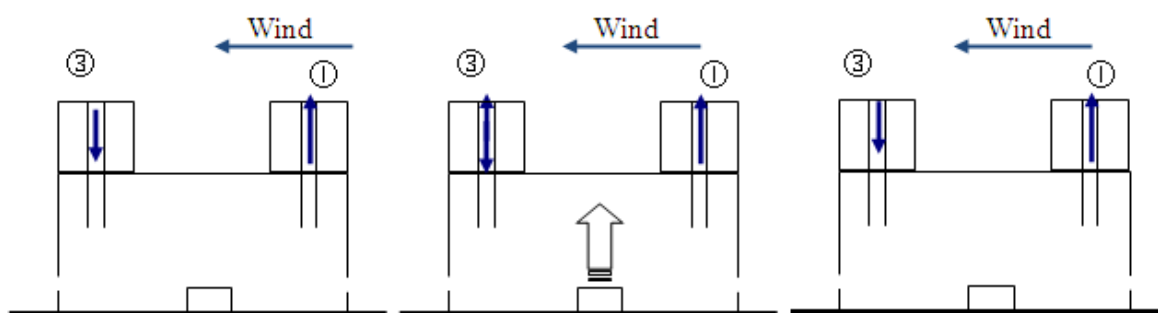


Figure 5.4 Transition from wind dominated to buoyancy dominated, and then back to wind dominated ventilation for two-stack case (stacks 1 and 3)

The quantitative results are shown in Figure 5.5 and Figure 5.6, in the form of time plots of temperature measurements and reversal percentage of stack 3. The fixed wind speeds in the two figures are $U_{ref} = 1.2 \text{ m/s}$ and $U_{ref} = 1.4 \text{ m/s}$ respectively. The environment temperature in the wind tunnel T_{room} was constant. There are several phenomena shown in these two figures. In the following, process one refers to the change from wind dominated to buoyancy dominated, and process two to the return to wind dominated.

5 Experiments – wind and buoyancy combined

- During the process of increasing box temperature, the temperature difference between T_1 and T_2 is greater than when the temperature is decreasing.
- T_{wire} (ambient temperature of the hot-wires in stack 3) is more close to T_1 (lower layer box temperature) in the first half process (process one), and more close to T_2 in the second half process (process two).
- The flow through stack 3 fluctuates more during the first process.

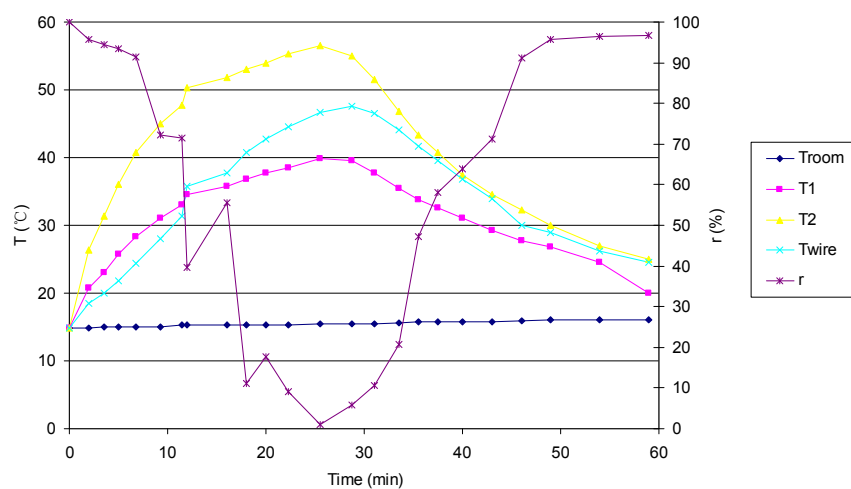


Figure 5.5 Variation of temperature and reversal percentage of stack 3 for $U_{ref}=1.2$ m/s (S13_O1234_U1.2)

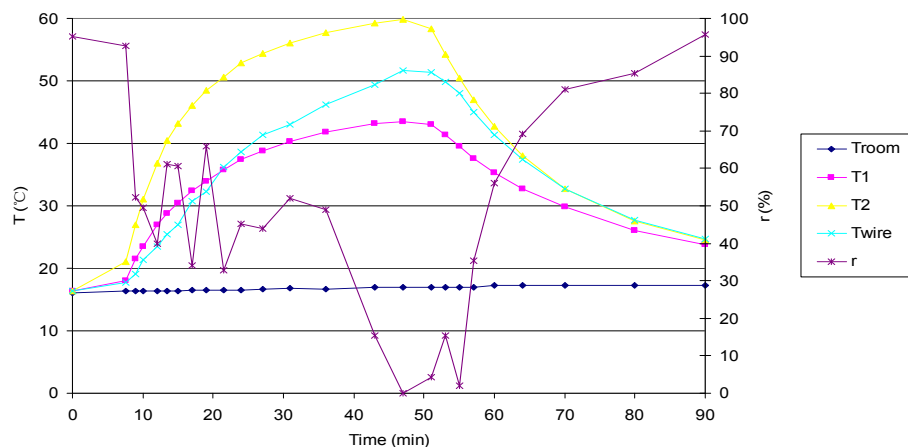


Figure 5.6 Variation of temperature and reversal percentage of stack 3 for $U_{ref}=1.4$ m/s (S13_O1234_U1.4)

5 Experiments – wind and buoyancy combined

For both fixed wind speeds, there is obvious stratification within the box during process one. It also can be seen that the reversal percentage fluctuates more during process one. This might be because the heat convection of the internal layers causes more uncertainties of the flow through the openings. It is hard to tell if there is a hysteresis effect (see Figure 5.7, in which dT is the temperature difference between the averaged box temperature $\frac{T_1+T_2}{2}$ and T_{room}) between the two processes, again because there are more uncertainties during process one.

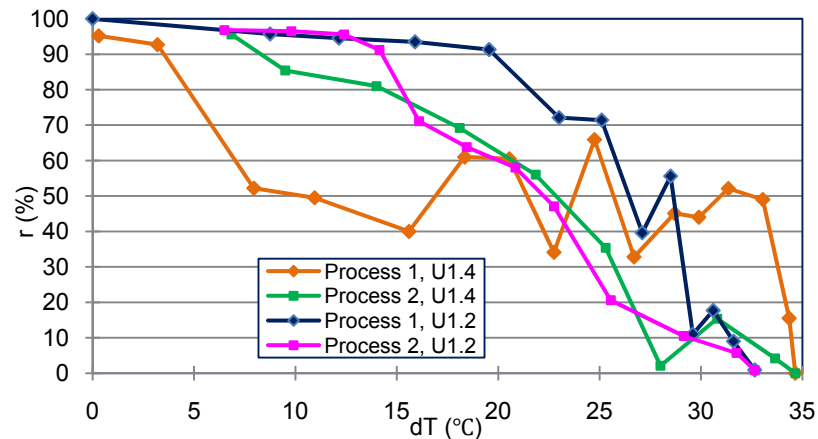


Figure 5.7 Reversal percentage against difference between the averaged box temperature and T_{room}

5.3.1.2 Fixed wind speed, changing temperature

The changing of flow directions are shown in Figure 5.8. Starting with only a fixed buoyancy force, the flow direction in stack 3 is upward, i.e. the reversal percentage r of stack 3 is 0 %. By gradually increasing the wind speed of the wind tunnel, the flow through stack 3 starts to fluctuate; r starts to increase from 0 % till 100 % (flow direction sign from - to +), when the wind force is great enough to make the flow direction of stack 3 totally change to downward. After the fan was switched off, the flow direction of stack 3 gradually turned back to upward again to its original status (flow direction sign from + to -).

5 Experiments – wind and buoyancy combined

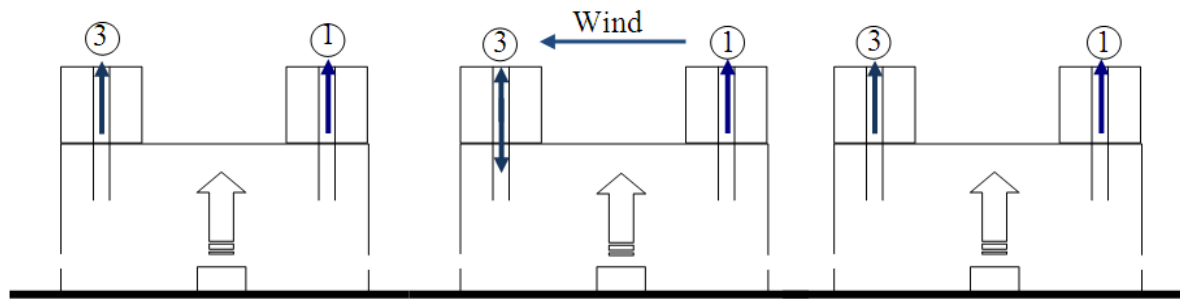


Figure 5.8 Transitions from displacement ventilation to mixing ventilation, and then back to displacement ventilation

The quantitative results are shown in Figure 5.9 and Figure 5.10. The main y axis shows the temperatures and reversal percentage, the secondary y axis is the wind speed. Since the wind speed was increased manually, the results are not presented in the form of time slots. The x axis is just a number of records; the time interval is about three minutes. Figure 5.9 shows the results of fixed upper layer model box temperature measured by thermocouple 1: $T_1 = 57^\circ\text{C}$; Figure 5.10 shows the results of $T_1 = 60^\circ\text{C}$. One can see that with a higher T_1 by 3°C , the wind speed has to reach 2.1 m/s to cause 100% flow reversal in stack 3, whereas it is 1.7 m/s in Figure 5.9.

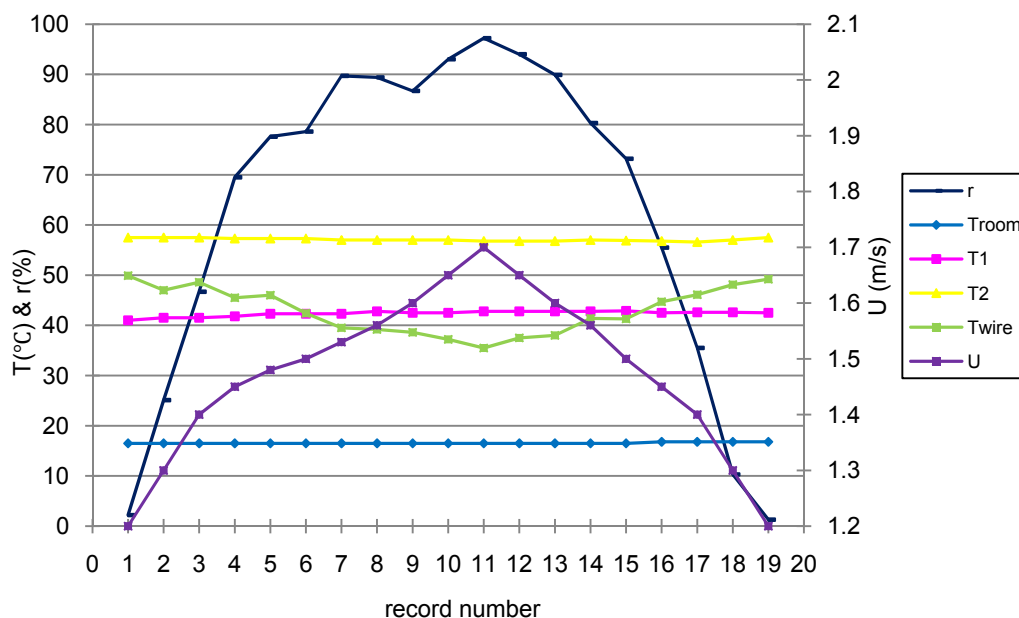


Figure 5.9 Variation of temperature and reversal percentage of stack 3 for $T_1 = 57^\circ\text{C}$ (S13_O1234_T57)

5 Experiments – wind and buoyancy combined

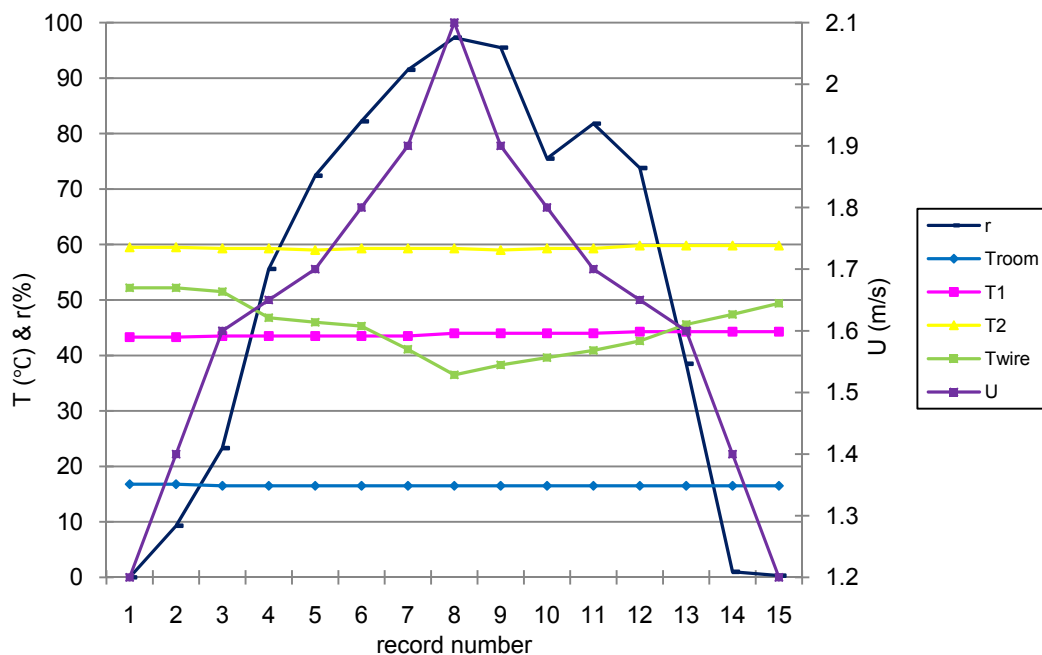


Figure 5.10 Variation of temperature and reversal percentage of stack 3 for $T_1 = 60\text{ °C}$ (S13_O1234_T60)

Figure 5.11 shows the results of reversal percentage changes with increasing and decreasing wind speed for the above two cases of $T_1 = 57\text{ °C}$ and $T_1 = 60\text{ °C}$ ('- to+' means the change of flow sign in stack 3). Again, no obvious hysteresis effects could be observed between the two processes. Lishman and Woods (2009) stated that, for the typical one zone building with two openings, transition from the wind dominated state to buoyancy dominated state occurs as the wind force decreases below a critical value. However they stated that the reverse transition (from buoyancy dominated to wind dominated state) occurs only if there is a sufficiently large and rapid increase in the wind force. In this thesis, the two transition processes happen with a gradually changing wind speed. The possible explanation could be that the long stack slows down the transitional process, thereby mitigating the need of the sudden jumping of the wind force to transit from buoyancy dominated state to wind dominated state.

5 Experiments – wind and buoyancy combined

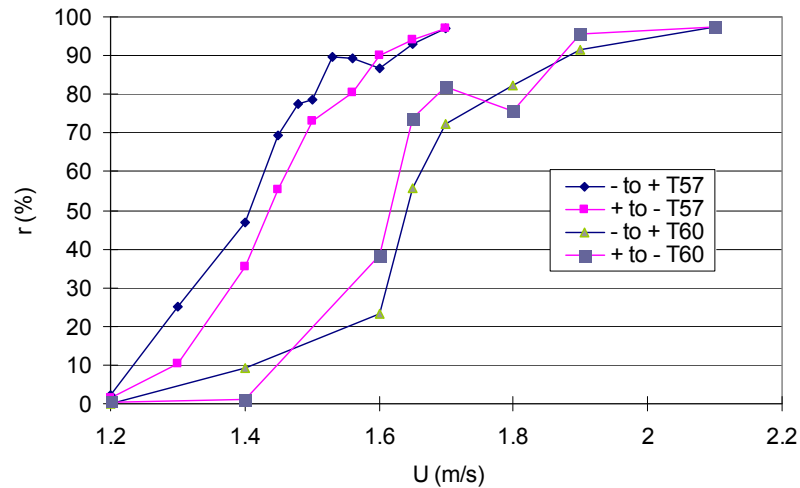


Figure 5.11 Reversal percentage against wind speed

In addition, from Figure 5.5, Figure 5.6, Figure 5.9, and Figure 5.10, one can see that when buoyancy force was fixed, in the stacks through which flow direction change, the fluctuation through the stack is more severe when the wind force was increasing; the reversal percentage changes more smoothly when the wind force was receding. Yet this phenomenon was not observed when the wind force was fixed and buoyancy force was changing, in which case the reversal percentage changed relatively smoothly during both processes of increasing and decreasing buoyancy force.

5.3.1.3 Transition from wind dominated ventilation to buoyancy dominated ventilation for the opening configuration of one stack and one orifice

The aim of these tests was to provide confirmation of the effect of turbulence as described in Etheridge (2009). As shown in Figure 5.12, a wooden block was put on top of the model to generate an initial downward flow in stack 3, a wind dominated ventilation state, with $U_{ref} = 0.6 \text{ m/s}$. After the heater was turned on, the flow direction in stack 3 started to change from downward to totally upward. Temperatures and reversal percentage change with time can be found in Figure 5.13.

5 Experiments – wind and buoyancy combined

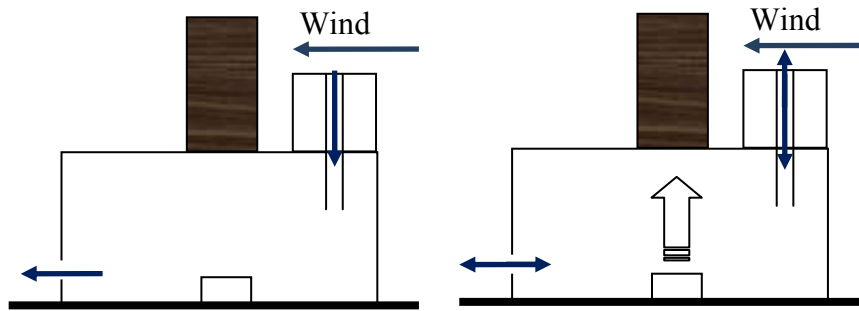


Figure 5.12 Transition from wind dominated ventilation to buoyancy dominated ventilation

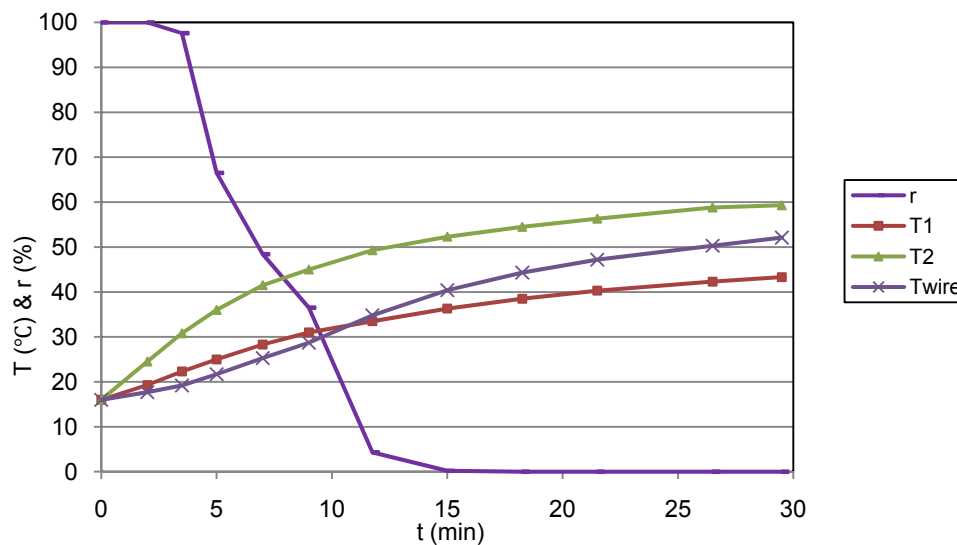


Figure 5.13 Temperatures and flow direction change with time

To give the correct velocity through the stack, temperature corrections are made to hot-wire calibration equations. The corrected voltage E_{corr} used to calculate velocities are obtained using equation (1.4) (Jorgensen, 2002, p. 29)

$$E_{corr} = \left(\frac{T_w - T_0}{T_w - T_a} \right)^{0.5} \times E_a \quad (5.4)$$

where E_a is the acquired voltage. T_w is the sensor hot temperature, which is 250 °C in for the tests in this thesis. T_0 is the ambient reference temperature related to the last overheat set-up before calibration, which is around 16 °C in the tests. T_a is the ambient temperature during acquisition, which is measured by the temperature probe in stack 3.

5 Experiments – wind and buoyancy combined

For the other stacks, T_2 is used when it is upward flow, T_{room} is used when it is downward flow, averaged T_1 and T_2 is used when it is fluctuating, based on the trend shown in Figure 5.5.

Figure 5.14 shows the reversal percentage, flow rate of stack 3 and total ventilation flow rate against temperature difference between the box and the room. Assuming that the flows through the two openings (stack 3 and orifice 1) are always equal and opposite, and also the air coming in each of the opening will mix entirely with the air inside the box, the fresh air ventilation rate is given the absolute value of either one of the two openings. Thereby the fresh air flow rate q_f used here is the mean absolute flow rate q of stack 3. However, in practice, the air coming in the opening will not entirely mix with the air inside the box, especially when it is fluctuating (when r is around 50 %) through the long opening (stack 3). Therefore the total ventilation rate with r around 50 % should be lower than that shown in the figure, but still not reaching zero. This is caused by the nature of the unsteadiness of the wind force. If one assumes that there is no fluctuation of the wind, the total ventilation rate would be zero when $r = 50 \%$, which could not happen in practice.

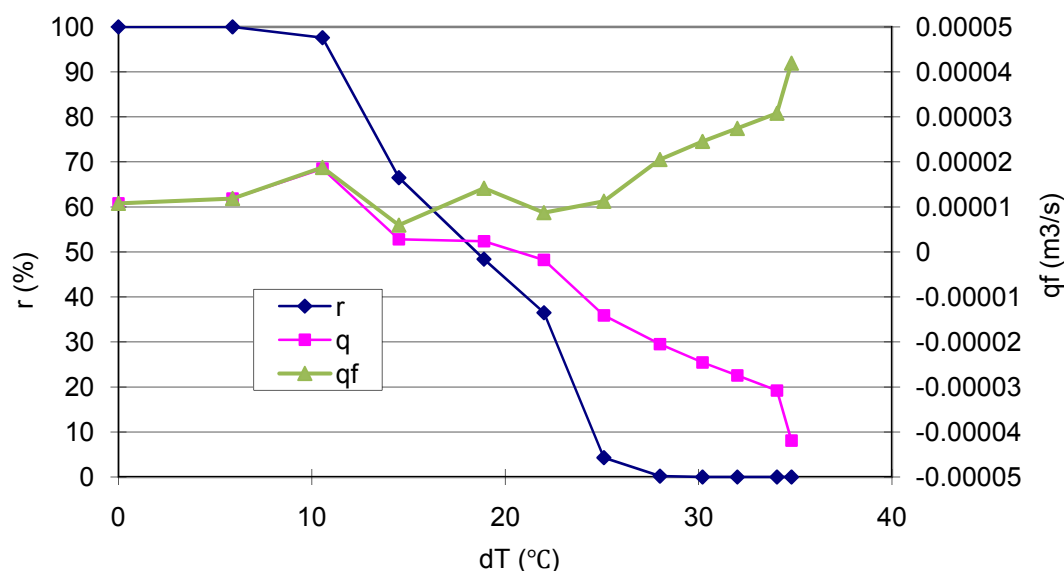


Figure 5.14 Reversal percentage, flow rate of stack 3 (q) and ventilation flow rate (fresh air) of the box (q_f) against temperature difference

5 Experiments – wind and buoyancy combined

Figure 5.15 illustrates the dimensionless total flow rate against relative dimensionless wind force and buoyancy force. The dashed line indicates what it should be were it for steady wind case. The dimensionless total flow rate is defined by

$$\frac{q_f}{AU_b} \quad (5.5)$$

where q_f is the total flow rate, A is the area of the opening. U_b is the equivalent wind speed of the buoyancy force, which is defined by

$$U_b \equiv \sqrt{\frac{\Delta\rho gh}{\rho_{E0}}} \quad (5.6)$$

The relative dimensionless wind force and buoyancy force is defined by

$$\frac{\Delta C_p}{Ar} \quad (5.7)$$

where ΔC_p is the difference between the wind pressure coefficients of the two openings, since there are only two openings here. When there are multiple openings, Figure 5.15 should be used to analyse the quantities of each opening, thus in that situation ΔC_p should be the difference between the opening pressure coefficient and internal pressure coefficient. Ar is the Archimedes number which is defined by equation (5.3).

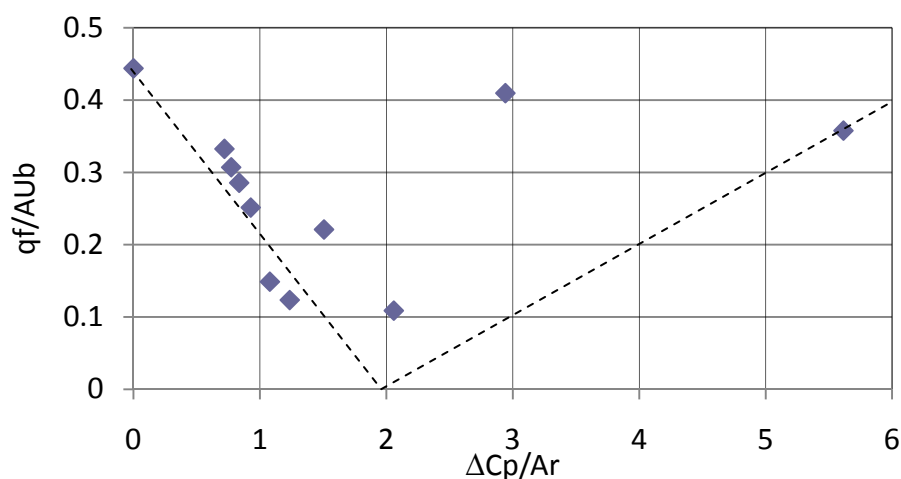


Figure 5.15 Dimensionless flow rate against relative wind force and buoyancy force

5 Experiments – wind and buoyancy combined

The dashed lines in Figure 5.15 correspond to the transition from wind dominated ventilation to buoyancy dominated ventilation. Etheridge (2009) stated that wind fluctuation should be severe enough to eliminate the occurrence of multiple solutions when the term $\frac{\Delta C_p}{\sigma_{\Delta C_p}} < 1.5$, where $\sigma_{\Delta C_p}$ is the standard deviation of ΔC_p . In this study, $U_{ref} = 0.6 \text{ m/s}$, when $\frac{\Delta C_p}{\sigma_{\Delta C_p}} = 1.79$, which is not satisfying the requirement. However one should still see an effect, i.e. $\frac{q_f}{AU_b} > 0$ for $\frac{\Delta C_p}{\sigma_{\Delta C_p}} = 2$ and this is apparent in Figure 5.15. Nevertheless, higher wind speeds are suggested to be tested to satisfy the requirement, in which case a greater buoyancy force is needed to produce the transition to buoyancy dominated force, which is out of the range of the tests in this thesis.

Figure 5.16 presents the results in the form of dimensionless ventilation rate $\frac{q_f}{A(U_{ref}+U_b)}$ against $1/Ar$, which is a way of providing non-dimensional data for design purposes (Carey and Etheridge, 1999). It should be noted that, the pressure data used for each point in the figures are taken from the wind alone case, when no buoyancy force component was present in the pressure measurements.

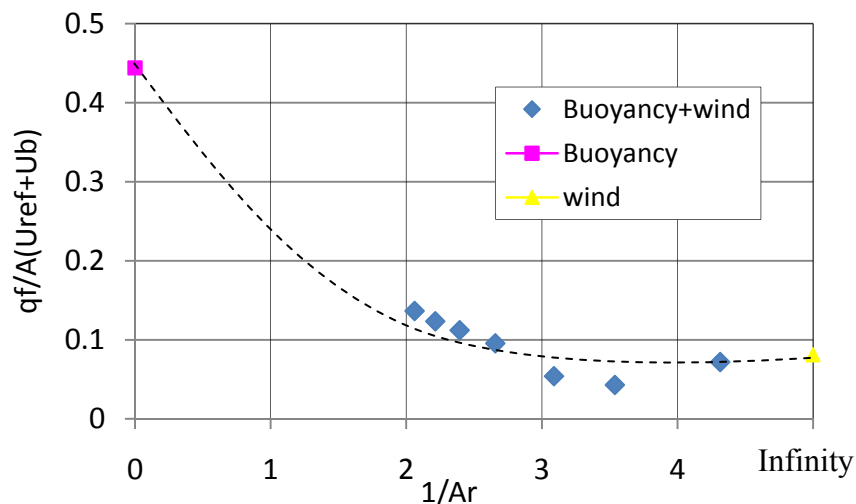


Figure 5.16 Dimensionless ventilation rate against $1/Ar$

5 Experiments – wind and buoyancy combined

Figure 5.17 provides an indication of the value of relative wind force and buoyancy force $\frac{\Delta C_p}{Ar}$ needed to cause flow reversal. The cases of the same opening configuration of two stacks and four orifices (2S_4O) have the same $\frac{\Delta C_p}{Ar}$ when flow reversal started to occur. The other two lines representing two cases with the same opening configuration of one stack and one orifice (1S_1O) but different separation distance of a block used to generate flow reversal in stack 3. The spread is due to the buoyancy force.

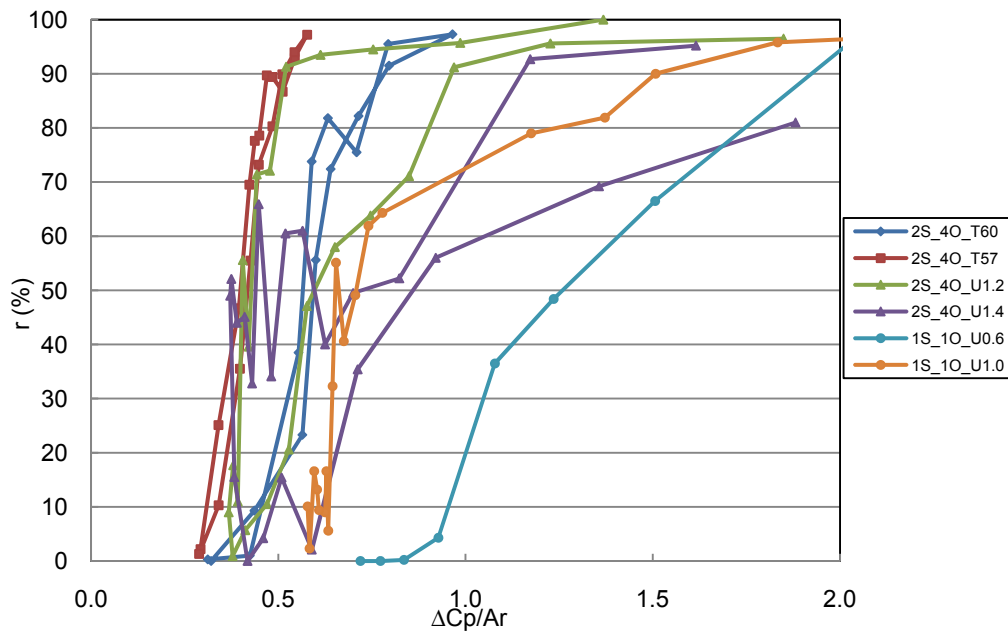


Figure 5.17 Reversal percentage against relative wind force and buoyancy force for all cases

5.3.2 Initial condition effects

The aim here was to investigate the effect of initial conditions on the subsequent steady conditions.

5.3.2.1 Flow directions

For buildings with multiple stacks, there are uncertainties in the flow pattern arising from the effects of initial conditions. The flow directions through stacks in the final steady state with the same buoyancy force are likely to depend on the initial conditions such as the gust wind. Figure 5.18 shows the flow direction changes of two-stack alone case (stack 1 and

5 Experiments – wind and buoyancy combined

stack 3). It started off with upward flow in stack 1 and downward flow in stack 3 when there was a constant temperature difference between the box and the room of 36 °C. A wind speed of $U_{ref} = 2.5 \text{ m/s}$ caused the flow directions of the two stacks to completely change to the opposites. Ten minutes after the wind was switched off, when the driving force turned back to the original buoyancy alone state, the flow directions followed the status when the wind was on. This is presumably due to the cooling effect of the downward flow in stack 1. In the initial state, upward flow was established in stack 1, due to some asymmetry in the heating. If the asymmetry had been such that the flow in stack 1 was downward, there would have been no effect of wind. i.e. the thermal mass of stack 1 is cooled and therefore the flow in stack 1 remains downward.

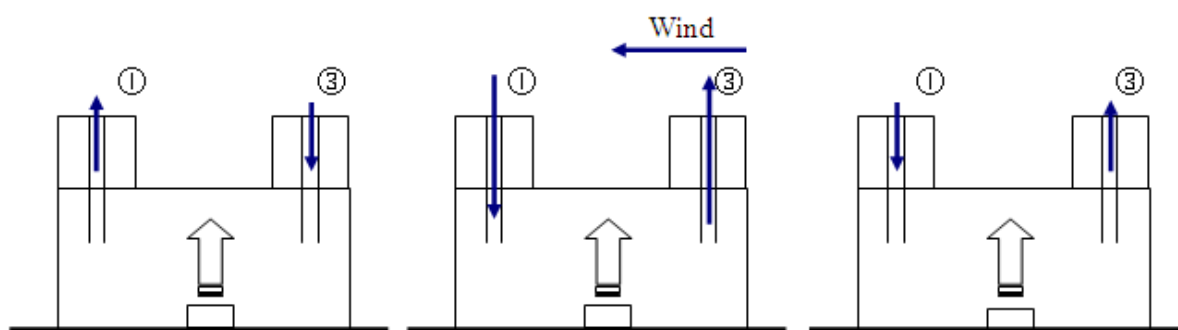


Figure 5.18 Initial condition effects of two-stack (stack 1 and stack 3) case

Results of the four-stack case are shown in Figure 5.19. The final flow directions in all four stacks follow the directions when the wind was on, $U_{ref} = 4 \text{ m/s}$. It should be noted that if the initial condition effect is due to cooling of thermal mass of the stack, it can not be simulated with the salt bath technique.

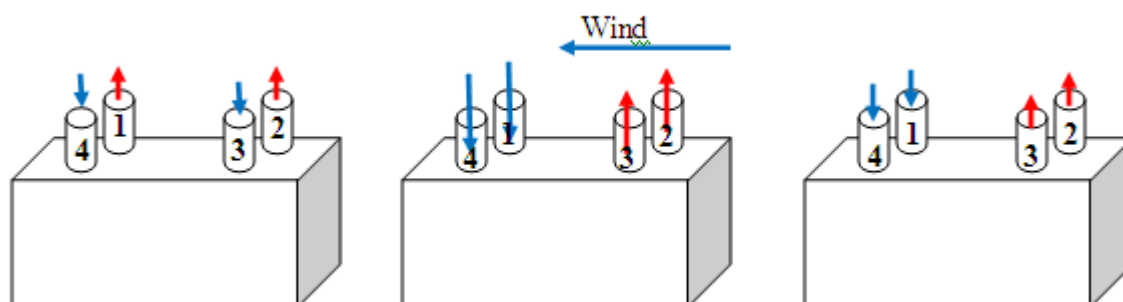


Figure 5.19 Initial condition effects of four-stack case

A question is raised: will the effects be the same when there are lower orifices open? Similar tests were carried out for the opening configuration of four stacks and one orifice (orifice 1). Results are shown in Figure 5.20. The final flow directions through the stacks do not follow the status when the wind was on ($U_{ref} = 4 \text{ m/s}$). The flow direction in stack 1 and 4 changes when there is wind, but returns to the original direction soon after U_{ref} turns back to 0 m/s. This is simply because air could come in the box through the lower orifice due to the pressure difference between the orifice outlet and stack outlets driven by buoyancy force alone. Bearing in mind the behaviour observed in Figure 5.19 and Figure 5.20, there is a value of the lower opening area for which the flow pattern will not return to its original state. The author carried out the same test shown in Figure 5.20, but sealed part of the opening area of orifice 1. The same flow pattern was obtained as that in Figure 5.19 until the area was reduced to about 2.5 % compared to the stack areas. The porosity of lower orifice area has to be very small (less than 0.01%) for which the flow pattern would not return to its original state. Additionally, there could be different steady states of different flow directions within the stacks for the buoyancy alone case, when the lengths of the stacks are different. Results were obtained experimentally and theoretically in literature (Chenvidyakarn and Woods, 2005).

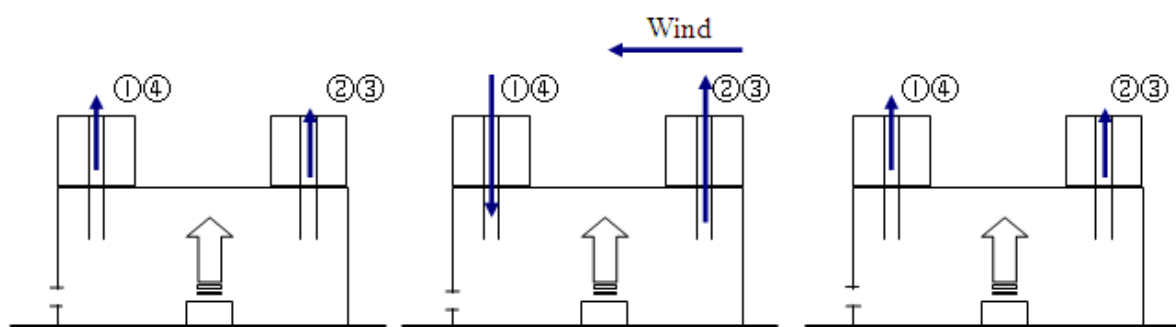


Figure 5.20 Initial condition effects of four stack and one orifice (Orifice 1)

5.3.2.2 Flow magnitudes

Figure 5.21 shows the stack velocities for the three conditions of the first case: i.e. stack 1 and stack 3 alone (corresponding flow directions are shown in Figure 5.18).

5 Experiments – wind and buoyancy combined

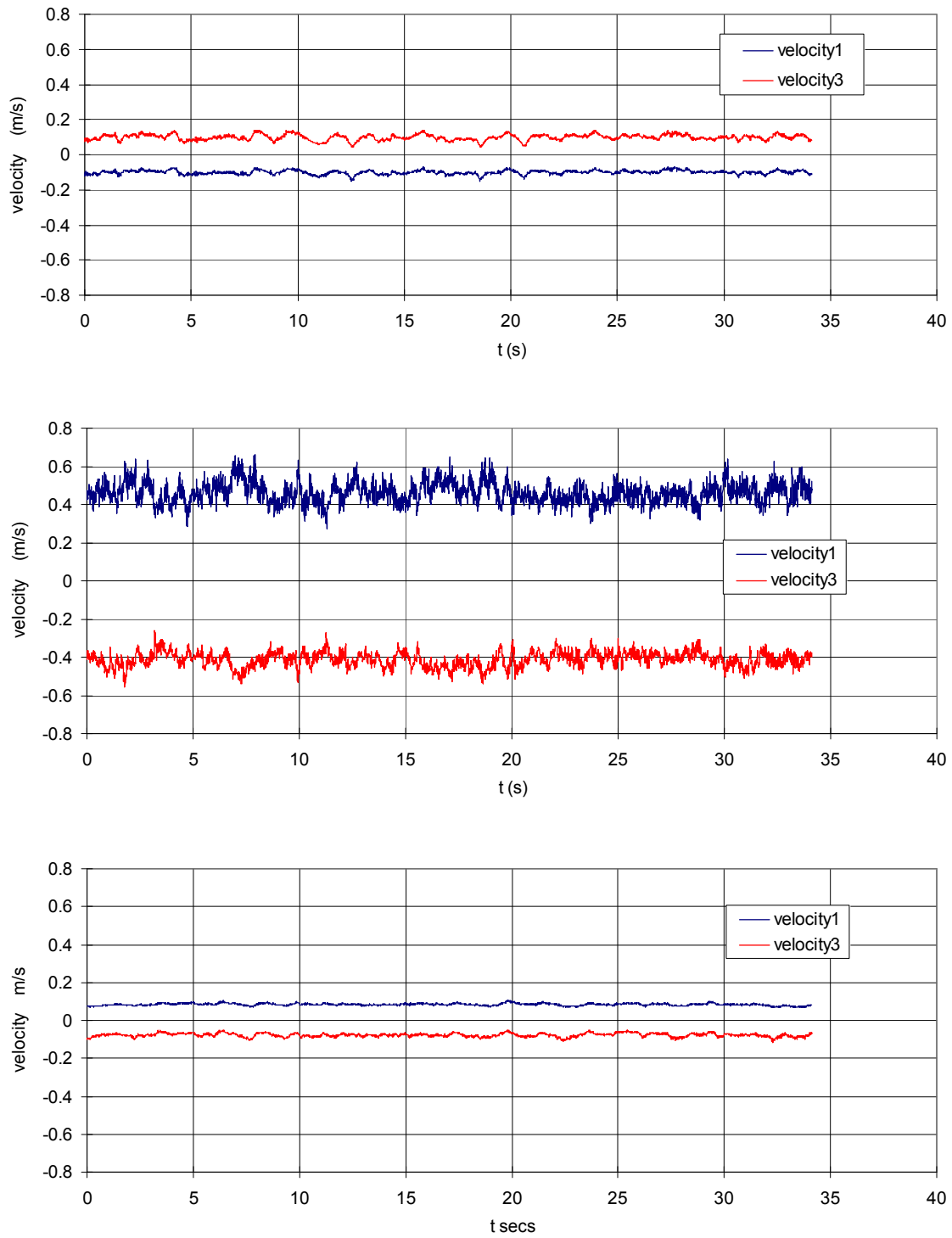


Figure 5.21 Velocities of initial condition effects for the case of two stacks (stacks 1 and 3)

5 Experiments – wind and buoyancy combined

It should be noted that there are some differences between buoyancy alone cases and wind and buoyancy combined cases. In the second graph (wind and buoyancy combined case), the velocity magnitude (absolute value) of stack 1 and stack 3 change in a same trend, that is to say they increase and decrease simultaneously as expected when wind force is dominant. However, the absolute velocities change in opposite ways when there is buoyancy alone, as shown in the first and third graphs, which is unexpected. Here follows the explanations (see Figure 5.22).

When there is buoyancy only, the box is heated to a constant temperature, and flow directions were established as shown in Figure 5.22, i.e. upward flow in stack 1 and downward flow in stack 3. Assumptions about temperature are made: the red part is the uniform box temperature; the white part is the external uniform room temperature. The two parts with gradient colour are the mixing zones. At time t_1 , pressure profiles are shown in solid lines, P_r is room pressure, P_b is box pressure, P_s is stack pressure (red for stack 1, blue for stack 3). At time t_2 , the heat fluctuates, generating a trivial temperature increase in the coloured areas, hence the pressure profiles of the stacks turn to the dashed lines. dP in Figure 5.22 is the pressure difference across the stack outlet/inlet (outlet of stack 1, inlet of stack 3). As one can see, dP increases for stack 1, whereas it decreases for stack 3. In other words, the temperature increase enhances the driving force of stack 1, yet weakens the driving force of stack 3. Therefore, the magnitudes of velocity 1 and velocity 3 change in opposite directions (one increases, the other decreases). It should be noted that continuity (mass conservation) should still apply.

5 Experiments – wind and buoyancy combined

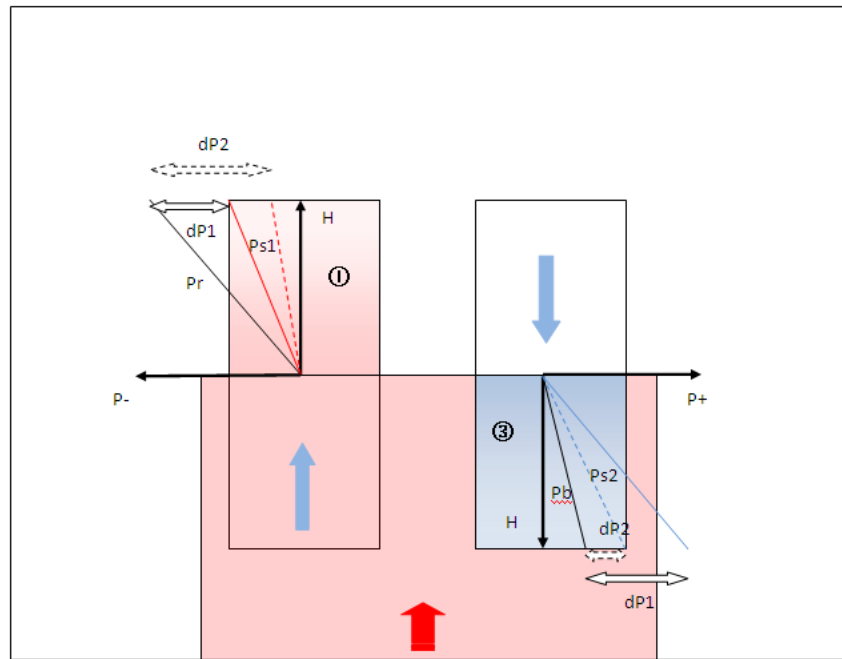
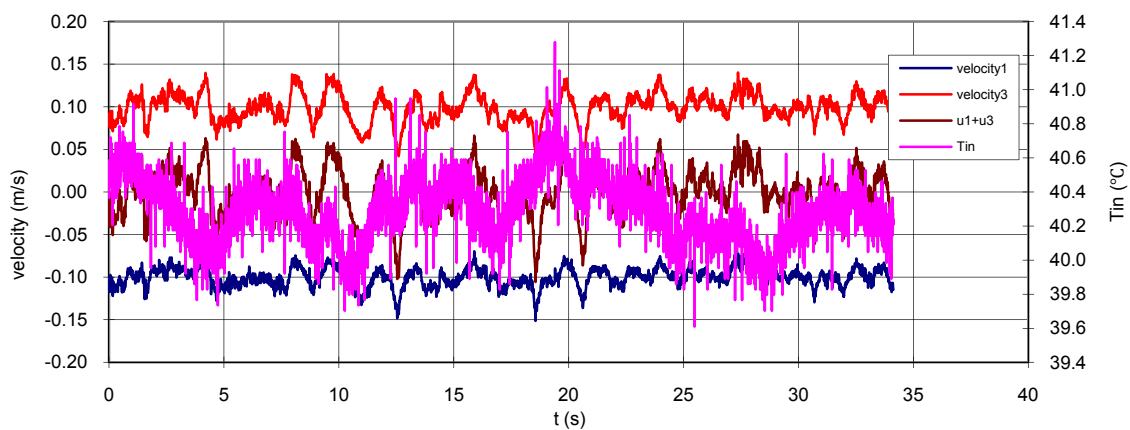


Figure 5.22 Effect of heat source fluctuation

In order to check mass conservation, i.e. the changes in stack flow rates correspond with the temperature fluctuation. Figure 5.23 shows the temperature and velocities fluctuations for the case when there was buoyancy only, and an expanded period of 5 s. The following explanations are for the consequence of temperature fluctuation (heat source fluctuations) on the sum of the velocity fluctuation.



5 Experiments – wind and buoyancy combined

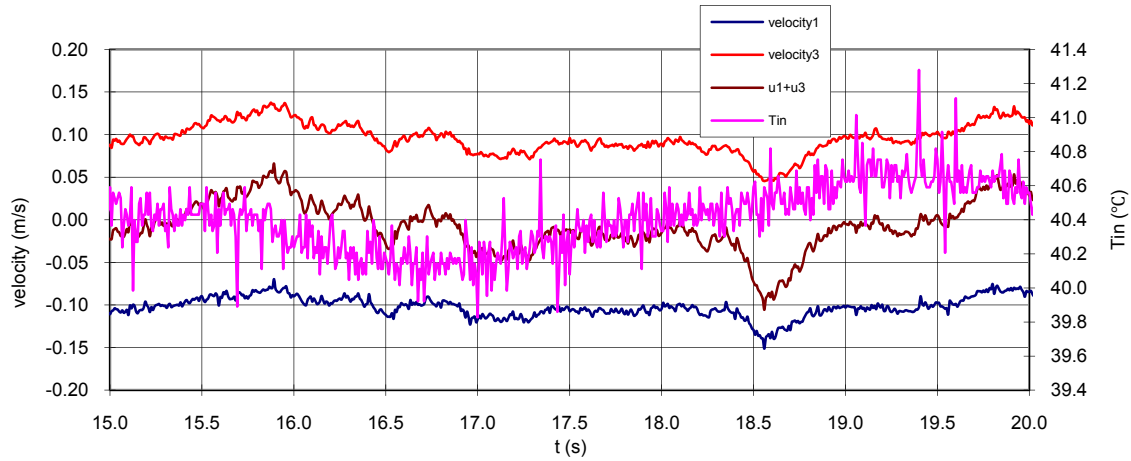


Figure 5.23 Temperature and velocity fluctuations of buoyancy alone two-stack case (stacks 1 and 3)

Relations between internal density fluctuation and total flow rate is

$$q_1\rho_1 + q_3\rho_3 = V \frac{d\rho_I}{dt} \quad (5.8)$$

where ρ_I is the internal air density, q_1 and q_3 are the flow rates through stack 1 and 3. The values of ρ_1 and ρ_3 depend on the flow directions through individual stacks.

The relationship between ρ_I and internal temperature T_I is

$$\frac{d\rho_I}{dt} = -\frac{\bar{\rho}_I}{\bar{T}_I} \frac{dT_I}{dt} \quad (5.9)$$

Substituting equation (5.9) into equation (5.8) gives

$$q_1\rho_1 + q_3\rho_3 = -\frac{V\rho_i}{T_i} \frac{dT_i}{dt} \quad (5.10)$$

Ignore the differences between ρ_1 , ρ_3 and ρ_I ,

$$q_1 + q_3 = -\frac{V}{\bar{T}_I} \frac{dT_I}{dt} \quad (5.11)$$

$$u_1 + u_3 = -\frac{V}{\bar{T}_I A} \frac{dT_I}{dt} \quad (5.12)$$

5 Experiments – wind and buoyancy combined

When $\frac{dT_I}{dt} > 0$, $u_1 + u_3 < 0$, which is shown most of the time in the graph, take the period between 17 s and 19.5 s for example. For $dT_I = 0.4^\circ\text{C}$, $dt = 2.5 \text{ s}$, $V = 0.5 \times 0.2 \times 0.25 \text{ m}^3$, $A = 0.00022 \text{ m}^2$, $\bar{T}_I = 425 \text{ K}$. The term $-\frac{V}{\bar{T}_I A} \frac{dT_I}{dt} = -0.05 \text{ m/s}$, which is just about the average value of $u_1 + u_3$ shown in the second graph of Figure 5.23. Therefore, the mass conservation is satisfied. Therefore, it is concluded that the unexpected observation in the first and third graph of Figure 5.21 is due to the temperature fluctuations for the buoyancy alone case. However, for the buoyancy and wind combined case in the second graph, in which the fluctuations of wind dominates, the effects of temperature fluctuations on stack flow rates are eliminated.

5.4 Summary and conclusions

Tests have been carried out to investigate the hysteresis effects, the effects of turbulent wind pressure fluctuations on stack flow rates, and the initial condition effects on the final flow pattern through multiple stacks. Main conclusions are as follows.

- 1) During the transitional process between buoyancy dominated and wind dominated states, the reversal percentage change relatively smoothly when wind force was fixed than when buoyancy force was fixed.
- 2) When transitions between different ventilation statuses happen in a model with long openings, there is no obvious hysteresis effect like what was stated in the literature, probably because the long opening could mitigate the transitioning process. More tests might be needed to prove this hypothetical conclusion.
- 3) In the one stack and one orifice tests when transition from wind dominated to buoyancy dominated ventilation happens, the influence of wind fluctuation eliminates the zero ventilation rate point, which in theory should exist regardless of the fluctuation of the driving forces. This supports the observation in Carey and Etheridge (1999)
- 4) When there are only stacks open with a fixed buoyancy force, the flow directions through the stacks could change due to an outside perturbation which could cause a

5 Experiments – wind and buoyancy combined

new initial condition, like a gust wind (lasts long enough to change flow directions).
However this will not happen when there are lower level openings of sufficient area.

6 Theoretical calculations and comparisons with measurements

6.1 Introduction

The envelope flow models were introduced in Chapter 2. The testing results were presented in Chapters 3 and 4. In this chapter, theoretical calculations are carried out using both steady and unsteady models; pressure data inputs are from testing results. The steady model calculations are solved in dimensional forms, whereas the QT model calculations are solved in nondimensional form using Matlab. The calculated results of opening flow rates and internal pressure are compared with measurements in nondimensional forms for consistency. Exceptions are comparisons of instantaneous values, which are made in dimensional forms.

6.1.1 Structure of chapter

Two methods of determining flow direction from pressure measurements alone are examined. Firstly, given the mean values of wind pressure coefficient of each opening, is it possible to determine the flow direction of each opening? Secondly, if given both the measured pressure coefficients of openings and the internal pressure coefficient, will it be more accurate in determining flow directions? These two methods and results are given in Section 6.2.

Given the wind pressure coefficients, envelope flow models can be used. Steady model and QT model calculations of wind only cases and comparisons with measurements are presented in Section 6.3.

Section 6.4 presents comparison of instantaneous values of QT model and measurements. Prediction of full scale reversal percentage using QT model is also described. Comparison of

6 Theoretical calculations and comparisons with measurements

measurements and QT model of the relations between reversal percentage and nondimensional pressure difference across an opening are given.

Steady model and QT model calculations for the wind and buoyancy combined tests and comparisons with measurements are presented in Section 6.5.

Finally, comments are made on all methods based on their complexity and accuracy (Section 6.6).

6.1.2 Range of calculations

The following tables show the range of theoretical calculations. Table 6.1 shows the range of calculations of determining flow directions from external pressure measurements. Table 6.2 shows the calculations of wind alone cases. Table 6.3 shows the calculations of wind and buoyancy combined cases.

Table 6.1 Determination of flow direction from pressures

Case No.	Opening configuration		Wind direction	Wind speed (m/s)
	Stack	Orifice		
1	1,2,3,4		0,45,90	6.5
2	1,2,3,4	1,2	0,45,90	6.5
3	1,3	1,2,3,4	0,45,90,135,180	6.5

Results of stacks 1 and 3 will be presented in Section 6.2 for all building configurations.

6 Theoretical calculations and comparisons with measurements

Table 6.2 Steady model calculations of wind alone cases (high-lighted cases are also calculated with QT model)

Case No.	Opening configuration		Wind direction	Wind speed (m/s)
	Stack	Orifice		
1	1,2,3,4		0,45,90	6.5
2	1,2,3,4	1,2	0,45,90	6.5
3	1,3	1,2,3,4	0,45,90,135,180	6.5
4	1,2,3,4		0	1.5 ~ 6.5
5	1,2,3,4	1,2	0	1.5 ~ 6.5

Table 6.3 QT model calculations of wind and buoyancy combined cases

Case No.	Opening configuration		Wind Speed (m/s)	Temperature (°C)
	Stack	Orifice		
1	3	1	0.6	Increasing
2	1,3	1,2,3,4	1.2	Increasing

The steady model is also used for the highest temperature case in Table 6.3, when there is no reversing flow.

6.2 Determination of flow direction from pressures

Two possible methods for determining stack flow direction from external wind pressure coefficients are considered here.

Method 1 Measurement of mean wind pressure coefficients $\overline{C_p}$ of each opening. With this information and with an estimated value for the mean internal pressure coefficient, $\overline{C_{pi}}$, the mean pressure difference across each opening is obtained e.g.

$$\text{Stack} \quad \overline{\Delta C_{ps}} = \overline{C_{ps}} - \overline{C_I} \quad (6.1)$$

$$\text{Orifice} \quad \overline{\Delta C_{po}} = \overline{C_{po}} - \overline{C_I} \quad (6.2)$$

By assuming that the sign of the flow rate is the same as the sign of $\overline{\Delta C_p}$ (which is a valid assumption, except possibly when intermittent flow reversal occurs), the flow direction is

6 Theoretical calculations and comparisons with measurements

immediately obtained. If the only concern is to maintain a fixed flow direction in the stacks, this information may be all that is required. This is the simplest technique, but it requires an estimate of $\overline{C_{PI}}$ and the results are sensitive to the chosen value.

The estimated value of $\overline{C_{PI}}$ is taken as the weighted arithmetic mean of the $\overline{C_{pi}}$. The weighting uses the product $C_{zi}A$, where C_z for the stacks has been taken as one-half that for the orifices.

$$\overline{C_{PI}} = \sum_{i=0}^n \left(\overline{C_{pi}} \frac{C_{zi}A_i}{\sum_{i=0}^n C_{zi}A_i} \right) \quad (6.3)$$

Method 2 Measurement of mean wind pressure coefficients and the internal pressure coefficient. This is the same technique as method 1, except $\overline{C_{PI}}$ is measured, and in that sense the values of $\overline{\Delta C_{pi}}$ are accurately known. However, $\overline{C_{PI}}$ is likely to be dependent on R_{eo} (the dependence of $\overline{C_{PI}}$ on R_{eo} is investigated in more detail in Chapter 7).

Since the principle of a steady envelope model is to determine $\overline{C_{PI}}$ by iterations till the mass conservation is satisfied, then this $\overline{C_{PI}}$ is used to calculate $\overline{\Delta C_{pi}}$ and q_i . As long as the measured $\overline{C_{PI}}$ is obtained from the wind-tunnel, one can use the steady model to calculate the flow rate through each opening including both magnitude and direction. It is unlikely that one would go to the expense of wind tunnel testing just for the purpose of applying methods 1 and 2 to determine flow directions. In this sense, methods 1 and 2 are of little practical significance. Nevertheless it is of interest to see how they compare with steady envelope model in determining flow directions. It should be noted that equation (6.3) is not the only way for estimating $\overline{C_{PI}}$. One can use other estimating methods e.g. just taking the mean of the $\overline{C_{pi}}$ values.

6 Theoretical calculations and comparisons with measurements

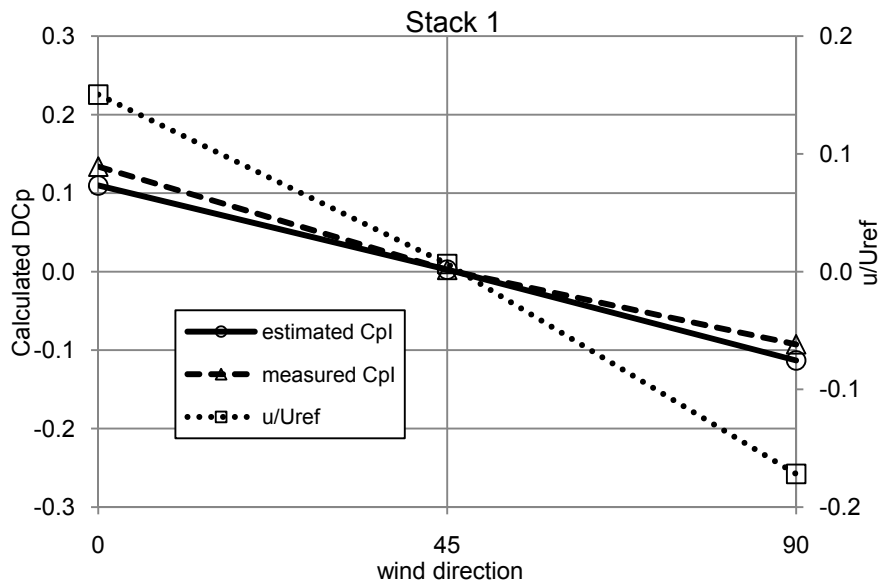


Figure 6.1 Calculated $\overline{\Delta C_{pi}}$ and measured u_i/U_{ref} of stack 1 (S1234)

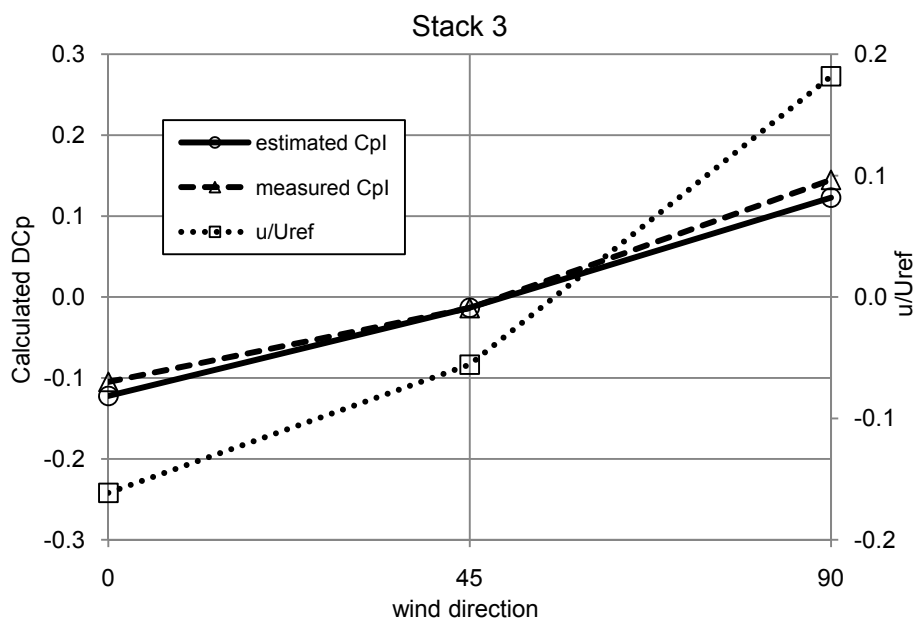


Figure 6.2 Calculated $\overline{\Delta C_{pi}}$ and measured u_i/U_{ref} of stack 3 (S1234)

Figure 6.1 and Figure 6.2 show the measured values of $\frac{u_i}{U_{ref}}$ and calculated values of $\overline{\Delta C_{pi}}$ using method 1 and 2 respectively for stack 1 and stack 3 of Case 1 in Table 6.1. If the

6 Theoretical calculations and comparisons with measurements

two methods could correctly detect the flow directions, the measured $\frac{u_i}{U_{ref}}$ and calculated $\overline{\Delta C_{pi}}$ should have the same sign, i.e. when flow reversal occurs, both of the two parameters should be positive. It can be seen from Figure 6.1 and Figure 6.2, both methods 1 and 2 correctly determine flow directions for the four stack and no orifice case.

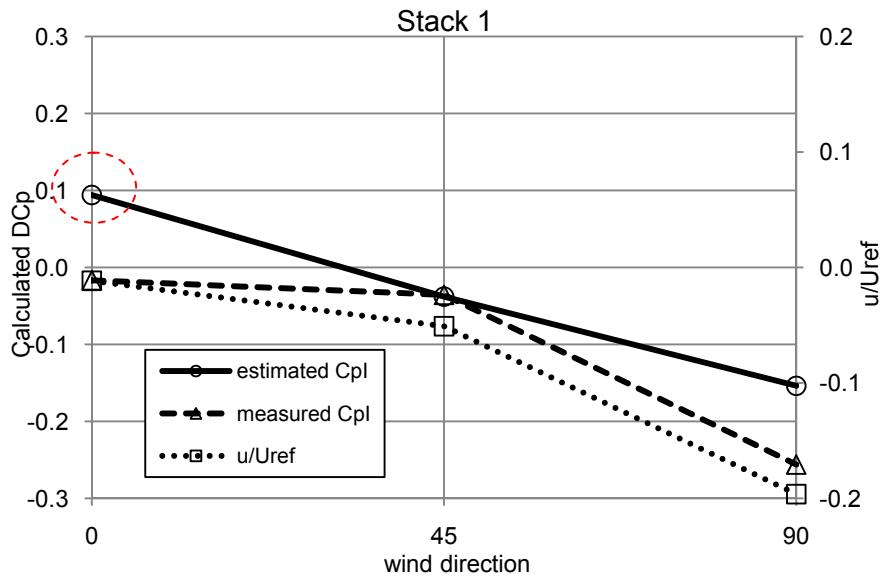


Figure 6.3 Calculated $\overline{\Delta C_{pi}}$ and measured u_i/U_{ref} of stack 1 (S1234_O12)

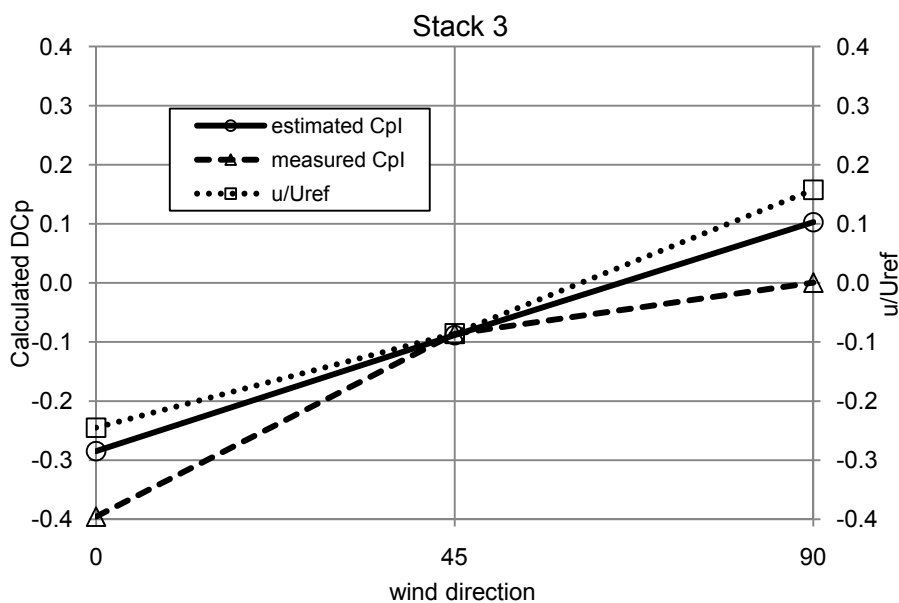


Figure 6.4 Calculated $\overline{\Delta C_{pi}}$ and measured u_i/U_{ref} of stack 3 (S1234_O12)

6 Theoretical calculations and comparisons with measurements

Figure 6.3 and Figure 6.4 show the measured values of $\frac{u_i}{U_{ref}}$ and calculated values of $\overline{\Delta C_{pi}}$ using method 1 and 2 respectively for stack 1 and stack 3 of Case 2 in Table 6.1. There is one error (marked by dashed line circle) in Figure 6.3: method 1 (using estimated $\overline{C_{PI}}$ values) fails to estimate the flow direction for stack 1, wind direction 0 degree.

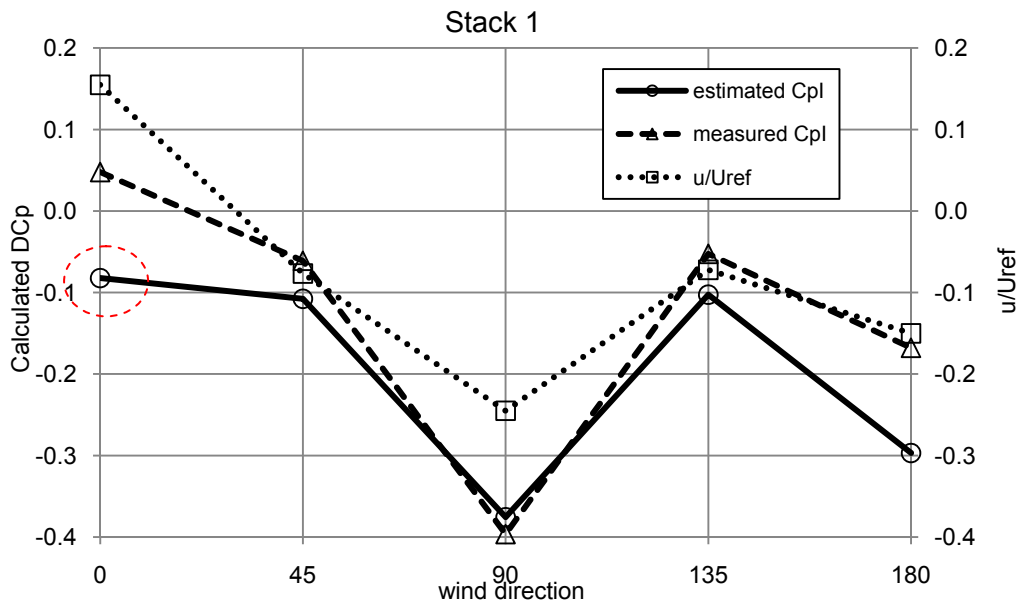


Figure 6.5 Calculated $\overline{\Delta C_{pi}}$ and measured u_i/U_{ref} of stack 1 (S1234_O1234)

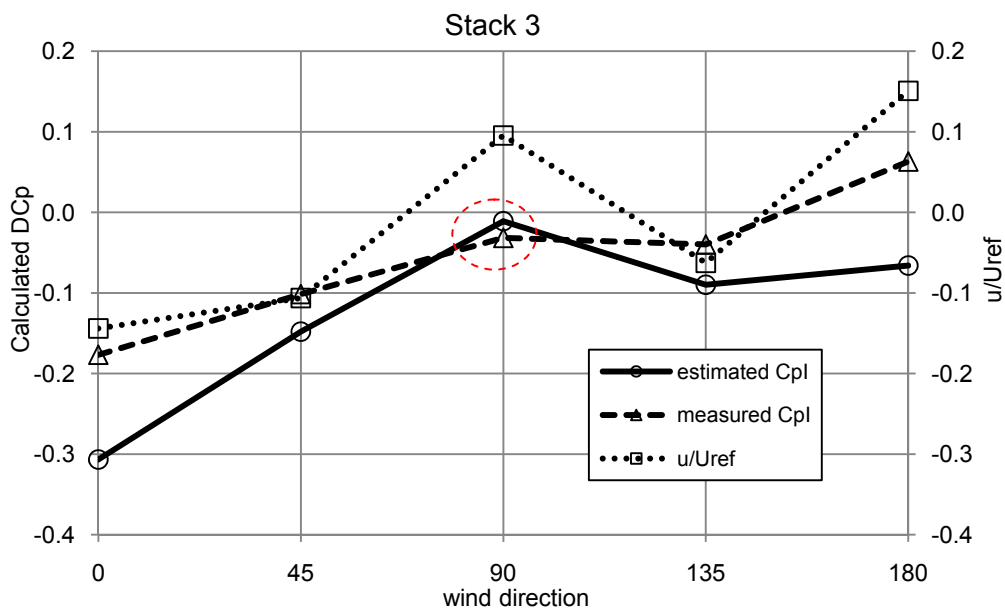


Figure 6.6 Calculated $\overline{\Delta C_{pi}}$ and measured u_i/U_{ref} of stack 3 (S1234_O1234)

6 Theoretical calculations and comparisons with measurements

Figure 6.5 and Figure 6.6 show the measured values of $\frac{u_i}{U_{ref}}$ and calculated values of $\overline{\Delta C_{pi}}$ using method 1 and 2 respectively for stack 1 and stack 3 of Case 3 in Table 6.1. In Figure 6.5, method 1 fails to show the flow direction of stack 1, wind direction 0 degree. In Figure 6.6, both methods 1 and 2 fail to determine the flow direction of stack 3, wind direction 90 degree.

In summary, with the increasing number of sharp-edged orifices, both methods become more unreliable. However, method 2 using the measured $\overline{C_{PI}}$ performs better than method 1 using the estimated $\overline{C_{PI}}$.

6.3 Envelope flow model comparisons - wind alone tests

As stated in Chapter 2, the flow characteristics of the stacks are taken from a quadratic curve-fit to the still-air measurements i.e.

$$\frac{1}{C_z^2} = C \frac{L}{Re_{st}d} + D \quad (6.4)$$

where L is the length of the stack and d is the diameter of the stack. C and D are factors obtained from steady calibration (See Chapter 3), which relate to stack geometry and flow directions. For upward flow, $C=153.07$ $D=5.7391$, for inward flow, $C=140.08$ $D=3.6929$. Except where stated otherwise, the discharge coefficient of the orifices is taken to be 0.68.

6.3.1 Variation of nondimensional flow rate with wind direction

In the figures, ‘calculated’ means using the steady envelope model, ‘calculated QT’ means using the QT model. Figure 6.7 and Figure 6.8 compare the calculated and measured stack flow rates for the two configurations: (S1234) and (S1234_O12). QT model results are presented for the second configuration, which is case 2 in Table 6.2.

6 Theoretical calculations and comparisons with measurements

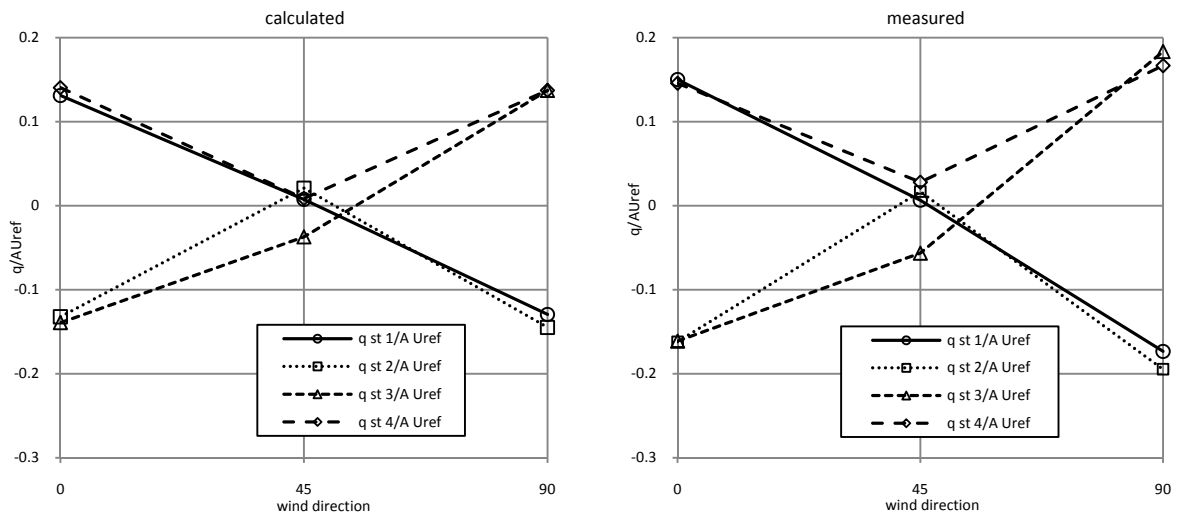
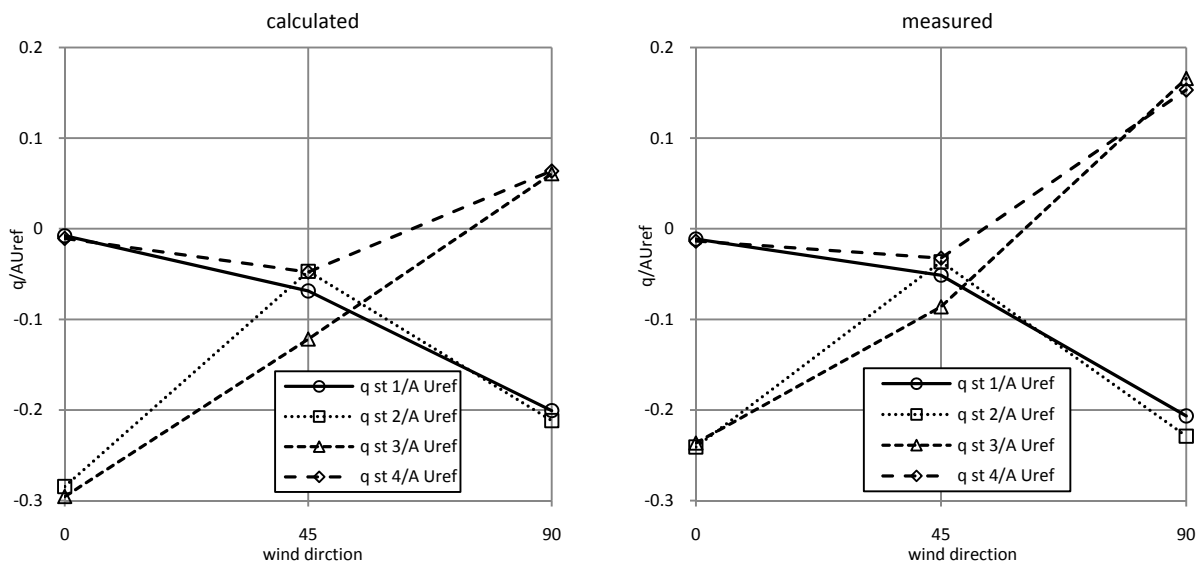


Figure 6.7 Variation of q/AU_{ref} (S1234) – steady model



6 Theoretical calculations and comparisons with measurements

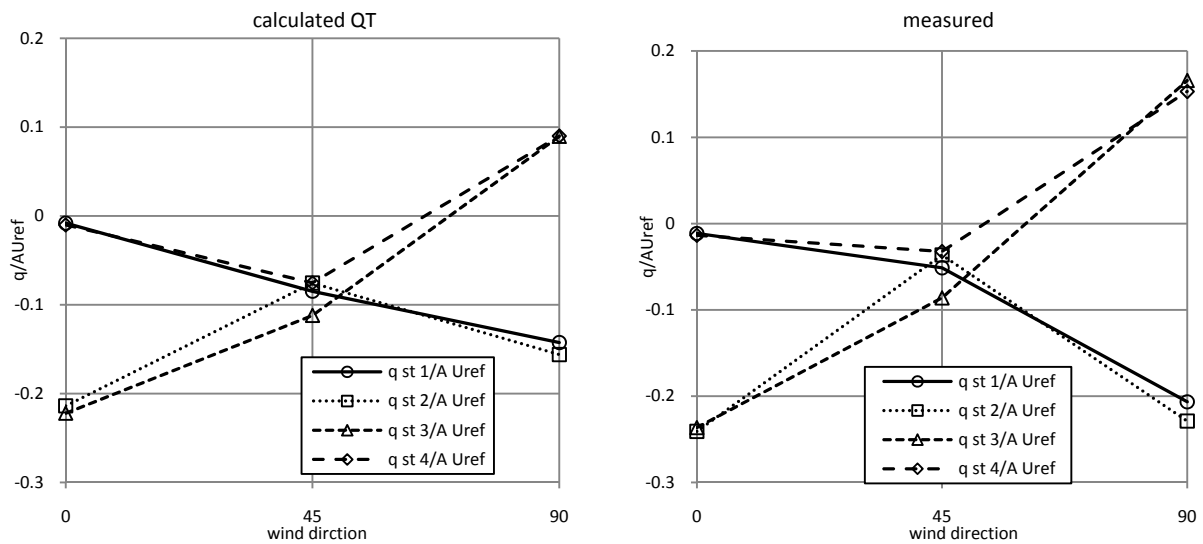


Figure 6.8 Variation of q/AU_{ref} (S1234_O12) – steady model and QT model

For both configurations the agreement is fairly good, but it is better with four stacks alone (no orifices). At all wind directions, including 45 degrees where intermittent flow reversal occurs, the sign of the flow is accurately calculated.

Figure 6.9 shows the case of two stacks and four orifices (S13_O1234). The discharge coefficient of the orifices were set as constant $C_z = 0.68$. The steady model gives wrong flow directions for stack 1 for the case of 0° and stack 3 for the cases of 90° and 180° .

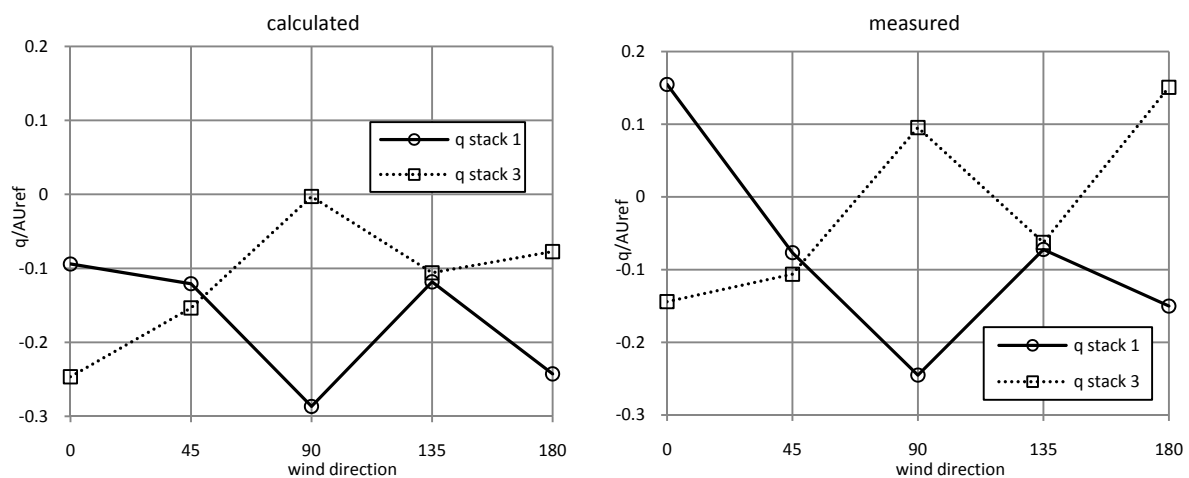


Figure 6.9 Variation of q/AU_{ref} (S13_O1234) – steady model

6 Theoretical calculations and comparisons with measurements

It is known from previous tests on a similar model (Chiu and Etheridge, 2007) that the discharge coefficient of a sharp-edged orifice can be significantly affected by external cross flow (wind component parallel to the envelope), particularly when the flow is inward. The evidence from previous work is that C_z can be reduced by 50 % or more depending on the ratio of cross flow velocity and mean velocity through the opening. Figure 6.10 shows the discharge coefficient of the orifice for still-air and wind-on cases (Carey and Etheridge, 1999). Values of C_z for wind on conditions (wind direction 67.5°) were calculated from tests with one stack and one orifice, in which the volume flow rates of the orifice and the stack are equal. It can be seen that C_z is reduced by the wind.

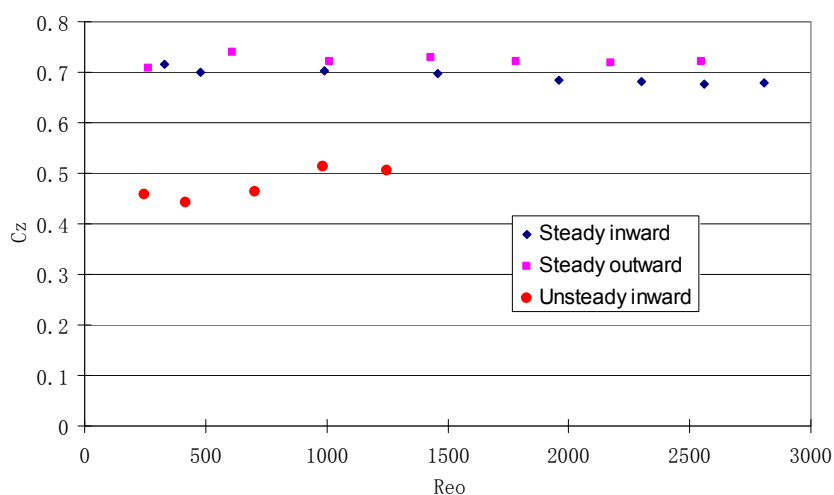


Figure 6.10 C_z of sharp-edged orifice for steady (still-air) and unsteady (wind) conditions

Therefore different C_z values were chosen to obtain a better match between calculation and measurement. Since in theory C_z can be as low as 0.1 due to cross flow effect, one can assume that $C_z = 0$ when $v/u = \infty$ as an extreme case. The best results obtained are shown in Figure 6.11. C_z values used are listed in Table 6.4.

6 Theoretical calculations and comparisons with measurements

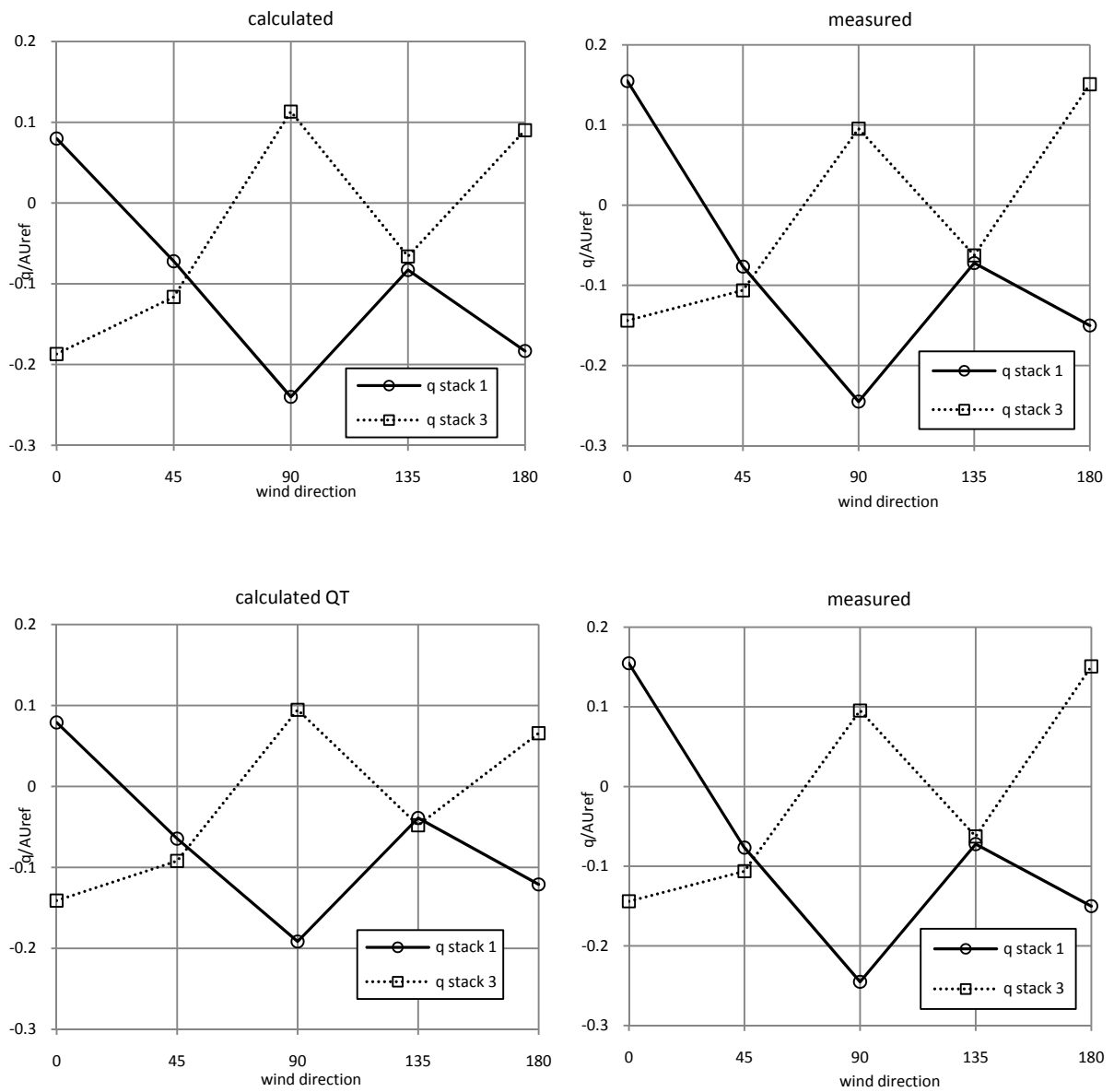


Figure 6.11 Variation of q/AU_{ref} (S13_O1234); changed C_z – steady model and QT model

Table 6.4 C_z values of orifices

Wind direction	Orifice 1	Orifice 2	Orifice 3	Orifice 4
0	0	0	0.5	0.5
45	0.3	0.3	0.3	0.3
90	0.1	0.1	0.1	0.1
135	0.3	0.3	0.3	0.3
180	0	0	0.5	0.5

6 Theoretical calculations and comparisons with measurements

The main conclusion for the above is that the best agreement is observed when there are no orifices and seems to deteriorate with the increasing number of orifices. This could reflect the greater sensitivity of sharp-edged orifices to crossflow effects.

6.3.2 Variation of nondimensional flow rate with building Reynolds number (wind speed)

Calculations were carried out to see if the observed variations with Re_b could be calculated/ Most of the calculations are with the steady model. Results with the QT model are given at the end.

Figure 6.12 and Figure 6.13 compare the calculated and measured stack flow rates for the two configurations (S1234) and (S1234_O12).

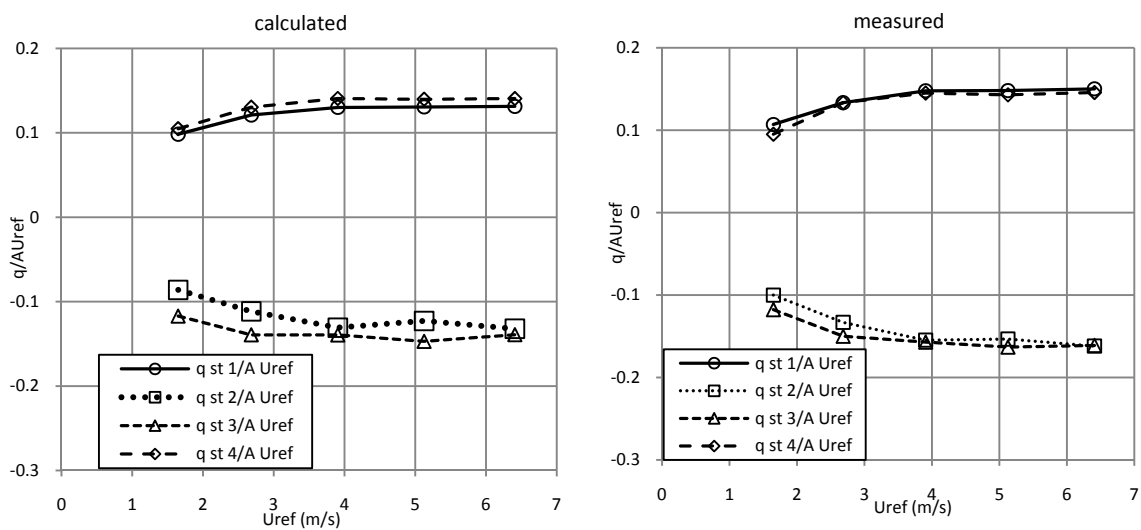


Figure 6.12 Effect of Reynolds number (S1234) – steady model

6 Theoretical calculations and comparisons with measurements

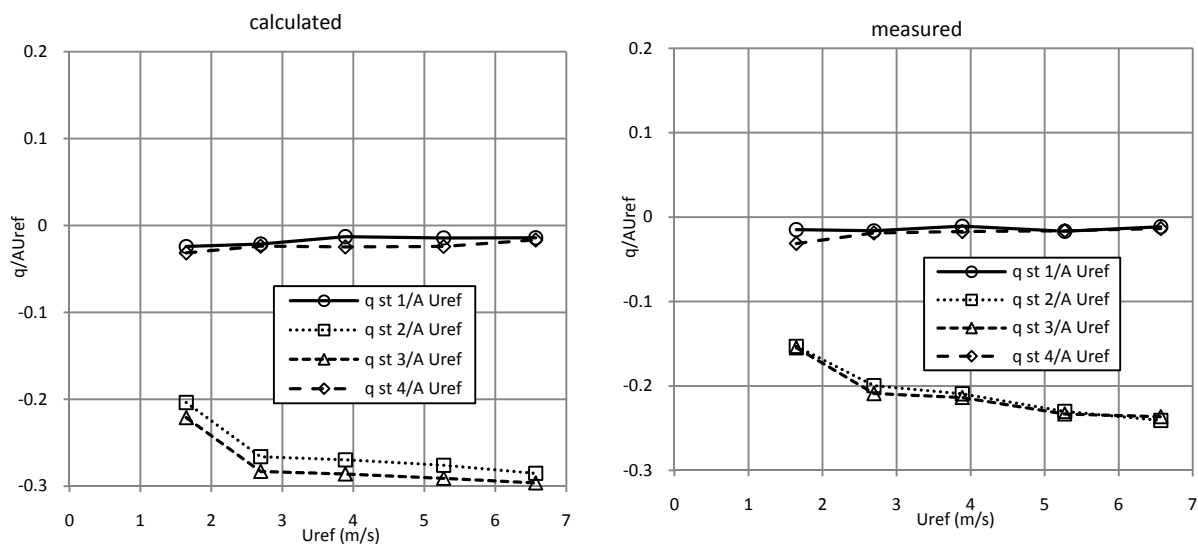


Figure 6.13 Effect of Reynolds number (S1234_O12) – steady model

Again it is clear that the agreement is good for the stacks alone case, but relatively poor for the configuration with two orifices. There are two likely reasons for this, one associated with crossflow effects and the other with intermittent flow reversal. To appreciate this, Figure 6.14 shows the flow directions for the two cases.

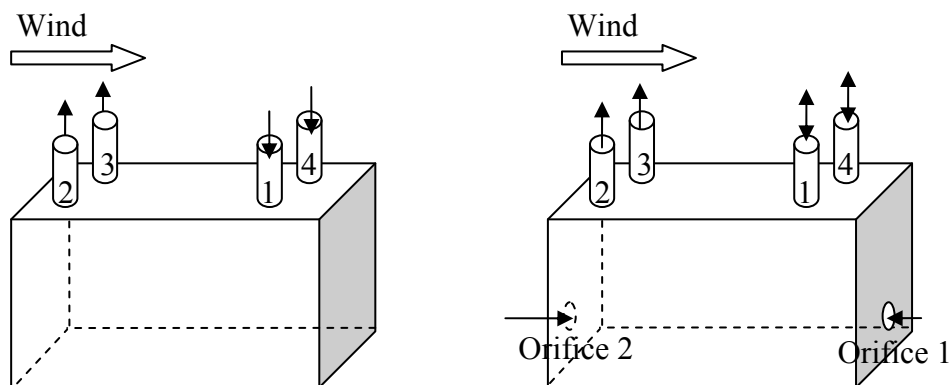


Figure 6.14 Flow directions for two cases (S1234) and (S1234_O12)

From Figure 6.13 one can see that the calculated flow rates through stack 2 and 3 (outward flows) are larger than the measurements. Since the C_z of stack with upward flow only depends on the flow through the stack, it is likely that the error comes from the chosen orifice

6 Theoretical calculations and comparisons with measurements

C_z values. If the chosen orifice C_z value is larger than the actual value, resulting in larger flow rates of orifice 1 and 2, then the flow rates of stack 2 and 3 would be larger than the measurements to satisfy mass conservation. Therefore calculations were carried out with (i) C_z of both orifices reduced from 0.68 to 0.5 and (ii) with one $C_{z1} = 0.5$ and the other $C_{z2} = 0.61$. The results are shown in Figure 6.15.

As one can see from Figure 6.15, there is a very small improvement in the agreement of calculated and measured values of volume flow rate of stack 3 and 4 for both $C_z = 0.61$ and 0.5. The decrease of C_z from 0.68 to 0.5 marginally (at low reference wind speed) improved the results of stacks 2 and 3, but worsened the results of stacks 1 and 2 (wrong directions). It suggests that lower C_z values should make the agreements of stacks 2 and 3 better. However, that will influence the agreement of stacks 1 and 2 in the opposite way. Does it indicate that one should use different values of C_{zo} for the two orifices, of which one is sited in the windward wall; the other is sited in the leeward wall? Because the values of wind on cases were obtained from an orifice on the windward wall, there are no suggested values to use for the other orifice.

There is another possible reason causing the inaccuracy of stacks 1 and 4. For stacks 1 and 4 the reversal percentage was around 30 % and the still-air relationship may well be invalid.

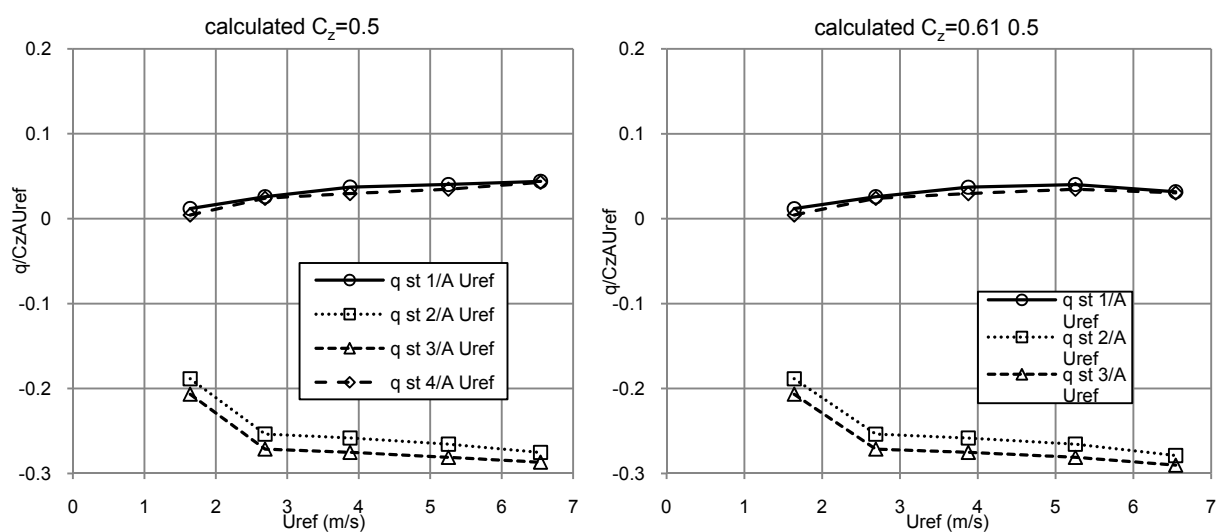


Figure 6.15 Calculated effect of Reynolds number (S1234_O12) with changed C_z – steady model

6 Theoretical calculations and comparisons with measurements

Figure 6.16 presents the results of QT model for the same case, the discharge coefficients for the orifices are $C_{z1} = 0.1$ (leeward), $C_{z2} = 0.68$. Two types of pressure inputs were used, the first one ‘calculated QT mean’ was using the mean measured pressure (input the mean value at each instantaneous time); the second one ‘calculated QT instantaneous’ was using instantaneous measured pressures. It shows that the improvements on stacks 2 and 3 still exists, yet the results of stacks 1 and 4 stay correct, showing the right directions. This is the advantage of QT model, which can calculate intermittent reversing flows.

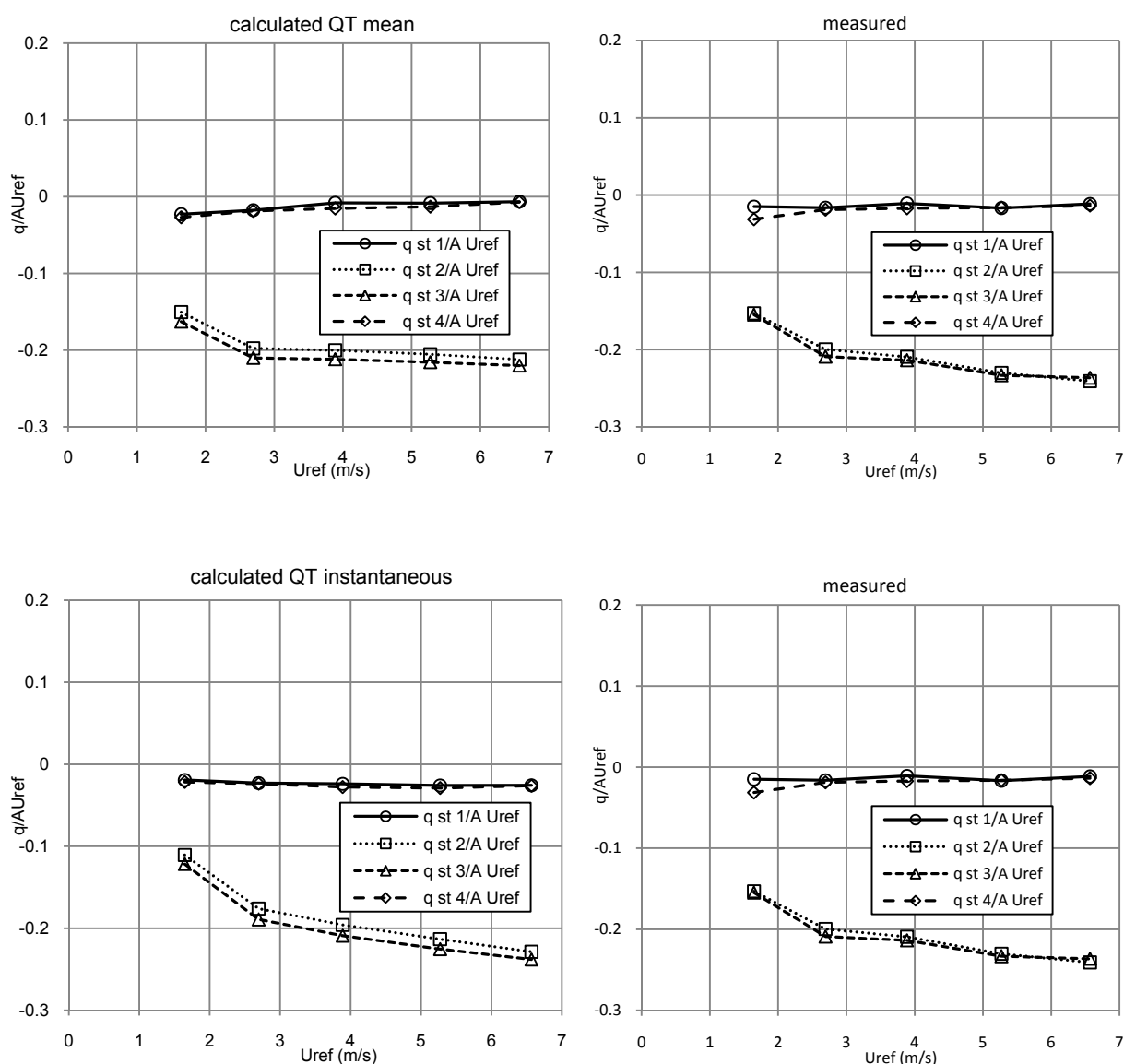


Figure 6.16 Calculated and measured effect of Reynolds number (S1234_O12) with changed C_z - QT model

6.4 Reversal flow prediction using QT model for wind alone ventilation

6.4.1 Comparisons for instantaneous flow rate and internal pressure

The solutions of the QT model are the instantaneous flow rate of each opening, and the internal pressure. Examples of comparisons between QT model and measurements are given in Figure 6.17, Figure 6.18 and Figure 6.19 for the case of (S1234_O12), wind direction 0 degree, $U_{ref} = 6.5 \text{ m/s}$, which is one of case 2 in Table 6.2. Figure 6.17 shows the results for stack 1, whose measured reversal percentage is 35.5 %. Figure 6.18 shows the results for stack2, which is unidirectional upward flow (flow sign negative). Figure 6.19 shows the results of internal pressure. It is safe to say that QT model is an accurate ventilation prediction method. It offers accurate instantaneous flow rate for unidirectional flow, and also reliable solutions for reversing flow, which can not be treated in the conventional steady model.

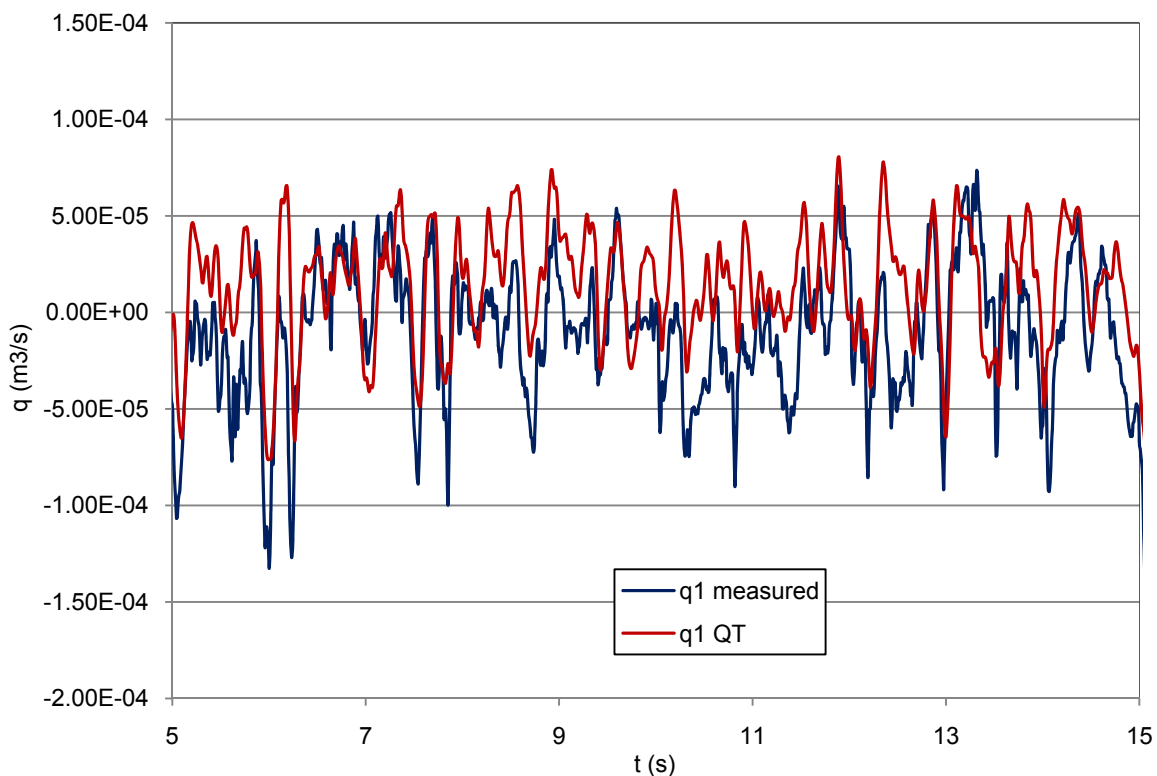


Figure 6.17 Comparison for stack flow rate; stack 1 (S1234_O12)

6 Theoretical calculations and comparisons with measurements

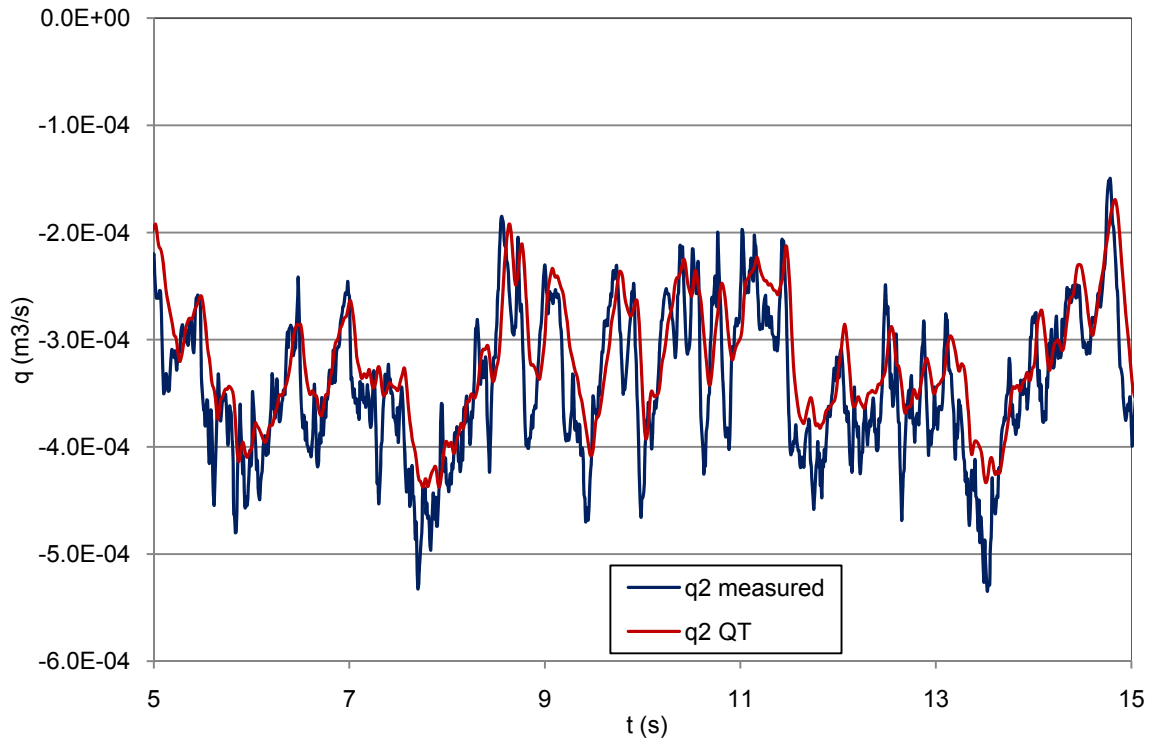


Figure 6.18 Comparison for stack flow rate; stack 2 (S1234_O12)

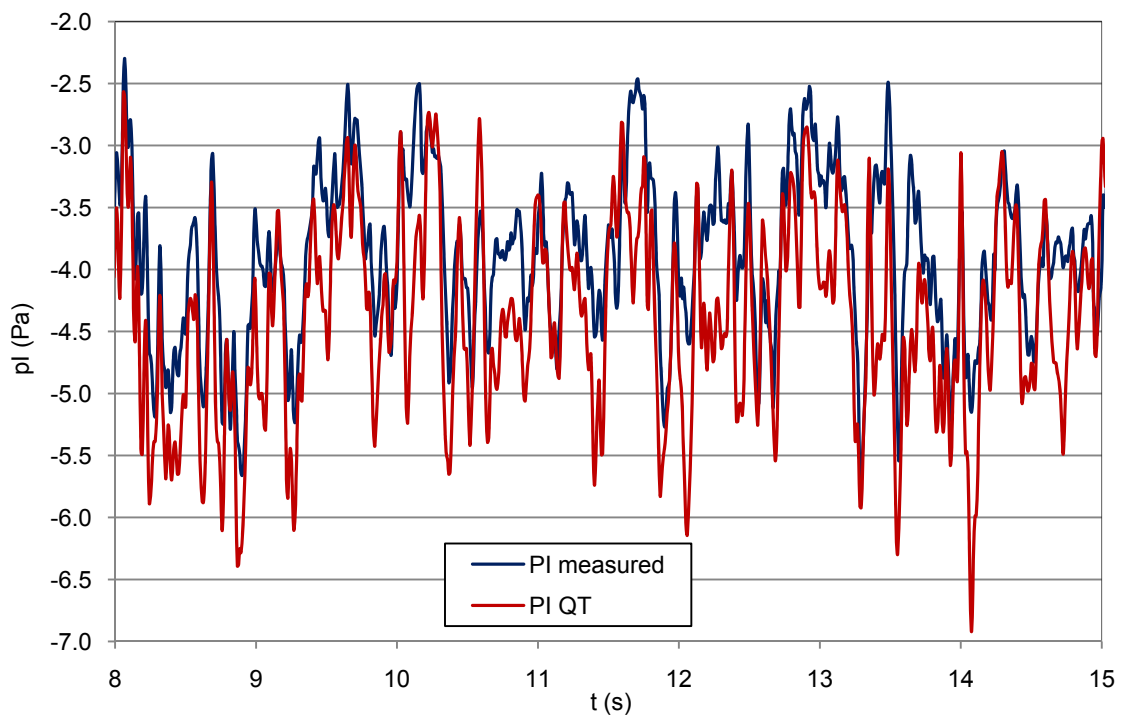


Figure 6.19 Comparison for internal pressure (S1234_O12)

6.4.2 Flow reversal and wind direction

Figure 6.20 and Figure 6.21 show the comparison between QT model and measurements for (S1234_O12) with different wind directions (case 2 in Table 6.2). Again, the QT model accurately predicts the reversal percentage for all four stacks with different wind directions.

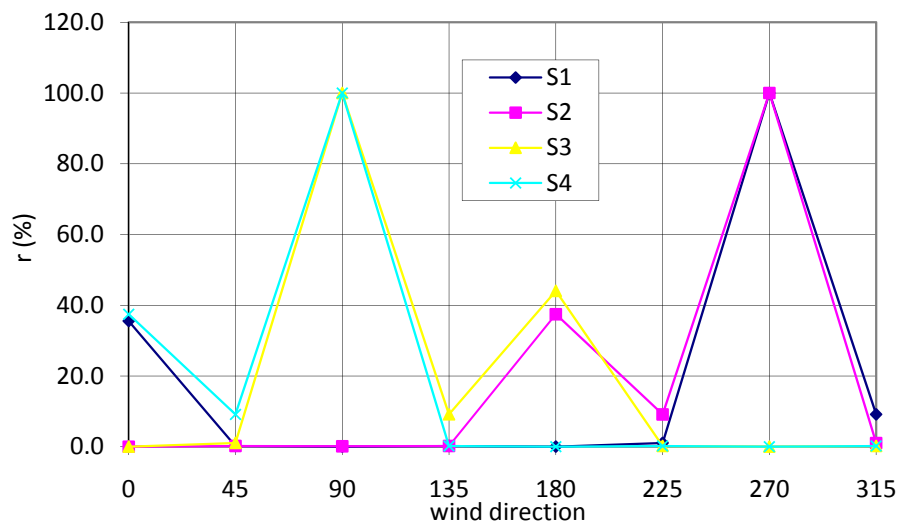


Figure 6.20 Reversal percentage from measurements (S1234_O12)

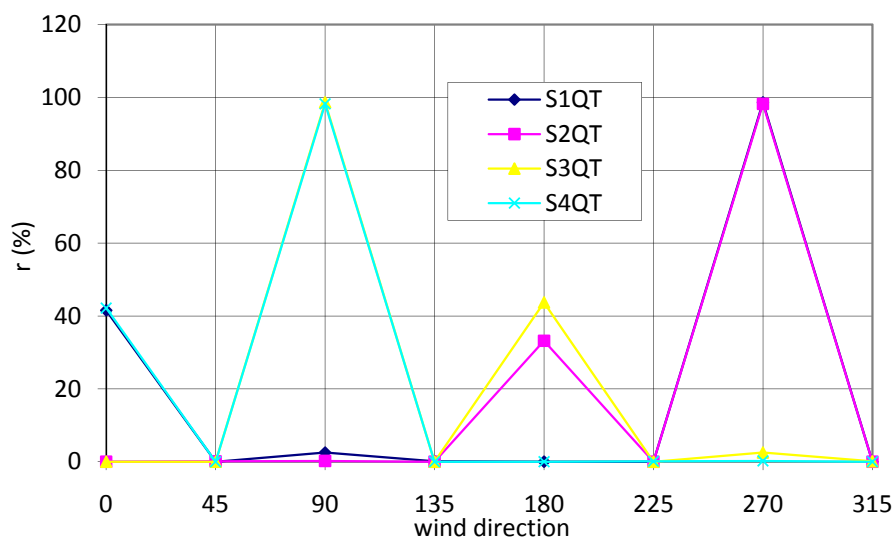


Figure 6.21 Reversal percentage from QT model (S1234_O12)

6.4.3 Flow reversal and Reynolds number

In Section 6.4.2, comparisons were made with different wind direction. In this section, Figure 6.22 shows the comparisons for reversal percentages of stack 1 and 4 of (S1234_O12) with different wind speed (building Reynolds number), which is Case 5 in Table 6.2. The QT results present the correct trend and reversing range, but there are significant differences at the higher wind speeds. The most likely explanation for this is that the values of C_z used in the QT model are not appropriate when the flow is reversing.

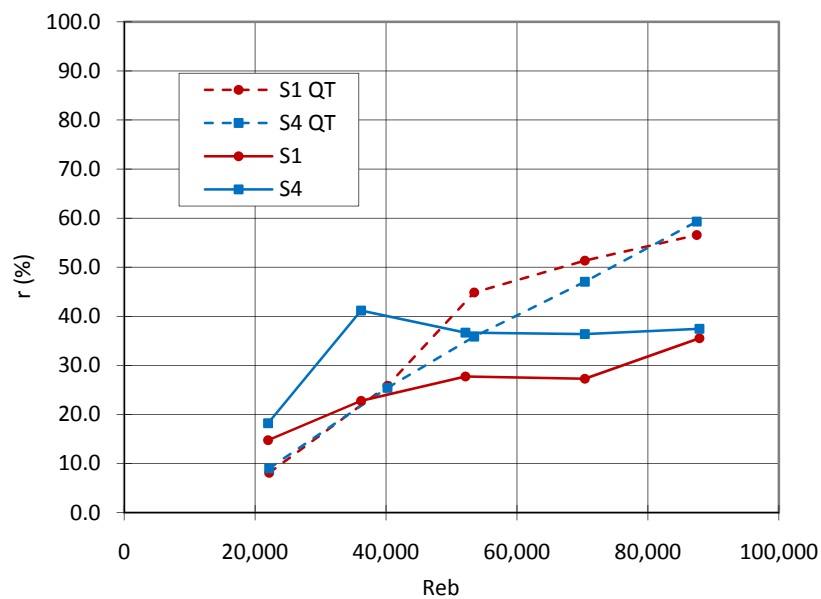


Figure 6.22 Comparison of reversal percentage of scale model (S1234_O12)

For design purposes, the interest lies in using the QT model at full-scale Re_b . Figure 6.23 presents the predicted reversal percentage for a 20 m high full scale building, which is 100 times the model scale. As stated in Chapter 2, different flow equations are used for turbulent flow (full scale), which are equations (2.42) and (2.43). The same orifice discharge coefficients are used for full scale. A range of wind speeds are used, from $U_{ref} = 1.5 \text{ m/s}$ to $U_{ref} = 6.5 \text{ m/s}$, wind direction 0 degree. It shows that there is a higher reversal percentage for the full scale building. Figure 6.24 plots out both model scale and full scale results in logarithmic form, which shows an increasing trend with the increasing Reynolds number.

6 Theoretical calculations and comparisons with measurements

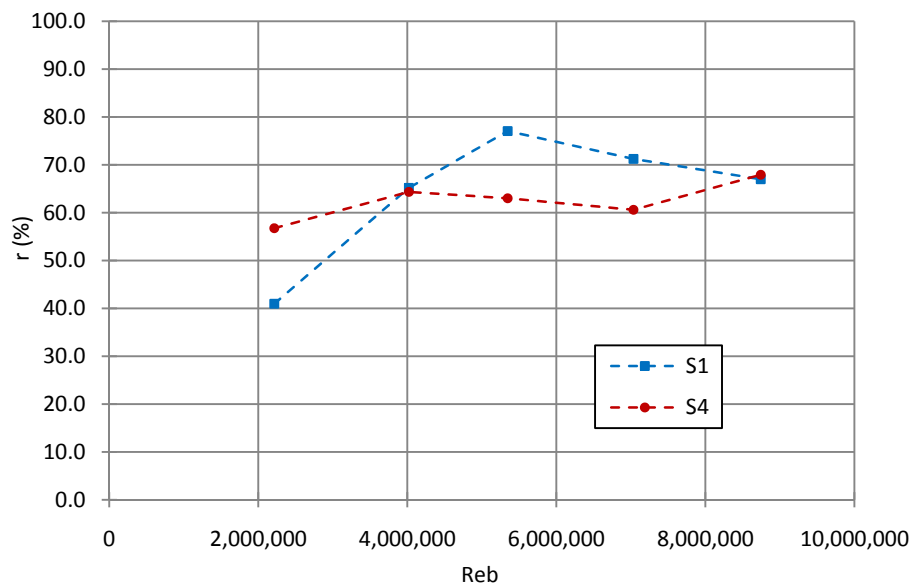


Figure 6.23 Predictions of reversal percentage for full scale cases (1:100)

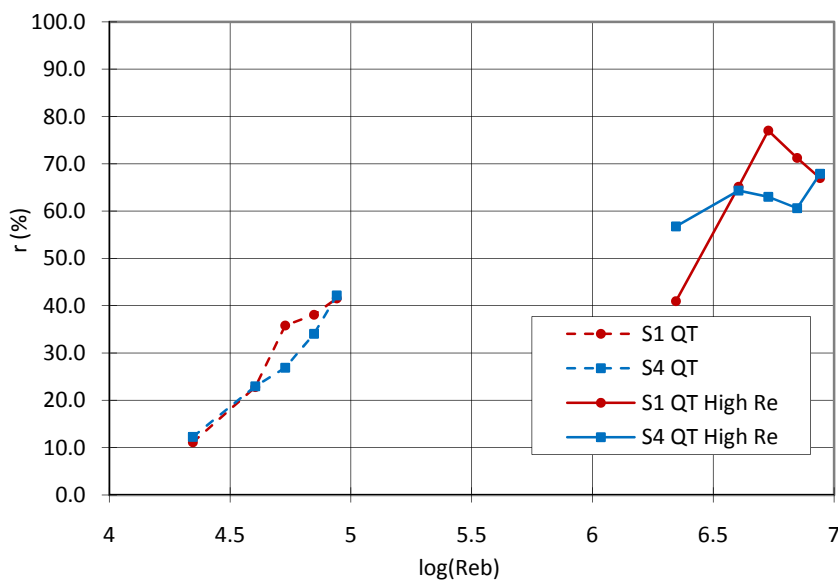


Figure 6.24 Variation of r with $\log(Re_b)$ for model scale and full scale.

Comparison of the values measured at very low Re_b in the wind tunnel (Figure 6.22) with the full-scale values in Figure 6.24, shows that the wind tunnel technique gives a reversal percentage of about 35 % compared to about 65 % for full-scale. Whether this error in the wind tunnel technique is significant for design is open to question.

6.4.4 Reversal and $\Delta C_p / \sigma_{\Delta C_p}$

Figure 6.25 shows the relationship between reversal percentage and pressure parameter $\Delta C_p / \sigma_{\Delta C_p}$ as obtained from the QT model and measurements. Measurement data is from different opening configurations, but with the improved pressure measurements (see Chapter 7, Section 7.4). QT model is used for two types of model configurations. One is for the case of (S1234_O12) with increasing wind speed, in which stacks 1 and 4 have reversing flows. The other is for a 1 stack and 1 orifice model (for the interest of comparing the present QT model results with those obtained by Cooper and Etheridge (2007)). One can see that the results in this figure are consistent with the measured results shown in Figure 3.34. e.g. for $\Delta C_p / \sigma_{\Delta C_p} < -2$, no reversal occurs.

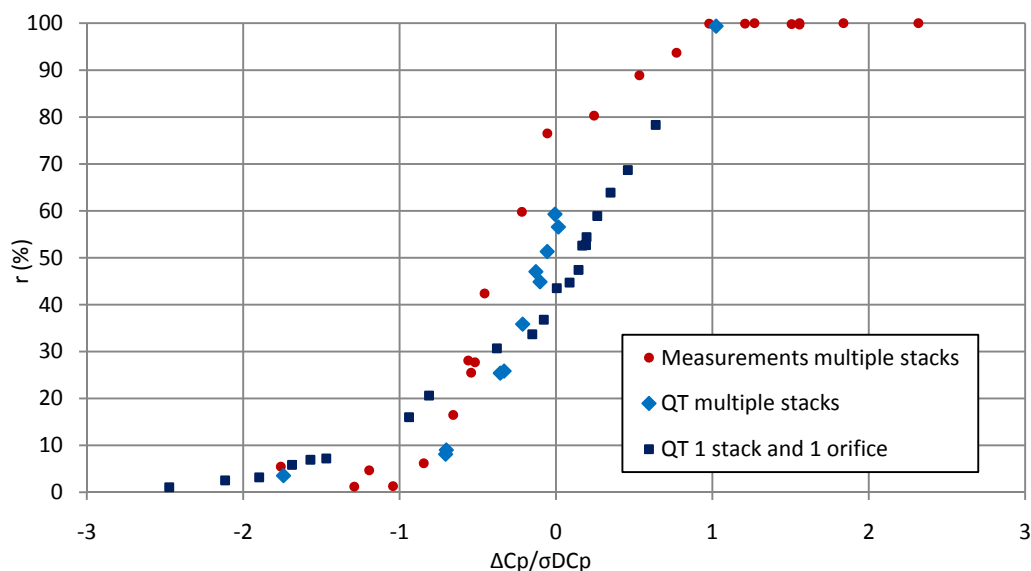


Figure 6.25 Variation of r with $\Delta C_p / \sigma_{\Delta C_p}$ – measurement and QT model

6.5 Wind and Buoyancy combined

6.5.1 Steady model calculations

The steady model can only be used for unidirectional flows (e.g. Figure 6.12 fails to predict the flow directions of stacks 1 and 4), thus two calculations are carried out for buoyancy dominated cases when there is no reversal. One is (S3_O1), the other is (S13_O1234). These

6 Theoretical calculations and comparisons with measurements

two calculations correspond to test 1 ($U_{ref} = 1.2 \text{ m/s}$) and test 3 ($U_{ref} = 0.6 \text{ m/s}$) in Table 6.3. For both opening configurations, the wind speed is fixed; internal temperature was increased till the system turned to buoyancy dominated ventilation. Wind pressures input were taken from the wind alone case before the heater was switched on (When the model is heated, some of the pressure tubing is heated because it lies inside the model. This introduces errors in the pressure measurements). The total driving force includes both buoyancy and wind forces. Since the internal temperature is stratified, yet the buoyancy term in equation (2.33) assumes that the internal temperature is uniform; there are assumptions made for this term, which will be explained in the next section for the QT model. As shown in Figure 6.26, the results of steady model are not entirely accurate, yet still show reasonable agreement with the measurements. It should be noted that the flow rate of orifice 1 (marked with dashed line circle) was not measured (because there were no direct measurements of flow rates through orifices). It was obtained from mass conservation (same magnitude of the flow rate through stack 3, but opposite sign).

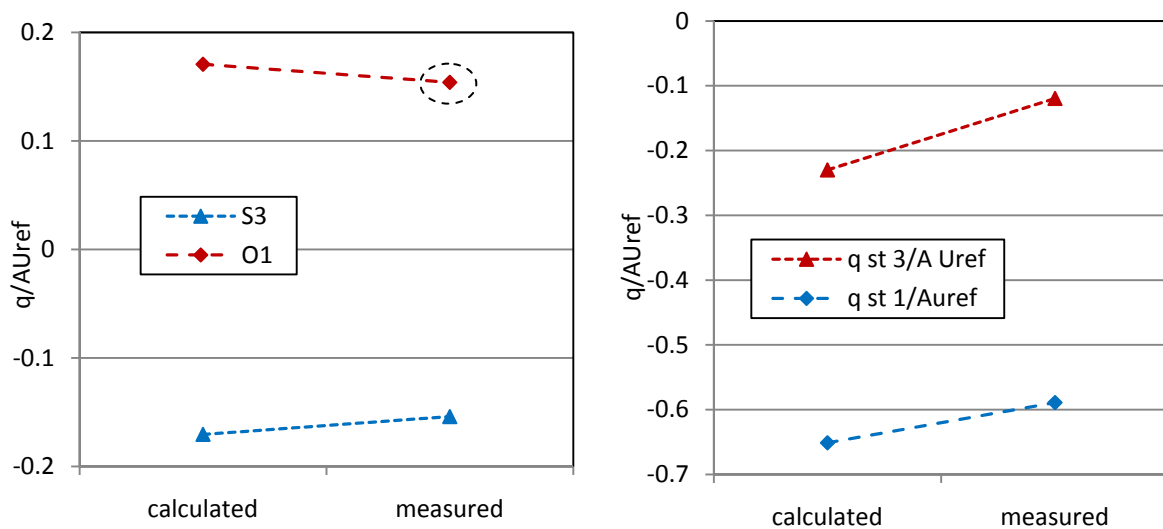


Figure 6.26 Comparison of flow rate between steady envelope model and measurements for two opening configurations (S3_O1), (S13_O1234)

6.5.2 QT model calculations

6.5.2.1 Buoyancy term assumptions

As shown in Figure 6.27, the averaged temperature of the two internal layers $\frac{T_1+T_2}{2}$ is used to represent the mean ‘uniform’ model temperature to calculate the temperature difference between the internal and outside ($dT = \frac{T_1+T_2}{2} - T_{room}$). For the term h there are three possibilities.

- 1) When flow through the stack is outward, h_1 is adopted
- 2) When flow through the stack is inward, h_3 is adopted
- 3) When flow through the stack is fluctuating, h_2 is calculated based on the reversal percentage r . $h_2 = H - \frac{L}{2} + L(1 - r)$

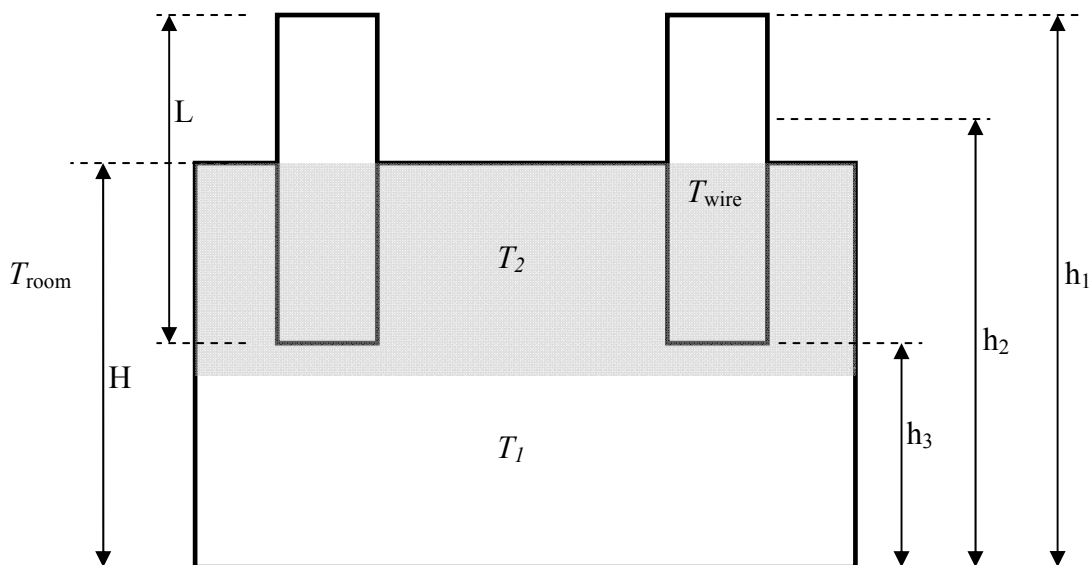


Figure 6.27 Assumptions about buoyancy term

6.5.2.2 Comparison of instantaneous values between the QT model and measurements

The QT model was used to calculate two opening configurations: (S3_O1) and (S13_O1234). Figure 6.28 shows the flow rate of the wind alone case (S3_O1). Figure 6.29 shows another comparison for when the flow through stack 3 is fluctuating ($r = 66.5\%$). The comparison of instantaneous internal pressure between QT model and measurements is shown in Figure 6.30, which is the same case as in Figure 6.29. Better agreement is observed in the wind alone case. For the wind and buoyancy combined case, the mean values seem to match, yet not the instantaneous values. This is not surprising simply because the pressure input is taken from the wind alone measurement. Although they satisfy the mean value of the wind and buoyancy combined case (since the wind speed was fixed), one can obviously not expect good agreement for instantaneous values. The other reason is that there are assumptions made for the buoyancy term, i.e. not taking into account the effects of stratification and temperature fluctuations. One can see the effect of using the wind pressure of the wind alone case as an input for the wind and buoyancy combined case: in Figure 6.29, the fluctuations of the calculated flow rate has the same shape as in Figure 6.28, but the magnitude is shifted. In addition, as shown in Figure 6.30, the calculated internal pressure of the wind alone case shows a reliable match with the measurements.

6 Theoretical calculations and comparisons with measurements

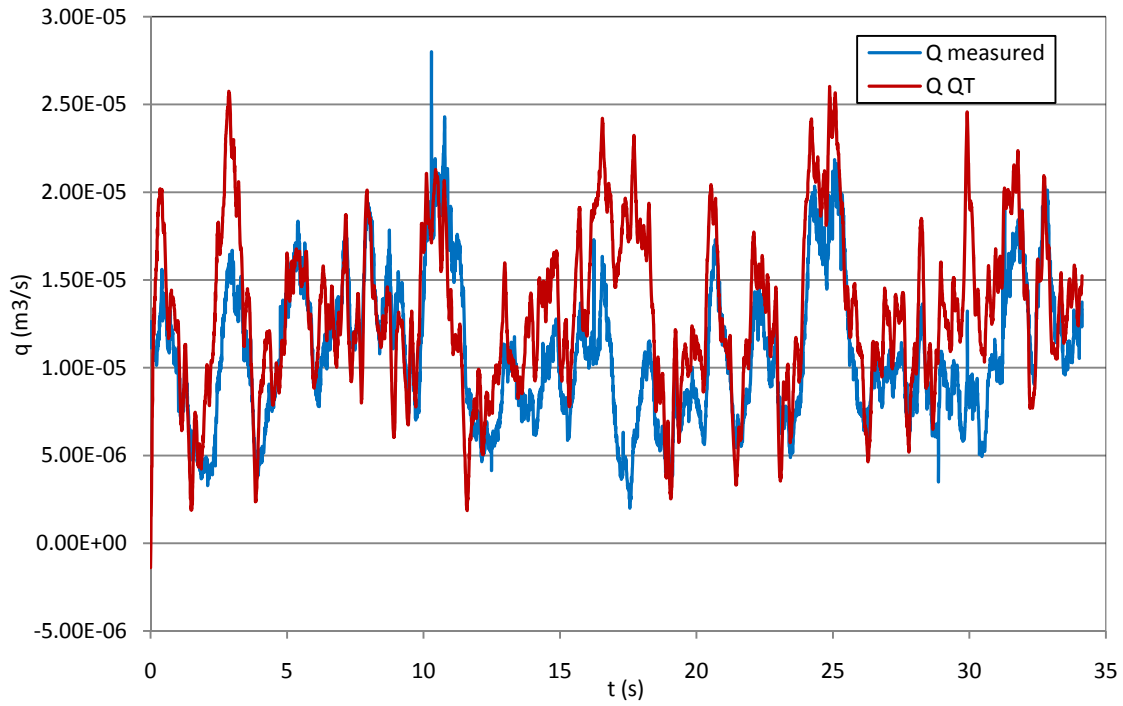


Figure 6.28 Comparison of instantaneous flow rate of wind alone case (S3_O1)

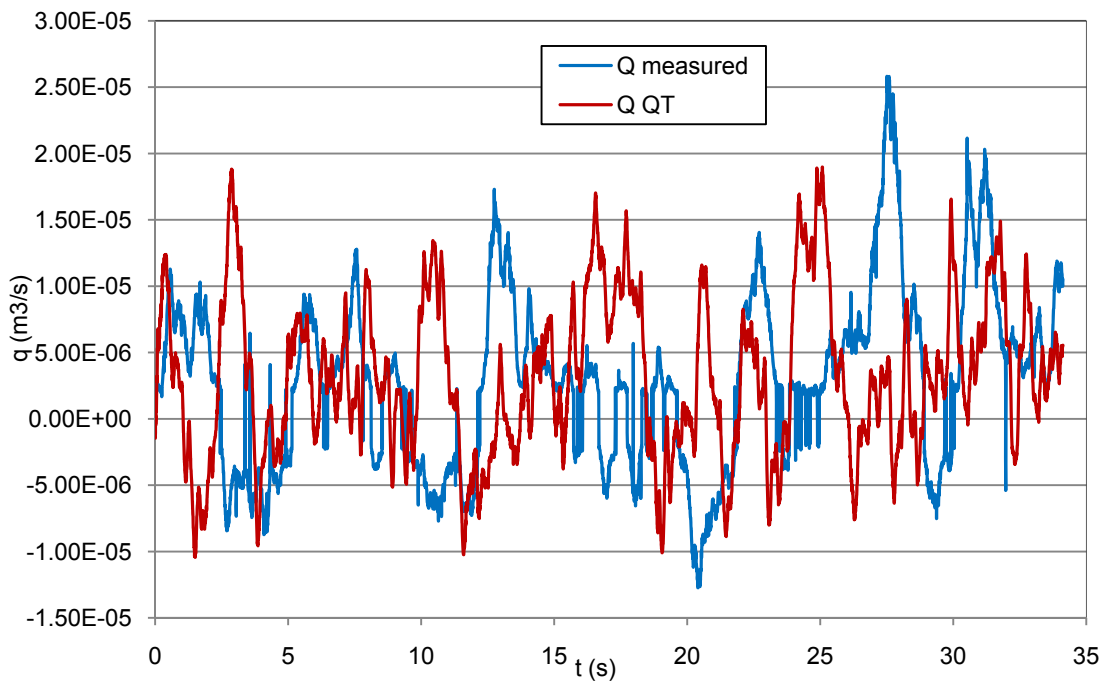


Figure 6.29 Comparison of instantaneous flow rate of wind and buoyancy combined case (S3_O1)

6 Theoretical calculations and comparisons with measurements

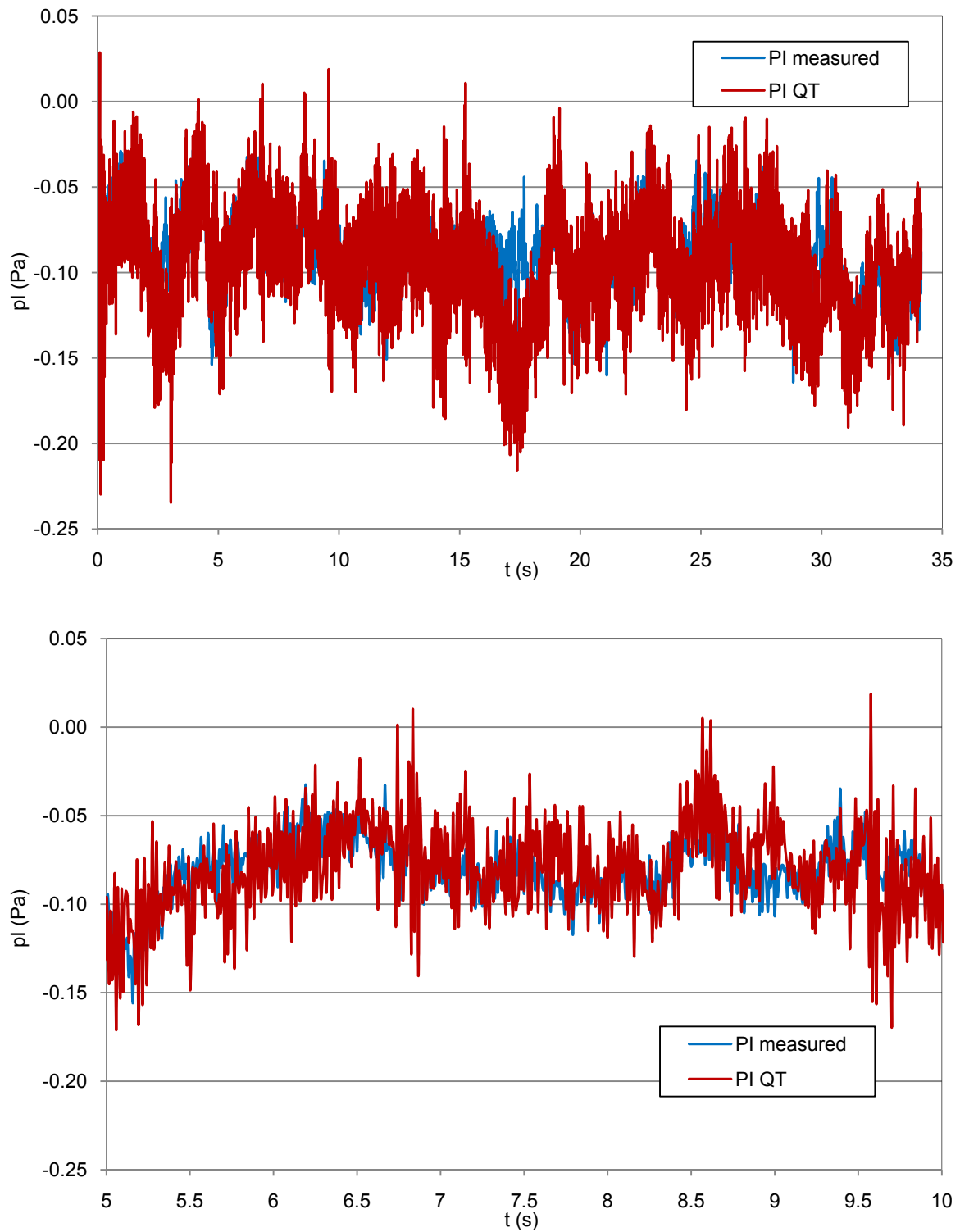


Figure 6.30 Comparison of instantaneous internal pressure (S3_O1); Second graph x axis expanded

6 Theoretical calculations and comparisons with measurements

Figure 6.31 and Figure 6.32 present the comparisons between the QT model and measurements of instantaneous flow rates through stacks 1 and 3, and the instantaneous internal pressure for the case of (S13_O1234). Measured P1 and P3 are also shown in Figure 6.32 for comparison. Again the case of fluctuating flow through stack 3 is chosen ($r_3 = 58\%$) (wind and buoyancy combined case). One can see that the QT model does not perform as well as that for the above case of one stack and one orifice, i.e. the calculated flow rate (magnitude) of stack 1 is smaller than the measurement. Similar as wind alone cases, the accuracy decreases with the increasing number of sharp-edged orifices. However, the match of the mean flow rate of stack 3 which is the fluctuating one is not bad. This may be an indication that QT model is reliable in terms of predicting flow reversals.

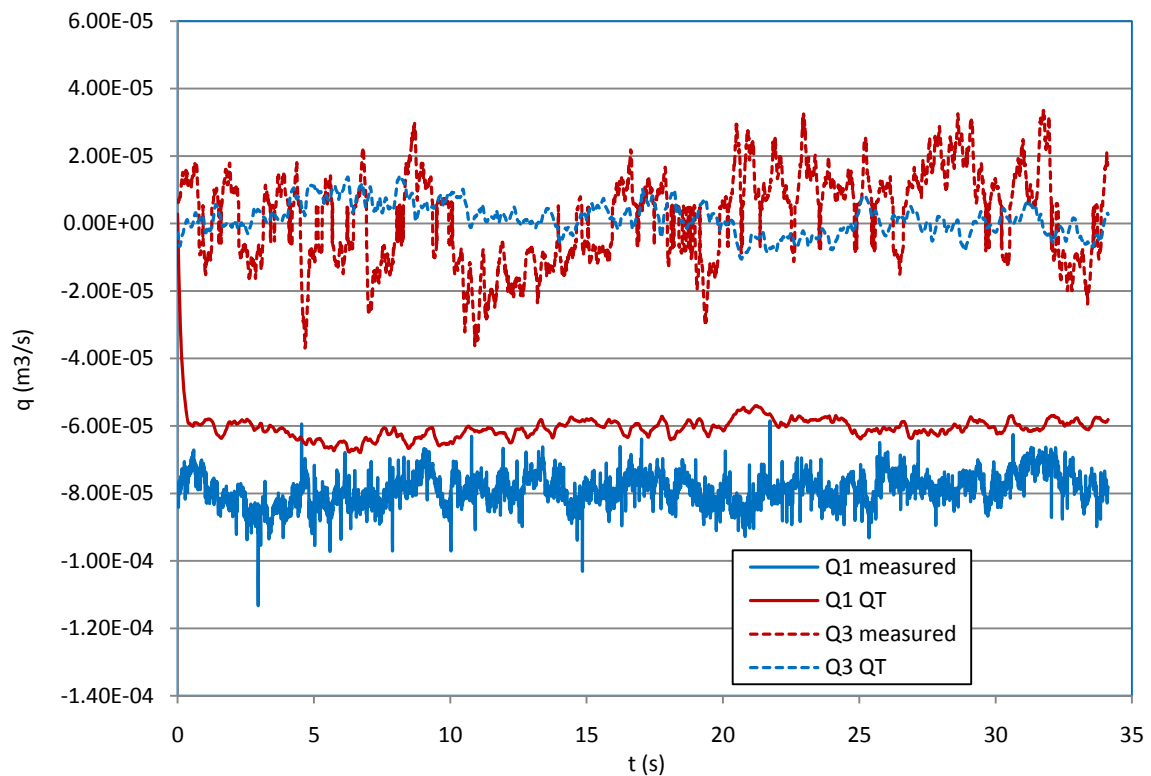


Figure 6.31 Comparison of instantaneous flow rates (Stack 1,3; Orifice 1,2,3,4)

6 Theoretical calculations and comparisons with measurements

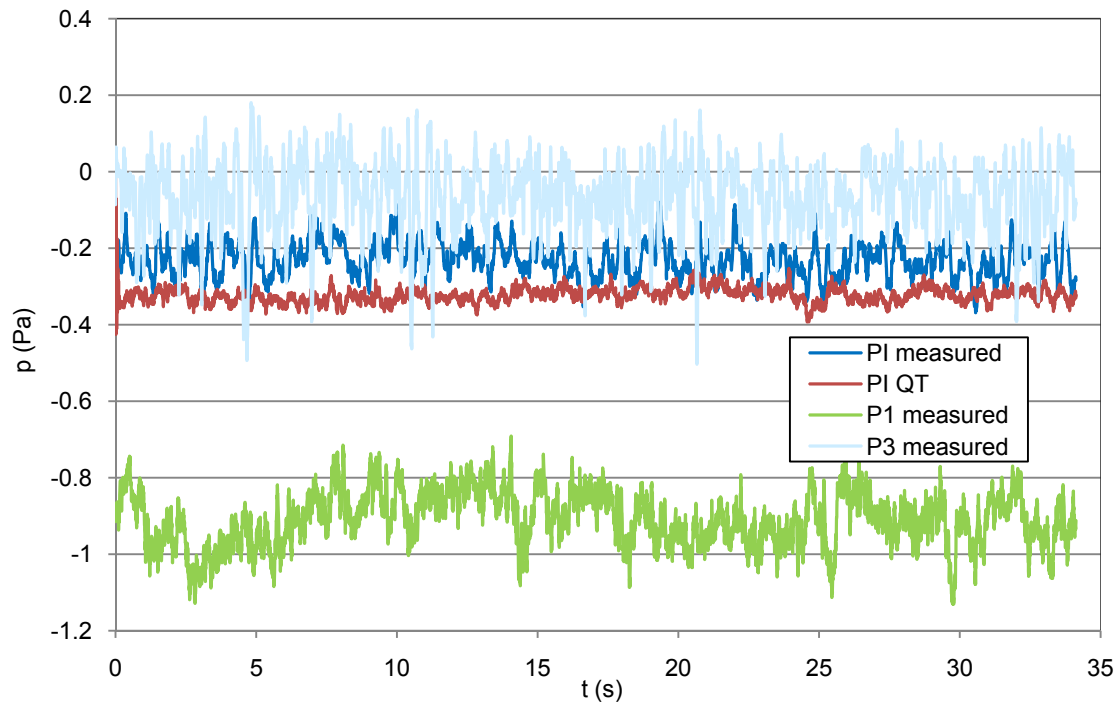


Figure 6.32 Comparison of instantaneous internal pressure (S13_O1234), measurements of P_1 and P_3 are presented as reference.

6.5.2.3 Comparison of reversal percentage between QT model and measurements

Figure 6.33 shows the comparison for the case of one stack and one orifice. The wind speed was fixed; the reversal percentage of stack 3 decreases with the increasing buoyancy force till the system becomes buoyancy dominated ventilation. Figure 6.34 shows the comparison for the case of two stacks and four orifices. Measurements are taken from the internal temperature decreasing period when fewer uncertainties occur. Seen from the good agreement between the measurements and QT model, the later is proved to be a useful tool to predict flow directions. However, during the calculation process, it was found that the results are very sensitive to the chosen h_2 values in Figure 6.27. It means one can trust QT model to detect the flow direction, but not the exact value reversal percentage. This may not be a crucial defect of QT model, since the flow direction is of most interest in terms of natural ventilation design.

6 Theoretical calculations and comparisons with measurements

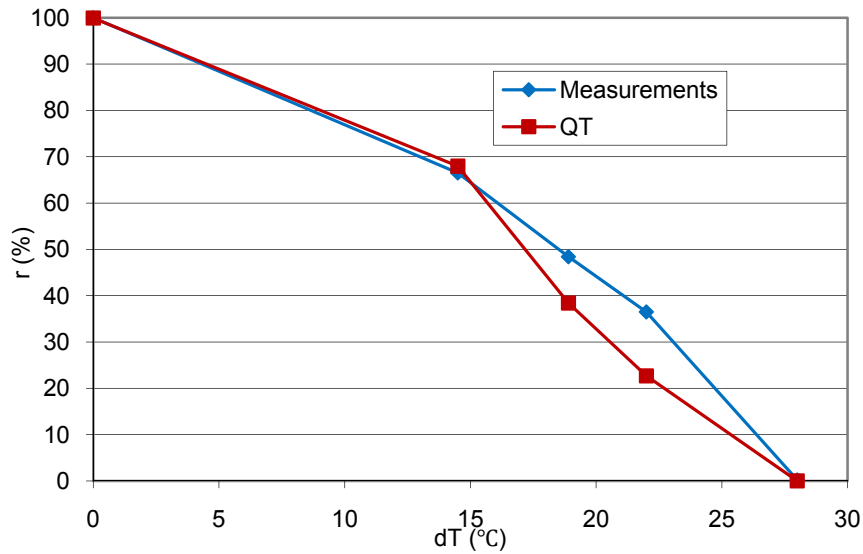


Figure 6.33 Comparison of reversal percentage of stack 3 as a function of dT (S3_O1)

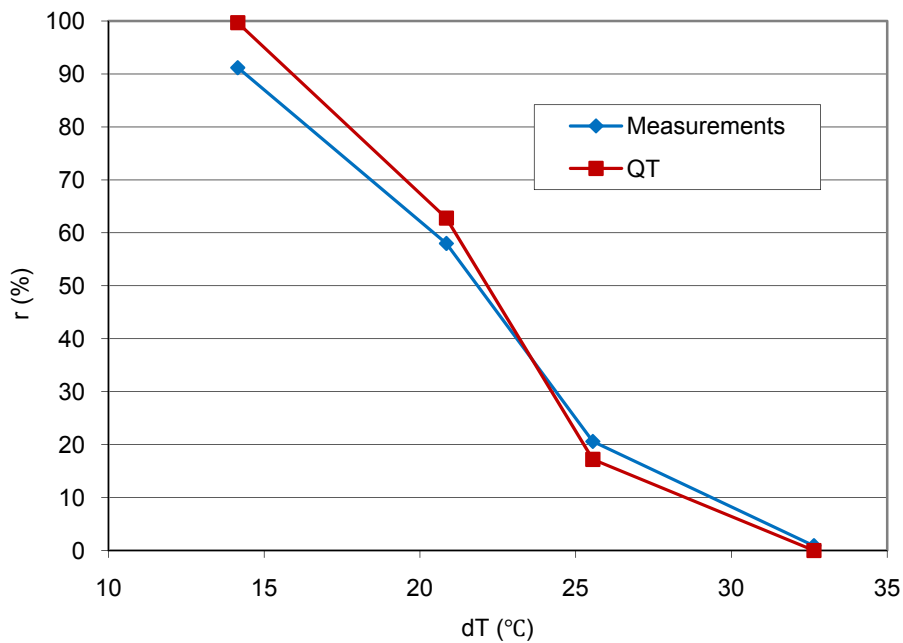


Figure 6.34 Comparison of reversal percentage of stack 3 (Stack 1,3; Orifice 1,2,3,4)

6.6 Summary and conclusions

In this chapter, three methods are used to obtain flow patterns. The first one aims at predicting flow directions by the pressure difference across an opening either using estimated

6 Theoretical calculations and comparisons with measurements

mean internal pressure or using measured mean internal pressure. They both correctly predict the flow directions for the case when there is no orifice. Errors occur with the increasing number of orifices. Using the measured internal pressure performs better than the other. Due to the accuracy of this method, it is of limited practical use.

The second and third methods are the steady and unsteady envelope flow models. The QT model gives promising agreement with the measurements, yet it is discovered that this theoretical model is also sensitive to the chosen C_z values, which is similar to that for steady flow model. The steady model performs equally well with QT model for mean values of unidirectional flows. The advantage of QT model is that it can be used for reversal flow; and predict flow reversal percentage for full scale buildings. This indicates that the inertia of air mass in the opening and the compressibility of the air in the envelope flow model are less important for unidirectional flow; yet have to be considered for fluctuating flows.

In terms of design guidance, to get reliable predictions, three important data sources are needed: instantaneous pressures, precise C_z values, and correct estimation of the height term in buoyancy force. Thereby it may be difficult to totally rely on theoretical calculations for design purposes. Wind tunnel testing or computer simulation should still play important roles.

7 Improvements in experimental techniques

7.1 Introduction

This is a relatively independent chapter. It presents some of the developments and investigations of the experimental techniques. Individual sections are also independent. Section 7.2 describes the checking of the consistency of simultaneous pressure and velocity measurements, in relation to the effect of the stiffness of the model box. Section 7.3 describes the improved unsteady calibration method. In section 7.4, a hot-film probe is tested for measurement of bi-directional flow through the stack, including comparisons with the dual hot-wire probe. Section 7.5 describes the investigation to improve pressure measurements.

7.2 Comparison of instantaneous pressure and hot-wire measurements

In Chapter 3, Section 3.4.1, the mean flow balance was checked with the two-stack model. Ideally the volume reversal percentage r_v of the two stacks should sum up to zero over a period of time. It was discovered that the sum is less than 100 % for most cases, especially when the individual r is around 50%, the sum is about 90%. After fixing a rod within the model to keep the walls stiff and the volume fixed, the error was reduced from 10% to 3%. In order to prove the effect of the stiffness of the model, and to check the consistency of simultaneous pressure and velocity measurements, instantaneous measurements are compared here.

As illustrated in Chapter 2, in the QT model, the continuity equation for the case of two openings is

7 Improvements in experimental techniques

$$\frac{V}{\gamma} \frac{1}{\bar{P}_I} \frac{dP_I}{dt} = q_1(t) + q_2(t) \quad (7.1)$$

where γ is the ratio of specific heat, $\gamma = 1.4$

\bar{P}_I is the time averaged internal pressure

V is the volume of the box

From the measured results of instantaneous internal pressure, the left side of equation (7.1) can be calculated. From the measured results of instantaneous velocities of the two stacks, the right side of equation (7.1) can be calculated. One example of the results for the case $U_{ref} = 2.74 \text{ m/s}$, $\phi = 90^\circ$, block distance $S=140 \text{ mm}$ is shown in Figure 7.1. The whole test period is 34 seconds, but results of the first two seconds are shown in Figure 7.1

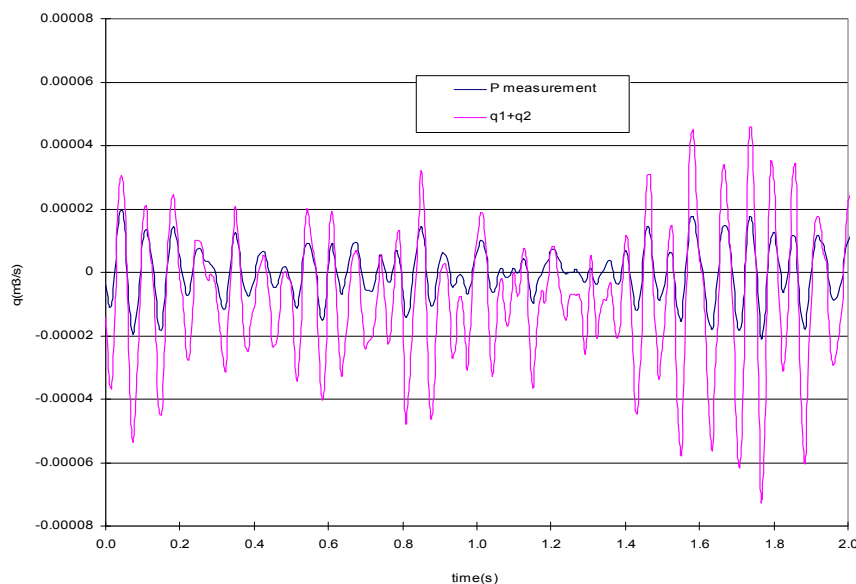


Figure 7.1 Comparison of pressure and velocity measurement

The two independent measurements agree qualitatively. There is encouraging agreement in the shapes of the two curves with the same trend of fluctuation. However, the curve calculated from the internal pressure measurement, which is $\frac{V}{\gamma} \frac{1}{\bar{P}_I} \frac{dP_I}{dt}$ shows a damping and a slight time lag behind the curve $q_1(t) + q_2(t)$. That could be because the response of the pressure transducer is slower than the hot-wire. In this case, the time reversal percentages of the two stacks are 82.2 % and 20.6 %, the volume reversal percentages of the two stacks are

7 Improvements in experimental techniques

90.0 % and 8.1 %. The maximum sum flow rate during the test period of 34 seconds of the two stacks is less than $1.0 \times 10^{-4} \text{ m}^3/\text{s}$, comparing with the volume of the box 0.025 m^3 . That means the change in air density is less than 1 %. Thereby, it might be possible to consider the air incompressible for ventilation purposes at low wind speed.

7.2.1 Effect of fixing the rod

The volume changes of the box due to vibrations of the envelope and the stacks could have a big effect on the results. When intermittent flow reversal occurs in the stack, the magnitude of the mean velocity can be very low, which could possibly make the influence of the vibration of the box and the stack more severe on the testing results. To detect the possible vibration source of the model box before putting in the rod, three parts of the model were gently tapped during the zero run (zero flow velocity). The three parts in turn are the surface of the rectangular stack, the outer surface of the wall, and the surface of the circular stack. Results are shown in Figure 7.2.

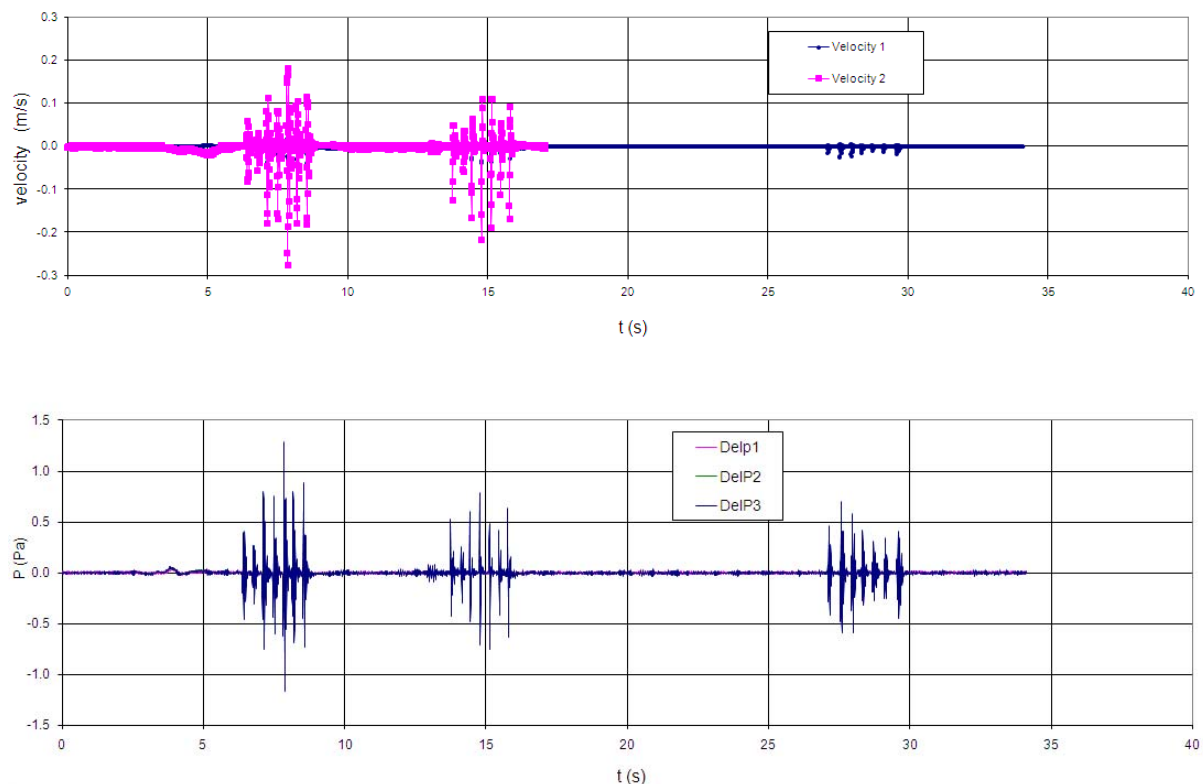
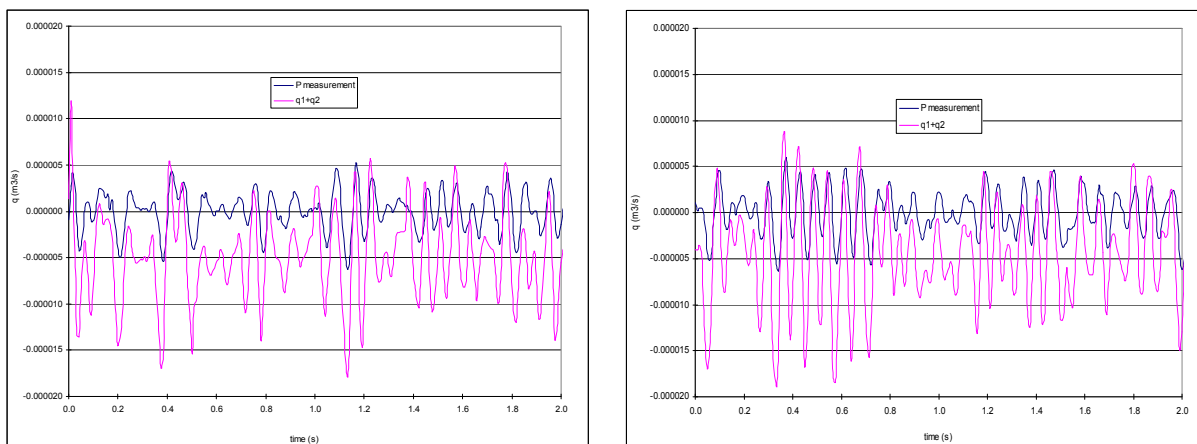


Figure 7.2 Velocity and pressure signals from tapping different parts of the model

7 Improvements in experimental techniques

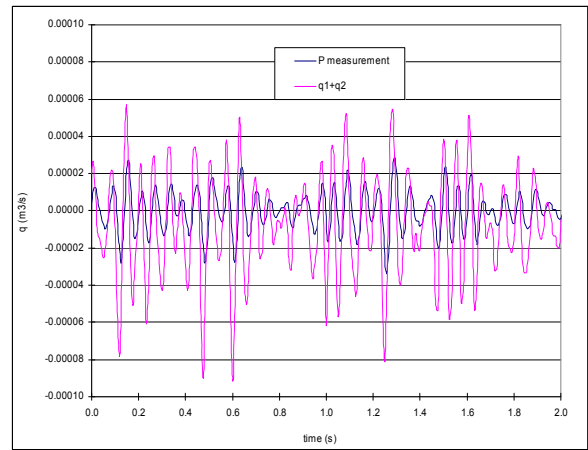
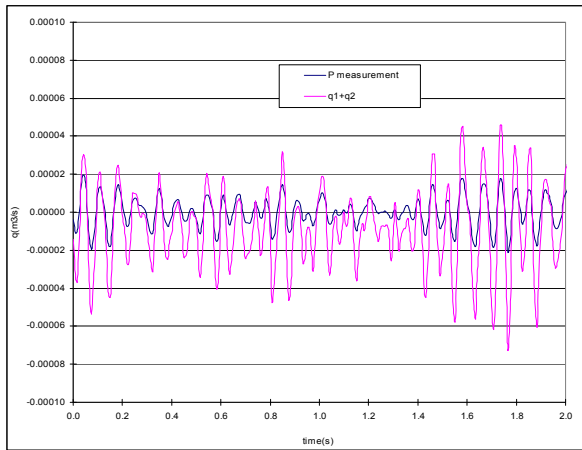
It can be seen that the velocity result is more sensitive to the tapping on the box and the rectangular stack. Therefore, a metal rod was fixed between the two parallel walls inside the box (figure 3.20) to keep the volume of the box relatively more constant, and the rectangular stack was screwed to the box more rigidly.

Figure 7.3 shows the comparisons of pressure measurement ($\frac{V}{\gamma} \frac{1}{P_I} \frac{dP_I}{dt}$) and velocity measurement ($q_1(t) + q_2(t)$) before and after the rod was fixed in the model. With the rod and the rectangular stack fixed, the value of $q_1(t) + q_2(t)$ has been effectively shifted closer to the value of $\frac{V}{\gamma} \frac{1}{P_I} \frac{dP_I}{dt}$, especially for the cases of $\phi=90$, and a low $U_{ref} = 1.35 \text{ m/s}$, in which the wall of the box is perpendicular to the wind.

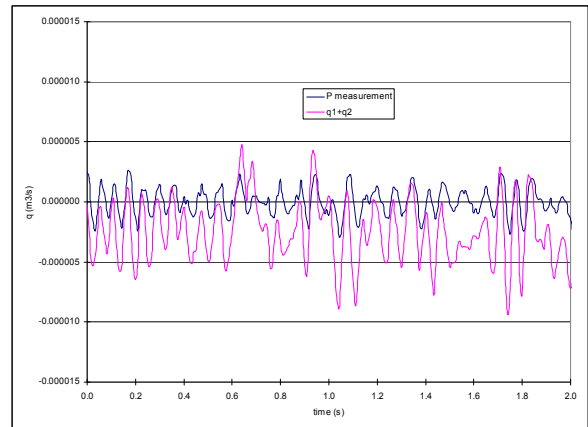
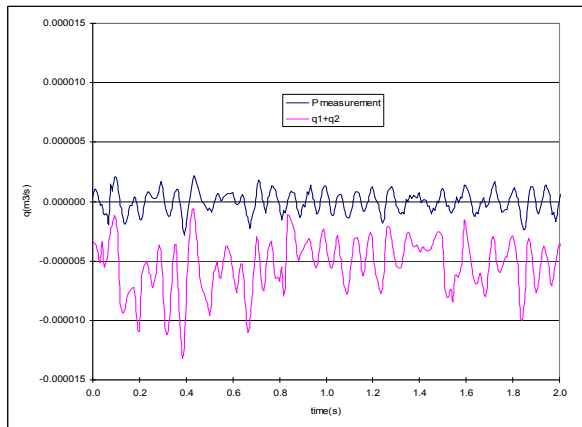


$$\phi=45, U_{ref} = 1.35 \text{ m/s}, S=140 \text{ mm}$$

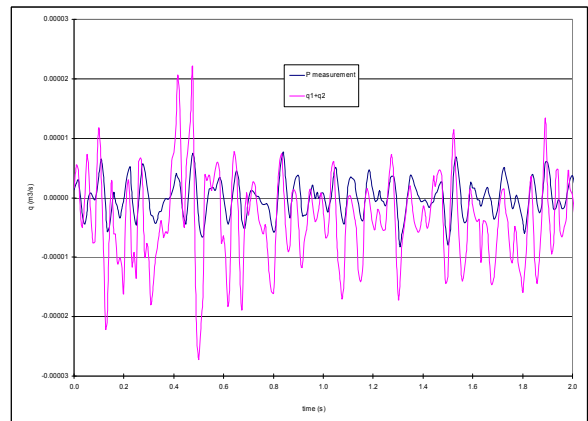
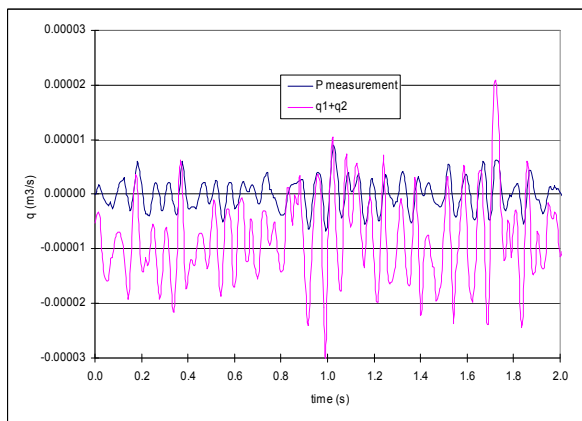
7 Improvements in experimental techniques



$\phi=45, U_{ref} = 2.74 \text{ m/s}, S=140 \text{ mm}$



$\phi=90, U_{ref} = 1.35 \text{ m/s}, S=210 \text{ mm}$



$\phi=90, U_{ref} = 2.74 \text{ m/s}, S=230 \text{ mm}$

Figure 7.3 Comparison of pressure measurement and velocity measurements (graphs in the right column are with the rod fixed)

7 Improvements in experimental techniques

The results obtained from two independent measurements agree better after the rod is fixed in. This is a proof of the importance of the stiffness of the model; and a demonstration of the consistency of the simultaneous pressure and velocity measurements.

7.3 Precise unsteady calibration of hot-wire

Conventional calibration may be performed in a precision calibrator or in a wind-tunnel, with a pitot-static tube as the velocity reference (Jorgensen, 2002). However, the most satisfactory arrangement is to calibrate *in-situ* (Bruun, 1995, pp. 93-94). This is particularly true for the current application, where the interest lies in volume flow rate rather than the local velocity. It is recognized that the relation between the local velocity and the volume flow rate will depend on the instantaneous velocity profile in the venturi, due to unsteady effects, and for this reason each wire has been calibrated with steady and unsteady flow. Both the steady and unsteady calibrations are carried out *in-situ*, using different devices: a small fan with a gas flow meter for measuring the flow rate for steady calibration; a specially designed piston calibrator. With the original piston calibrator, the rotational speed was assumed to be constant and the frequency was determined by measuring the time for one complete cycle. There was some evidence that the assumption of constant rotational speed was introducing avoidable errors into the calibration. Thus an improved version of the calibrator was developed, to measure the instantaneous rotational speed of the motor.

For this purpose a disc was attached to the drive shaft. The disc contained one hundred laser-cut slots, through which an LED generating a constant voltage pulse each time the slot passes by (Figure 7.4). In terms of data acquisition, the sampling frequency is set high enough (5000 Hz) to detect the voltage change of the sensor (Figure 7.6). Thereby, one can acquire 100 instantaneous rotational speeds of the stroke, providing the genuine flow rate of the piston, which is used to calculate the air velocity of the venturi area of the stack where the hot-wire is mounted. What is more, a powerful motor is used to generate a broad range of frequencies of the stroke, so the velocity range of unsteady calibration could be enlarged to merge with the steady calibration.

7 Improvements in experimental techniques

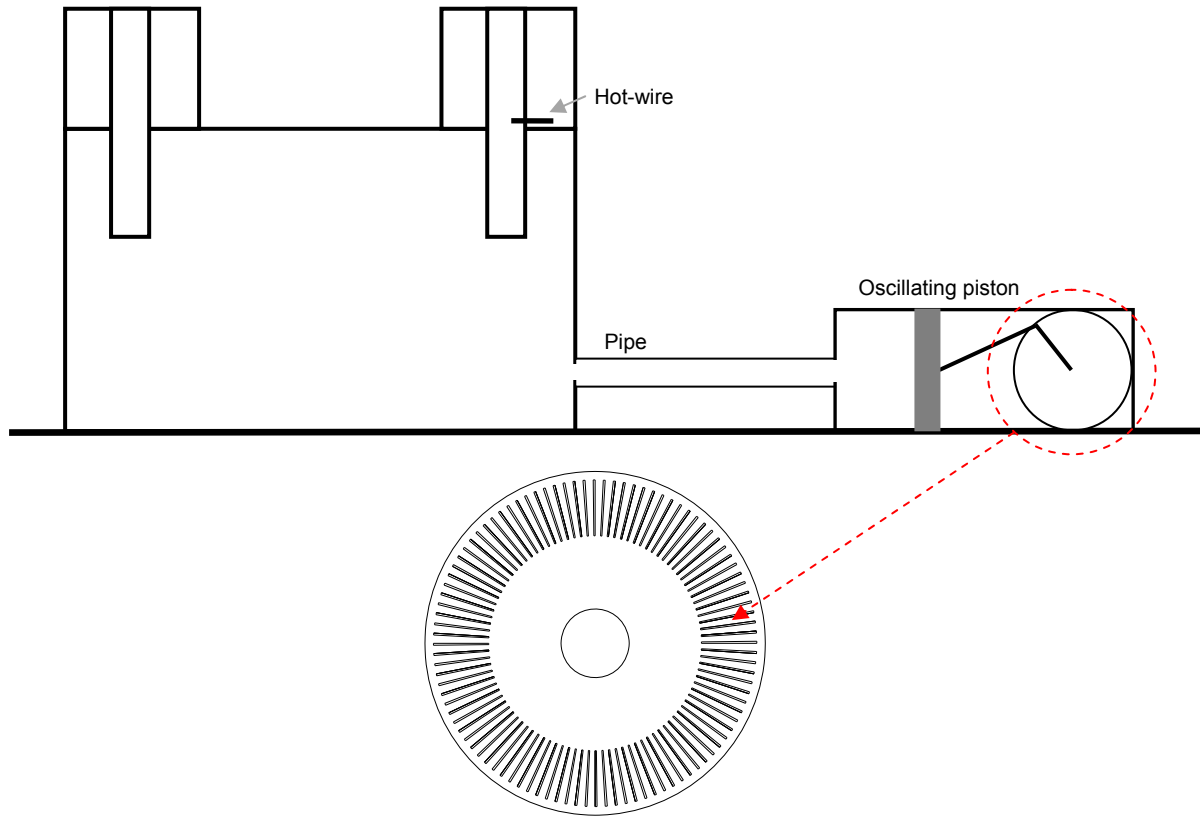


Figure 7.4 New sensor for unsteady calibration

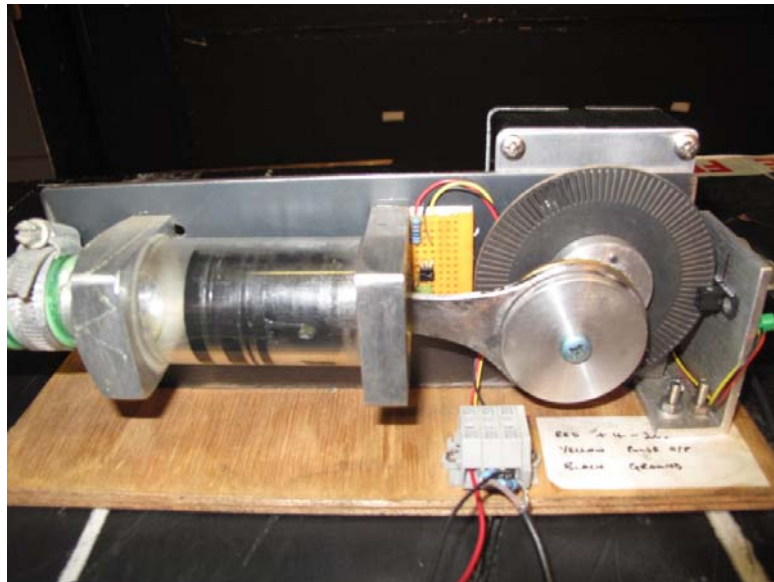


Figure 7.5 Photo of the piston with the new sensor

7 Improvements in experimental techniques

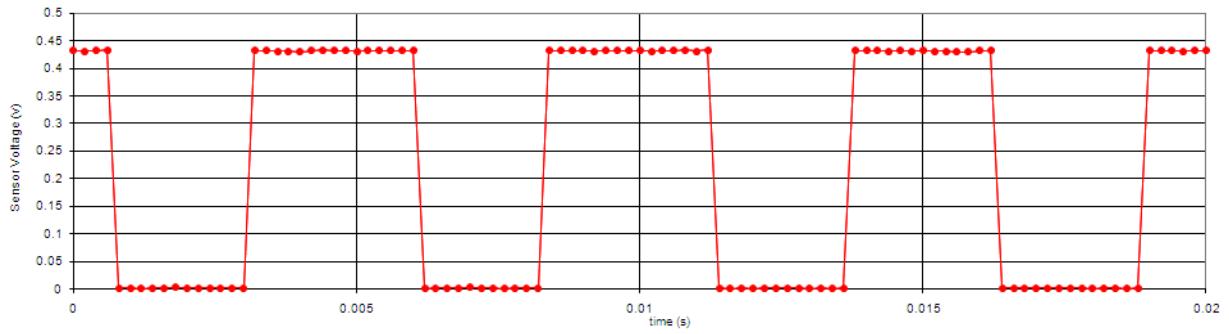
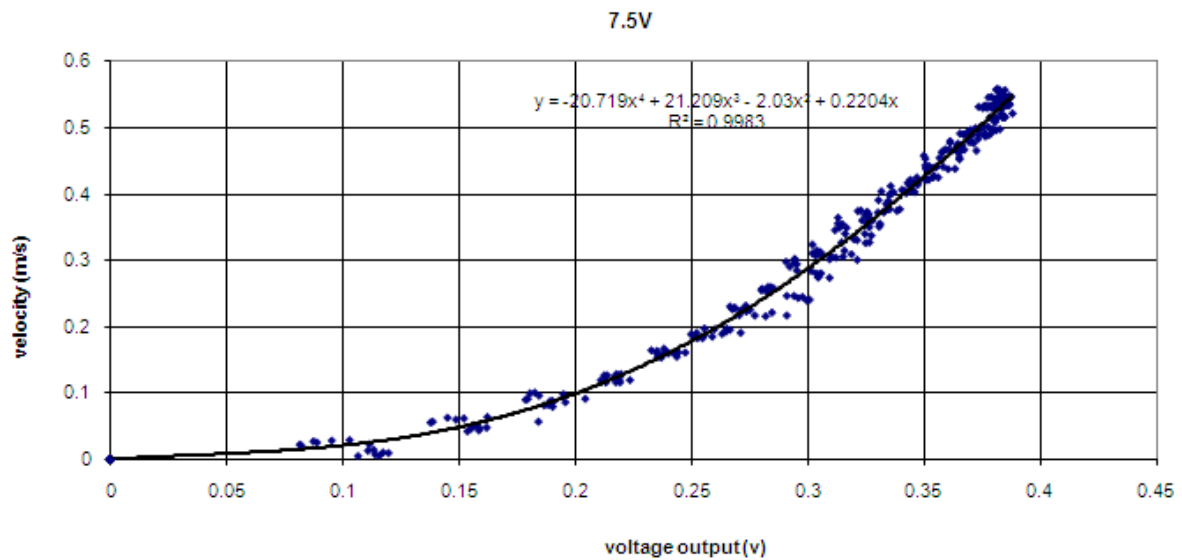


Figure 7.6 Signal from the sensor over a period of 0.02 s

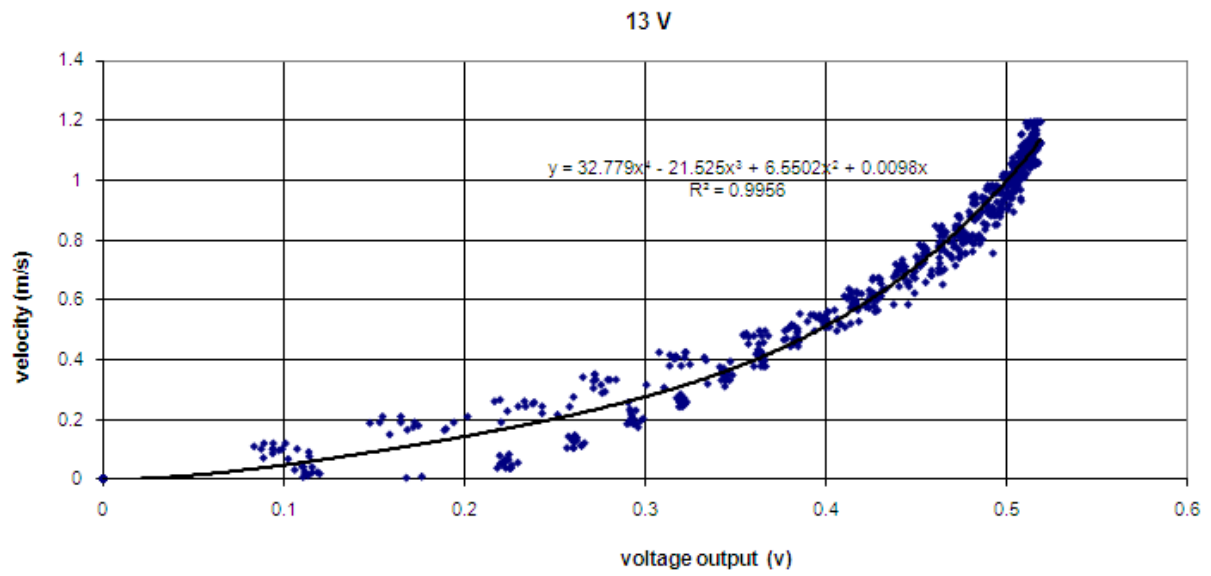
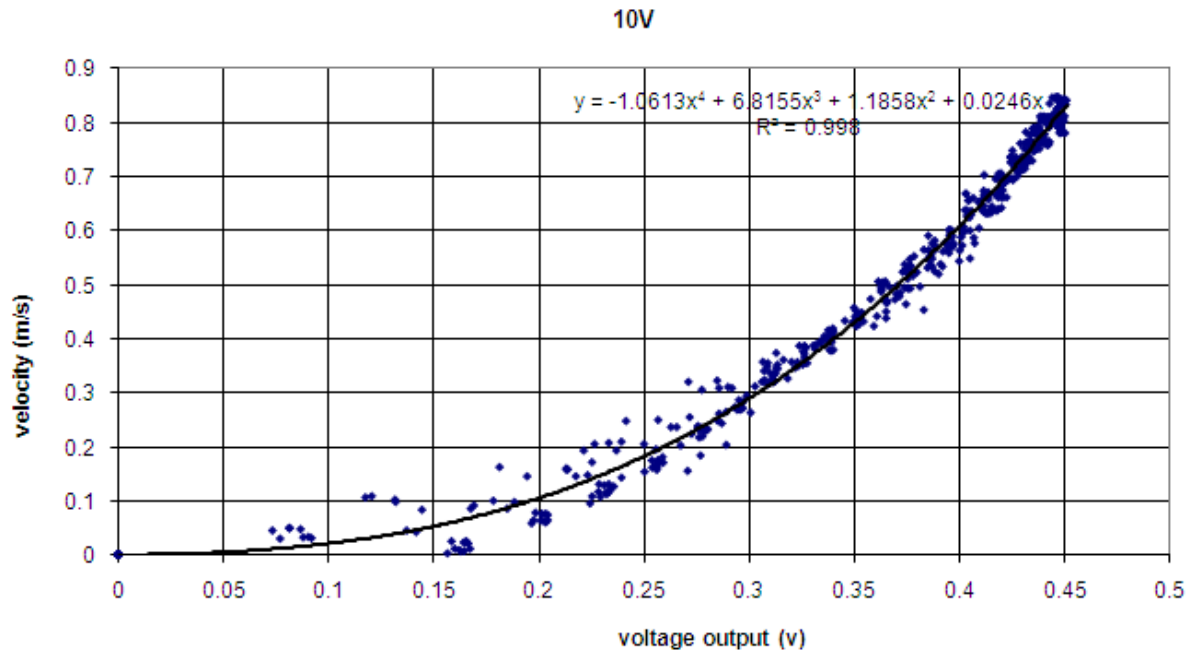
Table 7.1 shows the frequencies and corresponding maximum velocities obtained with the improved calibrator.

Table 7.1 Oscillation frequency and maximum velocity of unsteady calibration

Oscillation frequency (Hz)	1.39	2.11	2.95	4.86
Maximum velocity (m/s)	+/- 0.55	+/- 0.85	+/- 1.2	+/- 2.0



7 Improvements in experimental techniques



7 Improvements in experimental techniques

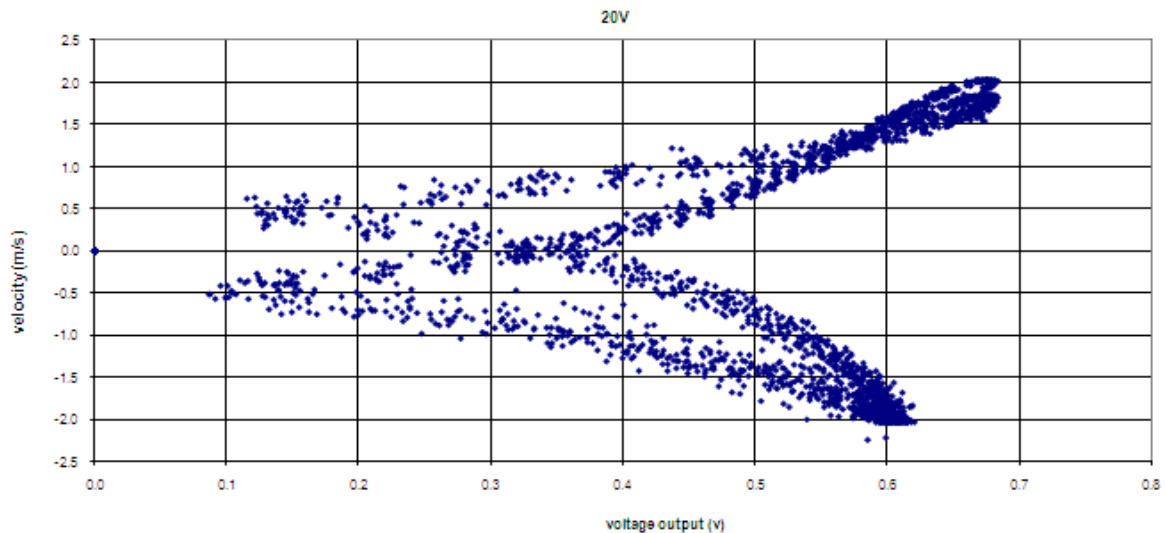


Figure 7.7 Curve fittings of four different oscillating frequencies of the piston

Figure 7.7 shows the calibration curves obtained for one wire at the four frequencies. It can be seen that the calibration deteriorates as the frequency is increased. As noted in (Haddad et al. (2010), this is believed to be due to the change in shape of the velocity profile associated with the pulsating flow. Different calibrations occur for the acceleration and deceleration phases. Near-wall flow reversal occurs with the increasing pulsating frequency. In this thesis, the highest velocity encountered is less than 2 m/s, the stack Reynolds number is 2200, which is laminar flow, thereby similar phenomena can occur with a high oscillating frequency of the piston.

7 Improvements in experimental techniques

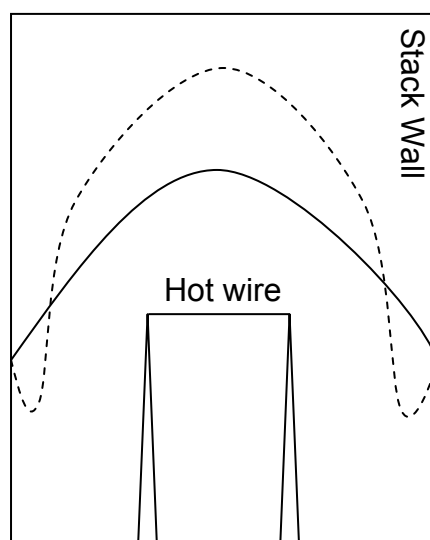


Figure 7.8 Velocity profile of accelerating and decelerating period within a half oscillating circle (accelerating: solid line; decelerating: dashed line)

The hot-wire goes through each velocity apart from the maximum value twice during the half cycle, first one within the accelerating period, and the other one within the decelerating period. Figure 7.7 shows the profile of the two periods within one half oscillating cycle. Assume the two velocity profiles show the same average velocity, the hot-wire should have the same voltage outputs. However, the hot-wire is located in the centre of the stack, measuring the middle part of the velocity profile, thereby the measured velocity in the accelerating period is higher than that of the decelerating period.

Although the calibration at a frequency of 4.86 Hz is poor, this is not representative of the calibration errors that occur in the measurements. A frequency of 4.86 Hz corresponds to 9.72 zero crossings per second. The flow produced by the piston is a sinusoidal oscillation (zero mean). In the model tests, this corresponds to a reversal percentage of 50 %. Figure 7.9 shows a stack velocity (Stack 4) record with $r = 53.9$ % of (S14_O34), 90 degree wind direction, wind speed 5.3 m/s. The number of zero crossings is 175 over the measurement period i.e. 5.15 per second. On this basis, a calibration frequency of 2.67 Hz would be more representative. In fact the situation is probably better than this, because many of the zero crossings are associated with small-scale turbulence (see Figure 7.9). On this basis the

7 Improvements in experimental techniques

calibration frequency of 1.39 Hz is probably more appropriate. The final calibration was in fact obtained using the unsteady calibration for 1.39 Hz and the steady calibration, as shown in Figure 7.10.

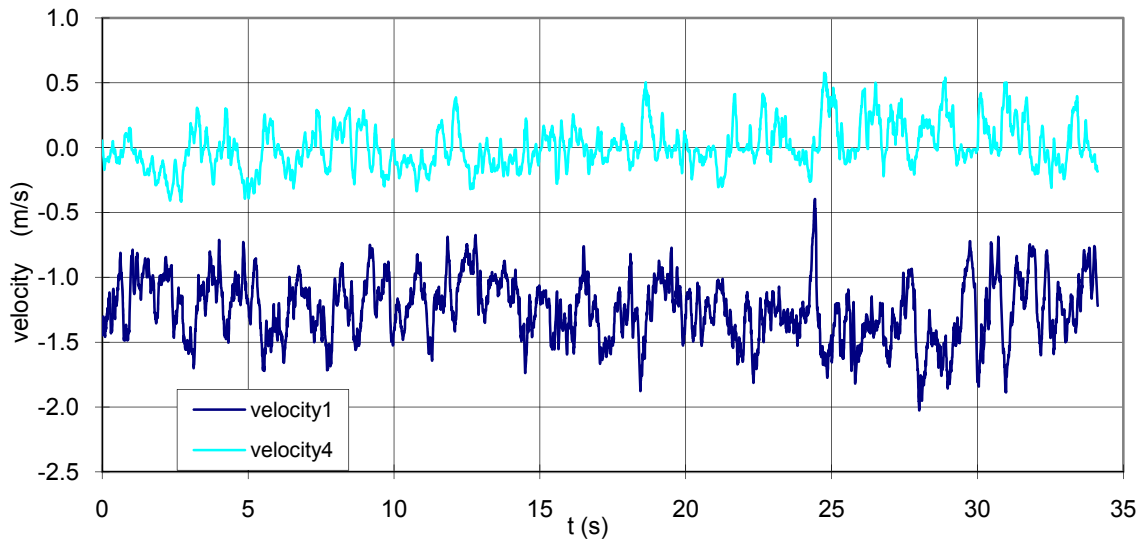


Figure 7.9 velocity signal of (S14_O34_90)

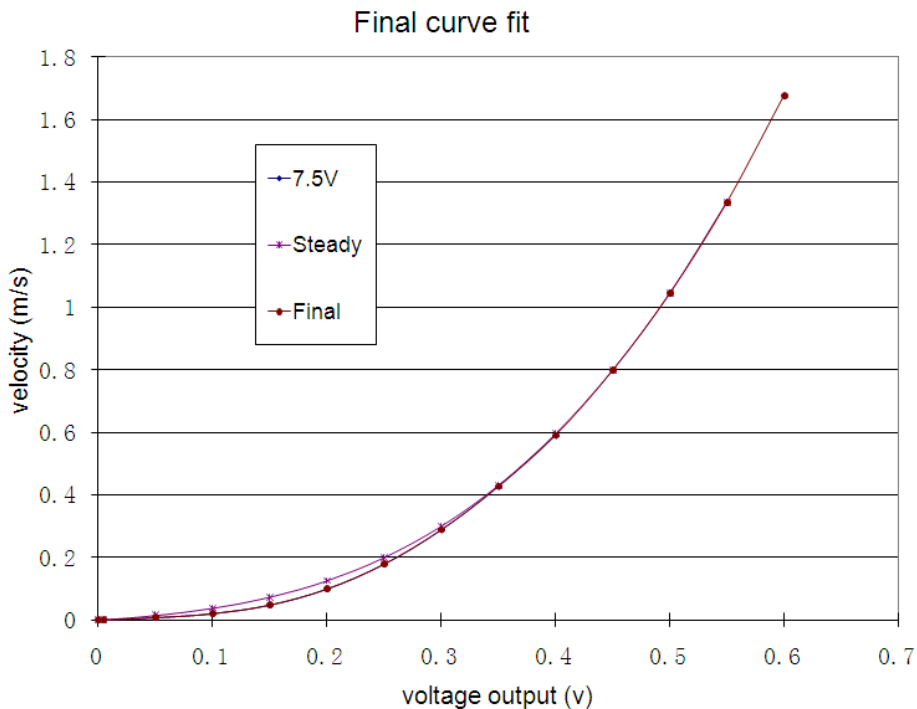


Figure 7.10 Final curve fitting

7 Improvements in experimental techniques

To sum up, the final calibration is a combination of unsteady and steady calibrations, at lower and higher velocities respectively. For unsteady calibration, the instantaneous velocity at the hot-wire location is calibrated against the precise flow rate obtained from piston signals. The oscillating frequency used for the final curve fit was chosen based on the maximum fluctuating frequency that occurs in the measurements.

7.4 Tests of split film probe

The sensitivity of the probes is mostly concerned when fluctuation occurs within the stacks. Standard parallel hot-wires and modified 5 degree hot-wires (Costola and Etheridge, 2007) have been used effectively to detect the direction changes when the air fluctuate within the stacks. A different type of probe named split film probe was tested in order to see if it could give more accurate measurements of fluctuation. As shown in Figure 7.11, the upper film detects flow in downward direction, the lower film detects upward flow. In principle voltage difference should be greater than that of the hot-wire probe, thereby increasing sensitivity to flow direction.

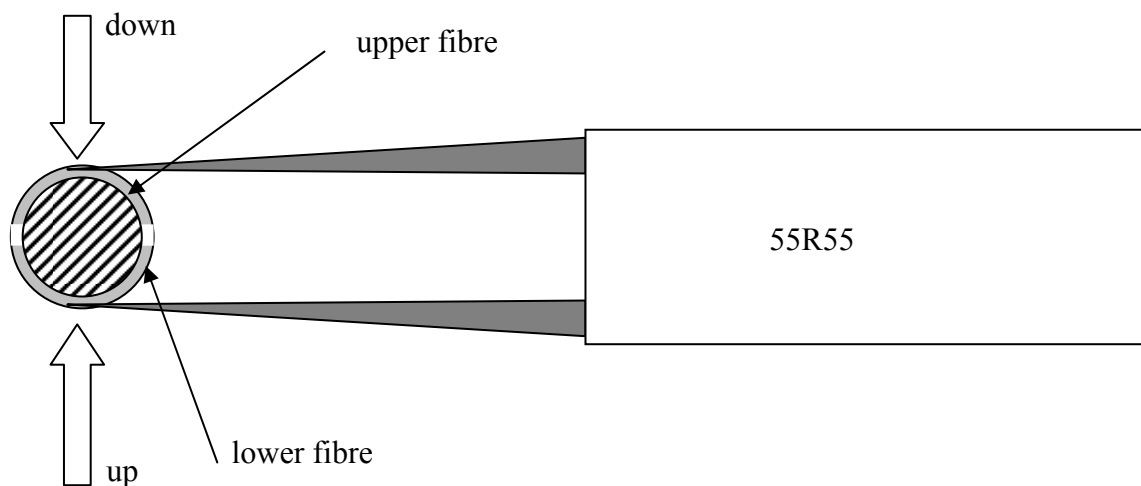


Figure 7.11 Split-film probe

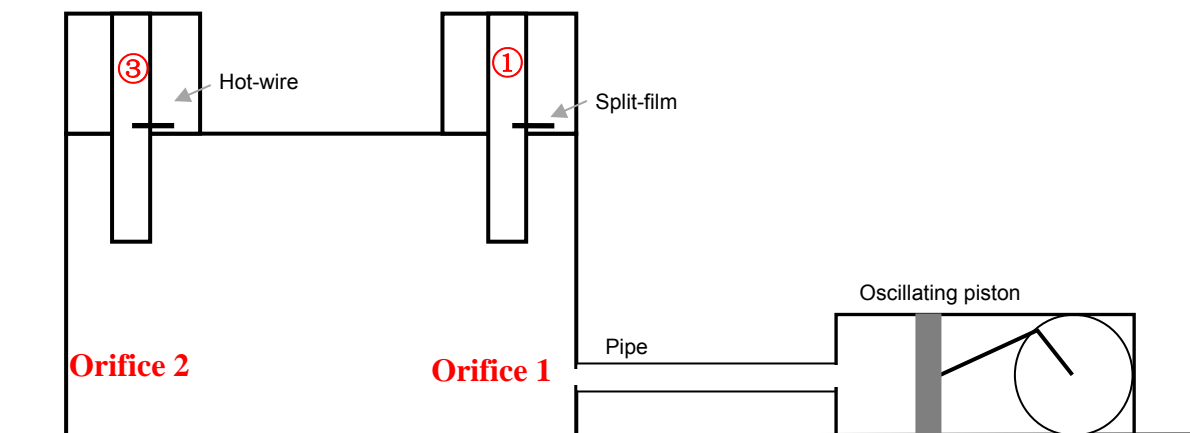
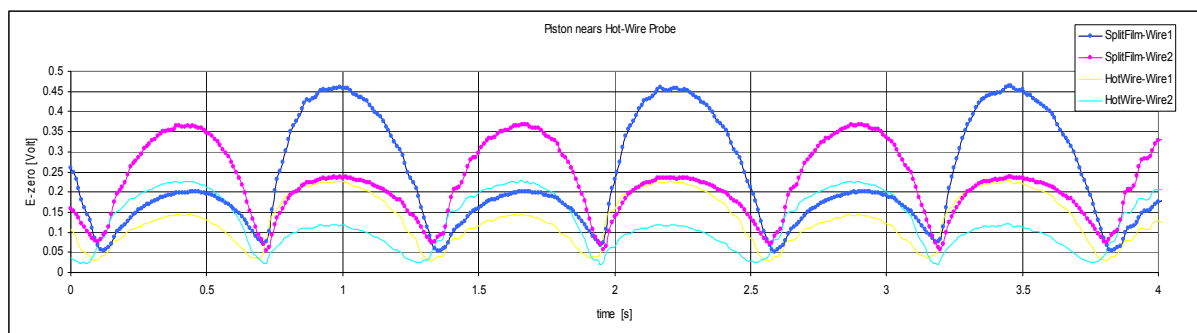


Figure 7.12 Hot-wire and split-film probe fitted in the stack box

As shown in Figure 7.12, the split film probe was mounted in stack 1, the 5 degree hot-wire probe was mounted in stack 3. Firstly the oscillating piston was connected with orifice 2, which was closer to stack 3 (hot-wire probe), and all the other stack outlets and openings were sealed rigidly. The piston was run at two different voltages 7.5 volts and 15 volts, providing different rotational speeds of 0.76 Hz and 1.56 Hz. Results are shown in Figure 7.13 and Figure 7.14. ‘E-zero’ denotes the voltage output of individual wire/film, ‘E1-zero- (E2-zero)’ denotes the difference between the voltage outputs of the two wires/films of a probe, which determines the flow direction. When the piston was nearer to the hot-wire probe, results show that the hot-wire probe responded slightly more quickly than the split-film probe. Since the hot-wire is nearer to the piston, the same tests were carried out with the piston connected to opening 1, which is closer to the split-film probe. But the hot-wire probe still responded more quickly.



7 Improvements in experimental techniques

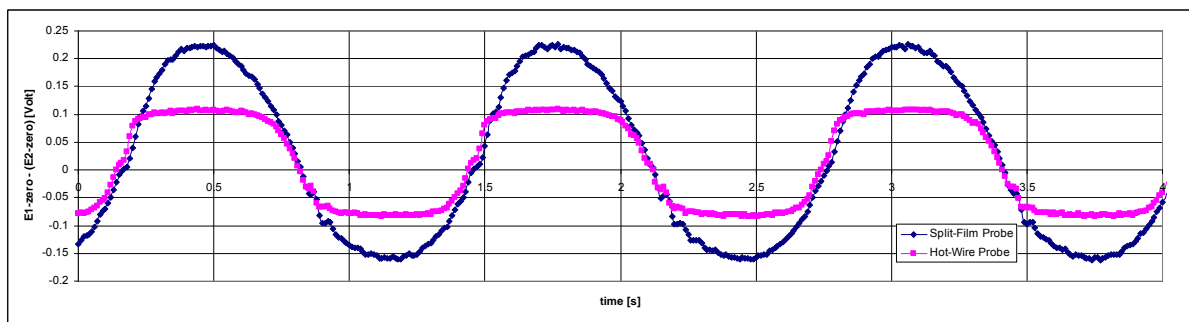
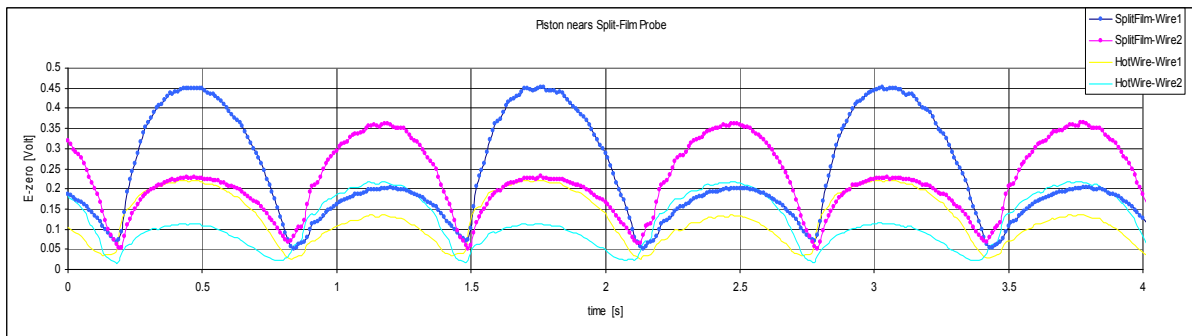
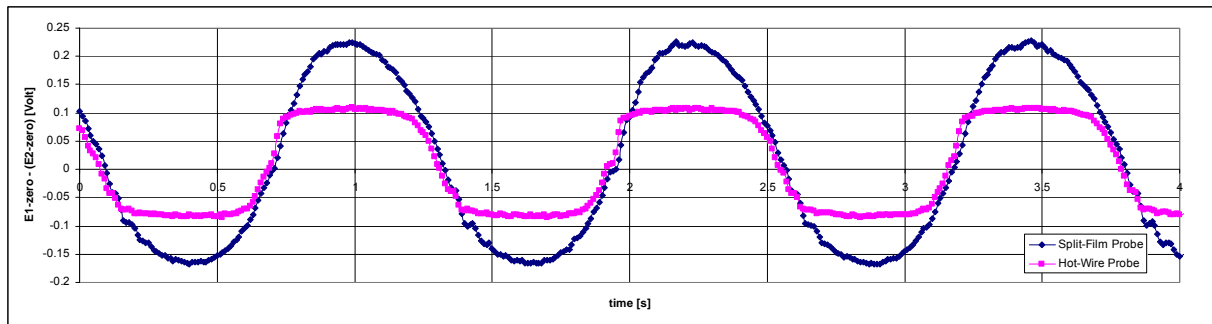
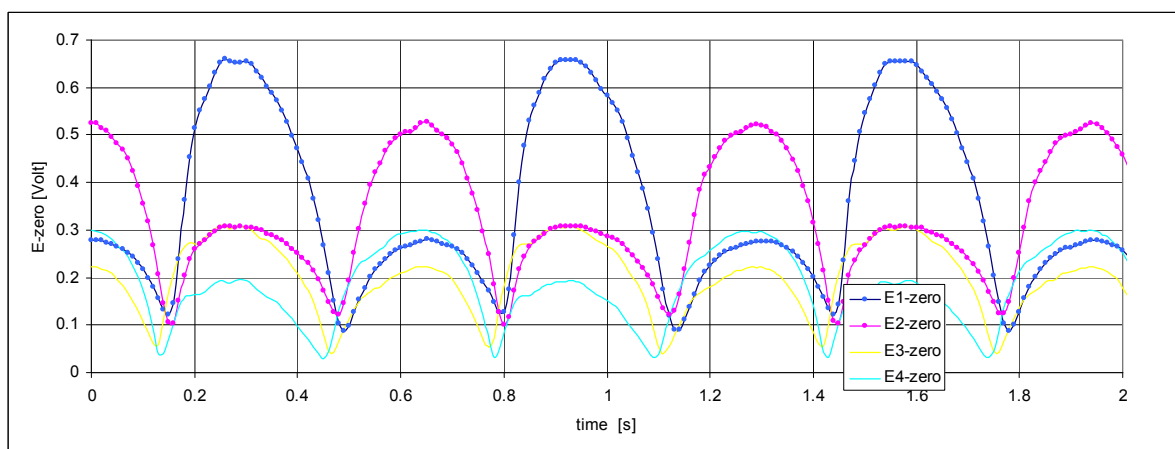
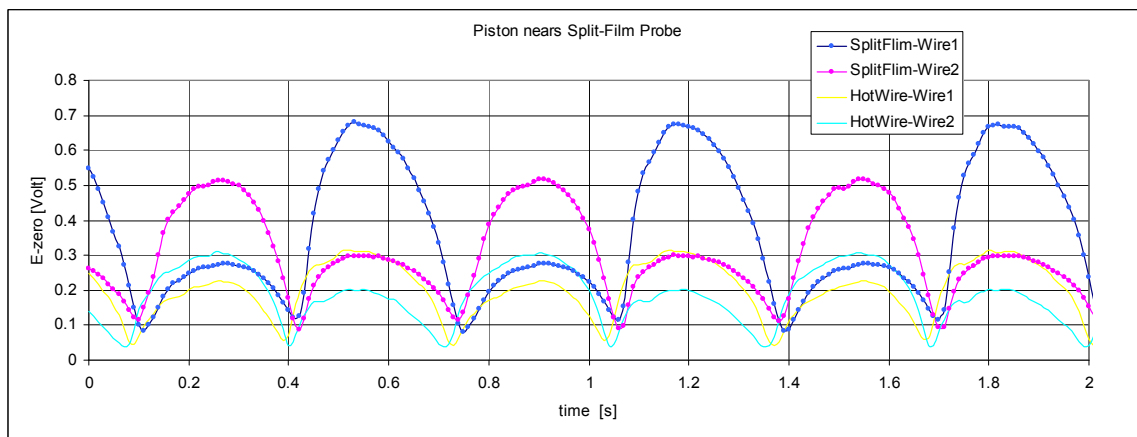
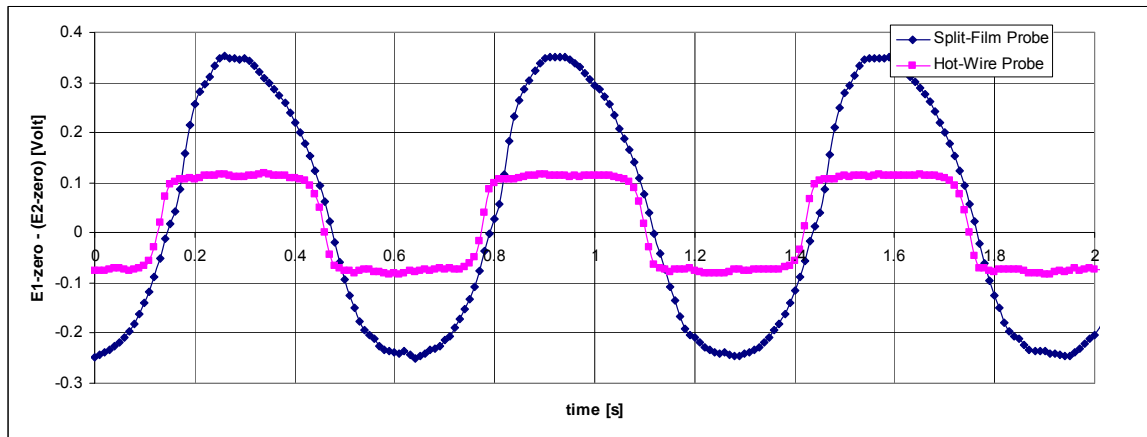
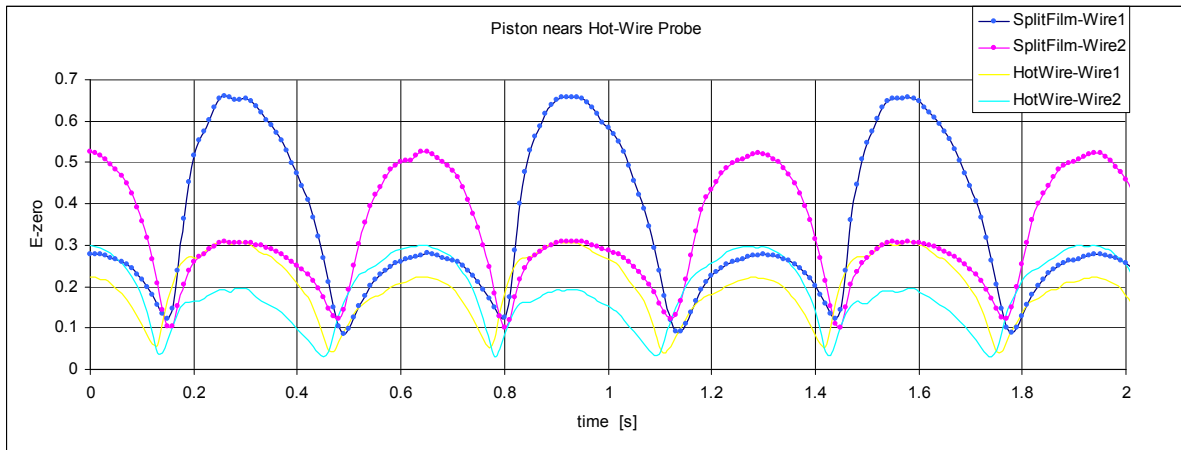


Figure 7.13 Results for 0.76 Hz



7 Improvements in experimental techniques



7 Improvements in experimental techniques

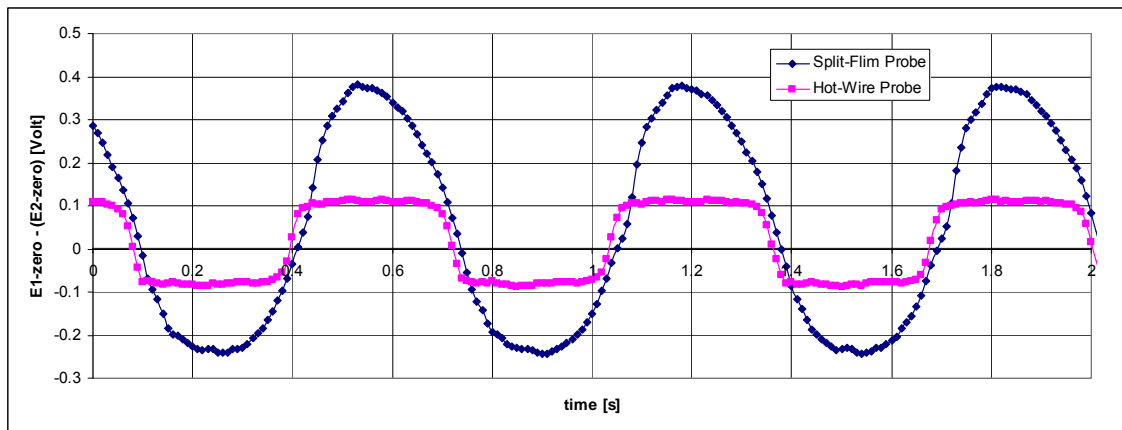
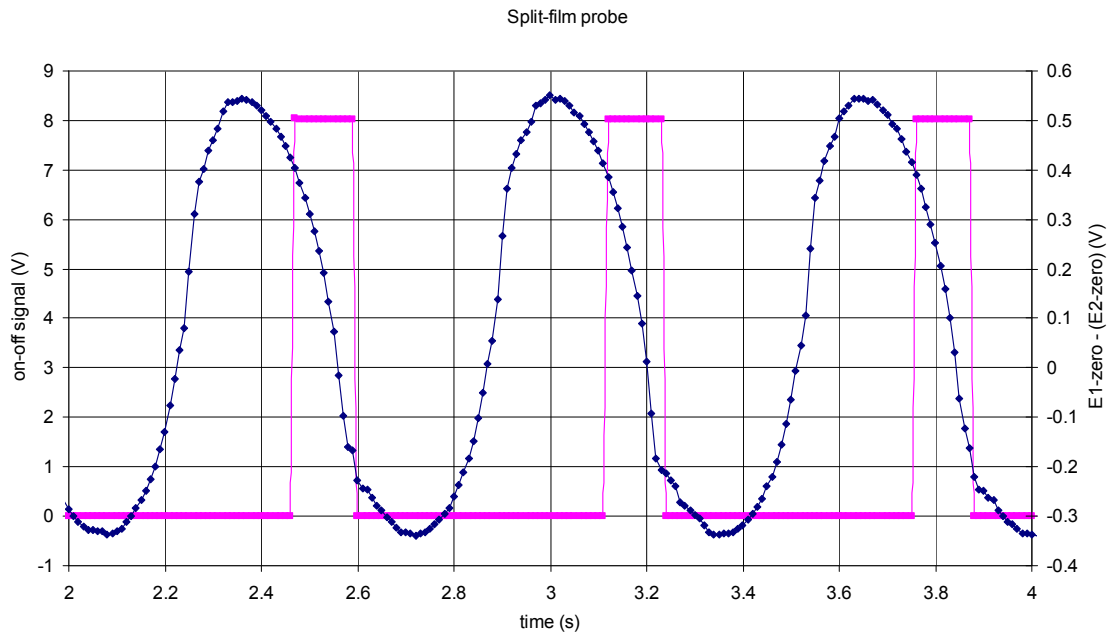
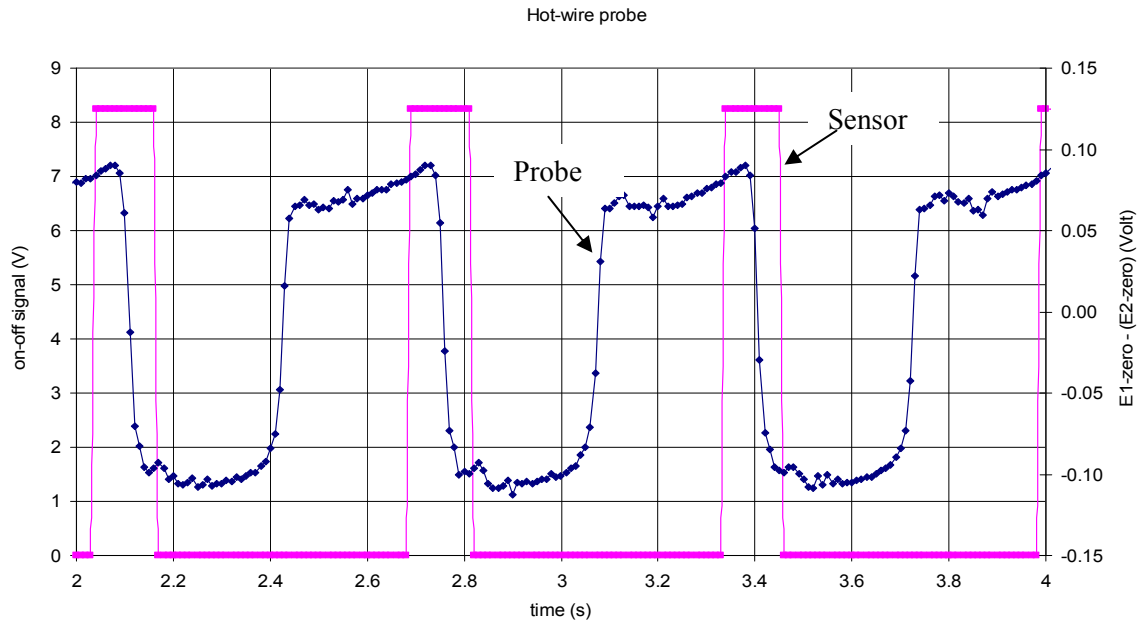


Figure 7.14 Results for 1.56 Hz

For both positions of the piston, the hot-wire probe always responded more quickly than the split-film probe. Since the flow reversal is detected by the changing of the sign of the voltage difference between the two wires/films, the slope and the magnitude of the voltage difference across 0 volts is of most importance. In terms of this, the hot-wire probe performs better than the split-film probe. Although the split-film probe gives a bigger voltage difference at uni-directional flow, it is not beneficial.

In order to find out the exact time lag of the probes, a sensor was fixed at one end of the piston to detect the position of the piston, from the on-off signal of which the flow directions within stacks 1 and 3 can be determined. Results of the 1.56 Hz tests are shown in Figure 7.15. The middle point of the on/off signal of the sensor is the time when flow reversal occurs. If there is no time lag of the probe, the difference of the voltage outputs from the two wires/films of a probe should cross zero. In practice, the probe signal crosses zero slightly after the middle point of the on/off signal of the sensor, which is the time lag (see the third and fourth graph in Figure 7.15 for example).

7 Improvements in experimental techniques



7 Improvements in experimental techniques

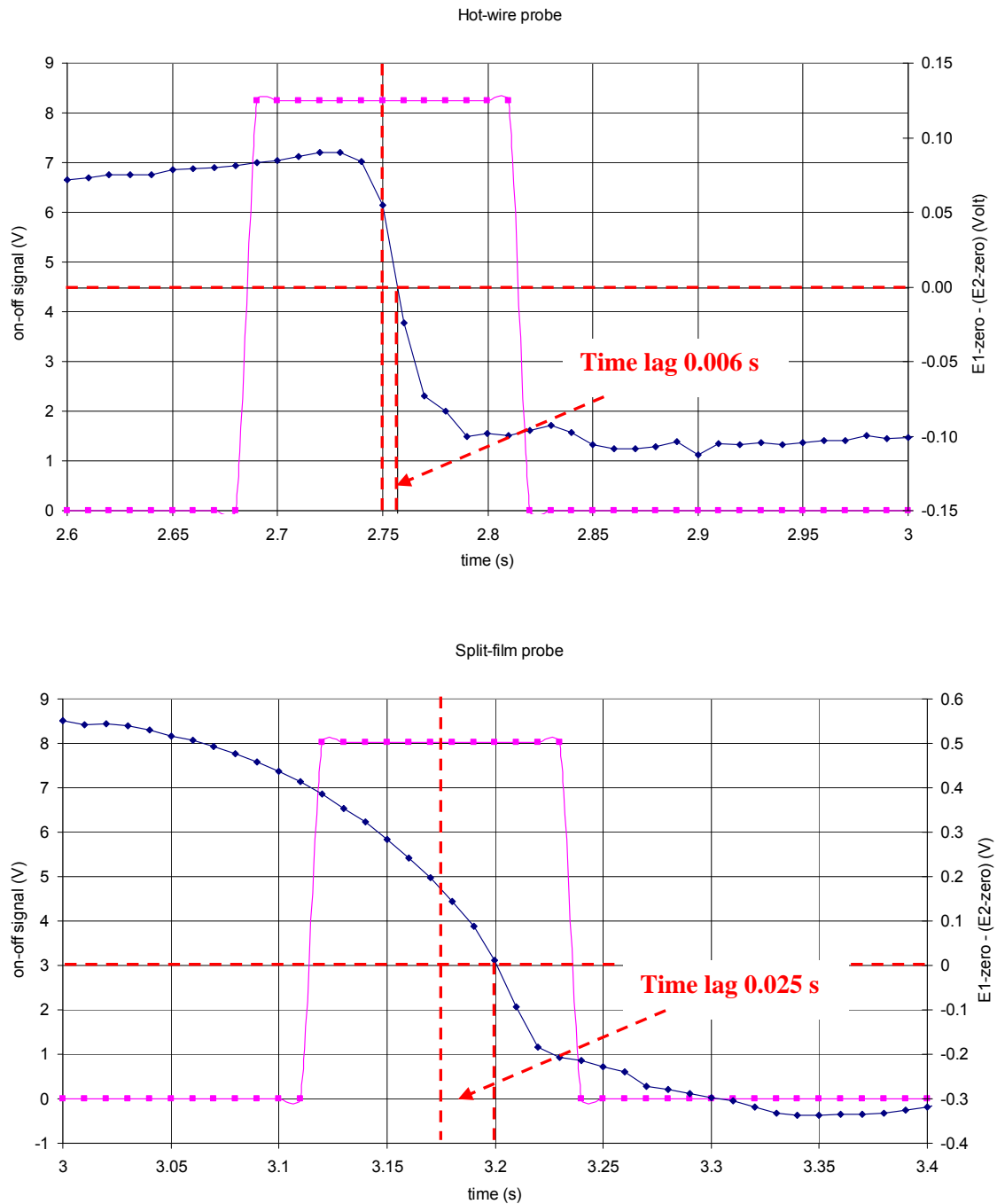


Figure 7.15 time lag of the probes

In the 1.56 Hz tests, both the hot-wire probe and the split-film probe responded behind the piston (when the piston changes direction, the wires detect the flow reversal shortly after). However, the hot-wire probe responds slightly more quickly than the split-film probe. The

7 Improvements in experimental techniques

time differences are shown in Table 7.2 ('Down' means flow direction changes from inward to outward). The hot-wire probe responded 0.019 s more quickly than the split-film when the flow direction changes from inward to outward, and 0.014 s more quickly when the flow direction changes from outward to inward.

Table 7.2 Time lag to detect flow reversal for the two probes

	Hot-wire probe (s)	Split-film probe (s)	Time difference (s)
Down	0.006	0.025	0.019
Up	0.002	0.016	0.014

It was concluded that the hot-wire probes perform better than the split film probes, for the following reasons:

- 1) The hot-wire zero crossing time agrees better with the pulse output from the piston.
- 2) The hot-wire zero crossing voltage difference slope is higher than that of the split film probe

It seems therefore that the hot-wire probe is better at detecting flow reversal (where the velocities are low) than the split-film probe. This could be due to the fact that the split-film sensors are mounted on the same cylinder i.e. they are directly connected in terms of heat transfer. Heat transfer between the films could be significant at low velocities where the cooling effect of the flow is small.

With the hot-wire we have the opposite problem – the voltage difference due to upstream heating becomes relatively small at high velocities, compared to the cooling effect of the air flow. This problem can be seen with uni-directional flow – where it can be eliminated with software, because the indicated $\frac{\Delta u}{\Delta t}$ exceeds what is physically possible.

7.5 Improvements of pressure measurements

7.5.1 Introduction

Since the model is equipped with small openings, it is assumed that the pressure inside the model is uniform, which means the internal pressure tapping could be put anywhere on the internal surfaces of the model (for wind alone tests). In all the previous tests, the internal pressure tapping was put in the centre of the floor. Similarly, a pressure tapping is put close to the outlet of the stack to measure the static pressure of the stack outlet. The difference between the two measurements of internal pressure and stack outlet pressure is used as the driving force of the flow through the stack. However, some of the TPU results show inconsistency between the flow direction through the stack and the direction of the pressure difference, which indicates inaccurate measurements of either of those two static pressures. Therefore, some repeat tests were carried out in the Nottingham wind tunnel to investigate the accuracy of the pressure measurements. The contents of this section are presented in the sequence of the exploration process.

7.5.2 Inaccuracy in pressure parameter and possible reasons

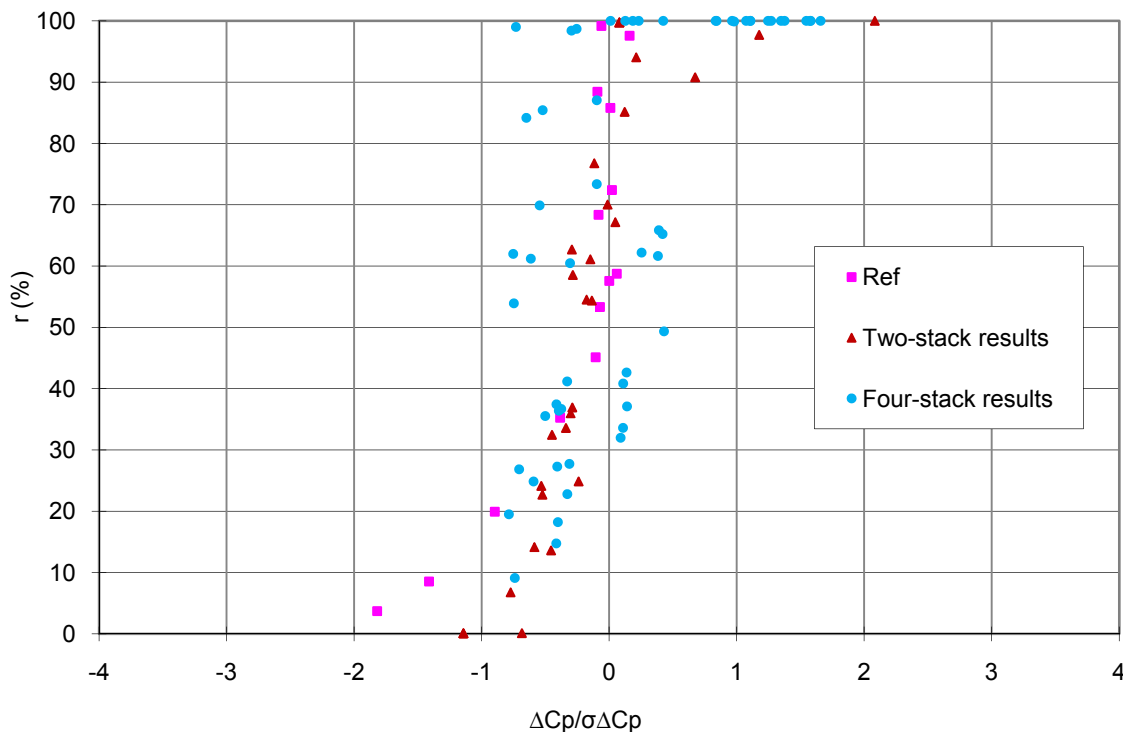


Figure 7.16 Variation of r with $\Delta C_p / \sigma \Delta C_p$ for two-stack and four-stack cases compared with Ref (Cooper and Etheridge, 2007)

7 Improvements in experimental techniques

In Figure 7.16, the upward flow results in TPU show overall agreement with the results of Cooper and Etheridge (2007). Yet for r above approximately 30%, there are some disagreements. For a certain number of downward flow results, the values of $\Delta C_p / \sigma_{\Delta C_p}$ lie

between -1 and -0.5, which in theory should be positive. ΔC_p is defined by $\Delta C_p = \frac{P_{st} - P_{in}}{0.5\rho U_{ref}^2}$,

where p_{st} is the stack pressure and p_{in} is the internal pressure. The actual pressure difference that determines the stack flow rate is $P_2 - P_1$ where P_2 is the pressure in the region of the lower part of the stack (see Figure 7.17). To reduce the number of pressure transducers, P_2 is assumed to be equal to P_{in} (for wind alone case).

There are two possible reasons for the differences in Figure 7.16:

- 1) One pressure tapping at a fixed position of the stack outlet is not an accurate measurement of the average static pressure at the outlet.
- 2) For certain opening configurations and wind directions, the internal pressure tapping might be affected by the internal flow e.g. the higher internal flow rates with the increased number of openings, will increase the pressure difference between P_2 and P_{in} in Figure 7.17, especially when the opening facing the approaching wind is open.

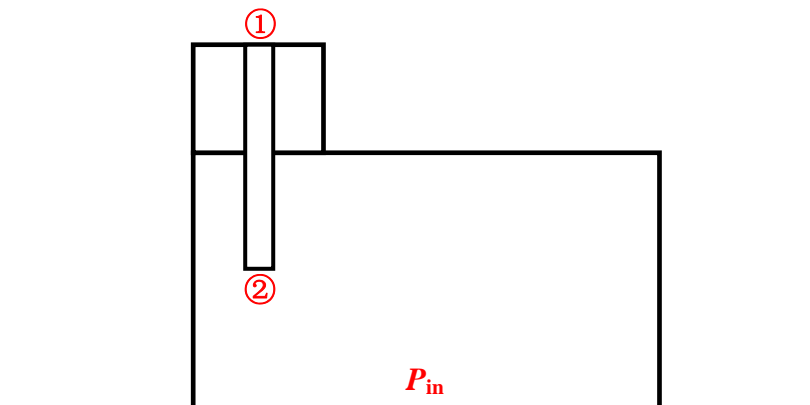


Figure 7.17 Pressure measurement

7 Improvements in experimental techniques

If the measured stack outlet pressure were less than the appropriate average value, or the measured internal pressure were higher than P_2 , or both of them happen, $\Delta C_p / \sigma_{\Delta C_p}$ could turn negative when $P_2 - P_1$ is positive.

The following methods were used to investigate the reasons, while repeating some of the inconsistent points observed at TPU. The first three were experimental tests, the fourth one was CFD simulation.

- 1) The effect of taking the average of the four pressure tapings at the stack outlet.
- 2) The effect of changing the opening configuration (e.g. closing the orifice facing the approaching wind, or increasing the number of orifices)
- 3) The effect of fixing a topless cover over the internal pressure tapping in order to keep away the approaching flow through the opening to reduce any vertical momentum component going into the internal pressure tapping.
- 4) CFD simulation to investigate the flow pattern around the internal pressure tapping.

7.5.3 Investigation of the possible reasons

Test 1) Taking Average stack outlet pressure

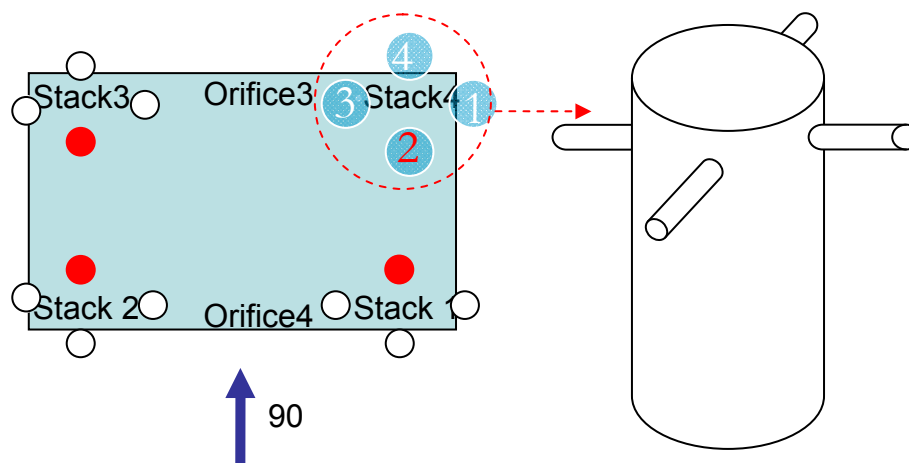


Figure 7.18 Pressure measurements and wind direction

7 Improvements in experimental techniques

As shown in Figure 7.18, the red one of the four pressure tapplings at the stack outlet was used in the wind tunnel measurements, e.g. position 2 of Stack 4 was always used. It is found that most of the unexpected points are cases when the pressure tapping were back to the approaching wind, which is in accordance with the assumed reason 1). For example, as shown in Figure 7.18, the pressure tapping used was P_{st2} with a 90 degree wind direction.

To check the assumed reason 1), average pressures of the four tapplings of Stack 4 were taken, while repeating certain TPU tests. Results are listed in Table 7.3. All the P_{st2} values are less than P_{ave} (comparing the highlighted rows in the table). The ones facing the approaching wind have the highest value of the four pressure tapplings, indicating that the pressure tapplings facing the wind might be measuring partly dynamic pressure of the wind. Though taking the average pressure makes a small improvement, it is not a complete explanation.

Table 7.3 Comparison of average pressure measurements with the one fixed position measurements

	S34*_ 034_0	S1234*_ 45	S14*_ 034_90	S13*_ 01234_90	S3*4_ 01234_90	S3*4_ 012_67.5	S1*234_ 01245_0
\emptyset	0	45	90	90	90	67.5	0
Stack	4	4	4	3	3	3	1
r%	99.90	99.00	5.47	100.00	99.00	100.00	6.20
1	-1.67	-5.13	-2.77	-3.96	-3.17	-3.94	-0.98
2	-3.68	-6.33	-2.78	-4.10	-3.24	-4.41	-1.50
3	-4.04	-6.29	-2.75	-3.82	-3.10	-4.35	-1.51
4	-3.08	-5.01	-2.20	-2.76	-2.40	-3.83	-1.18
P_{ave}	-3.12	-5.69	-2.62	-3.66	-2.98	-4.13	-1.29
P_{in}	-3.65	-4.49	-1.76	-3.15	-2.29	-2.78	-0.94

Test 2) Effect of opening configurations**1) Effect of orifice facing the approaching wind on P_{in} .**

It is possible that the opening facing the approaching wind might result in a downward momentum component at the position of the internal pressure tapping. That is to say, the measured P_{in} has some dynamic pressure included, causing the measured value to be larger than P_2 .

The envelope flow model assumes that the room pressure is uniform, which permits the position of the internal pressure tapping to be set anywhere inside the box. However, in real cases, the difference between different measuring points might be significant (e.g. the difference between the floor and wall pressure tapplings $P_{in} - P_{wall}$, where P_{wall} was taken at the internal surface beside the Orifice 1). Comparison was made between these two cases: (S3*4_O1234_90) and (S3*4_O123_90), in the latter case the orifice facing the wind (Orifice 4) was sealed.

Table 7.4 Pressure difference between P_{in} and P_{wall}

	r (%)	$P_{in} - P_{wall}$ (Pa)
S3*4_O1234_90	99.4	0.14389
S3*4_O123_90	100	0.01034

The results in Table 7.4 show that

- 1) When opening 4 is closed, $P_{in} - P_{wall}$ reduces significantly.
- 2) Since the driving force of stack 3, $P_3 - P_{in}$, is less than 1 Pascal, $P_{in} - P_{wall}$ accounts for more than 10% of the total pressure difference, which is significant for the case of 90 degree.

Therefore, it is concluded that the opening facing the wind can have a significant effect on P_{in} .

For the case of 0 or 180 degree, the distance between the opening facing the wind and the internal pressure tapping is larger than the case of 90 degree, the effect of the approaching wind should have less effect on P_{in} .

2) **Effect of number of orifices**

With the earlier tests with only one sharp-edged orifice and one stack, when the pressure drop across the stack is small, the flow rate through the opening is also small. Thus the internal velocities are small and internal pressure changes are small. With more than two orifices, one can have a small stack flow rate (and pressure difference), but larger flows through the other orifices. Hence the effect is probably going to be worse as the number of orifices increases.

Table 7.5 Comparisons between two TPU tests (S14*_O12_90) and (S14*_O1234_90)

	P_{in} (Pa)	P_1 (Pa)	P_4 (Pa)	$P_4 - P_{in}$ (Pa)	$P_1 - P_{in}$ (Pa)	r (%) Stack1	r (%) Stack4
S14_O12_90	-5.793	-9.960	-5.568	0.225	-4.167	0	100
S14_O1234_90	-3.735	-9.980	-4.053	-0.318	-6.244	0	93.97

Seen from Table 7.5, increasing the number of orifices from two to four has the following effects:

- 1) No obvious change in stack pressure of outward flow (Stack1)
- 2) Both P_{in} and P_4 (reversal flow) increase, yet the effect on P_{in} is bigger, causing the driving force $P_4 - P_{in}$ to change sign.
- 3) To maintain upward flow (stack1), there was a large $P_1 - P_{in}$. However, the pressure difference between P_{in} and P_{st} is very small when the flow is downward (stack4), which causes the effect of increasing the orifice number on P_{in} to be relatively more significant.

Again, it supports the conclusion that the approaching wind has an effect on P_{in} , especially when the number of opening increases.

Test 3) Effect of putting a topless cover above the internal pressure tapping.

In order to keep away the dynamic pressure component at the internal pressure tapping, a plastic cup without top was fixed over the tapping. The following tests were made to investigate the effect of the cup (Figure 7.19).

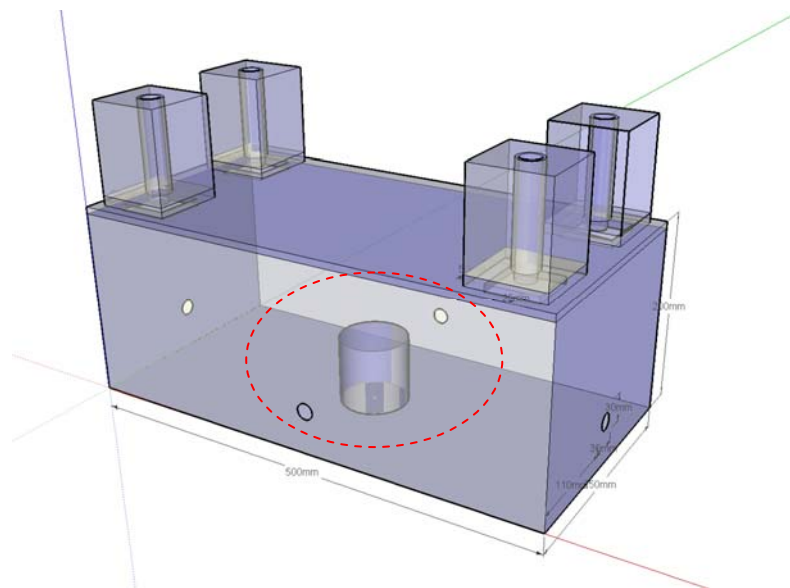


Figure 7.19 Model with the cup with no top above the internal pressure tapping

Table 7.6 Comparisons of Po-Pin between Pin covered and Pin exposed

	Wind direction	Stack	r (%)	$P_{in} - P_{wall}$ (Pa)
S3*4_O1234_90	90	3	99.4	0.144
S3*4_O123_90	90	3	100	0.010
Pin Covered				
S3*4_O1234_90	90	3	100	0.061
S3*4_O123_90	90	3	100	0.057

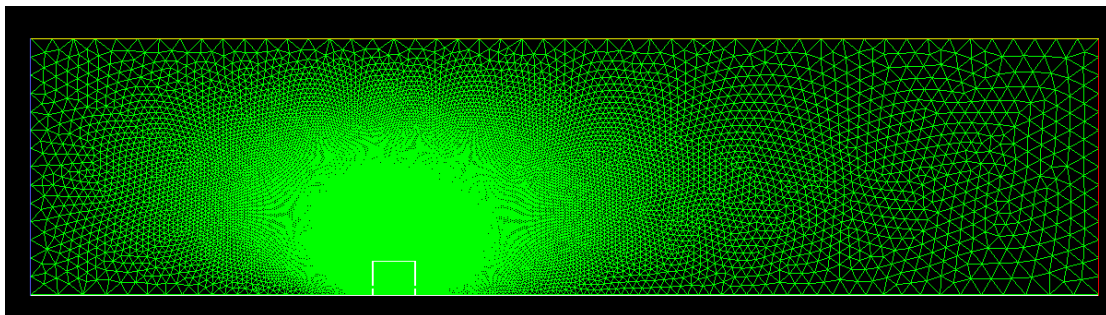
As can be seen in Table 7.6, when there was no cup, $P_{in} - P_{wall}$ reduced significantly after opening 4 was closed. However, when the internal pressure tapping was covered by the cup, the decrease of $P_{in} - P_{wall}$ was less than 10%. That is to say, the cup reduced the influence

7 Improvements in experimental techniques

of the opening facing the wind on the internal pressure tapping. It is worth noting that the values of $P_{in} - P_{wall}$ are small (<0.2 Pa) and place demands on the measurement technique, yet they are important because with flow reversal the pressure differences across the stacks are inherently small.

Test 4) CFD simulation

In view of the results in Table 7.6, two-dimensional CFD simulation was carried out to study the flow field within the box. The cross section of the wind tunnel is set into a domain of $6.25\text{m} \times 1.5\text{m}$. The dimension of the cross section of the model is $0.25\text{m} \times 0.2\text{m}$. There are approximately 71000 meshing cells (Figure 7.20). The inlet and outlet of the wind tunnel were set as uniform velocity inlet and pressure outlet respectively, all the other boundaries were set as walls. The standard $k - \xi$ turbulence model was used. These simulations were primarily intended to provide a qualitative indication of the internal flow field. Three-dimensional simulation of the internal flow field was carried out using the actual model geometry, but it was not possible to model the external flow field due to limitation on the number of cells. The 3D results are given in Appendix IV.



7 Improvements in experimental techniques

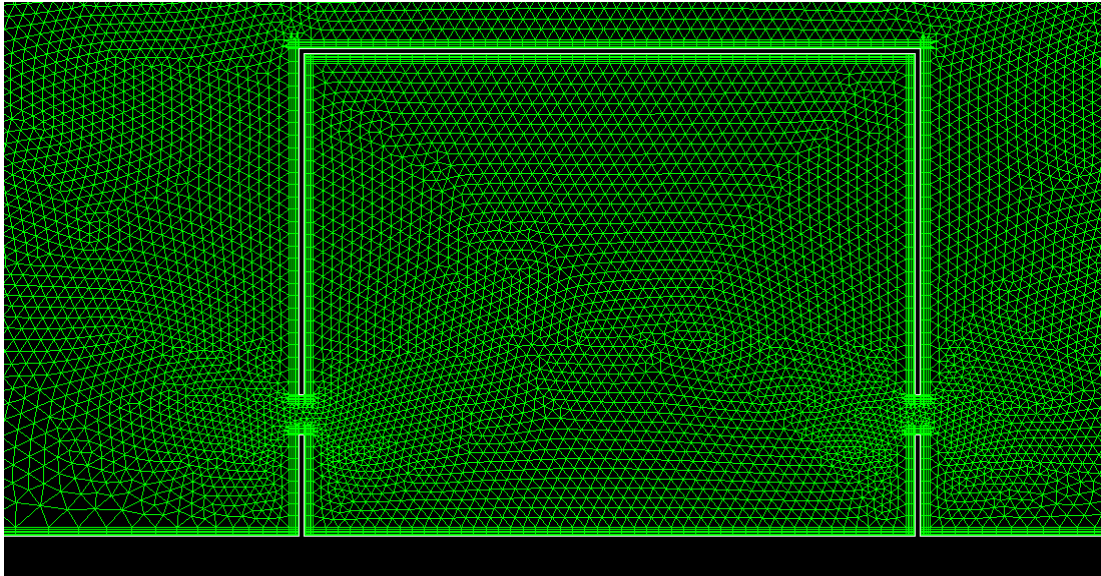


Figure 7.20 Meshing of model section

Figure 7.21 and Figure 7.22 show the flow field of the cross section of the model. The velocity inlet of the wind tunnel was 5m/s ($U_{ref} = 5 \text{ m/s}$).

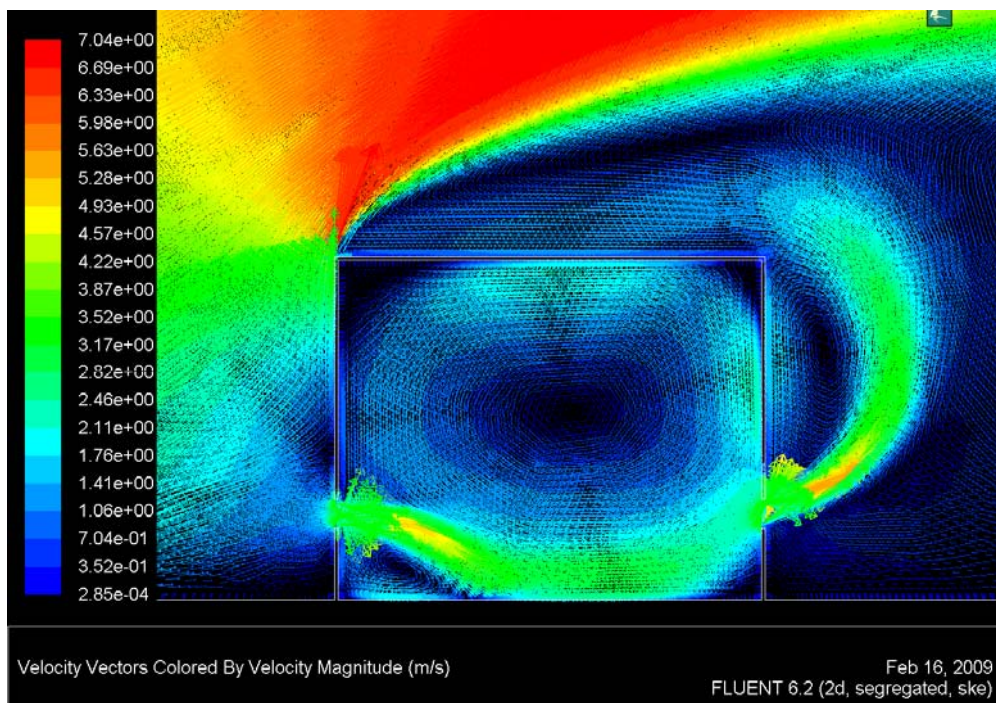


Figure 7.21 Velocity vectors of the flow field with no cover above internal pressure tapping

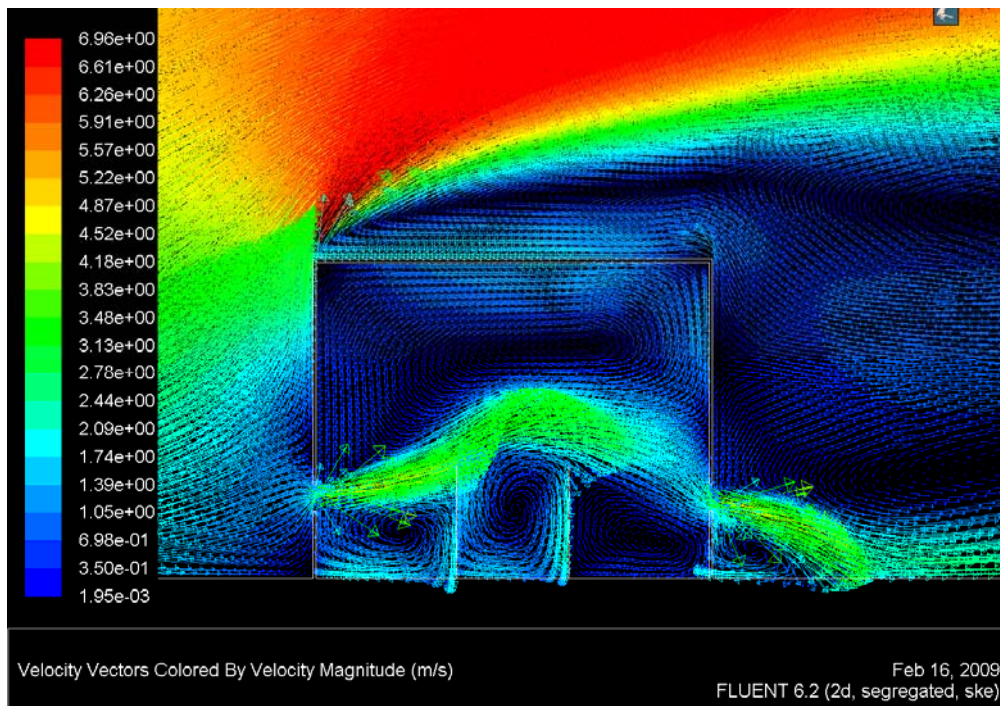


Figure 7.22 Velocity vectors of the flow field with a cover above internal pressure tapping

It can be seen that, when there is no cup, the internal pressure tap is located in the attaching area of the air coming in through the orifice facing the approaching wind.

Vertical velocity component (v) of the bottom line of the model, v is taken at a 0.002 m distance near the inner surface of the model box. For the case of $U_{ref}=5$ m/s, the velocity at the orifice $u_{op}=3$ m/s, and $v_{max}=0.025$ m/s when there is no cup. $v=0$ m/s when the internal pressure tapping was covered. Thereby, the results from two dimensional simulations support the conclusion that the cover could block away the vertical velocity component at the internal pressure tapping.

7.5.4 Improvements made by covering P_{in} and taking the average pressure of P_{st} .

In view of the results in Section 7.4.3, tests were carried out using the improved pressure measurements, i.e. putting a topless cover over the internal pressure tapping, and taking the average pressure of the four pressure tapings at the stack outlet.

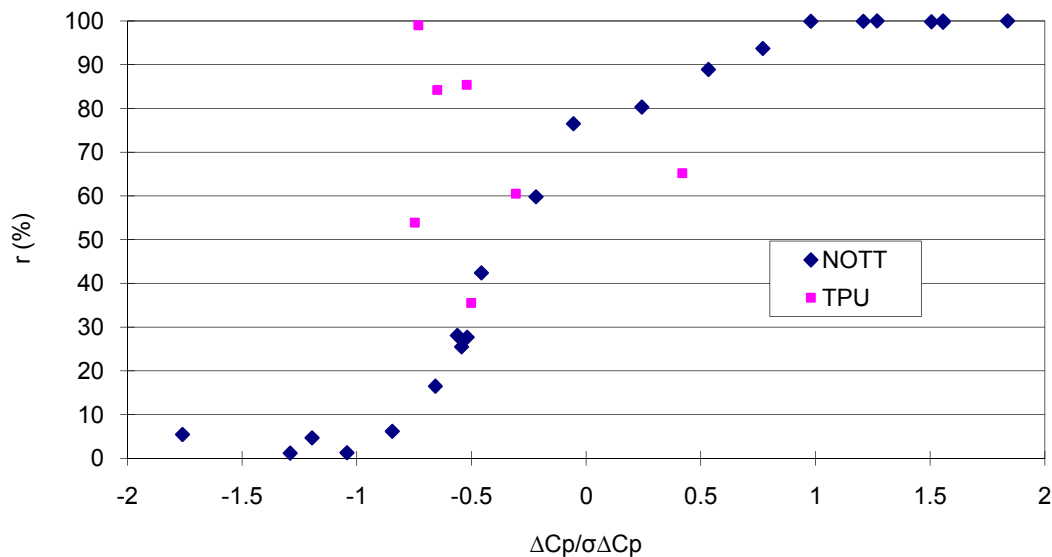


Figure 7.23 r against $\Delta C_p / \sigma \Delta C_p$ with P_{in} covered and the average pressure of P_{st} was taken, compared with results from TPU

Figure 7.23 compares the results obtained at Nottingham with the results at TPU, for the four-stack case over a range of wind directions. The values shown are for stack 4. Encouraging improvements are observed. It is clear that the modifications to the pressure measurement have significantly reduced the scatter. It is now at the level observed with the early single-stack model. This suggests that the main cause is the higher internal velocities that occur with multiple orifices.

In addition, to generate a range of flow reversal percentage through Stack 4, the wind direction was slightly changed. It was found that the reversal percentage r is very sensitive to wind directions. A slight change of wind direction as low as 1 degree could result in a big change in reversal percentage.

7 Improvements in experimental techniques

The above results are relevant to the C_z variations discussed in Chapter 4, Section 4.5.3. Plotting the improved measurement results in the form of C_z variation with Re_{st} could provide some insights into the question: whether the peak is caused by the influence of external flow, or the position of the stack pressure tapping? In Figure 7.24, the peak value is reduced to less than 1 (red dots) with the improved pressure measurements. This indicates that the peak is most likely due to the internal velocity effects on the internal pressure tapping. The external flow has some effects, but can not cause a peak C_z value as high as 2.5. However more tests are desirable for this conclusion. In Figure 7.25, C_z outward flow results (blue cross) are consistent with former tests as well.

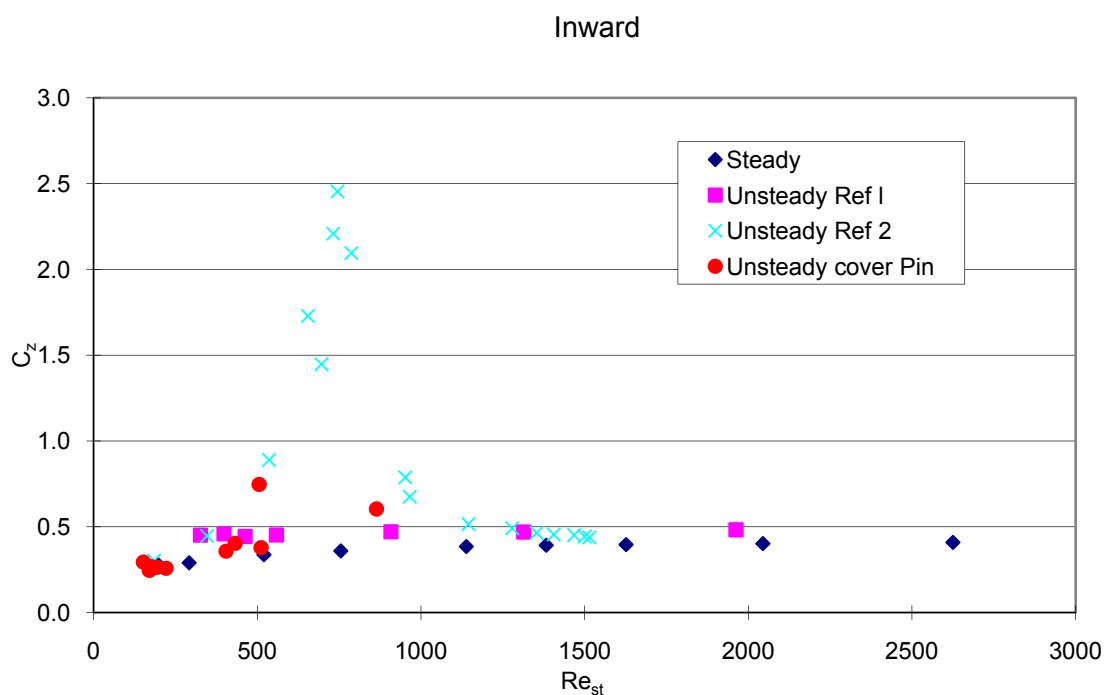


Figure 7.24 C_z variation with Re_{st} compared with steady state (still-air) result of inward flow; Ref 1 (Costola and Etheridge, 2007), Ref 2 (Cooper and Etheridge, 2007)

7 Improvements in experimental techniques

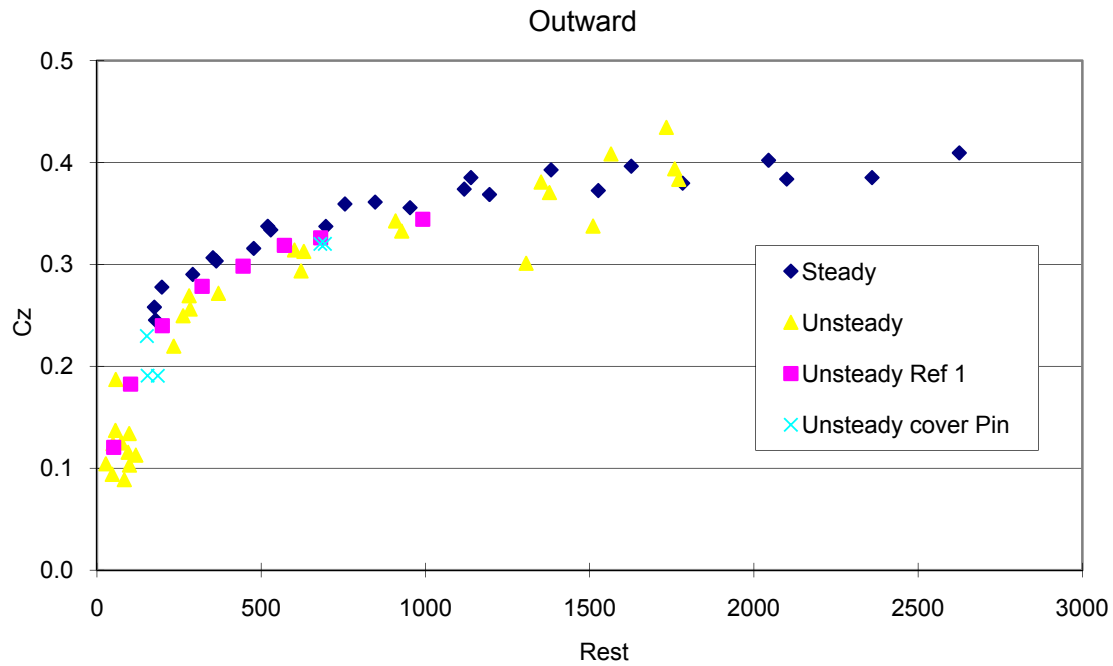


Figure 7.25 C_z variation with Re_{st} compared with steady state (still-air) result of outward flow; Ref 1 (Costola and Etheridge, 2007)

7.6 Summary and conclusions

Firstly the mass balance was checked by comparing the simultaneous pressure and velocity measurements. Secondly, an improved calibration method for the hot-wire was introduced. Thirdly, a different type of probe (split-film probe) was tested. Finally, improvements were made in pressure measurement. Main conclusions are as follow.

- 1) The simultaneous pressure and velocity measurements demonstrate consistency. The better agreement of the two independent measurements proved the importance of the stiffness of the model (after a rod was fixed in the model).
- 2) The unsteady calibration for the hot-wire was improved, the instantaneous velocity at the hot-wire location is calibrated against the precise flow rate obtained from piston signals.
- 3) The hot-wire probe is better at detecting flow reversal than the split-film probe.
- 4) The pressure measurements were improved using the following methods:

7 Improvements in experimental techniques

Firstly, when orifice 4 is facing the wind, the air flow through orifice 4 could influence the internal pressure tapping. A topless cover above the internal pressure tapping reduces the dynamic pressure component at the testing point P_{in} .

Secondly, taking the average of the four pressure tappings at the stack outlet gives a better result than just one pressure tapping.

8 Conclusions, discussion, and suggestions for future work

8.1 Overview of chapter

This chapter includes four parts:

- 1) Summary of the whole thesis
- 2) Originality and contribution to knowledge
- 3) Discussions about possibilities of integrating the findings of this thesis into design guides/tools.
- 4) Suggestions for future work

8.2 Summary of the thesis

This thesis is an investigation of unsteady natural ventilation based on the envelope flow theory, with special focus on stack ventilation. Both theoretical models and direct wind tunnel measurements were described, with comparisons made between theoretical calculations and measurements.

Main conclusions corresponding to the tasks listed in Chapter 1, Section 1.1.2 are:

8.2.1 Improvements of experimental techniques

- 1) A precise unsteady calibration method of a hot-wire probe was developed, resulting in a relatively precise measurement of the fluctuating flow through a stack.
- 2) The split-film probe was tested. It was found that the hot-wire probe performs better in detecting flow reversal.
- 3) Improvements were made to the pressure measurement by taking the average pressure of the stack outlet and by shielding the internal pressure tapping to reduce the effect of the internal velocity.

8 Conclusions, discussions, and suggestions for future work

- 4) Tests with multiple stacks and no other openings provide a stringent check on the accuracy of the hot-wire technique for both mean and instantaneous flow rates. The error of the mean flow rates is less than $\pm 10\%$. In terms of the instantaneous flow rates, it is important for the model box to be rigid.

8.2.2 Widening the scope of the technique to multiple stacks, and buoyancy and wind combined tests

- 5) The hot-wire technique works for multiple openings for both wind alone and wind and buoyancy combined cases.
- 6) Flow reversal was observed at some wind directions for all the opening configurations tested even though the stack outlets are situated at high level. It is not easy to prevent flow reversal. Increasing the number of orifices has some effect in reducing the reversal percentage, yet it depends on the size the orifices relative to the façade area (porosity).
- 7) For long openings, a dependence of r on Re_b was observed, which indicates that a higher r is expected at full scale. This is supported by theoretical calculation of a full scale building.
- 8) The process of transitions between wind dominated ventilation and buoyancy dominated ventilation were produced by gradually changing either of the two driving forces. No obvious hysteresis effect was observed, possibly because the long opening could mitigate the transitioning process. It has been confirmed experimentally that when the wind and buoyancy forces are in opposition and nominally equal, the turbulent wind fluctuation could cause effective ventilation rates. When there are only stacks open with a fixed buoyancy force, the flow directions through the stacks depend on the initial conditions.

8.2.3 The effects of opening configuration on pressure coefficient and the effects of external flow on discharge coefficient

- 1) With small openings, the mean pressure coefficients are expected to be independent of opening configurations. It is true for sharp-edged orifices; however it was found that C_p and C_d correlations of stacks have some dependency on opening configurations. This could be significant for design.
- 2) The observed variation of C_z with opening Reynolds number for multiple stacks is consistent with previous results for a single stack. For inward flow, some of this variation is due to external flow conditions at the inlet to the stack.

8.2.4 Assessment of theoretical models

- 1) Predictions of flow directions were made using the pressure coefficients of the openings. This simple method could correctly predict the flow directions for the cases of stacks alone. Errors occur with the increasing number of orifices.
- 2) The steady envelope flow model and QT model perform equally well in calculating mean flow rates for the cases of unidirectional flows. Both models are sensitive to the chosen C_z values. The advantage of QT model is that it can be used for reversal flow. There are good agreements between QT model and measurements of flow reversal percentage through long openings at model scale. Therefore, it is believed to be reliable to use the QT model to predict the reversal percentage at full scale. This could be useful for design purposes.

8.3 Originality and contribution to knowledge

- 1) The hot-wire technique has been successfully extended to multiple stacks for the cases of wind alone and wind and buoyancy combined. It is believed that this is the first time that detailed information on unsteady multiple stack flows has been obtained.
- 2) The effects of opening configuration on mean C_p and C_d correlations are investigated, which could lead to future research of unsteady wind effects on ventilation rates. Further information on the effects of external flow on C_z with multiple openings is provided. Additionally, the provisions of very detailed data on instantaneous and simultaneous

8 Conclusions, discussions, and suggestions for future work

pressure and flow rates are suitable for validating unsteady flow models (e.g. envelope models and Large Eddy Simulation in CFD).

- 3) New information on the detailed transitional process between wind dominated and buoyancy dominated ventilation modes, and the effects of initial condition has been obtained.
- 4) Predictions of flow directions through openings are made using C_p data alone. The steady model and the QT model have been extended to multiple openings and have been shown to work reasonably. Comparison of QT model with measurement for multiple openings was made with and without buoyancy.
- 5) Improvements have been made to the experimental techniques. Precise checks on the accuracy of the techniques with multiple-stack model with no orifices have been made. A more precise unsteady calibration technique has been developed. It was found that the higher internal velocities associated with multiple openings can affect the internal pressure measurements when there is flow reversal. Therefore, the pressure measurement technique has been improved to remedy this problem.

8.4 Discussion about possibilities of integrating the findings of this thesis into design guides/tools.

Natural ventilation is a broad topic. In terms of initial design process of a natural ventilated building, it can be treated as simple as using an empirical theoretical model given pressure input from secondary source regardless of any uncertainties encountered in practice. One can also carry out wind tunnel tests to obtain the pressure source for the conventional theoretical calculations. Additionally, CFD simulation is a powerful tool to acquire detailed flow pattern of a ventilated building, yet in some extent rely on the user's level of experience; it is more suitable for later stage detailed design. There are many ventilation design guides, i.e. (Allard, 1998; Liddament, 1996; CIBSE AM10, 2005). The design procedure was also reviewed by many researchers, i.e. (Chiu, 2004; Carey, 2005). However they all require that the designers be familiar with basic physical knowledge of ventilation. How to link the research outcome and the design guidance? As an effective solution, software is a convenient tool for designers such as architects and engineers.

8 Conclusions, discussions, and suggestions for future work

There are numerous building simulation software, some concentrate on ventilation (e.g. COMIS), more of them incorporate natural ventilation in whole building energy simulations, such as IES, ESP-r, etc. There are basically two main types of calculation methods for natural ventilation, which are CFD and envelope flow model (conventional steady model). The former is time consuming and more suitable for detailed design stage. The latter is more applicable for initial design stage. As stated in Chapter 6, the envelope flow model results are sensitive to the chosen discharge coefficients and pressure coefficients. Yet, the uncertainties of these are represented in the software which uses simplified data of those two important parameters. Take ESP-r for example, a fixed C_z of 0.65 is used for all openings. C_p only relates to the building aspect ratio and wind direction. It is straightforward how to improve the accuracy of this kind of software.

In terms of C_p , wind tunnel measurement is preferable yet expensive and time consuming. It is worth a 'once for all' efforts to measure C_p of various building shapes, surrounding building densities and wind directions, etc. An adequate database of pressure coefficients is needed e.g. (Tamura, 2010). These databases could be developed into software like a ' C_p generator'; or they could go directly into ventilation or building simulation software. In terms of C_z , for sharp edged openings, wind direction should be required as an input from the user. For long openings, the curve fit of Figure 4.18 could be used as a simple source. For special openings, the software could function a 'shape factor' or 'installation factor' to formulate the user input of the physical descriptions of the opening such as hung window shape, cowl length and angle, etc., linking the built in data source of special opening C_z .

Certain nondimensional graphs can be used as a diagnosis tool, for example Figure 6.25 could be used to detect flow reversal of stacks in extreme weather conditions. In a word, the principle is to limit the user input to the description of the building and the local climate, make the input of the two parameters C_p and C_z as an optional function for people who know

8 Conclusions, discussions, and suggestions for future work

the physical details. The ideal situation would be: the user input a building and local climate, the flow pattern of natural ventilation is correctly presented to the user.

The conventional steady model is mostly adequate for the initial design stage, yet if the steady model predicts possible undesirable flow reversals, one may need to use the QT model to investigate the flow reversal in more detail. If details of flow pattern of a natural ventilated building are required, wind tunnel measurement is still a preferable way.

In addition, there is a design ‘warning’ for stack ventilation. As discovered in Chapter 5, Section 5.3.2, for multiple stack ventilation without lower orifices, the flow pattern through the stacks could change due to an initial perturbation, thus a mechanical system can be installed to assist establishing an initial condition to avoid any undesirable flow patterns.

8.5 Suggestions for future work.

- 1) Test C_z of sharp-edged orifice in the leeward wall.
- 2) There are uncertainties about the effect of external flow on C_z of sharp-edged orifices. e.g. C_z relates with the local cross flow velocity, which changes with the wind direction, and the values are different for different façade. Therefore more information is needed. C_z of leeward side orifice be treated separately based on future testing results.
- 3) Investigate the effect of correlation of pressures coefficients on ventilation rates theoretically. One can also look into the measurements: are there any effects of the pressure correlation on flow patterns?
- 4) Buoyancy and wind combined tests are still in preliminary stage, in future studies one could use a heater and temperature probes of broader capacity to reach steady states, e.g. to reach higher internal temperature to satisfy similarity requirement.
- 5) The datasets in this thesis maybe used to test the role of CFD as a method to predict ventilation, to validate CFD as a reliable tool for the purpose of natural ventilation design.

Appendix I Matlab programme

I.1 Main programme

```
% EUS2TH5lap.m
% 2 sharp-edged orifice (1) and 4 stack (2) with non-constant Cz.
% The Cz coefficients for the stack depends on flow direction.
% Cp from Time History. "1" for orifice, "2" for stack

global A1 A2 B1 B2 D1Windward D1Leeward D2
global runn yinit tinit hr
global tcp
global npoints
global pc11 pc12 pc13 pc14
global pc21 pc22 pc23 pc24
global jperiod
global mqf11 mqf12 mqf21 mqf22 mqf23 mqf24 mq11 mq12 mq21 mq22 mq23 mq24 mcomp mabsc
global mcp11 mcp12 mcp21 mcp22 mcp23 mcp24 mdelcp11 mdelcp12 mdelcp21 mdelcp22 mdelcp23 mdelcp24
global mrtdelcp1
global t1 kdum
global CZREL2 CZREL1 CZINF1 CZINF1Windward CZINF1Leeward CZINF2
global KC2 KBb2
global m1 m2 m3 m4 r1 r2 r3 r4
global tcp pc11 pc12 pc13 pc14 pc21 pc22 pc23 pc24

% Basic properties
dynam=25.18;
%dynam=input('Enter dynamic pressure in Pa ')
density=1.207;
%density=input('Enter density ')
kinv=0.000015;
ur=sqrt(2*dynam/density);
volume=0.02275;
speedsnd=340;
```

Appendix I Matlab programme

```
% Input data Opening - sharp edge
dh1=0.0163
l1=0
%CZINF1=input('Enter CZINF1 ')
CZINF1Windward=0.1;
CZINF1Leeward=0.68;
% Input data Stack - long opening
dh2=0.0168;
l2=0.188;
%C2=input('Enter C for stack opening 2 upward flow ')
C2=195.57
%Bb2=input('Enter B for stack opening 2 upward flow ')
Bb2=6.5305
%C2rev=input('Enter C for stack opening 2 REVERSED flow ')
C2rev=154.88
%Bb2rev=input('Enter B for stack opening 2 REVERSED flow ')
Bb2rev=4.0109
KC2=C2/C2rev
KBb2=Bb2/Bb2rev

% Calcs for Stack
area2=3.1416*dh2*dh2/4
aa2=density*Bb2rev/(2*area2*area2)
bb2=density*kinv*C2rev*l2/(2*area2*dh2*dh2)
ab22=aa2/(bb2*bb2)
ab2=aa2/bb2
CZINF2=sqrt(1/Bb2rev)
CZREL2=0.5*sqrt(1/(0.5*density*ur*ur*ab22));

% Other data
%H=1.0;
B1=0.0;
B2=0.0;
% h ref = length of stack l2
```

Appendix I Matlab programme

```
hr=l2;

% Calcs from input data

le1=l1+dh1;

A1=hr/le1;

%A1=input('Enter A1 = H/Le ')

area1=3.1416*dh1*dh1/4;

le2=l2+1.67*dh2;

%le2=l2+dh2;

A2=hr/le2;

%A2=input('Enter A2 = H/Le ')

area2=3.1416*dh2*dh2/4;

D1Leeward=2*CZINF1Leeward*area1*hr*speedsnd*speedsnd/(volume*ur*ur);

D1Windward=2*CZINF1Windward*area1*hr*speedsnd*speedsnd/(volume*ur*ur);

D2=2*CZINF2*area2*hr*speedsnd*speedsnd/(volume*ur*ur);

tinit=0;

% B1=input('Enter B1 = ArZ/H ')

% B2=input('Enter B2 = ArZ/H ')

%D=input('Enter D ')

% Define Pressure coefficient/time matrices

npoints=4096

%npoints=input('Enter number of pressure data points ')

pc11=zeros(npoints,1);

pc12=zeros(npoints,1);

%pc13=zeros(npoints,1); not enough PT

%pc14=zeros(npoints,1);

pc21=zeros(npoints,1);

pc22=zeros(npoints,1);

pc23=zeros(npoints,1);

pc24=zeros(npoints,1);

tcp=zeros(npoints,1);
```

Appendix I Matlab programme

```
% file elp11.txt is dimensional pressure (Pa) for opening 1
% file elp12.txt is dimensional pressure (Pa) for opening 2
% file elp21.txt is dimensional pressure (Pa) for Stack 1
% file elp22.txt is dimensional pressure (Pa) for Stack 2
% file elp23.txt is dimensional pressure (Pa) for Stack 3
% file elp24.txt is dimensional pressure (Pa) for Stack 4
```

```
[fid,message]=fopen('elp11.txt','r');
```

```
disp(message)
```

```
[pc11,count]=fscanf(fid,'%g',npoints);
```

```
status=fclose(fid)
```

```
d=size(pc11);
```

```
[fid,message]=fopen('elp12.txt','r');
```

```
disp(message)
```

```
[pc12,count]=fscanf(fid,'%g',npoints);
```

```
status=fclose(fid)
```

```
d=size(pc12);
```

```
[fid,message]=fopen('elp21.txt','r');
```

```
disp(message)
```

```
[pc21,count]=fscanf(fid,'%g',npoints);
```

```
status=fclose(fid)
```

```
d=size(pc21);
```

```
[fid,message]=fopen('elp22.txt','r');
```

```
disp(message)
```

```
[pc22,count]=fscanf(fid,'%g',npoints);
```

```
status=fclose(fid)
```

```
d=size(pc22);
```

```
[fid,message]=fopen('elp23.txt','r');
```

```
disp(message)
```

```
[pc23,count]=fscanf(fid,'%g',npoints);
```

```
status=fclose(fid)
```

Appendix I Matlab programme

```
d=size(pc23);

[fid,message]=fopen('elp24.txt','r');
disp(message)
[pc24,count]=fscanf(fid,'%g',npoints);
status=fclose(fid)
d=size(pc24);

% Fill the matrix tcp (time)
fsamp=120
%fsamp= input('Enter sampling frequency in Hz = ')
for j=1:count
    tcp(j)=(j-1)/fsamp;
end

% Nondimensionalise the pressures
pc11=pc11/(0.5*1.2*ur*ur);
pc12=pc12/(0.5*1.2*ur*ur);
pc21=pc21/(0.5*1.2*ur*ur);
pc22=pc22/(0.5*1.2*ur*ur);
pc23=pc23/(0.5*1.2*ur*ur);
pc24=pc24/(0.5*1.2*ur*ur);
tcp=tcp*ur/hr;

pc11bar=mean(pc11);
pc12bar=mean(pc12);
pc21bar=mean(pc21);
pc22bar=mean(pc22);
pc23bar=mean(pc23);
pc24bar=mean(pc24);
tend=tcp(count);

yinit1=0.02;
yinit2=-0.02;
yinit3=0.02;
```

Appendix I Matlab programme

```
yinit4=-0.02;
yinit5=0.02;
yinit6=-0.02;
yinit7=0.0;
%runn=1
runn=input('Enter Run number ')

ncalc=1
%ncalc=input('Enter number of calculation periods ')
tper=tend/ncalc;
nperiod=(npoints)/ncalc;

% main loop. End comes at end
for jperiod=1:ncalc
clear t y

t2=jperiod*nperiod;
t1=(jperiod-1)*nperiod;
if t1==0
    t1=1
end

kdum=t1+2;
tspan=tc(t1:t2);

% options=odeset('reltol',1e-2,'abstol',1e-4);
[t,y]=ode45('EUS2T5',[tspan],[yinit1 yinit2 yinit3 yinit4 yinit5 yinit6 yinit7]);

n=size(y,1)
jperiod

% initial values for next period
yinit1=y(n,1)
yinit2=y(n,2)
yinit3=y(n,3)
```

Appendix I Matlab programme

```
yinit4=y(n,4)
yinit5=y(n,5)
yinit6=y(n,6)
yinit7=y(n,7)
tinit=t(n)

q11(t1:t2,1)=y(:,1);
q12(t1:t2,1)=y(:,2);
q21(t1:t2,1)=y(:,3);
q22(t1:t2,1)=y(:,4);
q23(t1:t2,1)=y(:,5);
q24(t1:t2,1)=y(:,6);
cpi(t1:t2,1)=y(:,7);
end

% Allocate arrays to q1, q2 and comp etc. to speed up calculation
n=npoints
delcp1=zeros(n,1);
delcp12=zeros(n,1);
delcp21=zeros(n,1);
delcp22=zeros(n,1);
delcp23=zeros(n,1);
delcp24=zeros(n,1);

qf11=zeros(n,1);
qf12=zeros(n,1);
qf21=zeros(n,1);
qf22=zeros(n,1);
qf23=zeros(n,1);
qf24=zeros(n,1);
%rtdelcp=zeros(n,1);
%rtdelcp1=zeros(n,1);
comp=D1Leeward*q11+D1Windward*q12+D2*q21+D2*q22+D2*q23+D2*q24;

delcp11=pc11-cpi;
```

Appendix I Matlab programme

```
delcp12=pc12-cpi;
delcp21=pc21-cpi;
delcp22=pc22-cpi;
delcp23=pc23-cpi;
delcp24=pc24-cpi;

% Calculation of Qfresh1 and Qfresh2
qf11 = q11;
for i=1:n
    if q11(i) < 0
        qf11(i)=0;
    end
end

qf12 = q12;
for i=1:n
    if q12(i) < 0
        qf12(i)=0;
    end
end

qf21 = q21;
m1=0;
for i=1:n
    if q21(i) < 0
        qf21(i)=0;
    else m1=m1+1;
    end
end
r1=m1/npoints

qf22 = q22;
m2=0;
for i=1:n
    if q22(i) < 0
```

Appendix I Matlab programme

```
    qf22(i)=0;
else m2=m2+1;
end
end
r2=m2/npoints

qf23 = q23;
m3=0;
for i=1:n
    if q23(i) < 0
        qf23(i)=0;
    else m3=m3+1;
    end
end
r3=m3/npoints

qf24 = q24;
m4=0;
for i=1:n
    if q24(i) < 0
        qf24(i)=0;
    else m4=m4+1;
    end
end
r4=m4/npoints

mq11=mean(q11)*CZINF1Leeward
mq12=mean(q12)*CZINF1Windward
mq21=mean(q21)*CZINF2
mq22=mean(q22)*CZINF2
mq23=mean(q23)*CZINF2
mq24=mean(q24)*CZINF2

mqf11=mean(qf11);
mqf12=mean(qf12);
```

Appendix I Matlab programme

```
mqf21=mean(qf21);
mqf22=mean(qf22);
mqf23=mean(qf23);
mqf24=mean(qf24);

mcomp=mean(comp);
mabsc=mean(abs(comp));
mcp11=mean(pc11)
mcp12=mean(pc12)
mcp21=mean(pc21)
mcp22=mean(pc22)
mcp23=mean(pc23)
mcp24=mean(pc24)

mdelcp11=mean(delcp11);
mdelcp12=mean(delcp12);
mdelcp21=mean(delcp21);
mdelcp22=mean(delcp22);
mdelcp23=mean(delcp23);
mdelcp24=mean(delcp24);
%mrtdelcp1=mean(rtdelcp1);

% Plot results
figure(1)
subplot(2,1,1)
US2THQPL
subplot(2,1,2)
US2THCPL

[fid,message]=fopen('thres.txt','wt');
disp(message)
count=fprintf(fid,'%g\n',tcp,q11,q12,q21,q22,q23,q24,cpi,pc11,pc12,pc21,pc22,pc23,pc24)
status=fclose(fid)

fprintf(fid,'%10.8f',t(k));
```

Appendix I Matlab programme

```
fprintf(fid,'%10.8f\t',y(k,1));
fprintf(fid,'%10.8f\t',y(k,2));
fprintf(fid,'%10.8f\t',y(k,3));
fprintf(fid,'%10.8f\t',y(k,4));
fprintf(fid,'%10.8f\t',y(k,5));
fprintf(fid,'%10.8f\t',y(k,6));
fprintf(fid,'%10.8f\t',y(k,7));

end

fclose(fid)
```

I.2 Nondimensional equations

% 2 sharp-edged and 4 long openings in UNSTEADY flow with Cz dependent

% on flow direction for long opening 2

function dy = EUS2T5(t,y);

global A1 A2 B1 B2 D1Leeward D1Windward D2 t1

global CZREL2 CZINF1 CZINF1Leeward CZINF1Windward CZINF2

```
dy=[0.5*A1*(-y(7)-2*B1 + cp11th(t,t1)-(y(1)/abs(y(1)))2)*y(1)^2/CZINF1Leeward;
    0.5*A1*(-y(7)-2*B1 + cp12th(t,t1)-(y(2)/abs(y(2)))2)*y(2)^2/CZINF1Windward;
    0.5*A2*(-y(7)-2*B2 + cp21th(t,t1)-kflowb(y(3))*(y(3)/abs(y(3)))2)*y(3)^2-kflowc(y(3))*2*CZREL2*y(3))/CZINF2;
    0.5*A2*(-y(7)-2*B2 + cp22th(t,t1)-kflowb(y(4))*(y(4)/abs(y(4)))2)*y(4)^2-kflowc(y(4))*2*CZREL2*y(4))/CZINF2;
    0.5*A2*(-y(7)-2*B2 + cp23th(t,t1)-kflowb(y(5))*(y(5)/abs(y(5)))2)*y(5)^2-kflowc(y(5))*2*CZREL2*y(5))/CZINF2;
    0.5*A2*(-y(7)-2*B2 + cp24th(t,t1)-kflowb(y(6))*(y(6)/abs(y(6)))2)*y(6)^2-kflowc(y(6))*2*CZREL2*y(6))/CZINF2;
    +D1Leeward*y(1)+D1Windward*y(2)+D2*(y(3)+y(4)+y(5)+y(6))];
```

I.3 Import of pressures

% cp11th.m for time history values

function cp11th = cp11th(tpres, kinit)

% defines mean and fluctuating pressure as function of time

global tcp pc11 pc12 pc21 pc22 pc23 pc24

global kdum

Appendix I Matlab programme

```
if tpres <=tcp(kinit+1)
    k=(kinit+1);
    else k=kdum;
end
```

```
while tpres>tcp(k)
    k=k+1;
    kdum = k;
end
```

I.4 Flow sign function

```
function kflowb=kflowb(flowsign);
%Functions for determing flow coefficient B to be used in
%differential equations
global KBb2 KC2
%flowsign
kflowb=1;
if flowsign<0
    kflowb=KBb2;
end
%kflowb
%end
```

```
function kflowc=kflowc(flowsign);
%Functions for determing flow coefficient C to be used in
%differential equations
global KBb2 KC2
kflowc=1;
if flowsign<0
    kflowc=KC2;
end
```

Appendix II Deduction of nondimensional equations of QT model

Introduced in Chapter 2, the set of dimensional equations of QT model are:

$$\text{Long opening} \quad \rho \frac{dq_i(t)}{dt} \frac{l_{ei}}{A_i} = -p_{I0m}(t) - \Delta\rho g z_i + p_{wm}(t) - a q_i(t)^2 - b q_i(t) \quad (9.1)$$

$$\text{Sharp-edged opening} \quad \rho \frac{dq_i(t)}{dt} \frac{l_{ei}}{A_i} = -p_{I0m}(t) - \Delta\rho g z_i + p_{wm}(t) - a q_i(t)^2 \quad (9.2)$$

$$\text{Mass conservation} \quad \frac{V}{n} \frac{1}{p_{I0}} \frac{dp_{I0m}(t)}{dt} = \sum_{i=0}^n q_i(t) \quad (9.3)$$

1) Long opening: Equation (9.1)

For long opening, using different a and b for different flow directions, inward flow is defined as positive, equation (9.1) becomes (9.4) and (9.5) for different directions

$$\text{Inward flow} \quad \rho \frac{dq_i(t)}{dt} \frac{l_{ei}}{A_i} = -p_{I0m}(t) - \Delta\rho g z_i + p_{wm}(t) - a_+ q_i(t)^2 - b_+ q_i(t) \quad (9.4)$$

$$\text{Upward flow} \quad \rho \frac{dq_i(t)}{dt} \frac{l_{ei}}{A_i} = -p_{I0m}(t) - \Delta\rho g z_i + p_{wm}(t) + a_- q_i(t)^2 - b_- q_i(t) \quad (9.5)$$

The sign before a_- changes because for upward flow, flow rate $q_i(t)$ and total pressure difference are all negative. $|\overline{\Delta P}| = -a_- q_i\{t\}^2 + b_- q_i\{t\}$

Define two nondimensional terms:

$$\text{Nondimensional flow rate} \quad q'_i(t) \equiv \frac{q_i(t)}{C_{z\infty} A_i U} \quad (9.6)$$

$$\text{Nondimensional time} \quad t' \equiv t \frac{U}{H} \quad (9.7)$$

where H is the reference height

$C_{z\infty}$ is the discharge coefficient when Re_{st} is infinity in equation (9.8) and (9.9)

$$\text{Inward flow} \quad \frac{1}{C_z^2} = C_+ \frac{L}{Re_{st} d} + D_+ \quad (9.8)$$

Appendix II Deduction of nondimensional equations of QT model

$$\text{Upward flow} \quad \frac{1}{C_z^2} = C_- \frac{L}{Re_{st}d} + D_- \quad (9.9)$$

where d is the diameter of the long opening

An arbitrary $C_{z\infty}$ is set to use the value when Re_{st} is infinity for either directions (in theory they should not be of much difference), but this has to be consistent through the calculation process. Here it is defined to use the inward flow value:

$$C_{z\infty} = \frac{1}{\sqrt{D_+}} \quad (9.10)$$

Substituting equation (9.10) into (9.6)

$$q_i(t) = A_i U \frac{1}{\sqrt{D_+}} q'_i(t) \quad (9.11)$$

Differential of equation (9.6)

$$\frac{dq_i(t)}{dt} = \frac{C_{z\infty} A_i U}{\frac{H}{U}} \frac{dq'_i(t)}{dt'} = C_{z\infty} A_i \frac{U^2}{H} \frac{dq'_i(t)}{dt'} \quad (9.12)$$

Substituting (9.11) and (9.12) into equation (9.4) and (9.5)

$$C_{z\infty} \frac{l_{ei}}{H} \rho U^2 \frac{dq'_i(t)}{dt'} = -p_{I0m}(t) - \Delta \rho g z_i + p_{wm}(t) - a_+ A_i^2 U^2 \frac{1}{D_+} q_i'^2(t) - b_+ A_i U \frac{1}{\sqrt{D_+}} q'_i(t) \quad (9.13)$$

$$C_{z\infty} \frac{l_{ei}}{H} \rho U^2 \frac{dq'_i(t)}{dt'} = -p_{I0m}(t) - \Delta \rho g z_i + p_{wm}(t) + a_- A_i^2 U^2 \frac{1}{D_+} q_i'^2(t) - b_- A_i U \frac{1}{\sqrt{D_+}} q'_i(t) \quad (9.14)$$

Divide equation (9.13) and (9.14) by $\frac{\rho U^2}{2}$, and substituting $A_r = \frac{\Delta \rho \cdot gh}{\rho U^2}$

$$\frac{dq'_i(t)}{dt'} = \frac{1}{2C_{z\infty}} \frac{H}{l_{ei}} (-C_{pI} - Ar \frac{z_i}{H} + C_{Pi} - a_+ \frac{2A_i^2}{\rho} \frac{1}{D_+} q_i'^2(t) - b_+ \frac{2A_i}{\rho U} \frac{1}{\sqrt{D_+}} q'_i(t)) \quad (9.15)$$

Appendix II Deduction of nondimensional equations of QT model

$$\frac{dq'_i(t)}{dt'} = \frac{1}{2C_{z\infty}} \frac{H}{l_{ei}} \left(-C_{pl} - Ar \frac{z_i}{H} + C_{pi} + a_- \frac{2A_i^2}{\rho} \frac{1}{D_+} q_i'^2(t) - b_- \frac{2A_i}{\rho U} \frac{1}{\sqrt{D_+}} q'_i(t) \right) \quad (9.16)$$

a , b are the same ‘things’ as C , D , but they are used in different equations: the former used in envelope flow equation, the latter in the curve fitting of discharge coefficient as a function of opening Reynolds number. For deduction process, see later part of this appendix.

$$a_+ = \frac{\rho D_+}{2A^2} \quad b_+ = \frac{C_+ L \rho v \pi}{8A^2} \quad (9.17)$$

$$a_- = \frac{\rho D_-}{2A^2} \quad b_- = \frac{C_- L \rho v \pi}{8A^2} \quad (9.18)$$

where L is the length of the long opening

Substituting (9.17) and (9.18) into (9.15) and (9.16)

$$\frac{dq'_i(t)}{dt'} = \frac{1}{2C_{z\infty}} \frac{H}{l_{ei}} \left(-C_{pl} - Ar \frac{z_i}{H} + C_{pi} - \frac{D_+}{D_+} q_i'^2(t) - C_+ \frac{Lv\pi}{4A_i U} \frac{1}{\sqrt{D_+}} q'_i(t) \right) \quad (9.19)$$

$$\frac{dq'_i(t)}{dt'} = \frac{1}{2C_{z\infty}} \frac{H}{l_{ei}} \left(-C_{pl} - Ar \frac{z_i}{H} + C_{pi} + \frac{D_-}{D_+} q_i'^2(t) - C_- \frac{Lv\pi}{4A_i U} \frac{1}{\sqrt{D_+}} q'_i(t) \right) \quad (9.20)$$

Define another two nondimensional terms

$$\text{Buoyancy} \quad B_i \equiv Ar \frac{z_i}{H} \quad (9.21)$$

$$\text{Inertia} \quad F_i \equiv \frac{H}{l_{ei}} \quad (9.22)$$

Equation (9.15) and (9.16) finally become

$$\frac{dq'_i(t)}{dt'} = \frac{F_i}{2C_{zi\infty}} \left(-C_{pl} - 2B_i + C_{pi} - \frac{D_+}{D_+} q_i'^2(t) - C_+ \frac{Lv\pi}{4A_i U} \frac{1}{\sqrt{D_+}} q'_i(t) \right) \quad (9.23)$$

$$\frac{dq'_i(t)}{dt'} = \frac{F_i}{2C_{zi\infty}} \left(-C_{pl} - 2B_i + C_{pi} + \frac{D_-}{D_+} q_i'^2(t) - C_- \frac{Lv\pi}{4A_i U} \frac{1}{\sqrt{D_+}} q'_i(t) \right) \quad (9.24)$$

Appendix II Deduction of nondimensional equations of QT model

Equation (9.23) and (9.24) are the forms used in Matlab programme for solving QT model set of equations.

2) Sharp-edged orifice: Equation (9.2)

The same process for the long opening applies, yet without the term $bq_i\{t\}$. It is easier than long opening, will not be repeated here. The final nondimensional equation used in Matlab programme is

$$\frac{dq'_i(t)}{dt'} = \frac{F_i}{2C_{zi\infty}} (-C_{pl} - 2B_i + C_{pi} - S_i q_i'^2(t)) \quad (9.25)$$

where S_i is the sign of flow direction.

3) Mass conservation: Equation (9.3)

Dimensional mass conservation equation is

$$\frac{V}{\gamma} \frac{1}{\bar{p}_{I0}} \frac{dp_{I0m}(t)}{dt} = \sum_{i=0}^n q_i(t) \quad (9.26)$$

where γ is the ratio of the specific heat of the air

The internal pressure coefficient is defined as

$$C_{pl} = \frac{P_I - P_{ref}}{0.5\rho U^2} = \frac{p_{I0m}}{0.5\rho U^2} \quad (9.27)$$

P_{I0m} is the measured internal pressure

Differential of equation (9.27)

$$\frac{dp_{I0m}}{dt} = \frac{\rho U^3}{2H} \frac{dC_{pl}}{dt'} \quad (9.28)$$

Substituting (9.28) into (9.26)

$$\frac{V\rho U^3}{2H\gamma p_{I0m}} \frac{dC_{pl}}{dt'} = \sum_{i=0}^n dq'_i(t) (C_{zi\infty} A_i U) \quad (9.29)$$

Appendix II Deduction of nondimensional equations of QT model

For an isentropic process

$$\frac{\rho}{\rho_{10m}} = \frac{\gamma}{c^2} \quad (9.30)$$

where c is the speed of sound

Therefore equation (9.29) becomes

$$\frac{VU^3}{2c^2H} \frac{dC_{pl}}{dt'} = \sum_{i=0}^n dq'_i(t) (C_{zi\infty} A_i U) \quad (9.31)$$

$$\frac{dC_{pl}}{dt'} = \sum_{i=0}^n dq'_i(t) \left(\frac{2c^2 H C_{zi\infty} A_i}{VU^2} \right) \quad (9.32)$$

Another nondimensional term is defined

$$\text{Compressibility } D_i \equiv \frac{2C_{zi\infty} A_i H c^2}{VU^2} \quad (9.33)$$

The mass conservation equation finally becomes

$$\frac{dC_{pl}}{dt'} = \sum_{i=0}^n D_i q'_i(t) \quad (9.34)$$

To sum up, the set of nondimensional equations are

Long opening

$$\frac{dq'_i(t)}{dt'} = \frac{F_i}{2C_{zi\infty}} (-C_{pl} - 2B_i + C_{Pi} - \frac{D_+}{D_+} q_i'^2(t) - C_+ \frac{Lv\pi}{4A_i U} \frac{1}{\sqrt{D_+}} q'_i(t)) \quad (9.35)$$

$$\frac{dq'_i(t)}{dt'} = \frac{F_i}{2C_{zi\infty}} (-C_{pl} - 2B_i + C_{Pi} + \frac{D_-}{D_+} q_i'^2(t) - C_- \frac{Lv\pi}{4A_i U} \frac{1}{\sqrt{D_+}} q'_i(t)) \quad (9.36)$$

Sharp-edged orifice

$$\frac{dq'_i(t)}{dt'} = \frac{F_i}{2C_{zi\infty}} (-C_{pl} - 2B_i + C_{Pi} - S_i q_i'^2(t)) \quad (9.37)$$

Appendix II Deduction of nondimensional equations of QT model

where S_i is the sign of flow direction.

Mass conservation

$$\frac{dC_{pl}}{dt'} = \sum_{i=0}^n D_i q_i'(t) \quad (9.38)$$

4) Transform between a, b and C, D

$$\frac{1}{C_z^2} = C \frac{L}{Re_{st}d} + D \quad (9.39)$$

$$C_z \equiv \frac{|q|}{A} \sqrt{\frac{\rho}{2|\Delta P|}} \quad (9.40)$$

$$\frac{|q|}{A} = u, \quad A = \frac{\pi d^2}{4}, \quad Re_{st} = \frac{\rho u d}{\mu}$$

Substituting (I.40) into (I.39)

$$\Delta P = \frac{\rho D}{2A^2} q^2 + \frac{\pi L \mu C}{8A^2} q \quad (9.41)$$

Therefore

$$a = \frac{\rho D}{2A^2} \quad (9.42)$$

$$b = \frac{\pi L \mu C}{8A^2} \quad (9.43)$$

Appendix III Three-dimensional CFD simulation

Three-dimensional CFD simulations were carried out in order to get some insights of the flow field within the box. The two dimensional simulation is to investigate the influence of the opening facing the approaching wind on the internal pressure tapping. The three-dimensional simulation is to study the flow field within the box (with and without the internal pressure tapping cup cover), and the variation of internal surface static pressure compared to the pressure difference across the openings (without the internal pressure tapping cup cover).

III.1 Case description

The internal space of the model was set as the calculation domain. The inputs for the velocities of the openings and the two stacks were obtained from TPU tests results. There were approximately 20000 meshing cells (Figure III.1). For example, for the case of (S4_O2_0_NoCup), the velocity of orifice 2 is from TPU results (inward as positive) which is 0.62 m/s, stack 4 was set as outflow. Orifice 2 has to be set as a uniform velocity inlet, the flow is a forced jet. This is not the true flow pattern through orifice 2 in the wind tunnel. Therefore in addition to the coarse meshing, the 3D simulation results should be treated qualitatively rather than quantitatively. N.B. due to the capacity of the computer, the simulation domain was set to be the space within the box, rather than the wind tunnel; $k - \xi$ model was used rather than Large Eddy simulation.

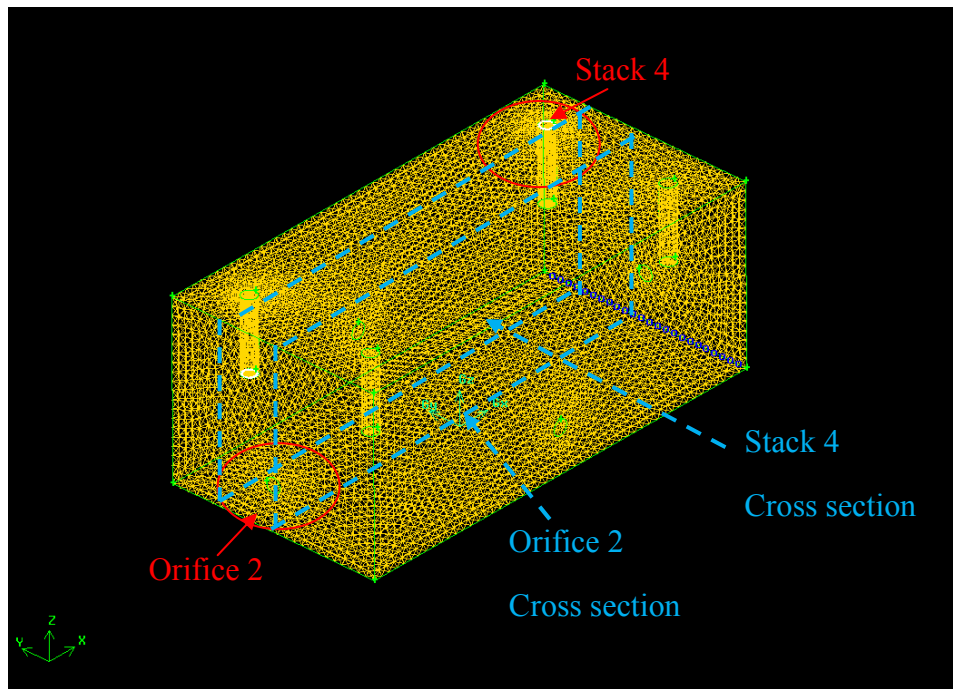


Figure III.1 Meshing cells of three dimensional model

Figure III.2 and Figure III.3 show the flow field with and without the toplless cover of P_{in} , for two cross sections (combined), one is orifice 2 cross section, the other is the stack 4 cross section.

Appendix III Three-dimensional CFD simulation

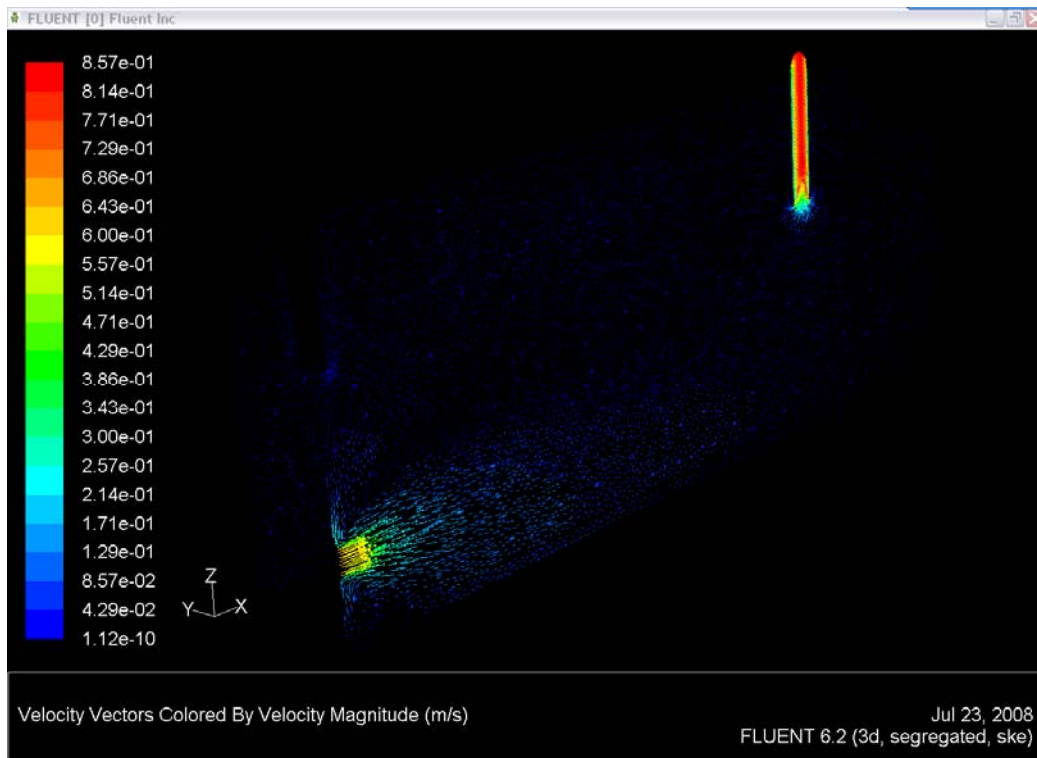


Figure III.2 Flow field of two cross sections of (S4_O2_0_NoCup)

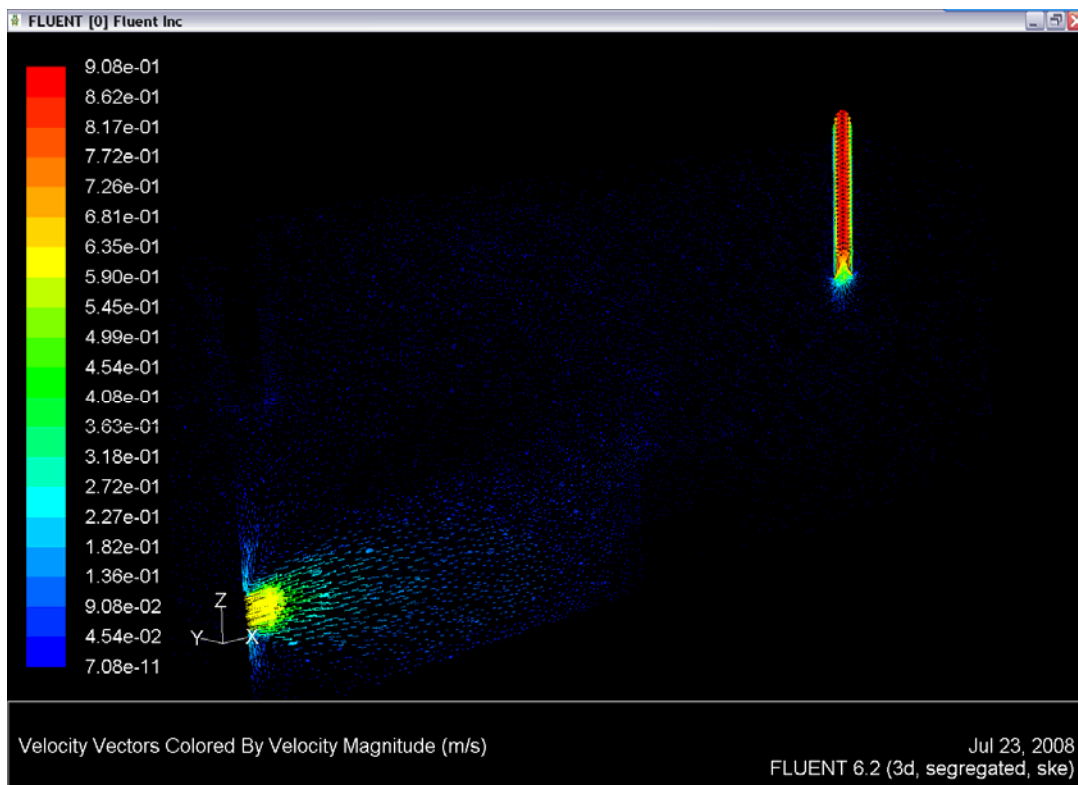


Figure III.3 Flow field of two cross sections (S4_O2_CoverPin)

III.2 Investigation of the location of the internal pressure tapping by studying the static pressure distribution within at the internal surface

III.2.1 Static pressure across the internal surface

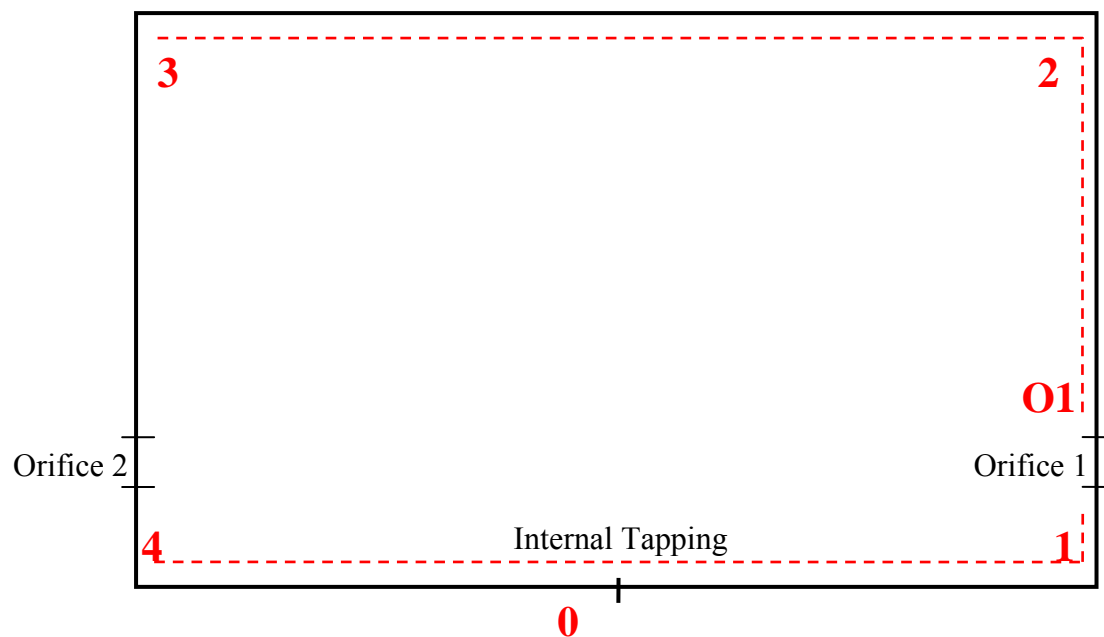


Figure III.4 Central cross section

Figure III.5 and Figure III.6 show the static pressure of the bottom line and the top line of the central cross section (orifice 2 cross section Figure III.4) with a change of opening flow rate. Velocities of orifice 2 are 0.62 m/s, 1.24 m/s, and 2.48 m/s. They also show the increasing factors of the static pressure, e.g. 'Increase Factor 1.24 vs 0.62' means the static pressure of $U_{ref} = 1.24 \text{ m/s}$ divided by the static pressure of $U_{ref} = 0.62 \text{ m/s}$.

Appendix III Three-dimensional CFD simulation

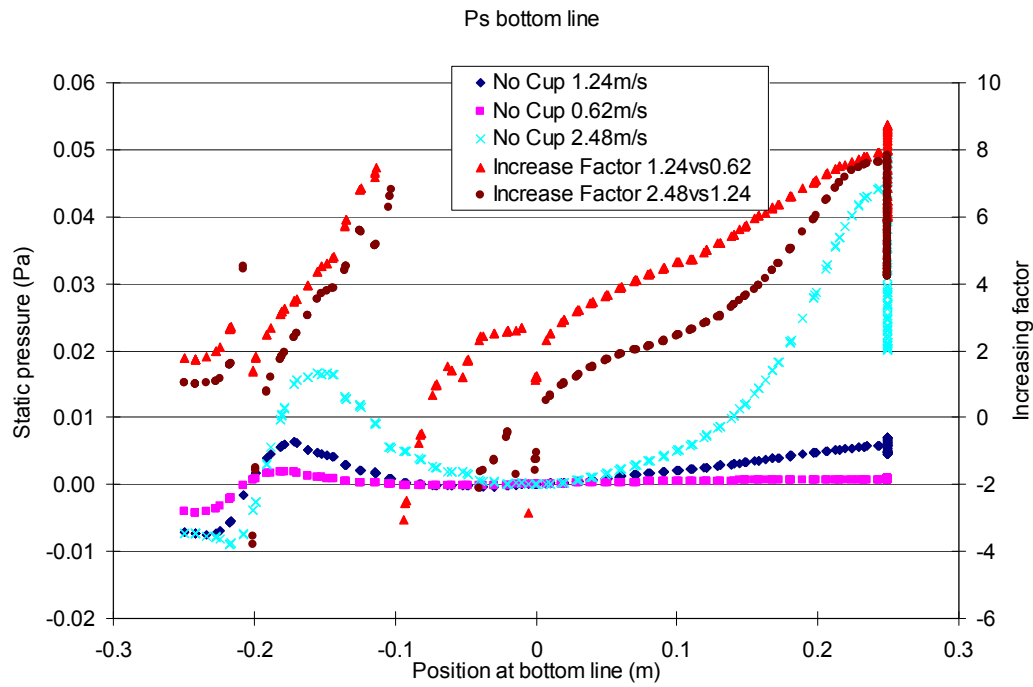


Figure III.5 Comparison of static pressure of the bottom line (0-1, 1-01, 01-2, 4-0)

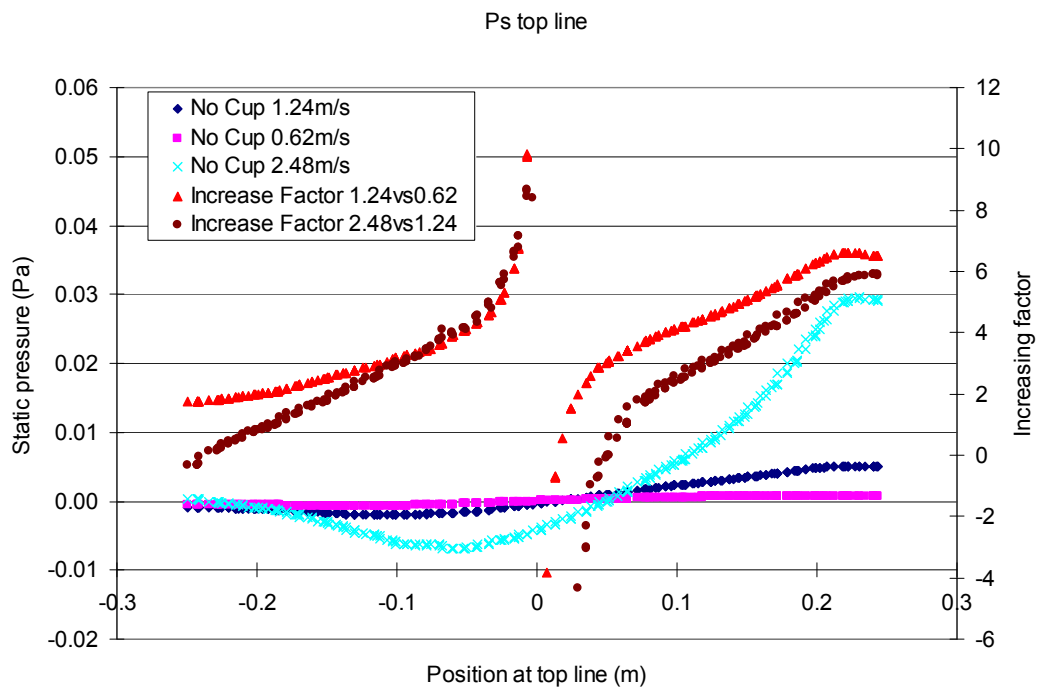


Figure III.6 Comparison of static pressure of the top line (2-3)

Appendix III Three-dimensional CFD simulation

It can be seen from the above two figures that when the flow rate doubles, the static pressure of the cross section increases by a factor of approximately 4 (as roughly expected from dimensional analysis). Average factors are 4.59 (1.24 m/s vs. 0.62 m/s) and 3.49 (2.48 m/s vs. 1.24 m/s).

Figure III.7 and Figure III.8 are non-dimensional forms of Figure III.5 and Figure III.6, which show the variation of the static pressure coefficient C_p along the cross section surface. The three curves of three different opening flow rates partly line up, which indicates that the non-dimensional static pressure of the middle part of the cross section is independent of the flow rate, whereas it is not the case for the that of the corners, where the opening Reynolds number effect occurs. Nevertheless it is clear that the static pressure variation (Pa) increases rapidly with the number of openings. Although the pressures are small (see Figure II.05 where they are all less than 0.1 Pa), these changes are significant when the stack flow is reversing.

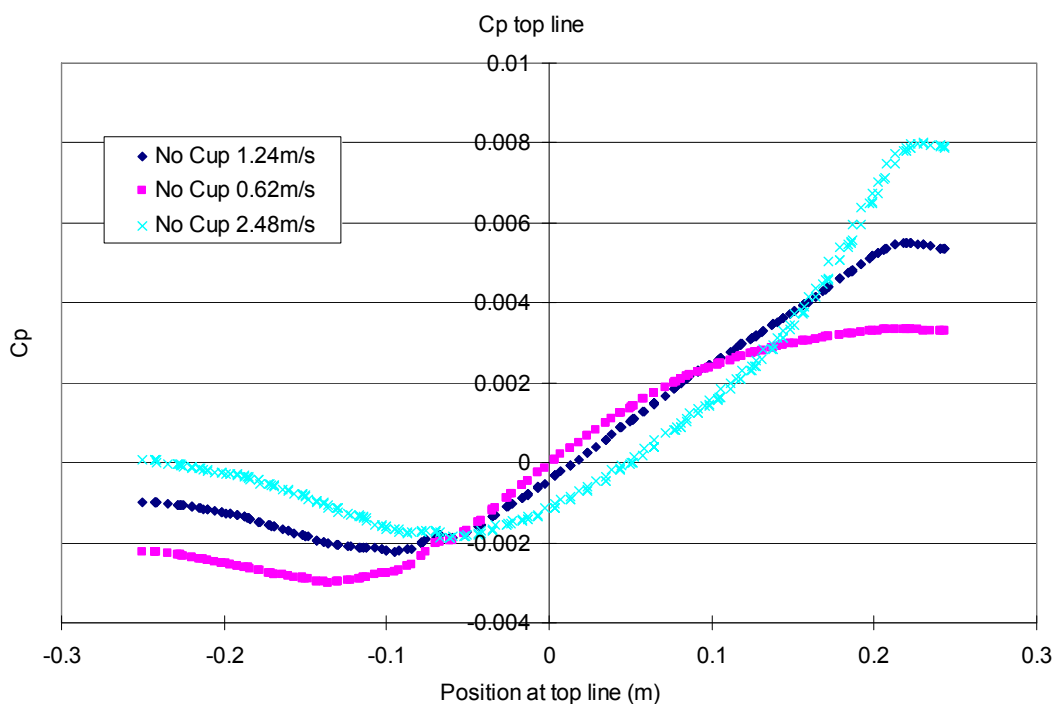


Figure III.7 Pressure Coefficient C_p Top line

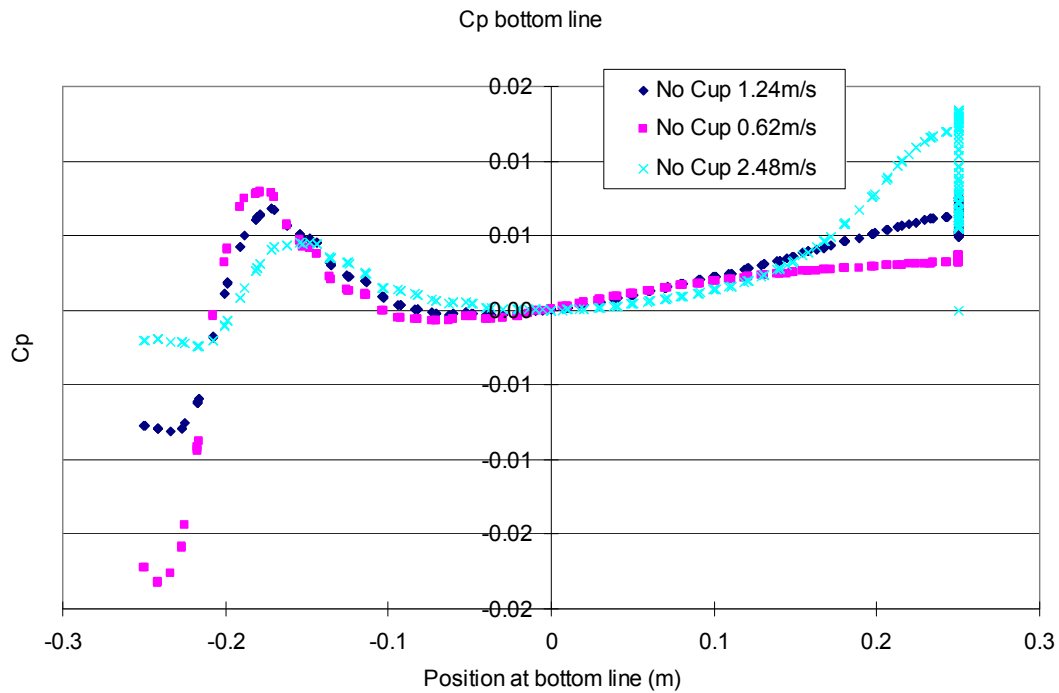


Figure III.8 Pressure Coefficient C_p Bottom line

III.2.2 Importance of internal pressure tapping location

From equations: $C_z \equiv \frac{\bar{q}}{A} \sqrt{\frac{\rho}{2|\Delta P|}}$, $|\Delta P| = \frac{1}{2} \rho U_{ref}^2$, one can get that $|\Delta C_p| = \left(\frac{\bar{u}}{U_{ref}} \right)^2 \frac{1}{C_z^2}$. When the flow is reversing and ΔP is close to zero, the position of the internal pressure tapping matters the most, and the problem of the internal velocity is at its most.

Reference List

- Wind-induced natural ventilation analysis (2007). *Solar Energy*, 81, 20-30.
- Allard, F. (1998). *Natural ventilation in buildings--A design handbook*. James & James (Science Publishers) Ltd.
- Awbi, H. B. (1991). *Ventilation of Buildings*. E & FN Spon.
- Beste, F. & Cermak, J. E. (2007). Correlation of internal and area-averaged external wind pressures on low-rise buildings. *Journal of Wind Engineering and Industrial Aerodynamics*, 69-71, 557-566.
- Bruun, H. H. (1995). *Hot-Wire Anemometry Principles and Signal Analysis*. New York, Oxford University Press Inc.
- Carey, P. S. (2005). *Direct wind tunnel modelling of natural ventilation for design purpose*.
- Carey, P. S. & Etheridge, D. W. (1999). Direct wind tunnel modelling of natural ventilation for design purposes. *Building Services Engineering Research and Technology*.
- Chang, C.-H. & Meroney, R. N. (2003). The effect of surroundings with different separation distances on surface pressures on low-rise buildings. *Journal of Wind Engineering and Industrial Aerodynamics*, 91, 1039-1050.
- Chenvidyakarn, T. & Woods, A. (2005). Multiple steady states in stack ventilation. *Building and Environment*, 40, 399-410.
- Chenvidyakarn, T. & Woods, A. W. (2010). On the natural ventilation of two independently heated spaces connected by a low-level opening. *Building and Environment*, 45, 586-595.

- Chiu, Y. H. & Etheridge, D. W. (2007). External flow effects on the discharge coefficients of two types of ventilation opening. *Journal of Wind Engineering and Industrial Aerodynamics*, 95, 225-252.
- Chiu, Y.-H. (2004). *Development of unsteady design procedures of natural ventilation stacks*. PhD thesis, the University of Nottingham.
- Chiu, Y.-H. & Etheridge, D. W. (2002). Calculations and notes on the quadratic and power law equations for modelling infiltration. *International Journal of Ventilation*, 1, 65-77.
- Chiu, Y.-H. & Etheridge, D. W. (2004). Experimental technique to determine unsteady flow in natural ventilation stacks at model scale. *Journal of Wind Engineering and Industrial Aerodynamics*, 92, 291-313.
- Chu, C. R., Chiu, Y. H., Chen, Y. J., Wang, Y. W., & Chou, C. P. (2009). Turbulence effects on the discharge coefficient and mean flow rate of wind-driven cross-ventilation. *Building and Environment*, 44, 2064-2072.
- CIBSE AM10 (2005). *Natural ventilation in non-domestic buildings CIBSE Applications Manual AM10*. CIBSE Publications.
- Cook, N. J. (1985). *The designer's guide to wind loading structures part 1*. The University Press, Cambridge.
- Cooper, E. W. & Etheridge, D. W. (2007). Wind tunnel investigation of unsteady flow in a natural ventilation stack. In *Second WERC International Symposium on Architectural Wind Engineering*.
- Costola, D. & Alucci, M. (2007). Pressure coefficient simulated by CFD for wind-driven ventilation analysis. In (pp. 999-1006).
- Costola, D., Blocken, B., & Hensen, J. L. M. (2009). Overview of pressure coefficient data in building energy simulation and airflow network programs. *Building and Environment*, 44, 2027-2036.

- Costola, D., Blocken, B., Ohba, M., & Hensen, J. L. M. (2010). Uncertainty in airflow rate calculations due to the use of surface-averaged pressure coefficients. *Energy and Buildings*, 8-15.
- Costola, D. & Etheridge, D. W. (2007). Unsteady natural ventilation at model scale--Flow reversal and discharge coefficients of a short stack and an orifice. *Building and Environment*, 43, 1491-1506.
- Eftekhari, M. M., Marjanovic, L. D., & Pinnock, D. J. (2003). Air flow distribution in and around a single-sided naturally ventilated room. *Building and Environment*, 38, 389-397.
- Etheridge, D. W. (2000a). Unsteady flow effects due to fluctuating wind pressures in natural ventilation design--instantaneous flow rates. *Building and Environment*, 35, 321-337.
- Etheridge, D. W. (2000b). Unsteady flow effects due to fluctuating wind pressures in natural ventilation design--mean flow rates. *Building and Environment*, 35, 111-133.
- Etheridge, D. W. (2002). Nondimensional methods for natural ventilation design. *Building and Environment*, 37, 1057-1072.
- Etheridge, D. W. (2004). Natural ventilation through large openings--measurements at model scale and envelope flow theory. *International Journal of Ventilation*, 2, 325-342.
- Etheridge, D. W. (2009). Wind turbulence and multiple solutions for opposing wind and buoyancy. *International Journal of Ventilation*, 7, 309-319.
- Etheridge, D. W., Chiu, Y.-H., & Cooper, E. W. (2004). *Effect of external flow on discharge coefficient of openings--Part 1 & 2*.
- Etheridge, D. W. & Sandberg, M. (1984). A simple parametric study of ventilation. *Building and Environment*, 19, 163-173.
- Etheridge, D. W. & Sandberg, M. (1996). *Building Ventilation Theory and Measurement*.
- Etheridge, D. W. & Stanway, R. J. (1988). A Parametric Study of Ventilation as a Basis for Design. *Building and Environment*, 23, 81-93.

- Fitzgerald, S. D. & Woods, A. W. (2004). Natural ventilation of a room with vents at multiple levels. *Building and Environment*, 39, 505-521.
- Gladstone, C. & Woods, A. (2001). On buoyancy-driven natural ventilation of a room with a heated floor. *Journal of Fluid Mechanics*, 441, 293-314.
- Haddad, K., Ertunt, Í., Mishra, M., & Delgado, A. (2010). Pulsating laminar fully developed channel and pipe flows. *Physical Review E*, 81.
- Haghighat, F., Rao, J. W., & Fazio, P. (1991). The Influence of Turbulent Wind on Air Change Rates - a Modelling Approach. *Building and Environment*, 26, 95-109.
- Heiselberg, P. & Sandberg, M. (2005). Evaluation of discharge coefficients for window openings in wind driven natural ventilation. *International Journal of Ventilation*, 5, 43-52.
- Heiselberg, P., Svidt, K., & Nielsen, P. V. (2001). Characteristics of airflow from open windows. *Building and Environment*, 36, 859-869.
- Hunt, G. R. & Linden, P. (1999). The fluid mechanics of natural ventilation--displacement ventilation by buoyancy-driven flows assisted by wind. *Building and Environment*, 34, 707-720.
- Hunt, G. R. & Linden, P. (2001). Steady-state flows in an enclosure ventilated by buoyancy forces assisted by wind. *Journal of Fluid Mechanics*, 426, 355-386.
- Hunt, G. R. & Linden, P. (2004). Displacement and mixing ventilation driven by opposing wind and buoyancy. *Journal of Fluid Mechanics*, 426, 355-386.
- Ji, Y., Cook, M. J., & Hunt, G. R. (2007). CFD modelling of natural displacement ventilation in an enclosure connected to an atrium. *Building and Environment*, 42, 1158-1172.
- Jorgensen, F. E. (2002). *How to measure turbulence with hot-wire anemometers - a practical guide*. Dantec Dynamics.
- Karava, P., Stathopoulos, T., & Athienitis, A. K. (2004). Wind driven flow through openings--a review of discharge coefficients. *International Journal of Ventilation*, 3, 255-266.

- Karava, P., Stathopoulos, T., & Athienitis, A. K. (2005). Wind driven flow through building openings. In *International conference 'Passive and Low Energy Cooling for the Built Environment', May 2005, Santorini, Greece.*
- Karava, P., Stathopoulos, T., & Athienitis, A. K. (2006). Impact of internal pressure coefficients on wind-driven ventilation analysis. *International Journal of Ventilation, 5*, 53-66.
- Kato, S., Kono, R., Hasama, T., Ooka, R., & Takahashi, T. (2006). A Wind Tunnel Experimental Analysis of the Ventilation Characteristics of a Room with Single-Sided Opening in Uniform Flow. *International Journal of Ventilation, 5*, 171-178.
- Kobayashi, T., Sagara, K., Yamanaka, T., Otani, H., & Sandberg, M. (2006). Wind driven flow through openings--analysis of the stream tube. *International Journal of Ventilation, 4*, 323-336.
- Kurabuchi, T., Akamine, Y., Ohba, M., Endo, T., Goto, T., & Kamata, M. (2006). A study on the effects of porosity on discharge coefficient in cross-ventilated buildings based on wind tunnel experiments. *International Journal of Ventilation, 5*, 67-78.
- Kurabuchi, T., Ohba, M., Endo, T., Akamine, Y., & Nakayama, F. (2004). Local dynamic similarity model of cross-ventilation, Part1--Theoretical framework. *International Journal of Ventilation, 2*, 371-382.
- Li, Y. & Delsante, A. (2010). Natural ventilation induced by combined wind and thermal forces. *Building and Environment, 36*, 59-71.
- Li, Y., Delsante, A., Chen, Z., Sandberg, M., Andersen, A., Bjerre, M. et al. (2001). Some examples of solution multiplicity in natural ventilation. *Building and Environment, 36*, 851-858.
- Liddament, M. W. (1996). *A Guide to Energy Efficient Ventilation*. Annex V Air Infiltration and Ventilation Centre.
- Lishman, B. & Woods, A. (2006). The control of naturally ventilated buildings subject to wind and buoyancy. *Journal of Fluid Mechanics, 557*, 451-471.

- Lishman, B. & Woods, A. W. (2009). On transitions in natural ventilation flow driven by changes in the wind. *Building and Environment*, 44, 666-673.
- Livermore, S. R. & Woods, A. W. (2006). Natural ventilation of multiple storey buildings: The use of stacks for secondary ventilation. *Building and Environment*, 41, 1339-1351.
- Livermore, S. R. & Woods, W. (2007). Natural ventilation of a building with heating at multiple levels. *Building and Environment*, 42, 1417-1430.
- Moeseke, G., Gratia, E., Reiter, S., & Herde, A. D. (2005). Wind pressure distribution influence on natural ventilation for different incidences and environment densities. *Energy and Buildings*, 37, 878-889.
- Nishizawa, S., Sawachi, T., Narita, K., Seto, H., & Ishikawa, Y. (2004). A wind tunnel full-scale building model comparison between experimental and CFD results based on the standard k- ϵ turbulence representation. *International Journal of Ventilation*, 4, 419-430.
- Ohba, M., Kurabuchi, T., Endo, T., Akamine, Y., Kamata, M., & Kurahashi, A. (2004). Local dynamic similarity model of cross-ventilation, Part 2--Application of local dynamic similarity model. *International Journal of Ventilation*, 2, 389-394.
- Sandberg, M. (2004). An alternative view on the theory of cross-ventilation. *International Journal of Ventilation*, 2, 409-418.
- Sawachi, T., Narita, K., Kiyota, N., Seto, H., ishizawa, S., & Ishikawa, Y. (2004). Wind pressure and air flow in a full-scale building model under cross ventilation. *International Journal of Ventilation*, 2, 343-357.
- Tamura, Y. (2010). Tamura Laboratory Wind Pressure Database. http://www.wind.arch.t-kougei.ac.jp/info_center/windpressure/.

Ref Type: Online Source

- Tieleman, H. W., Ge, Z., Hajj, M. R., & Reinhold, T. A. (2003). Pressures on a surface-mounted rectangular prism under varying incident turbulence. *Journal of Wind Engineering and Industrial Aerodynamics*, 91, 1095-1115.

- Tieleman, H. W., Reinhold, T. A., & Hajj, M. R. (2001). Detailed simulation of pressures in separated/reattached flows. *Journal of Wind Engineering and Industrial Aerodynamics*, 89, 1657-1670.
- Tieleman, H. W., Hajj, M. R., Janajreh, I. M., Reinhold, T. A., & Geurts, C. P. W. (1998). Velocity-pressure correlation in stagnation and separation regions on surface-mounted prisms. *Journal of Wind Engineering and Industrial Aerodynamics*, 77-78, 567-578.
- Turner, J. S. (1973). *Buoyancy effects in fluids*. Cambridge University Press.
- Yuan, C. S. (2007). The effect of building shape modification on wind pressure differences for cross-ventilation of a low-rise building. *International Journal of Ventilation*, 6, 167-176.
- Yuan, J. & Glicksman, L. R. (2007). Transitions between the multiple steady states in a natural ventilation system with combined buoyancy and wind driven flows. *Building and Environment*, 42, 3500-3516.
- Yuan, J. & Glicksman, L. R. (2008). Multiple steady states in combined buoyancy and wind driven natural ventilation: The conditions for multiple solutions and the critical point for initial conditions. *Building and Environment*, 43, 62-69.